A FINITE ELEMENT AND EXPERIMENTAL INVESTIGATION ON THE FATIGUE OF RIVETED LAP JOINTS IN AIRCRAFT APPLICATIONS

A Dissertation
Presented to
The Academic Faculty

by

Amarendra Atre

In Partial Fulfillment
of the Requirements for the Degree
Doctor of Philosophy in the
School of Mechanical Engineering

Georgia Institute of Technology
May 2006

A FINITE ELEMENT AND EXPERIMENTAL INVESTIGATION ON THE FATIGUE OF RIVETED LAP JOINTS IN AIRCRAFT APPLICATIONS

Approved by:

Dr. W. Steven Johnson, Advisor
School of Mechanical Engineering
Georgia Institute of Technology

Dr. Rami Haj-Ali
School of Civil and Environmental Engineering
Georgia Institute of Technology

Dr. Richard W. Neu
School of Mechanical Engineering
Georgia Institute of Technology

Dr. David Steadman
Prinicipal Engineer, Enabling Technologies
Delta Airlines, Atlanta, GA

Dr. Jianmin Qu
School of Mechanical Engineering
Georgia Institute of Technology

Dr. Christopher Lynch
School of Mechanical Engineering
Georgia Institute of Technology

Date Approved: March 29 2006

Mom, Dad, Bro, Sis-In-Law,

This is for you.

ACKNOWLEDGEMENTS

I would like to thank my advisor Dr. Steven Johnson for his support and guidance during my doctoral work. He has provided me numerous opportunities to present our work and improve upon my communication skills, given technical feedback and also the freedom to work independently. I would like to thank Dr. Rick Neu for not only serving on my committee but also for providing me an opportunity to work with him for the teaching practicum. I gained not only a lot of knowledge from the course but playing "detective" in the latter part of the semester was especially fun. I thank Dr. Chris Lynch, for serving on my committee and giving me an opportunity to learn about the exciting world of piezoelectrics. I thank Dr. Rami Haj-Ali for being a member of my committee and establishing a "thermographic" collaboration between his research group and our work. I also thank Dr. Jianmin Qu for taking the time to serve in my thesis committee.

It has been a pleasure to work with the team at Delta Airlines. Dr. David Steadman has provided me technical data whenever needed and also has always been there to discuss research ideas. He has helped immensely in preparing "good" specimens to ensure a collection of excellent data. I thank him for his time, advice and support. Dr. Ramesh Ramakrishnan and Doug Jury spent their valuable time in sharing with me their plethoric experience in damage characterization. I thank them for making me somewhat knowledgeable in this area. I would also like to thank the technicians at Delta Airlines for providing the experimental specimens critical for validation of the modeling effort.

I would also like to thank the Federal Aviation Administration specifically John Backuckas and Felix Abali and Jim Newman at Mississippi State University for providing the funding for this work and also an opportunity to present our results.

I would like to thank my parents for all their support in my education till date. I would like to thank my brother Suhrud and sister-in-law Gayatri for always being there to listen to my ramblings and for their support in my graduate education. Procrastination is the bane of any graduate student. However, I would like to thank my cousin Malavika for leading me down the path of procrastination, these past few months, with our endless conversations about nothing. The talks provided solace in an otherwise seemingly monkish lab existence.

For a while it seemed I might never recover my mental elasticity, stretched from working on this tome (soon to dissaparate in the annals of ProQuest?). Kyle Webber's drop in's at the lab were a welcome change of pace. I thank him for his friendship. The group we developed at the beginning of our graduate studies with Amelia Case and Matt Hammond has been the best study group I have been with. I would like to thank, Matt Hammond for his friendship during my tenure at Tech. I would like to especially thank him, his parents, his wife Loren, her sister Lydia and her parents for their hospitality and wonderful thanksgiving dinners. The visits to his house were a much needed getaway from geekland. Playing with Spencer and Caroline as "Mr. Amara" was really fun. I have to admit though, an entire day with them made me yearn for my cushy waterless, windowless existence in the depths of Tech. On a side note, of course, this thesis would not be complete without saying this to Matt: "She had man-hands!"

I would like to thank my research group specifically Don, Shelby and Paul for all of their help. Rick Brown has been invaluable in providing his experience much needed for the experimental work. I also enjoyed listening to his tales of the "Westinghouse mafia". I thank Shane Johnson for taking the time to work with me on the thermographic testing. I also thank him sharing some of his "lessons" in life with me. I thank Samer Tawfik for his initial help in the modeling work.

I would also like to thank Adrienne Lavine at UCLA. She has always provided me timely and sound advice. I thank her for her friendship and most importantly her support. I also thank Lisa Mauck Weiland for her advice and help throughout my graduate studies.

I would like to thank Ashish Shah for his friendship. It's been a long time since we met but he has always been there as a great friend. He has been a sounding board, has provided support at all times and has also led me down the path of procrastination reminiscent of our undergrad days.

Finally, I have to admit that taking coursework, working on this research, TA'ing and applying for faculty positions simultaneously did take its toll on me. At times I did come close to saying: "Screw it! Sandy beaches here I come". Thank you God for providing me the strength to finish my doctoral work.

Go Jackets!

A.P.A

March 29th 2006

TABLE OF CONTENTS

Page

LIST OF TABLES

LIST OF FIGURES

Page

Summary

Aircraft fuselage splices are fatigue critical structures and the damage associated with these structures has been widely recognized as a safety issue that needs to be addressed in the structural integrity of aging aircraft. An effective means for structural evaluations of airworthiness of aging aircraft and obtaining essential data for evaluation of such type of fatigue cracking is airframe teardown inspections and laboratory fatigue testing of lap joint coupons. The Federal Aviation Administration and Delta Airlines teamed up in such an effort to conduct destructive evaluation, inspection and extended fatigue testing of a retired Boeing 727-232 (B727) passenger aircraft near its design service goal.

Preliminary visual inspection revealed a large number of cracks in the aircraft fuselage lap joint emanating from the rivet/skin interface. Most of these cracks were observed in the lower skin such that they could not be detected under an operator's routine maintenance. The presence of these cracks was attributed to the sharp gradients of stress arising from contact between the installed rivet and rivet holes. The residual stress field generated during the rivet installation has a strong impact on the nucleation and propagation of fatigue cracks at and around the rivet/skin interface. The main objective of this research was to establish a link between critical riveting process parameters on the potential of fatigue damage in the joint.

From an analytical perspective, the significance of contact and plasticity in the riveting process made the problem well suited to a finite element modeling (FE) solution. In addition to the need to understand the mechanics of the process, there was also a need to understand how manufacturing process variations affect the residual stress state produced in the joint. Both of these objectives were addressed in this research.

The investigation conducted herein was carried out in four phases. In the first phase a two-dimensional (2D) axisymmetric model of the riveting process was developed using Implicit FE solvers, deliberately designed to simulate previous experiments conducted by a team of Canadian researchers involving force-controlled riveted specimens. A quarter-symmetry quasi-static three-dimensional (3D) model of the process was then analyzed using Explicit FE tools, to simulate previous experiments conducted by a team of French researchers. From a modeling standpoint the experimental comparisons offered a good set of validation measurements obtained under well-controlled laboratory conditions to establish solver capabilities. Additionally, the analyses also pointed out the difference in capabilities of the two solvers in simulating the same process. Overall the prediction quality of the models was good and it generated confidence in the ability to accurately capture the residual stress state from such a complex forming process.

The second phase of this investigation utilized the FEM approaches and the lessons learned from the first phase to specifically focus on the development of a three-dimensional displacement controlled riveting process model for the B727 lap joint configuration. Effects such as rivet hole defects, presence of sealant, presence of debris and rivet interference were considered using the developed model. The analyzed models demonstrated a strong dependence of the residual hoop stress on process variations. Effect of under-driven rivets was observed to be especially critical in altering the residual stress state qualitatively as well as quantitatively.

In the third phase of this investigation, the residual stress and strain results already generated from the riveting process models served as an input to a global three rivet lap joint model designed to approximate the in-service loading experienced by the B727 fuselage splice. A good comparison of the state of damage observed around the

rivet holes, as evident from the teardown inspection, to the critical stress location predicted by the FE model provided excellent validation to the analysis.

In the final phase of this research, experimental fatigue testing of riveted lap joint specimens was conducted with the specific goal of forging a link between rivet installation and hole quality effects on fatigue performance of the joint. A comparison of the surface strains predicted by the FE models to the surface strains of the tested specimen captured through thermal imaging techniques offered an additional source of validation to the analysis. An observed correlation between the fatigue lifetimes of the tested specimens and controlled parameters showed under-driven rivets to be the most threatening in reducing the fatigue life of the joint.

Chapter 1: Introduction

The fuselage of an aircraft consists of sheet panels, stringers and stiffeners held together by riveted lap joints. Although different joining techniques exist, the skin panels are typically fastened together with rivets. Numerous such rivets are required to join the skin completely. The flight fatigue loading is due to the pressurization and depressurization of the fuselage, which occurs once every flight. The concentrated stress state at the rivet/skin interface combined with a large number of loading cycles is a primary cause of crack initiation at and around the rivet/skin interface. The 1988 Aloha Airlines flight 243 incident in which an extensive section of the fuselage ripped off from the aircraft while in flight, demonstrates the importance of aircraft fastener hole fatigue. The incident was attributed to linking up of cracks at different rivet holes, caused by a combination of fatigue and corrosion.

An effective means for structural evaluations of airworthiness of aging aircraft and obtaining essential data for evaluation of such type of fatigue cracking is airframe teardown inspections and laboratory fatigue testing of lap-joint coupons. The Airworthiness Assurance Working Group (AAWG) under the Federal Aviation Administration (FAA) is currently using published technical recommendations on rulemaking to develop programs that monitor and prevent such long-term damage effects [1]. The destructive testing and analysis of aircraft structures will provide the aviation community with comprehensive guidelines for a structural maintenance program to assist the FAA to issue rules, policy and advisory circulars related to ensure continued safety.

For the primary focus of characterizing fatigue damage in aircraft fuselage structure the FAA and Delta Airlines (DAL) teamed in a three year effort to conduct destructive evaluation, finite element analysis, fatigue testing and inspection of nine lap-spliced panels obtained from a retired Boeing 727-232 (B727) airplane near its design service goal (DSG) [2]. This study is a part of the effort and is primarily concerned with the effects of the riveting process and subsequent load transfer on fatigue life of the airframe lap joints.

1.1 Description of findings

The aircraft selected for this program was a Boeing 727-232 (B727). The airplane was placed into service in 1974 and retired in 1998. During that time, the airplane accumulated 59,497 flight cycles and 66,412 flight hours and was near its DSG. The airplane was owned and operated exclusively by DAL and had a well documented service history. Throughout the operation of the aircraft, the average operating pressure was 8.6 psi [2]. Figure 1.1 shows a picture of the aircraft. Nine fuselage lap joint areas susceptible to Widespread Fatigue Damage (WFD) were removed from the aircraft. Out of these, five were destructively evaluated and four were subjected to extended fatigue testing at the FAA testing facility located at Atlantic City, New Jersey. Figure 1.2 shows a view of the aircraft with the fuselage panels removed for inspection. Prior to removal, all target sections were labeled with boundaries and identification marks to indicate the location and orientation of the section with respect to the aircraft [2].

A field inspection was also performed at the storage site to catalogue the condition of the aircraft and target structure. Detailed visual inspections (DVI) and non-destructive evaluations (NDI) were conducted using Mid-Frequency Eddy Current (MFEC) and external Low-Frequency Eddy Current (LFEC) methods. After the site

inspections the target structure was removed and transported to the analysis site at DAL in Atlanta, GA, for post removal inspections [2]. Figure 1.3 shows the schematic of the removed panels and the fuselage lap joint.

Figure 1.1 Aircraft selected for the FAA/Delta teardown program

Figure 1.2 Aircraft with panels removed for damage characterization

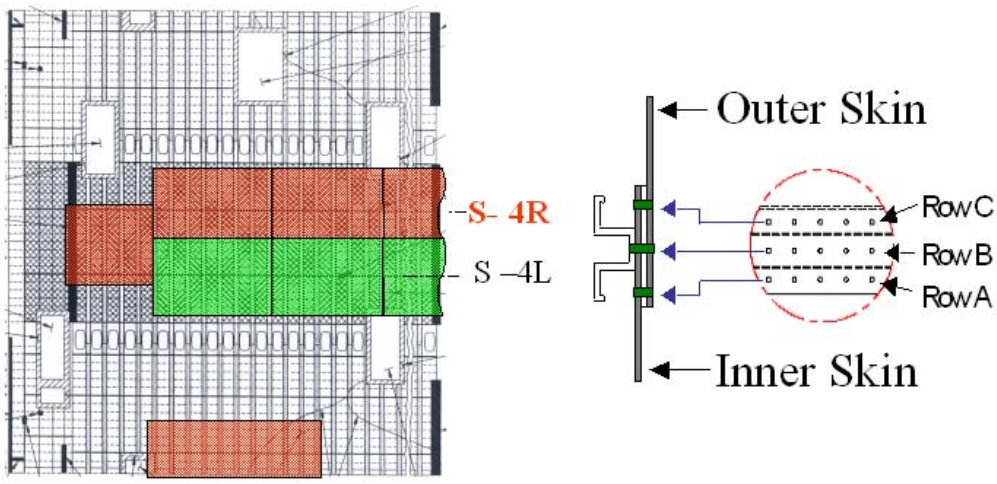

Figure 1.3 Schematic of the removed panels and the fuselage lap joint

Preliminary findings from the inspection included the following:

- Several cracks were observed along the **S4R panel (hereafter referred to as the right hand side panel)**, inner skin, outer row A.

- Each crack had several origins and the general direction of the cracks was normal to the hoop circumferential direction. The primary origin of the cracks was at the corner of the hole and the faying surface (Figure 1.4). While hole quality was not uniformly good, the defects in the holes were generally in the circumferential direction (Figure 1.5). Fracture surfaces appeared to be free of corrosion and any gross mechanical fretting damage.

- 60% of the rivets along the right hand side panel were observed to be under-driven (final installed rivet head diameter less than specifications).

- Significant variations in rivet interference were observed through the rivet rows along the right hand side panel combined with presence of embedded drill shavings in the sealant (Figure 1.6).

- Very few crack indications were observed along the **S4L panel (hereafter referred to as the left hand side panel).**

- Quality of installed rivets along the left hand side panel was significantly better (Figure 1.7).

- The right hand side panel used a different quality sealant than the left hand side panel.

- The right hand side panel rivet spacing along the lap joint was different than that along the left hand side panel.

The necessity of obtaining an accurate understanding of effects of the initial interference induced by rivet installation and the resulting residual stress field around the periphery of the hole is an obvious one. The nature of this residual stress field can have a profound impact on the nucleation and subsequent propagation of fatigue cracks emanating from near the edges of the hole. Motivated by teardown inspections and laboratory non-destructive examinations of the fuselage lap joint, this research was targeted at analyzing the localized stress conditions at the rivet/skin interface resulting from rivet installation and subsequent load transfer.

1.2 Approach

The adopted approach for this work is summarized visually in Figure 1.8 with a brief summary following.

Development of a two-dimensional (2D) axisymmetric force controlled rivet installation simulation using ABAQUS/Standard: The purpose of this analysis was to establish implicit simulation capabilities and check the extent of the accuracy of numerical tools in predicting the residual stresses. This was achieved by comparing the force-displacement curves, the rivet deformation parameters and strains from the simulation with experimental data for a range of installation forces. Development of a quarter-symmetry

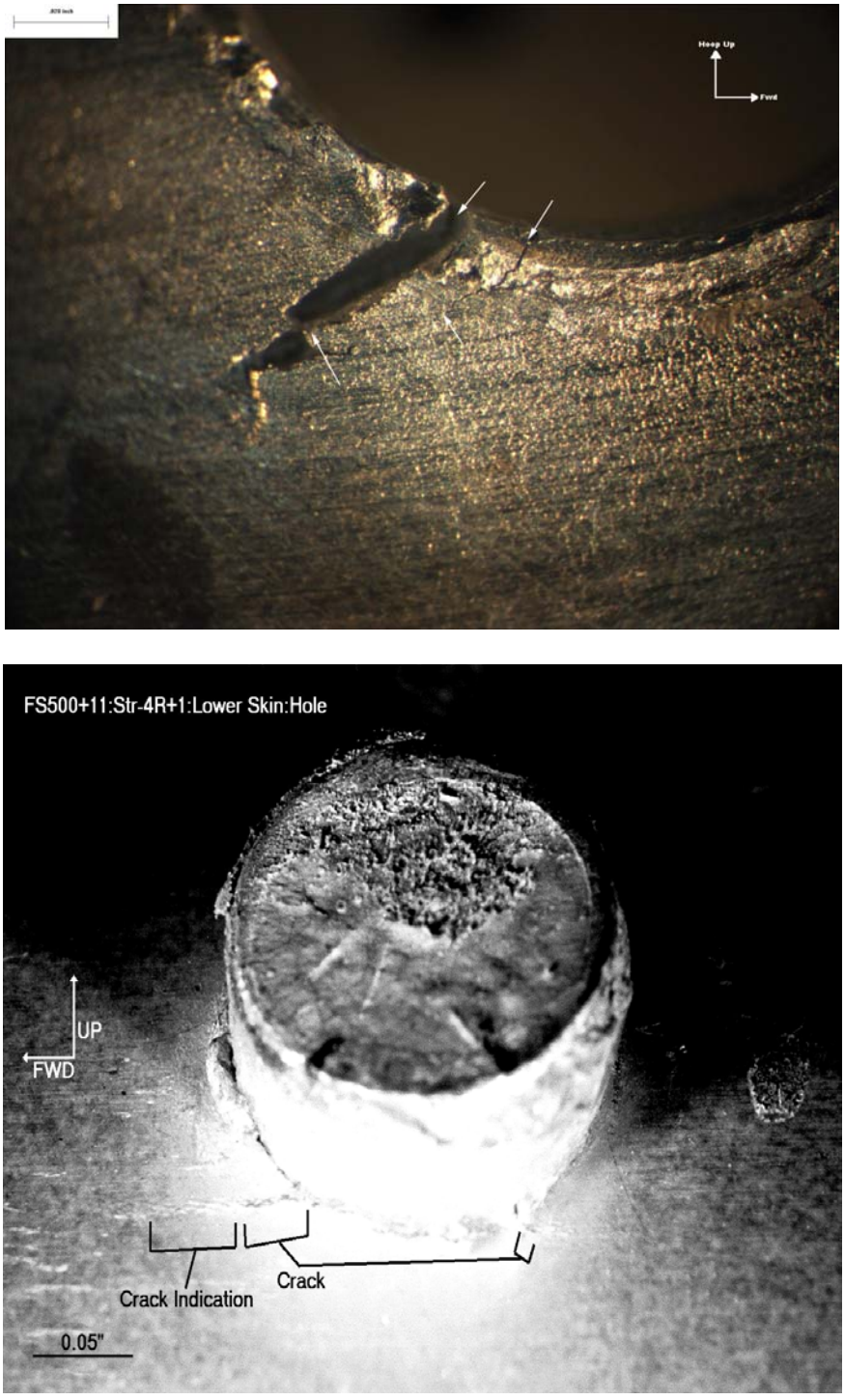

Figure 1.4 Example of crack indications at the rivet holes in the right hand side panel panels

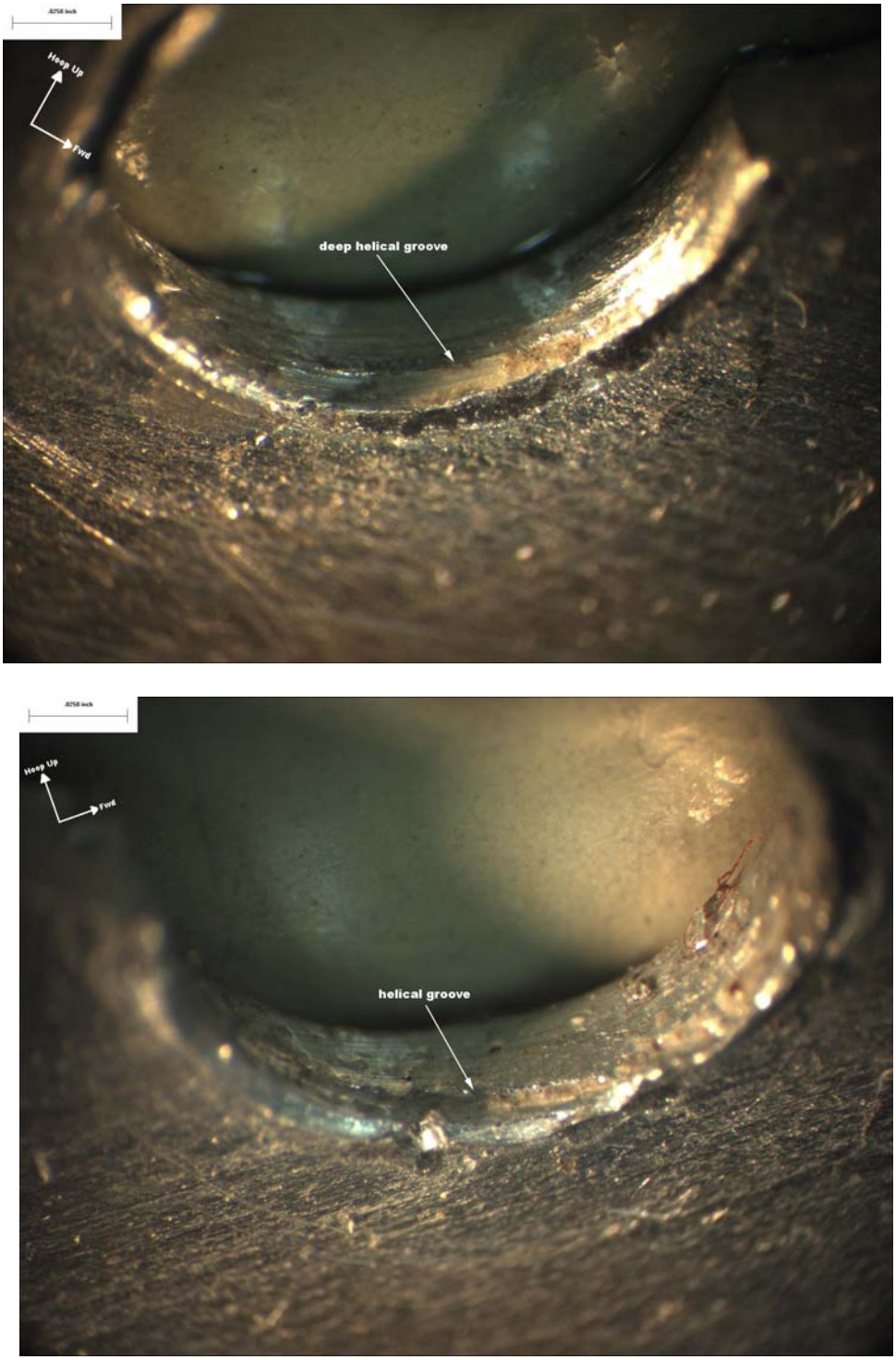

Figure 1.5 Example of the rivet hole defects in the right hand side panel panels

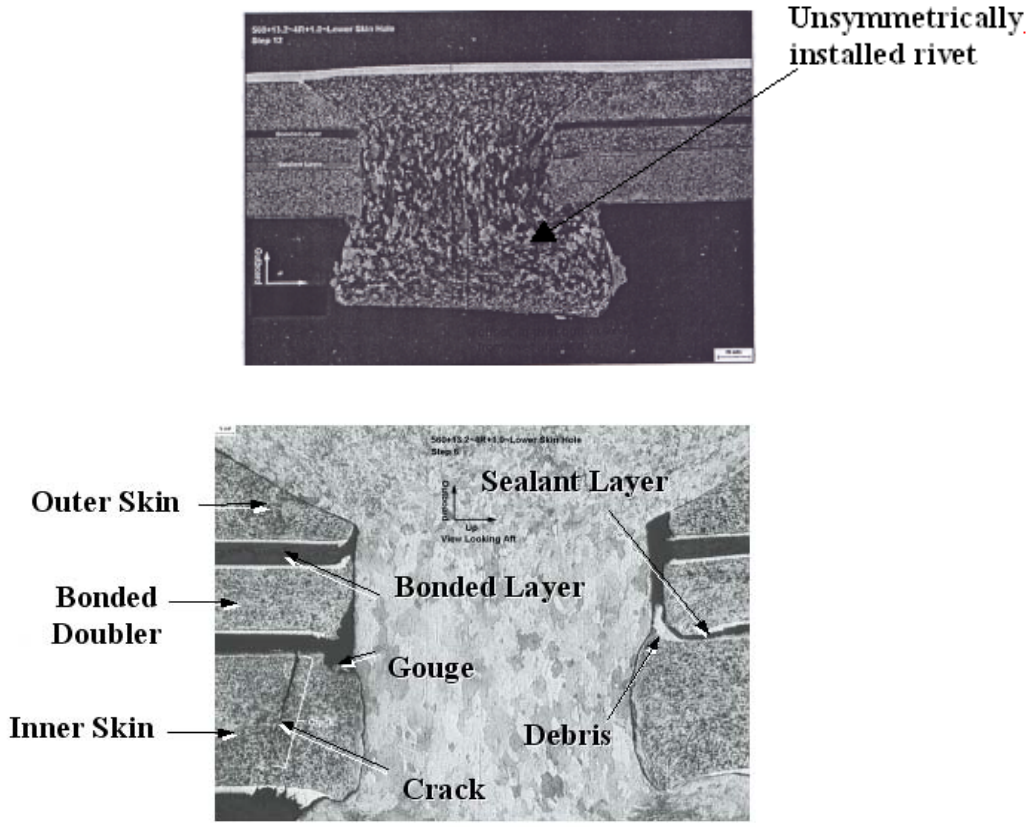

Figure 1.6 Microscopy of riveted sections along the right hand side panel. Evident are the differences in rivet interference, deformation of sealant and presence of drill shavings

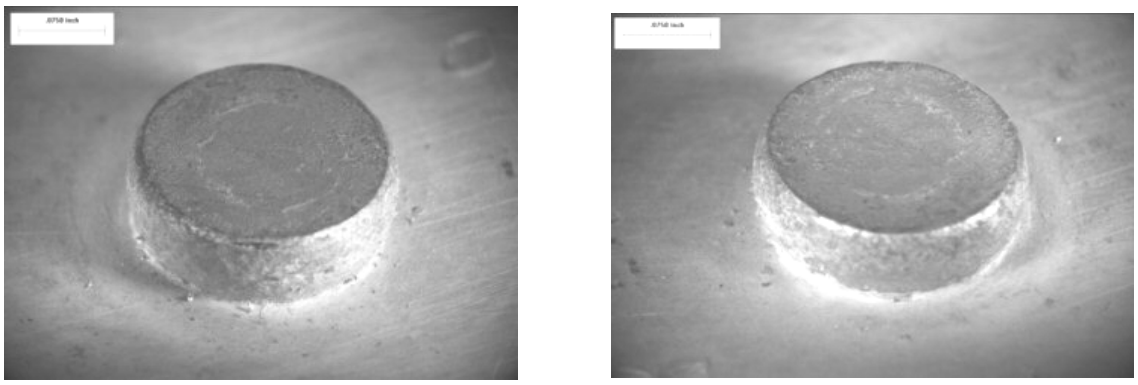

Figure 1.7 View of the installed rivets along the left hand side panel. General observations on rivet installation show that the rivets were all installed very uniformly with little or no tilt in the tail buttons and no offsets of the buttons' axes with respect to the rivet shank axes

three-dimensional (3D) quasi-static rivet installation simulation using ABAQUS/Explicit: The purpose of this analysis was to investigate the accuracy of explicit finite element tools in simulating the forming process. This was achieved by comparing the force-displacement curves and strains from the simulation to those measured by experiment.

The complex contact interactions and large deformations pose a significant problem in performing rivet simulations even for a commercial finite element program. Another aim of this work was to provide a detailed generalized documentation on element library, material behavior, contact formulations of the code and overcoming convergence difficulties (Appendix D). Particular emphasis was placed on specific capabilities of the code (Implicit/Explicit) with regard to correctly modeling such forming processes (Appendix D).

Development of a baseline 3D model based on the data available from DAL for the B727 rivet configuration: The 3D model has the capability of representing the manufacturing process variations more accurately and can be implemented for modeling subsequent load transfer effects. The results from the baseline model serve as a comparison for parametric variations. The effect of some critical process parameters on the residual stress state in the skin, were analyzed using the developed model. The simulated process variations as observed from the teardown inspection included: presence of hole defects such as gouges, presence of drill shavings, presence of sealant, varying hole sizes and varying rivet interferences. The developed 3D model was also implemented to investigate the effects of different percentages of load transfer on the stress state in the lap joint. Results were compared to the stress state predicted without taking into account initial rivet interference.

Results from the rivet installation models were input to a global lap joint model representing a three-rivet row joint. The rivet installation models applied the initial residual stress state. This was followed by application of the in-service loads to observe

the resulting stress state at and around the rivet holes. The model served to demonstrate the importance of load transfer through the fuselage splice. The model results were compared to the damage characterization results available from DAL. The effects of variation in interference through the rivet row, variation in friction and presence of sealant on load transfer and resulting stress state on the joint was also analyzed using the developed model.

Experimental fatigue testing of riveted lap-joint specimens: The goal of the experimental fatigue testing with riveted lap joint specimens was to form a link between rivet installation, nucleation of fatigue damage and subsequent fatigue performance of these joints. A summary of the goals can be given as: Manufacture lap joint specimens for critical parameters under controlled conditions; fatigue test joints under a range of loads representative of fuselage structure; identify critical areas of fatigue crack nucleation sites; correlate the process parameters with observed failure mechanisms to identify critical variables in nucleation of cracks.

1.3 Research Outcomes

The research work done will:

- Provide a relationship between the impact of riveting process parameters on potential fatigue damage in aircraft structural joint that can be implemented by aircraft fatigue designers to assist in retarding fatigue damage.
- Provide a comparison of the effectiveness of the finite element models, Implicit/Explicit methods to model the riveting process, particularly the sealant analysis.

- Provide stress/strain results that can be applied in crack growth analyses programs such as FASTRAN.
- Provide an observation on the effects of interference on the mechanics of load transfer and resulting stress state in the rivet rows for the fuselage splice joint.
- Provide a database to the FAA of the critical parameter models, recommendations, problem methodology, which will assist in improving structural integrity of aircraft structures.

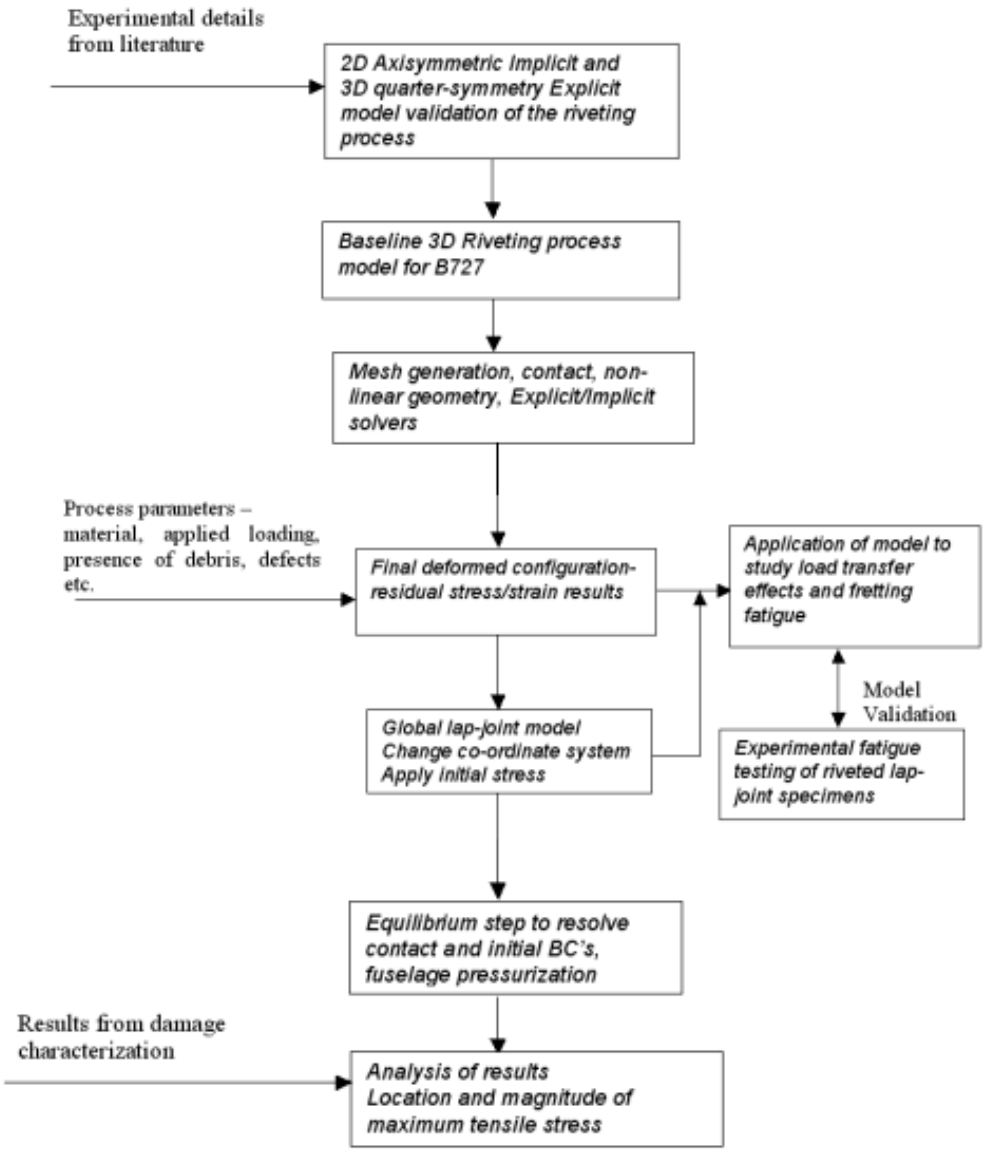

Figure 1.8 Flowchart outlining the approach of this work

Chapter 2: Background and Literature Review

Joining two sheets together with rivets forms a riveted single lap joint. The process is accomplished by driving the rivet shank with a rigid bucking bar while a rigid tool constrains the head of the rivet. This is illustrated in Figure 2.1. The bucking bar may be driven hydraulically, pneumatically or manually. When such aircraft skin panels are joined with an interference fit, a residual stress field is created. With increased interference plasticity strain hardening occurs. When the skin panels are subjected to in-service cyclic loads, load transfer takes place locally at the rivet/skin interface. The resulting contact stresses at the rivet/skin interface play a primary role in propagation of fatigue cracks at and around the rivet/skin interface. The primary goal of this investigation was to develop a model that accurately characterizes the residual stress state resulting from the riveting process and implement the model to study the effects of critical manufacturing process variations.

To date, there has not been comprehensive research published in open literature, which addresses manufacturing process variations (such as hole quality and sealant issues combined with rivet interference) in the riveting process. Despite its complex nature, however, when separating this problem into the general engineering issues that are germane to the application, one can find much published research that is pertinent. Once all the contributing subjects to the problem have been identified, a survey of the previous research in each of these areas can be done before tackling the more specific problem. What follows is an extensive survey of significant research conducted on crack growth in riveted lap joints, to include the implementation of analytical and experimental tools to characterize riveted lap-joint residual stresses, study

of fatigue life in riveted joints and development of analytical models to predict fatigue crack growth in lap-joints.

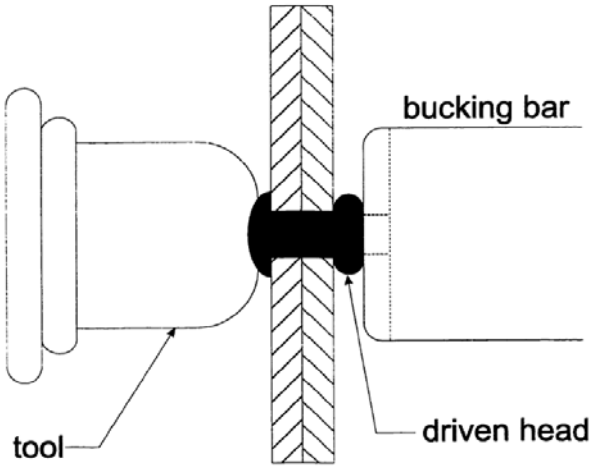

Figure 2.1 Schematic of rivet installation [3]

2.1 Analytical study of residual stresses around fastener holes

The rivet deformation is analogues to cold working of holes with an expanding mandrel. By squeezing the rivet a radial outward in-plane pressure p is applied inside the fastener-hole in an infinite sheet. The elastic solution for the stress field near the hole is:

[2.1] $$\sigma_r = -p\left(\frac{r}{R_o}\right)^{-2}$$

[2.2] $$\sigma_\theta = p\left(\frac{r}{R_o}\right)^{-2}$$

where r is the distance from the center of a hole with radius R_o .

Increasing the internal pressure can lead to plastic deformation of the sheet material. A relationship between the plastic deformation and stress distribution of elastic-perfectly-plastic materials was shown by Park and Atluri [4]:

[2.3a] $$\sigma_r = -p + \sigma_y \ln\left(\frac{r}{R_o}\right) \qquad R_o \le r \le r_y$$

[2.3b] $$\sigma_r = \frac{-\sigma_y}{2}\left(\frac{r_y}{r}\right)^2 \qquad r > r_y$$

[2.4a] $$\sigma_\theta = (\sigma_y - p) + \sigma_y \ln\left(\frac{r}{R_o}\right) \qquad R_o \le r \le r_y$$

[2.4b] $$\sigma_r = \frac{\sigma_y}{2}\left(\frac{r_y}{r}\right)^2 \qquad r > r_y$$

where σ_y is the material yield stress, r_y is the radius of the plastic region.

Park and Atluri obtained the residual stress field by subtracting the elastic stress field of Eq. 2.1 and 2.2 from Eq. 2.3 and 2.4 after releasing rivet squeeze force. Limitations of this analytical model were pointed out by Muller [5] as: the model does not include strain hardening, the model is one-dimensional and neglects hole expansion variation through the thickness, a 3D stress state results from the driven rivet head exerting a pressure on the sheets.

2.2 Experimental measurements of residual stresses around fastener holes

Strain gage methods, ultrasonics, X-ray techniques and magnetics are some of the methods that can be used to measured residual stresses. However, the structural peculiarities of riveted joints make it an extremely tenuous task to implement any of these methods for nondestructive determination of residual stresses on the surface, or in the immediate vicinity of a hole.

Langrand et al. [6] applied a strain gage method to measure radial sheet strains during and after riveting. They applied this method to circular and square shaped sheets. A single rivet was present in each specimen with an applied crushing velocity of 2 mm/min slow enough to be considered quasi-static. They observed more than 20% compressive strain levels near the crushing edge and lower than 1% strain levels away from the edge, while riveting. After riveting, the residual strains were similar to maximum observed during the process. The strain levels near the punching edge could not be observed accurately due to damage to the strain gage. Furthermore, the strain gages only measured the radial strain. The residual strain through thickness and inside the sheet could not be detected.

The X-Ray technique was applied by Fitzgerald and Cohen [7] to determine residual stresses around rivets in clad aluminum alloy plates. They assumed an in-plane stress state over the depth of penetration. The implemented technique was documented thoroughly in their research. This technique was limited such that the entire residual stress state at and around the rivet/skin interface could not be measured. Only residual stresses close to the sheet surface could be calculated.

The riveted joint interference can improve the lap joint's ability to resist fatigue. Nepershin and Knigin [8] suggested an interference of 2 to 3%, while Yarkovets et al. [9]

recommend an interference value of 2.2 to 3.4% for passenger aircraft. Demina and Volkov [10] define interference as

[2.5] $$\delta = \frac{d_1 - d}{d} X100\%$$

where d_1 is the deformed rivet diameter and d is the hole diameter.

Ryzhova [11] applied a nondestructive ultrasonic inspection method to determine rivet/hole interference. The ultrasonic method was based on echo signal amplitudes, which are a function of interference. Experimental data was used to establish a regression between the interference and the mean value of ultrasonic signal amplitude. Ryzhova [11] also established a linear correlation of the average echo signal amplitude value and the averaged residual stress along the rivet height based on the least-squares method. However, the ultrasonic method could only determine radial residual stresses along rivet height at the rivet/hole interface by using the relation between the rivet residual stresses and interference. No results for hoop or radial stresses in the sheets were reported in this study. A labor-intensive destructive method was utilized to measure residual stresses in the rivet body.

Muller [5] used photo-elastic stress measurements, rivet-sheet springback measurements and micro-hardness measurements to measure residual stress at the panel-mating surface. The experiments were however unsuccessful and he concluded that experimental measurement of residual stresses was not a simple task.

2.3 Finite element methods to characterize residual stresses around fastener holes

The finite element method is a powerful numerical tool to simulate complex forming problems. Review of the literature showed that this method had been applied to study riveted joints since the 1990's. A force-controlled 2D axisymmetric model, which consists of two circular pieces of sheet metal connected by a single rivet, had been implemented to simulate the rivet installation in majority of prior research. The axisymmetric finite element analysis models a one-quarter joint configuration with geometric, contact and material non-linearity.

Slater [12] analyzed this model for a non-countersunk configuration. He investigated the results (interference, residual stresses) for only one value of squeeze force. Based on this model, Muller [5] studied the residual stresses for a range of squeeze forces. He used Patran (preprocessor) and ABAQUS (solver) for his analysis. A slug type rivet (driven head on both sides) and a countersunk configuration were analyzed in his research. An elastic-linearly-plastic material behavior was assumed in the model. Muller concluded that a force-controlled rivet installation provides a more accurate control for the process. The results of residual stresses at the hole wall and along the mating surface as well as clamping stress (in thickness direction) were given and discussed in Muller's work. His conclusions for the slug and countersunk models can be summarized as follows [5]:

1. Slug model: The residual tangential stresses along the mating surface become compressive from tensile in the vicinity of the hole as a result of the increasing squeezing force. Tensile residual stresses increase away from the hole. Residual radial compressive stresses occur on the wall of the hole, but are not homogeneous through the thickness of the sheet. The maximum compressive residual stress occurs away from

the rivet hole. For large squeeze forces, significant compressive radial residual stresses occur at a considerable distance from the hole edge. With a larger driven head, significant clamping stresses can be induced. These are generated by increasing the squeeze force.

2. Countersunk model: In the finite element simulation, only one value of squeeze force was applied. A reduction of the hole expansion towards the rivet flush head was observed from Muller's finite element results. The average rivet expansion was smaller for the countersunk sheet than for the non-countersunk sheet. The residual stresses at the hole edge (both the tangential and radial compressive residual stresses) were larger for non-countersunk sheets than for countersunk sheets.

Muller's research was limited on the effects of material properties and the residual stress field. Szolwinski and Farris [13] implemented a strain-hardening material model for the rivet and the plates to analyze the riveting process. The material model was based on experimental compression testing of 2117-T4 rivet shanks. Squeeze forces ranging from 2500 to 5000 lbf were considered in the analysis. Szolwinski and Farris [13] observed that an increasing value of squeeze force pushed the zone of tensile hoop stress away from the hole and resulted in a larger driven head size. A non-countersunk model was analyzed. A through-thickness gradient of residual stresses was observed in the model with a compressive hoop zone dominating near the hole periphery and tensile hoop zone away from the hole. Their investigation showed that an increase in fatigue life could be obtained with larger squeeze force. None of the cases analyzed indicated appreciable levels of residual clamping pressure through the thickness contrary to that of Muller's [5] findings for a slug-type rivet with a driven head on both ends. Their results were consistent, however, with modeling results conducted by Fawaz [14]. Comments were also made regarding the relationship between the riveting process parameters and trends in observed failures of riveted lap joint test

articles. Their study showed that fatigue life increases with larger squeeze forces, and decreases with an increase in fatigue load.

A large number of aircraft manufacturers use rivet-tail shape parameters, such as tail height and tail diameters, as a means of determining whether a joint will operate successfully in service. Displacement controlled riveting is the main method of determining this. A displacement controlled riveting process was analyzed theoretically by Nepershin and Knign [8]. The analysis primarily characterized the interference and residual stresses in a riveted joint using a rigid-plastic-body model. A finite difference approach was applied to replace differential equations using Tresca plasticity conditions in the principal stress plane to analyze the plastic flow due to the upsetting of the rivet head. The formation process was solved by using a sequence of Cauchy, Riemann and mixed boundary-value equations defined by: the shape of the free side surface of the rivet head being formed, the boundaries of the tool, the plastic-friction coefficient at the boundaries between the plastic region, the tool, and the package. Though similar to the finite element method, finite elements provide an easier tool for analysis.

Nepershin et al. [8] also carried out nonlinear finite element simulations by using the previous finite difference model to form a riveted joint using the force boundary conditions of stack loading on upset rivet heads. Results for interference distribution across joint packages were compared with experimental data and a linear approximation for calculating interference values at certain positions, based on riveting stress, was also proposed. Comparisons between the calculated interference and the experimental results determined by measuring the rivet diameter after cutting the package were also covered in their paper. Significant discrepancies were observed between the calculated and experimental results.

Langrand et al. [6] conducted 3D finite element simulations of rivet forming. Circular and square sheet geometries were analyzed and experimental residual strain

data was used to validate the finite element model. The crushing velocity applied in the simulation was slow enough to be considered quasi-static. They applied a strain hardening material model for both the rivet and sheet based on experimental data. The finite element simulations agreed with experiment but full residual stress/strain field around the hole were not found.

The residual clamping stress exerted by the rivets on the joint was studied by Deng and Hutchinson [15]. Relation between the clamping and applied force was analyzed using finite element methods in the small strain framework. Full finite strain formulation was used for re-computation of some results. Results were analyzed for an elastic-perfectly-plastic material model for both the rivets and sheet and effects of strain hardening on the residual clamping stress were also discussed.

Ryan and Monaghan [16] simulated rivet installation with an elasto-plastic axisymmetric model for fiber laminate and typical aluminum alloy countersunk panels. A large deformation, non-linear quasi-static analysis was conducted since sheet materials, 2024-T3, fiber metal laminate, rivet, 2117-T3 alloy are not strain rate sensitive at room temperature. They concluded from the models that the localized compressive hoop stress after the riveting process increases fatigue life of panels. It was also observed that fiber metal laminates could extend fatigue life of the riveted joint as compared to monolithic aluminum alloys. They also noted that the behavior of aluminum alloy relative to the FML panels was very different, hence the squeezing load should be reduced while installing rivets in FML panels and tail height and tail diameters cannot be used successfully as a means of comparing the behavior of various panel materials.

Swenson et al. [17] analyzed a finite element model of crack growth in a riveted lap joint. The panels were modeled as 2D layers connected by elastic shear springs. The rivet was modeled as a disk in each layer connected by an adhesive. Automatic remeshing was implemented to model crack growth. The model however lacks sufficient

similarity to a riveted lap joint and the rivet is only realistic as a non-countersunk one without any heads.

Weissberg et al. [18] performed 3D linear elastic FE analysis of a bolted lap joint using NASTRAN. They investigated the compliance of riveted joints experimentally and found reasonable agreement between the two results. A major conclusion from the work was that the compliance measurements show considerable scatter due to unknown values of interference and clamping force.

Sundarraj et al. [19] studied 3D effects in double-shear single rivet lap joints via axisymmetric FE models. The model was however applicable only in the absence of frictional forces and for limited number of loads. Ekvall [20] modeled a four-rivet row lap joint with bar elements connected at node points offset from the rivet location. The model was linear elastic.

In a recent study conducted at the National Research Council at Canada, Li et al. [21,22] have presented 2D and 3D numerical techniques to characterize the stress state for a one-rivet joint through the entire loading history (rivet expansion and tensile loading). Their numerical results predicted that the residual stress induced by the rivet squeeze force had a considerable effect on the stress variations in the tensile loading stage.

For riveted lap joints with sealant, Imanaka [23] has analyzed the fatigue strength of adhesive-rivet lap joints experimentally. He has also investigated the stress distribution in the riveted joint for a high modulus adhesive using the finite element method. Similar analysis has also been conducted by Liu and Sawa [24] to evaluate the strength of single lap adhesive joints with rivets, subjected to external bending moments. Dechwayukul et al. [25] have presented a Thin Adhesive Layer Analysis (TALA) finite element method to investigate the effects of thin sealant layers on the fatigue performance of riveted countersunk and non-countersunk lap joints. They compared

their results to riveted lap joints without sealant and observed a reduction in the stress concentration factor at the rivet/skin interface. The analysis however does not take into account plasticity and the non-uniform interference produced by rivet installation.

2.4 Other methods to characterize residual stresses around fastener holes

The interference stresses resulting from the riveting process can be analyzed using other methods such as the misfit method. In this method radial and rivet height conformity is forced between initially oversized ratio of rivet shank and hole and undersized ratio of shank height over panel depth. Fung and Smart [26] employed a thermal expansion method by varying the temperature of the rivet shank to reduce its length and expand it in the radial direction. Their interference values were typically lower than those observed in practice. Bellinger et al. [27] and Shi et al. [28] implemented a squeezing force method by applying squeeze force at two heads of the rivet followed by external loads to predict stress distribution.

2.5 Mechanical properties of rivet materials

Most rivets are made from 2117, 2024 and 7075 aluminum alloy, and most sheets are made from 2024-T3 aluminum alloy. The extra weight penalty of the riveted joint is imposed by the upset rivet head. Aluminum riveting provides several advantages, such as low manufacturing cost, low material cost and fuel economy, to the aviation industry. The majority of aerospace manufacturers currently adopt the MS20426 type rivet to assemble the fuselage section. The rivet's mechanical property is also an important component in the structure. Patronelli et al. [29] have investigated rivet

performance in actual service conditions. They have developed an original micro-tensile test rig to test rivet specimens. The rig was first implemented by them to test 7050 aluminum alloy specimens with 5% compressive residual strains corresponding to a driven rivet head. Their results show that the 7050 alloy shows a kinematic hardening behavior.

2.6 Study of fretting fatigue

Fretting is a type of damage arising from a combination of wear, corrosion and fatigue. It is a contact mechanism driven by micro-motion and stresses at the contact zone. Early analyses conducted by Mindlin [30] reveal the division of contact into stick and slip, relevant to fretting damage. Fretting damage is commonly observed on roller bearings, riveted lap joints and even in artificial hip joints. In riveted lap joints fretting has been shown to be a primary cause of crack initiation [31-34]. In engineering materials, fretting is a three stage mechanism [35]. In the first stage, a thin layer of oxide layer is removed from the surface of the material through wear. In the first few cycles as the oxide degrades, the underlying material forms micro welds through an adhesive process causing wear debris between the contacting surfaces [36]. As the fretting contact cycles increase the coefficient of friction increases with wear debris accumulation [37,38]. As the cycles accumulate plastic deformation takes place near the surface promoting wear and oxide formation. This plastic deformation is a source of crack nucleation and fretting fatigue is a result of these micro cracks penetrating into the bulk of the material. The damage caused by fretting can reduce fatigue strength by 18 times [39]. 3D finite element simulations and experimental fretting wear tests were conducted by Iyer et al. [40]. They observed that rivet tilt and panel local bending enhance fatigue crack growth.

They also noted that fretting wear was more pronounced at the panel interface than at rivet/panel interface. This process was promoted by a countersunk head and low friction.

Szolwinski and Farris [32,33] assessed the applicability of conventional multi-axial fatigue theories to fretting. Szolwinski and Farris [32,33] predictions were in good agreement with the experiments of Nowell and Hills [41].

Socie [42,43] successfully applied multi-axial fatigue models to correlate crack nucleation observation in strain-controlled tension and torsion tests of AISI type 304 stainless steel tubular specimens. In 1993 he provided an excellent summary of work done on multi-axial fatigue, which was used to develop life models for two nucleation behaviors observed in the multi-axial loading of various materials. They were (1) cracks nucleating and growing on planes of maximum cyclic shear strain and (2) high-cycle fatigue behavior in which crack formation on shear planes consumes the majority of the fatigue life.

On a general side, Swalla [44] has conducted a detailed investigation on the application of different multi-axial fatigue theories for prediction of fretting crack damage in PH 13-8 Mo stainless steel. The advantages and disadvantages of the different criteria in fatigue crack prediction are discussed in detail using finite element and experimental methods.

2.7 Study of fatigue cracking in lap joints

Fung and Smart [26] used the Coffin-Manson [45,46] strain-life law along with the Walker [47] equation, which relates effective stress to fatigue life for prediction of the fatigue life of riveted joints. They applied a thermal expansion method for computing the local total strain range and effective stress. The method however assumes an artificially induced level of uniform through-thickness interference. Park and Atluri [4] and Beuth

and Hutchinson [48] investigated multiple-site cracking in fuselage lap joints, however not considering effects of rivet installation and interaction of rivet with surrounding material. Muller [5] studied fatigue life of riveted Al-to-Al and laminates-to-fiber metal laminate lap joints. Vlieger and Ottens [49] conducted uniaxial and biaxial fatigue tests for Al-to-Al riveted lap joints for countersunk configurations. Effects of different bonding qualities of the riveted joints on fatigue performance were investigated in their research. They observed that bonding quality was a major quality in fatigue life such that life increased with an improved quality of the bonded joint.

Fawaz et al. [50] conducted crack growth predictions by applying the Newman and Raju [51] equations for partially through and through cracks with crack shapes. From the point of view of crack growth prediction, if the cracks are nucleating and growing at the hole edge, then the new Newman and Raju [51] equations (ellipse crack shape considered) are applicable. If the cracks are not nucleating and growing from the hole edge, then the solution is not applicable. No residual stress was involved in the prediction model and the Newman and Raju [51] solution overestimates the value of stress intensity factor *K*. As a result, accurate theoretical work still needs to be done.

Piascik [52] conducted destructive and non-destructive on a bay part with several row of rivets. Cracks were found to originate in the skin with the loading end closest to the row for the extreme rows. In between, cracks were found to originate in both skins. The mating surface, rivet hole surfaces and rivet hole corners were all found to be sites of crack nucleation (Figure 2.2). At the extreme rows, however, the mating surface was found to be a major site of crack initiation. He also observed that a large quantity of fretting damage at a particular hole did not necessarily result in crack initiation.

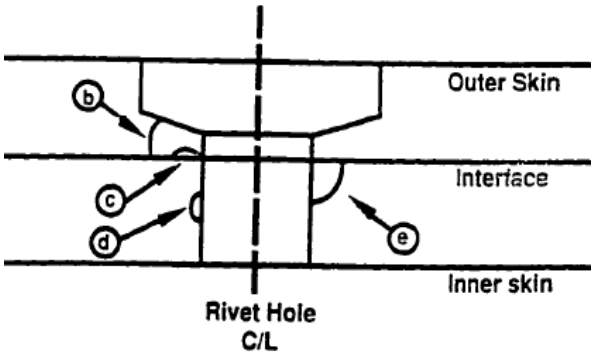

Figure 2.2 Locations of crack origins in the experimental tests conducted by Piascik [52]

Experimental studies conducted by Piascik et al. [52] showed that fatigue crack initiation occurs in region of high stress concentration factors located at or near the rivet holes. They found cracks to initiate at rivet hole corners, burrs, dents and fretted surfaces. In separate studies, Wang [53] and Potter and Yee [54] report crack nucleation at inclusions and tool marks. Small surface damage, which might have been induced by poor drilling techniques, was found to be a significant cause of fatigue damage.

Lucas et al. [55] conducted experimental fatigue testing and damage characterization of riveted lap joint bays to assess multiple site damage effects. They concluded that the loading of the lap joint results in a complex 3D stress distribution at the rivet holes resulting from residual stresses, remote loading and bending stress due to joint eccentricity. They noted that fatigue crack initiation occurred at regions of high stress concentration at or near rivet holes.

The environment also plays an important role. Fatigue cracks tend to initiate earlier and crack growth tends to be faster in moist environments [56]. Sealant applied to the faying surfaces and rivets prior to assembly can keep moisture out of the splice. Surface chemical treatments tend to slow its effects. Visual and high-frequency eddy current techniques are currently used for inspecting fuselage skin splices. These

techniques cannot reliably detect cracks until they are through the sheet and clear of the rivet head. Initiation is often considered as the appearance of a crack of size 0.02 in [57]. At this size, the crack generally just emerges from under a typical fastener head and becomes inspectable. The crack initiation stage and early crack growth (up to visible cracks) may cover the major part of the fatigue life [58]. Striation counts on the Aloha 737 provided evidence of crack growth underneath rivet heads for at least 25% of the total airframe fatigue life [59], while cracks have appeared beyond rivet heads during full-scale tests after approximately 50% of airframe life [60]. As regards the distribution in initiation life, Eastaugh et al. [56] report that there is a relation between the uniformity of cracks within an MSD cluster and the growth period from first link-up to critical length. In the 747, this period seems to vary from about 10,000 pressurization cycles for a small, non-uniform cluster of cracks down to 1000 cycles for a larger, more uniform cluster spanning most of the frame-bay [56].

Liao et al. [61] have implemented 3D FE models for fuselage splices to derive analytical expressions for the local stress at the rivet hole. They introduced a response surface technique to develop the expressions as a function of friction and squeeze force. A major finding from their study is that the squeezing force has a more significant effect on fatigue life distribution of the joint, than the coefficient of friction and material properties. Their model simulates a three-rivet row flat lap joint with only one cycle constant amplitude in-plane loading to determine the final stress state. Another important observation from their investigation was that cracks mainly initiated at the rivet holes in the countersunk skin (Figure 2.3)

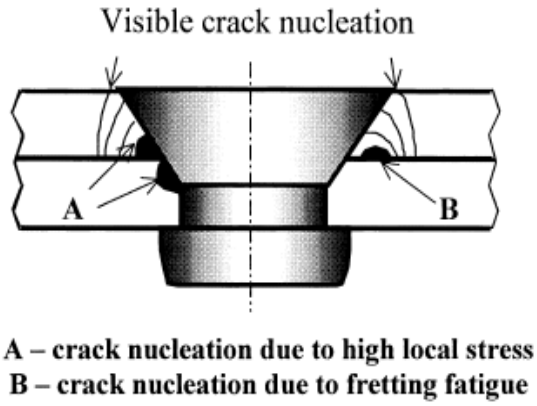

Figure 2.3 Locations of crack origins observed by Liao et al. [61]

Based on an extensive experimental database assembled form detailed teardown examinations of fatigue cracks at rivet holes, Harris et al. [62] have developed a comprehensive analysis methodology to predict the onset of widespread fatigue damage in lap joints of fuselage structure. In their study, several computer codes (such as FASTRAN) were developed with specialized capabilities to conduct the various analyses that make up the comprehensive methodology. The authors have questioned all aspects of the analysis methods to determine computational rigor required to produce accurate numerical predictions. Their study has led to the development of a practical engineering approach of predicting fatigue crack growth in riveted lap joints, which has been widely implemented by other researchers. Figure 2.4 shows an example of models developed by the researchers to predict fatigue crack growth.

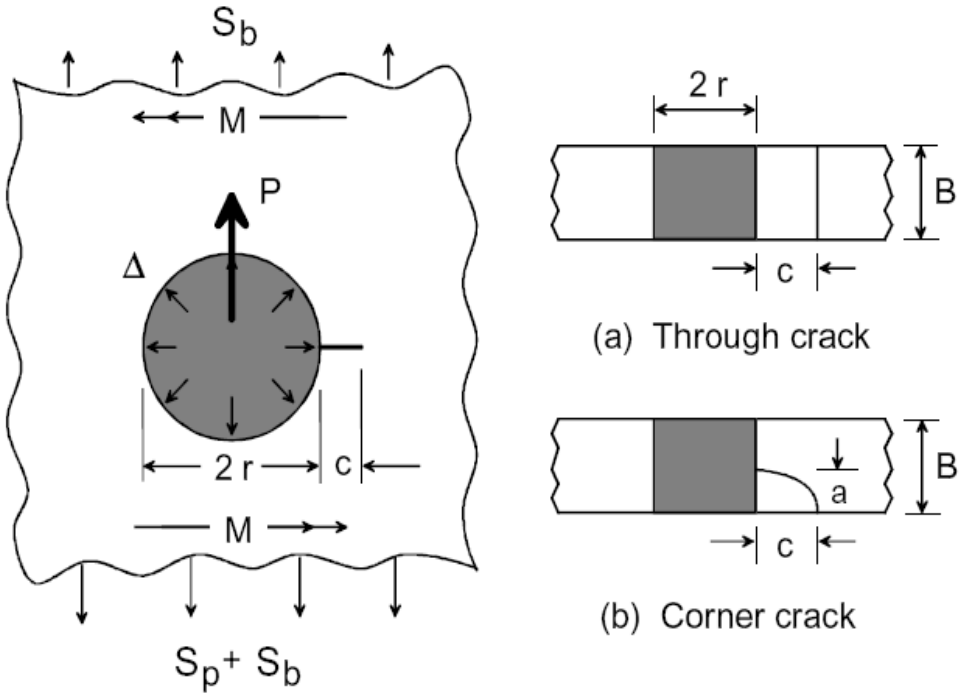

Figure 2.4 An example of models developed by Harris et al. [65] to predict fatigue crack growth in riveted lap joints

2.8 Summary

This chapter began with a review of the state-of-the art in characterization of residual stresses in riveted lap joints. It was pointed out that due to the complicated 3D residual stress state induced by the riveting process it is impossible to apply analytical theories to obtain the stress distribution at the rivet hole. Following, analytical methods the different experimental techniques implemented till date, to predict residual stresses in the joint were discussed. A review of the results obtained from these techniques led to the conclusion that their implementation was far from simple and numerical tools were necessary to pursue the problem more rigorously.

A review of the literature pertinent to application of finite element methods to characterize the residual stresses revealed that majority of the work conducted was on

non-countersunk configurations and based on 2D axisymmetric models. The most significant results from the studies of Muller and Szolwinski and Farris demonstrated the importance and complexity of the residual stress state in the skin resulting from rivet expansion. Their study (conducted separately) also showed the influence of increasing squeeze force on extending the fatigue life of riveted lap joints. In more recent numerical trade studies conducted by Li et al. it was observed that the residual stress induced by the rivet squeeze force had a considerable effect on the stress variations in the tensile loading stage.

In the third stage of the literature review, attention was focused on the mechanics of crack initiation in the joint. In this section, it was noted that fretting was a major cause of initiation at the mating surface of the joint. It was also worthy to note the successful application of multi-axial fatigue theories to predicting fretting fatigue crack growth in riveted joints. Results of extensive experimental lap joint testing conducted by researchers such as Piascik and Lucas were reviewed. Their investigation concluded that fatigue crack initiation occurred at multiple sites of stress concentrations in the lap joint. A similar investigation conducted by Liao et al. showed the countersunk skin more susceptible to cracking than the straight shank skin. Finally, the comprehensive methodology of crack growth analyses developed by Harris, Piascik and Newman was reviewed. It was noted that their study presented a significant development in prediction fatigue crack growth in riveted lap joints and their computational methods could be applied in conjunction with local FEA to predict crack growth curves and SIF's for different types of cracks arising at the rivet holes.

Chapter 3: Initial Model Validation

One of the earliest goals of the research carried out herein was to establish ABAQUS [63] capabilities to simulate the complex forming process. As such, the literature review revealed that a Canadian research team at the Institute of Aerospace Research led by Li [21] had conducted an experimental study in which twenty riveted lap joints were designed, manufactured and tested. Variations of the rivet driven head compressive displacement versus the applied squeeze force were measured experimentally in their investigation. In a separate study, Langrand et al. [6] at the University of Valenciennes had conducted quasi-static experimental tests and numerical simulations to characterize the local strains resulting from the rivet expansion. This chapter begins by providing background of the investigation followed by details of the finite element models. Following these details, the experimental results are compared with those predicted by the numerical simulations.

3.1 Implicit model validation

As stated before, the riveting process is accomplished by driving the rivet shank with a rigid bucking bar while a rigid tool constrains the head of the rivet. The specimen configuration analyzed in ABAQUS/Implicit is shown in Figure 3.1. It consisted of two 76.2 mm x 76.2 mm bare 2024-T3 Al alloy sheets each 2 mm thick and one 2117-T4 Al alloy countersunk type rivet MS20426AD8-9. The rivet had a total length of 14.2 mm and a shank diameter (D) of 6.35 mm. The mean inner sheet hole diameter was 6.4 mm. The rivet's mean protruding height above the inner sheet surface was 9.9 mm.

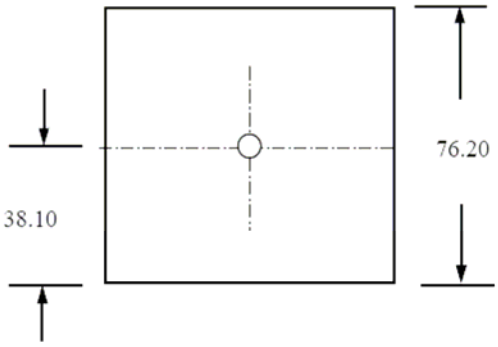

(a)

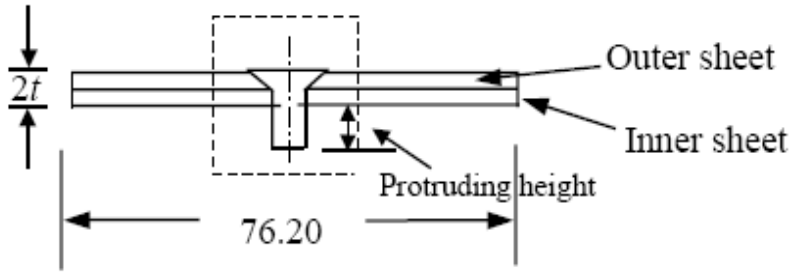

(b)

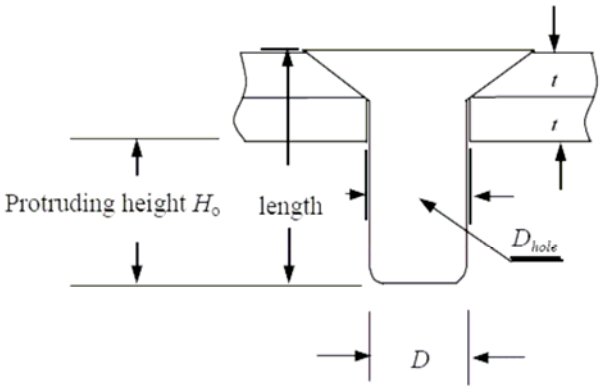

(c)

Figure 3.1 Specimen configuration analyzed in ABAQUS/Implicit [21]: (a) View above joint inner sheet surface (b) side view of specimen and (c) close-up of rivet

The material properties for the sheet and the rivet were implemented from the parameters obtained by uniaxial tensile tests on 2024-T3 and 2117-T4 aluminum alloy respectively. Table 3.1 shows the material property parameters for both the Al alloy sheet and the rivet used in the finite element models. A tabular input of the data was provided in ABAQUS/Standard using Eq. 3.1 based on experimental data. The material model assumed isotropic hardening with linear interpolation performed by ABAQUS between data points.

[3.1] $$\sigma_{true} = C(\varepsilon_{true}^{m})$$

Table 3.1 Material Property Parameters used in finite element models [6,21]

Material	Elastic Properties		Flow Stress Parameters		
	E [GPa]	ν		C [MPa]	m
Al 2024-T3	72.4	0.33	$\varepsilon_y \le \varepsilon_{true} \le 0.02$	765	0.14
			$0.02 \le \varepsilon_{true} \le 0.1$	744	0.164
Al 2117-T4 Al 2017-T4	71.7	0.33	$\varepsilon_y \le \varepsilon_{true} \le 0.02$	544	0.23
			$0.02 \le \varepsilon_{true} \le 0.1$	551	0.15
			A [MPa]	B [MPa]	n
Al 2024-T351	74	0.33	350	600	0.502
Al 7050	74	0.33	312.5	290.5	0.25

A detailed view of the meshed axisymmetric finite element model and the applied boundary conditions is shown in Figure 3.2. The model, which had 8214 nodes and 7254 elements, was generated using ABAQUS/CAE 6.4-1 with CAX4R reduced integration 4-node axisymmetric elements. Three deformable bodies, two sheets and a rivet and one rigid analytic tool were defined in the model. Geometric and surface interaction non-linearities were included in the model. Surface interactions were defined as contact pairs

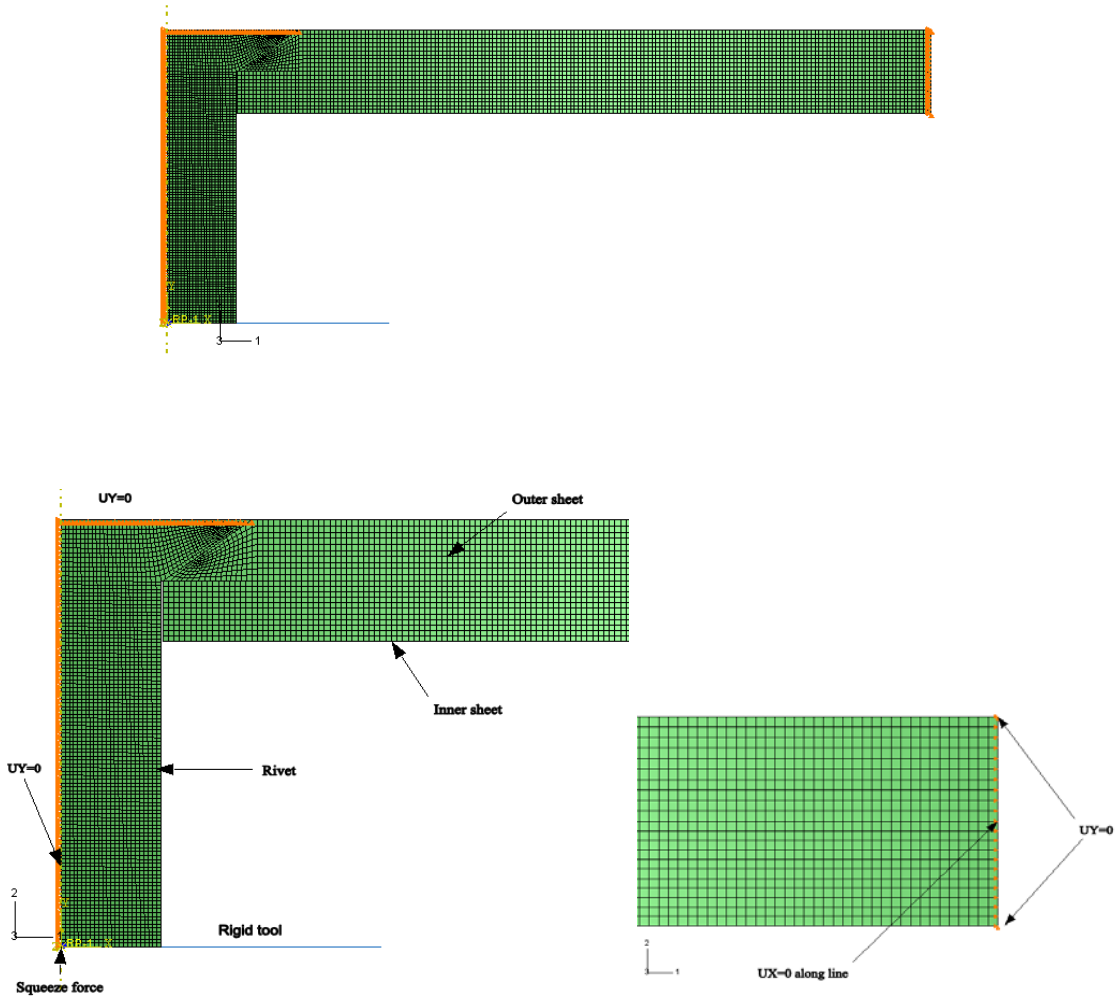

Figure 3.2 2D axisymmetric finite element model with three deformable bodies and one rigid pusher

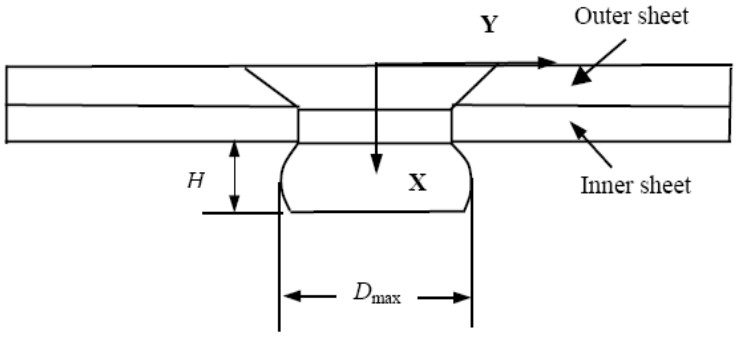

Figure 3.3 Deformed rivet parameters

using the master-slave algorithm available in ABAQUS/Standard with the finite sliding option. The surface contact was defined between the rivet and skin, rivet and the rigid tool and between the upper and lower skin surfaces. The constraint applied by the tool that constrains the head of the rivet was modeled indirectly using boundary conditions. This improved convergence as well as saved computational time. The contact interaction was modeled with the Coulomb friction model. A coefficient of friction of 0.2 was specified for all surface interactions. Formulation of the elemental stiffnesses based on current configurations from deformed nodal positions was provided using the NLGEOM option, which means a geometric non-linear analysis. Since the model undergoes large displacements the calculated stresses were then the true stresses.

The skin edge surfaces on one end were constrained in the x direction with the y direction nodes constrained at the top and bottom to prevent rigid body motion. The rivet displacement was fixed at the head while the squeeze force was applied at the rigid tool in contact with the rivet shank. The process was simulated in two steps: a loading step in which the rivet was deformed by the applied force and an unloading step in which the rivet was allowed to springback. The final deformed rivet driven head diameter and final deformed rivet head height predicted by the finite element analysis was compared with experimental measurements for the range of squeeze forces. These parameters are shown in Figure 3.3 while Table 3.2 shows the comparison. Figure 3.4 shows the final rivet deformations after unload for a range of applied squeeze forces.

A maximum difference of 3.4% was observed for the final deformed rivet diameter while a maximum difference of 1.3% was observed for the final rivet height. Figure 3.5 compares the measured and predicted force-displacement curves. A slight discrepancy can be observed at unload and also at higher squeeze forces. The differences in the curves and the rivet deformation parameters can be attributed to geometry surfaces, which the FE model assumes perfect, numerical errors and errors

associated with experimental uncertainties. Taking into account these uncertainties it can be observed that the FE predictions are in good comparison with the experiment.

Table 3.2 Comparison of rivet head deformation as predicted by the finite element method to experiment measurements [21]

Squeeze Force (kN)	D_{max} (mm) FEM	D_{max} (mm) Expt.	% Diff	H (mm) FEM	H (mm) Expt.	% Diff.
26.69	8.001	8.559	3.4	5.79	5.796	0.7
35.56	9.09	9.525	1.6	4.546	4.59	0.9
44.48	9.931	10.16	2	4.0463	4	1.3
53.37	10.61	10.795	1.5	3.484	3.49	0.362

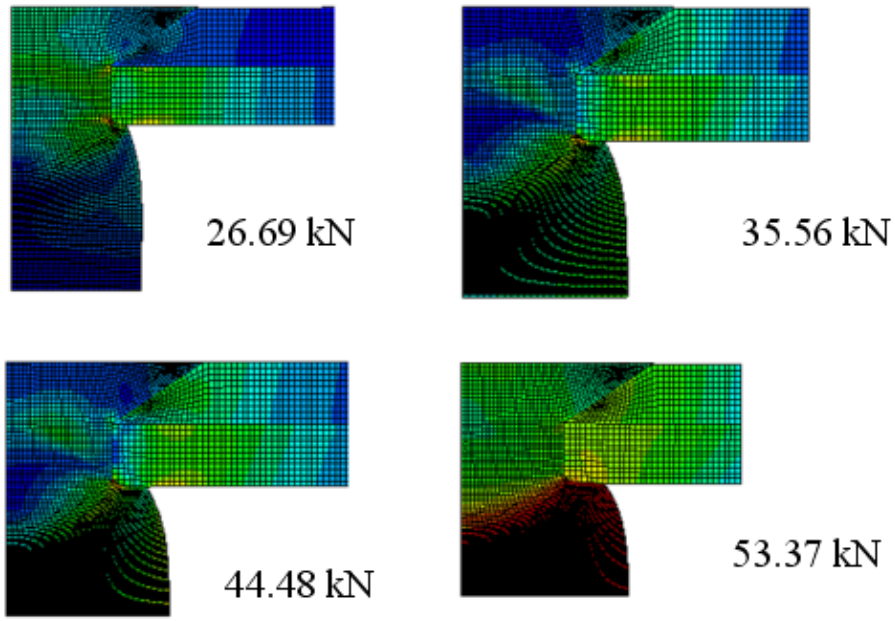

Figure 3.4 Deformed Configuration for a range of applied squeeze forces

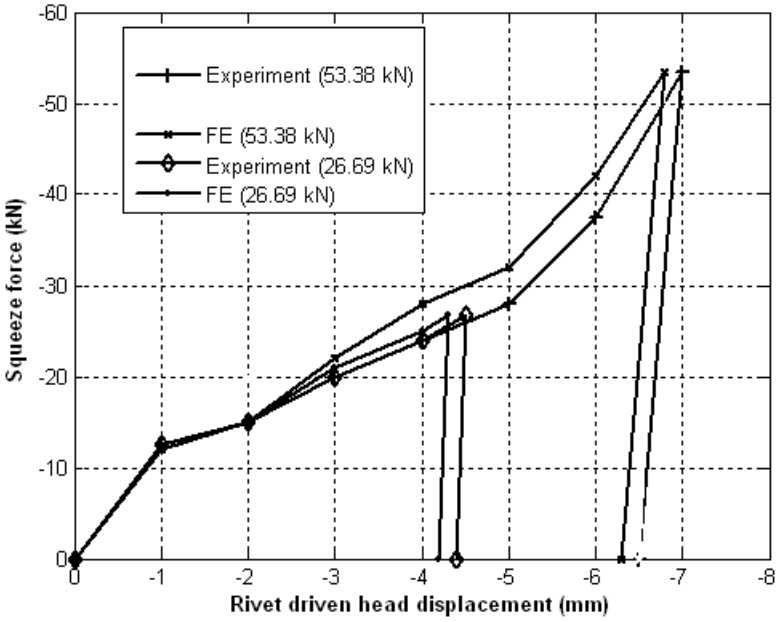

Figure 3.5 Comparison of force-displacement curves

3.2 Explicit model validation

The specimen configuration analyzed in ABAQUS/Explicit is shown in Figure 3.6. It consisted of two 15 mm x 15 mm bare 2024-T351 Al alloy sheets each 1.6 mm thick and one 7050 Al alloy countersunk type rivet. The rivet had a total length of 8 mm. The material properties for the sheet and the rivet were implemented from the parameters obtained by experimental characterization of 2024-T3 and 2117-T4 aluminum alloy respectively [6] (Table 3.1). A tabular input of the data was provided in ABAQUS/Standard 6.4-1 using Eq. 3.2 based on experimental data.

[3.2] $$\sigma(\varepsilon_p) = A + B\varepsilon_p^{\,n}$$

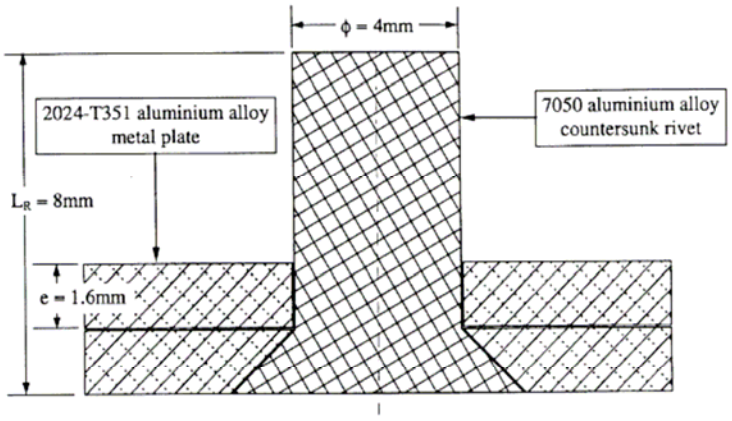

Figure 3.6 Riveted joint parameters for model validation in ABAQUS/Explicit [6]

The quarter-symmetry model, which had 31,541 nodes and 22,771 elements, was generated using ABAQUS/CAE 6.4-1 with C3D8R reduced integration 8-node solid continuum elements. Three deformable bodies, two sheets and a rivet were defined in the model. The kinematic predictor-corrector algorithm was implemented in defining the surface interactions with a balanced master-slave approach. Using this approach with hard kinematic contact, surface penetrations that might occur during the process were minimized. The surface contact was defined between the rivet and skin and between the upper and lower skin surfaces. The constraint applied by the tool that constrains the head of the rivet was modeled indirectly using boundary conditions. The contact interaction was modeled with the Coulomb friction model with a coefficient of friction of 0.2 assumed for all interactions. The skin edge surfaces on one were constrained in the x-direction with the y-direction nodes constrained at the top and bottom to prevent rigid body motion. A crushing velocity of 2 mm/min was applied to the rivet shank. Figure 3.7 shows the boundary conditions.

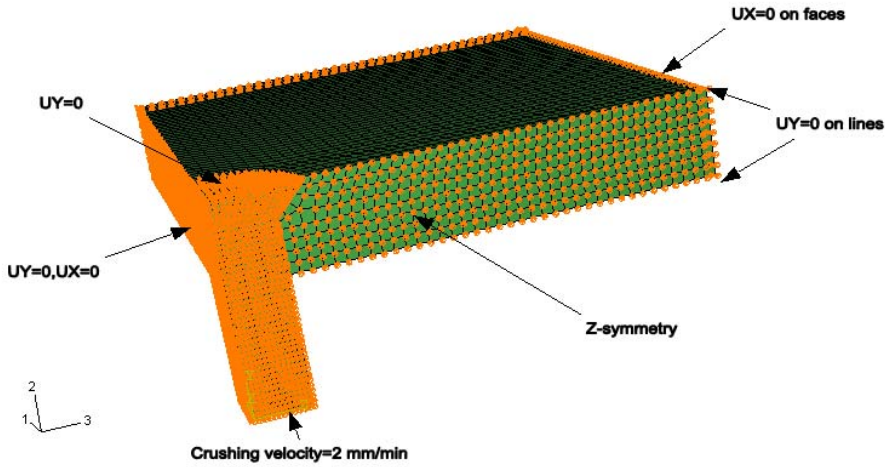

Figure 3.7 Boundary conditions for explicit model validation

In ABAQUS/Explicit the rivet driven head displacement was applied using a smooth step loading amplitude function. A small amount of material damping was also introduced in the explicit analysis to obtain a smoother kinetic energy response. Since explicit solutions typically require large run times compared to its implicit counterpart it was not feasible to analyze both the loading and unloading steps in one analysis. Hence, for all of the explicit problems the rivet loading was analyzed in the solver and the unloading step was completed in Implicit using the ***IMPORT** option provided by ABAQUS. Mass scaling was implemented in the explicit solution to speed up the solution time by artificially scaling the density of the materials. A mass scaling factor of 10 was found to be appropriate to obtain solutions in reasonable run times without introducing excessive spikes in the expended kinetic energy.

The simulation was validated using three criteria. The Von Mises stress of the deformed configuration and equivalent plastic strain at the end of analysis (after unloading) was compared to that predicted by the simulations conducted by Langrand et al [6]. The residual strains after riveting as predicted by finite element were compared to

values recorded by strain gauges along the length of the skin. Finally, the force-displacement response of the finite element solution was compared to the experimental response. The Von Mises stress predicted by the Explicit solver (Figure 3.8) was observed to be slightly lower than that predicted by Langrand et al. [6]. The equivalent plastic strain, which provides a measure of the plasticity in the model, showed that the plastic strains in the rivet reach a range of 1.2 (Figure 3.8). This is consistent to that reported by Langrand et al. [6].

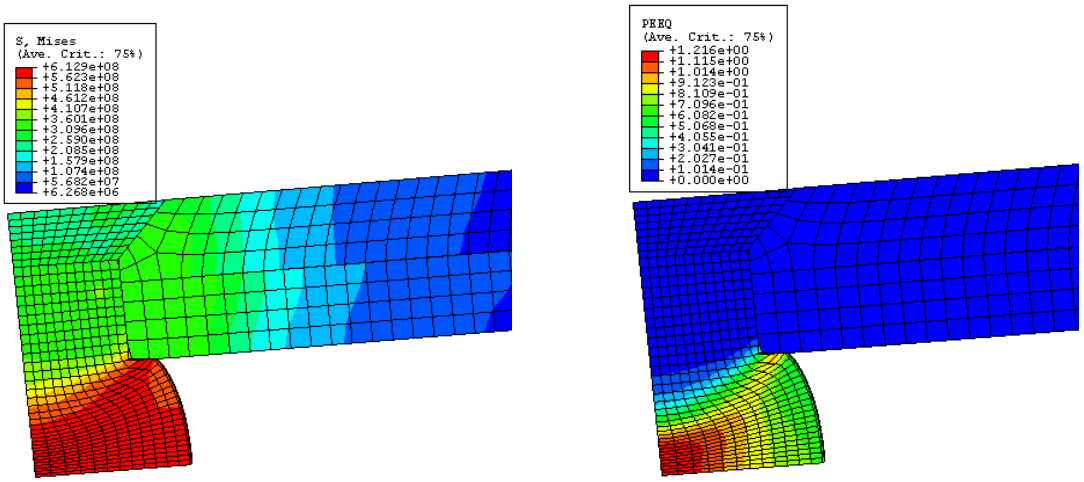

Figure 3.8 Von Mises stress contour in MPa (left) and equivalent plastic strains at end of the riveting (right)

From comparisons of the residual strains (Figure 3.9) it was observed that the measurements and the finite element results were essentially in agreement. The explicit predicted force-displacement curve compared to experiment shown in Figure 3.10 also showed reasonable agreement. The finite element model predicted lesser elastic recovery than observed in experiment for both the implicit and explicit solutions.

Gauge No.	Residual Strain- Expt.	Residual Strain - Finite Element
1	0.01e-02	0.018e-02
2	0.04e-02	0.05e-02
3	-0.28e-02	-0.32e-02

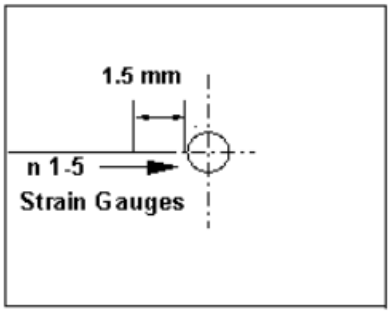

Figure 3.9 Comparison of residual strains

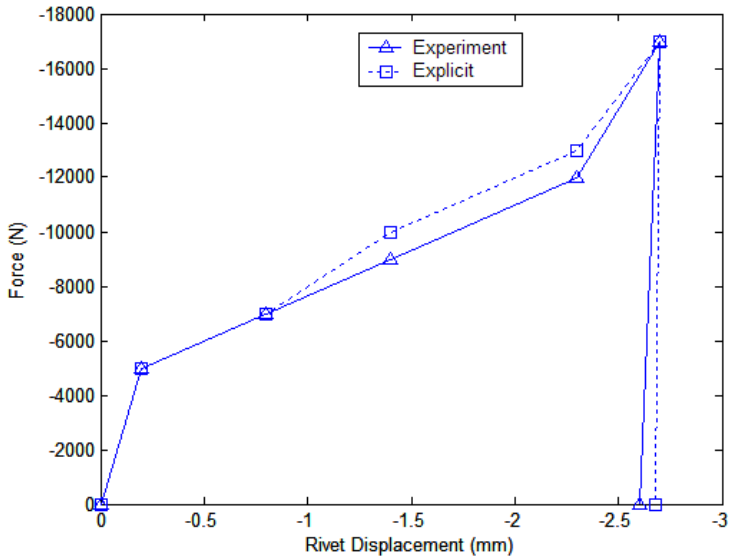

Figure 3.10 Comparison of force-displacement diagram for the explicit solution

As stated before, the explicit solution is a true dynamic solution algorithm developed to model events in which inertia plays a significant role. Figure 3.11 compares the energy response at the end of the riveting process. It was ensured that the kinetic energy was small enough in comparison to the internal energy for the solution to be considered quasi-static. An identical analysis was also conducted in Implicit to compare the residual stresses and plastic strains to those predicted by explicit. Figures 3.12 and

3.13 show the comparison of equivalent plastic strain contours and residual stresses in the skin after unload, for the implicit and explicit solutions.

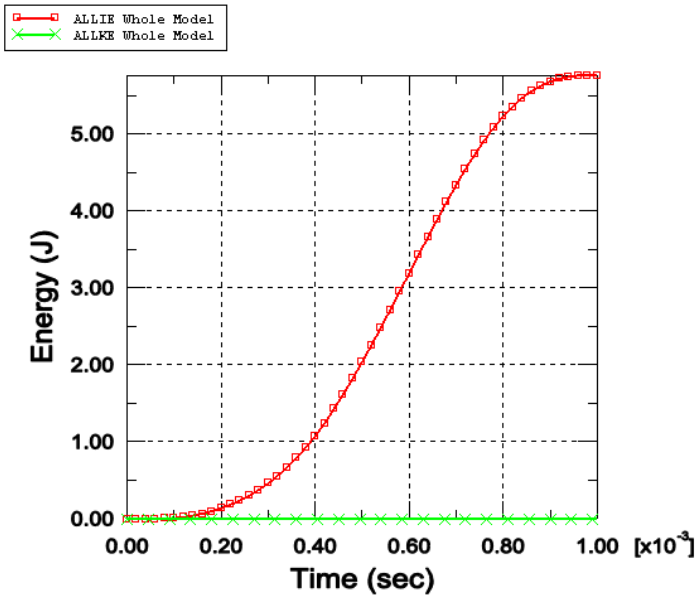

Figure 3.11 Energy response in the model

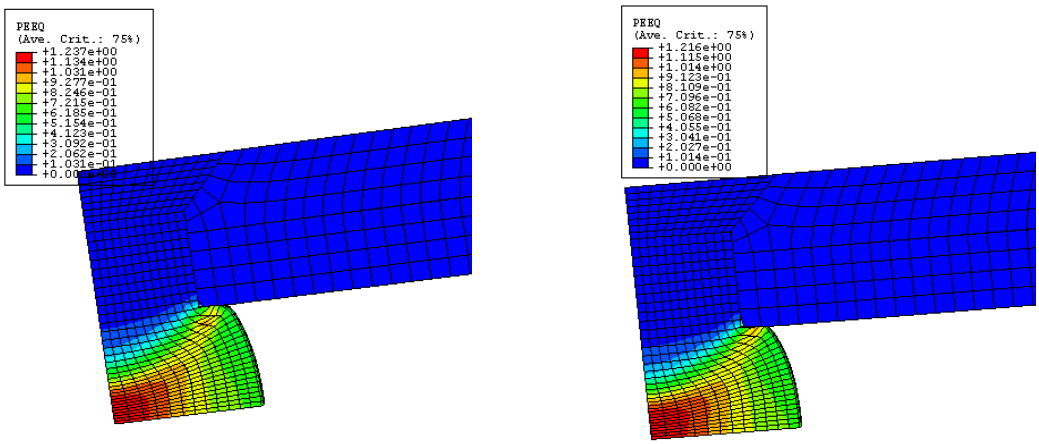

Figure 3.12 Equivalent plastic strain contours for the implicit (left) and explicit (right) analysis

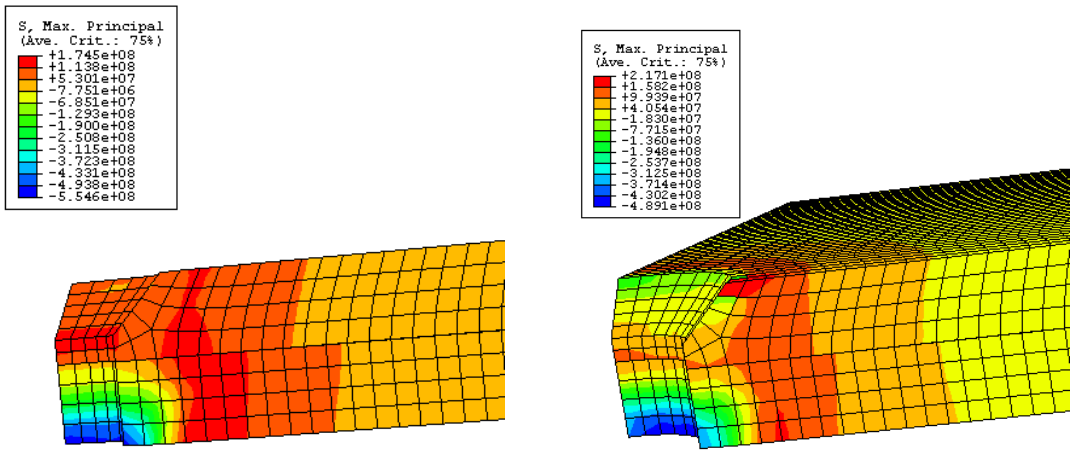

Figure 3.13 Residual stress contours in MPa for the implicit (left) and explicit (right) analysis

The results show a good agreement indicating the ability of the dynamic solver to model the quasi-static problem. The residual stresses are qualitatively the same but quantitatively the explicit solution shows around 20% larger values than that predicted by implicit. The difference in values must be taken in light of the dynamic nature of the solver based on stress wave propagation. Even though it was ensured that the analysis is quasi-static there will always be some inertia effects in the solution leading to the observed difference in residual stresses from the true quasi-static solution. Different forming quasi-static analyses (such as indentation of a foam and forging with sinusoidal dies) were also conducted separately based on examples provided in the ABAQUS manuals to confirm this trend.

As the rivet head was formed in the joint, friction between the skin and the rivet head led to the formation of a lug (material flow) trapped by the driven rivet head near the punching. The lug was visualized in the specimen sectioning conducted by Langrand et al. [6]. The FE analysis (from above and Langrand [6]) did not show this lug formation indicating the limitations of numerical tools in simulating forming processes. Figure 3.14

compares the driven rivet head from specimen sectioning to the one from the FE analyses.

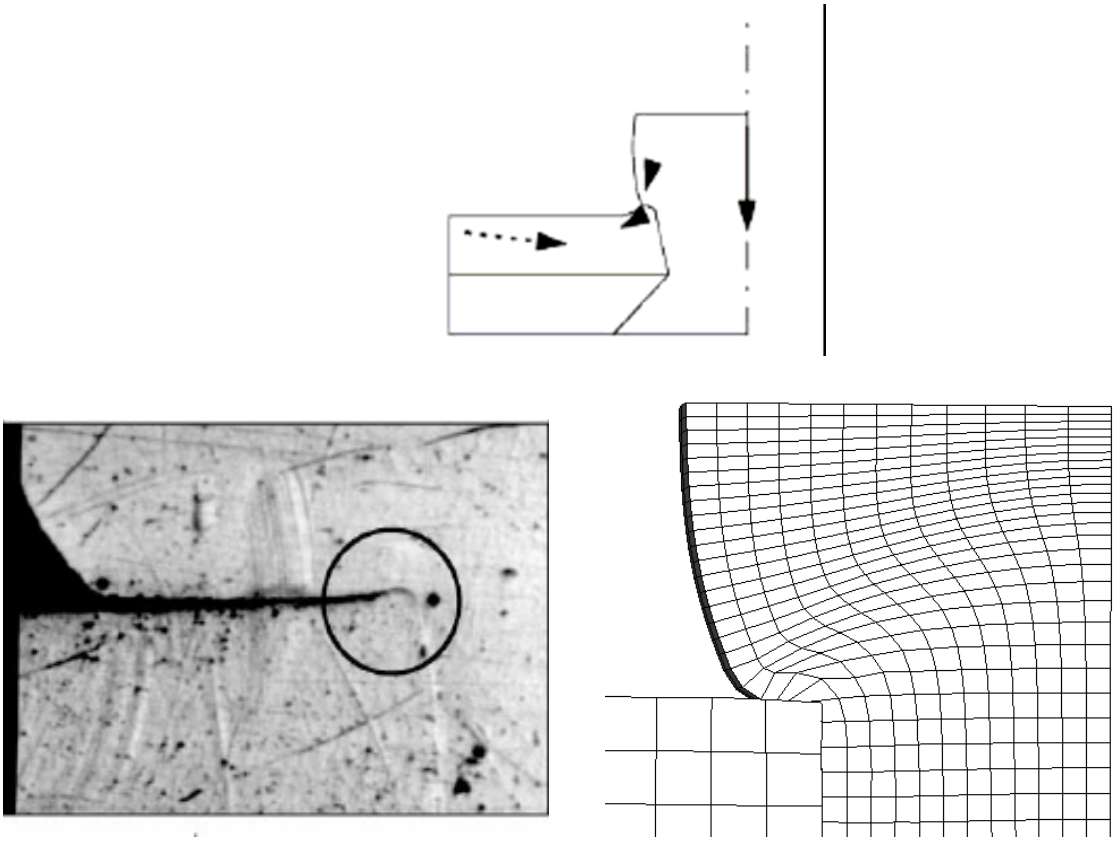

Figure 3.14 Comparison of rivet head deformation from experiment [6] to the FE analyses. A ‘lug’ formation was observed in the experiment [6].

3.3 Chapter Summary

This chapter presented verification and validation approach of the ABAQUS finite element code used to simulate the riveting process. This approach was accomplished through comparisons with a carefully obtained set of experimental results previously generated in separate investigations conducted by Li and Langrand. A review

of the details of the experimental specimens including the material models implemented for the analysis was presented for both the investigations.

A 2D axisymmetric representation was used to model the riveted lap joint of Li. The rivet deformation and force-displacement curves predicted by the simulations were compared to the experimental measurements. A reasonable comparison was observed for both taking into account effects of numerical and experimental uncertainties and thus establishing the capabilities of ABAQUS/Implicit in simulating this process

A quarter-symmetry 3D model was constructed to model the configuration of Langrand et al. The simulation was conducted quasi-statically invoking the “more forgiving” explicit solver to emulate the analysis and experiments. Although a good comparison was observed between the simulations and experiment, the simulation did not show the formation of a ‘lug’ observed in the experiments. Finally, a comparison was done between the residual stresses predicted by explicit and those predicted by the “less forgiving” implicit solver. A major finding from this comparison was that approximately 20% differences in residual stress predictions must be taken into account due to the inherent differences in the nature of the two solvers.

Chapter 4: Parametric Studies

The previous chapter demonstrated the viability of finite element simulations in analyzing the riveting process. While those demonstrated results provided the necessary validation of the modeling approach and pointed out simulation limitations, they did not implement the developed models to simulate actual service variations. As such, the present investigation was focused on a more realistic scenario with regard to simulating the residual stress state in the riveting process. In conducting this investigation, a baseline 3D model was established to capture the unsymmetrical residual stress state resulting from variations and rivet buckling. The model was then implemented to compare the effects of hole quality, sealant and load transfer effects on the residual stress state. The effect of the variations was analyzed separately for the baseline driven rivets and under-driven rivets. The different parameters considered in this chapter were based on actual service variations observed in the B727 teardown. As such, a full design of experiments optimization was not established for the parametric studies.

4.1 Baseline model

Figure 4.1 shows the joint parameters modeled in this study. The specimen configuration consisted of two 2024-T3 25 mm x 25 mm Al alloy sheets. The upper skin was 1.5 mm thick and the lower skin was 1 mm thick. The 2017-T4 Al alloy countersunk type rivet had a total length of 7.8 mm and a shank diameter of 3.9 mm. The lower skin hole diameter was 4 mm and the upper skin hole diameter was 6 mm at the top of the countersunk edge. The depth of the countersunk part measured from the top of the plate edge (h_c) was 0.09 mm. A coefficient of friction of 0.2 was assumed for lubricated

contact and 1.1 for dry contact. The same friction coefficient was applied for both rivet-skin and skin-skin contact. The finite element study was conducted as a quasi-static process (low-speed). Any thermal and inertial effects were ignored.

A detailed view of the meshed, symmetric 3D finite element model and the applied boundary conditions is shown in Figure 4.2. The model, which had 6457 nodes and 3947 elements, was generated using ABAQUS/CAE 6.4-1 with C38DR reduced integration 8-node linear solid brick elements.

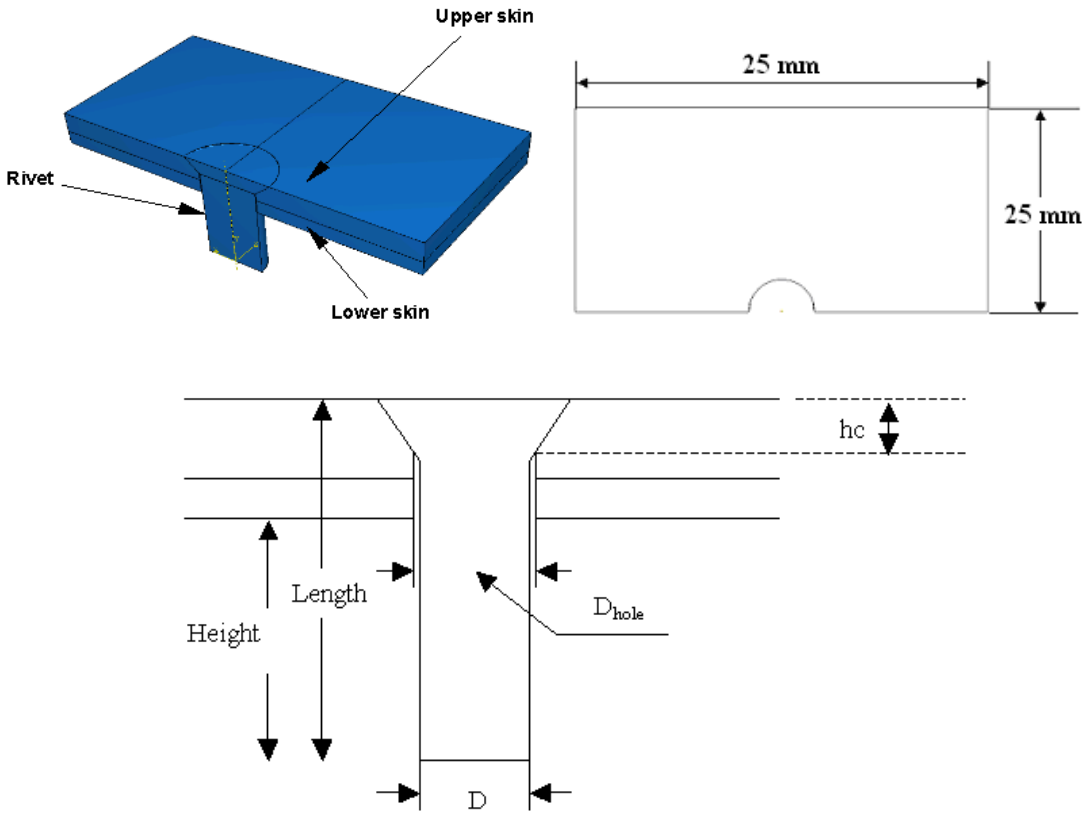

Figure 4.1 Geometry parameters for the baseline model

The modeled riveting configuration was from the end of a three-row lap joint. The skin edge surfaces on one end were constrained in the x direction with the y direction

nodes constrained at the top and bottom to prevent rigid body motion. The skin surfaces on the opposite end were unconstrained. The rivet displacement was fixed at the head

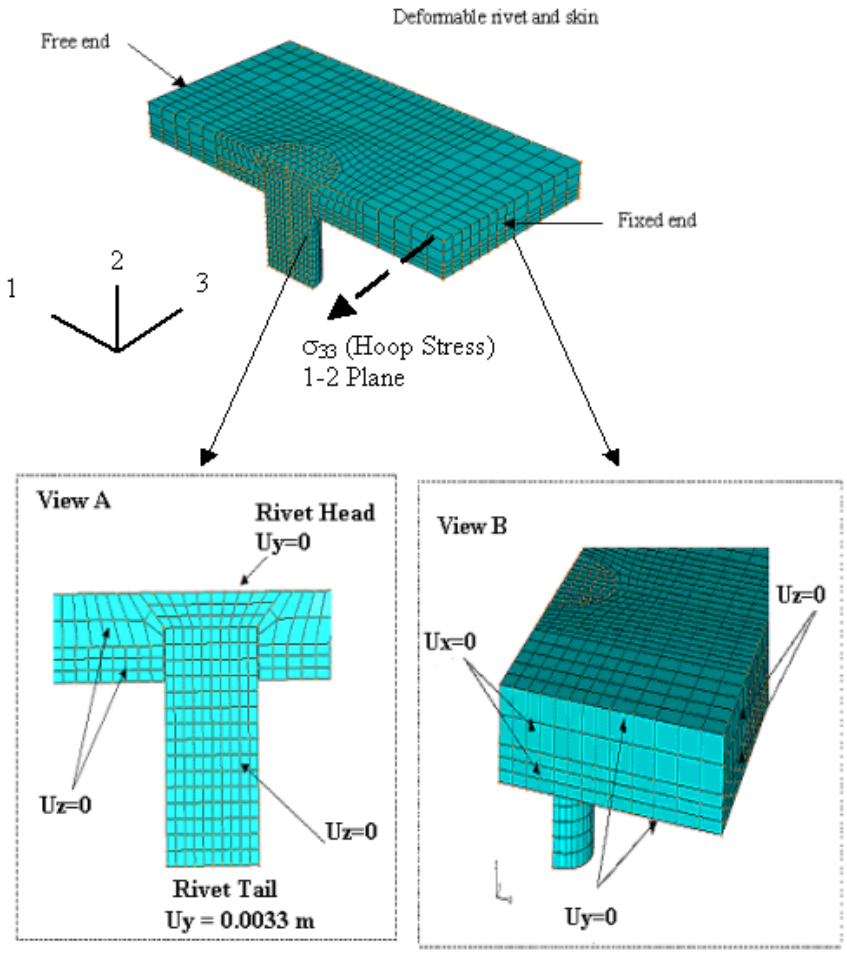

Figure 4.2 Boundary conditions

while a displacement of 3.3 mm (baseline) was applied at the rivet driven head surface. Symmetric boundary conditions were imposed in the z direction for both the rivet and the skin surfaces. The process was simulated in two steps: a loading step in which the rivet is deformed by an applied displacement and an unloading step in which the rivet was allowed to springback. The unloading step was important as at the end of the loading

step the stress state was above yield at the rivet/skin interface, but after unloading most of these locations showed a stress state below yield.

Several meshing techniques available in ABAQUS/CAE were tested, namely *Free*, *Edge by Number*, and *Edge Biased*. Since the riveting process presents a complex contact problem the mesh around the holes as well as the rivet needed to be refined to obtain a converged solution. The sought mesh in each of the latter techniques was hard to find in terms of a generalized expression, while by using *Free* meshing one mesh criterion was obtained. In the *Free* meshing a *Global Element Size* has to be suggested by the user. By using the same global element size for both the skins one can define,

[5.1] $$\text{Mesh Ratio} = \frac{\text{global element size in the rivet}}{\text{global element size in the plates}}.$$

A suitable mesh ratio to carry out the analysis successfully was found to be 0.7. Several mesh configurations were implemented based on the above ratio to analyze the problem. The mesh ratio was decreased iteratively until no appreciable difference was observed in the residual hoop stress in the skin. Table 4.1 summarizes the results from the mesh refinement study.

Table 4.1 Results from the mesh refinement study

Elem. Size (Skin)	No. of Elem.	No. of Nodes	Tensile nodal residual hoop stress in lower skin (MPa)
0.050"	1324	2417	68.947
0.025"	5318	8962	110.316
0.020"	9989	15538	137.895
0.008"	32681	44327	144.789

The stresses shown in the contour plots in this work represent the nodal averaged stresses (stresses extrapolated from the element integration points and averaged over all the elements containing the specific node). These stresses were compared separately to the stresses reported at the element integration points for the different meshes. The nodal maximum residual stress for the upper skin was 68.754 MPa while the element maximum was 65.562 MPa (4% difference). The nodal maximum residual stress for the lower skin was 138.8946 MPa versus the corresponding 146.5273 MPa element maximum (4.5% difference). The excellent agreement between these values also demonstrates the adequacy of the mesh in closely approximating the continuum being modeled.

Figure 4.3 shows the deformed plot and contours of residual hoop stress induced in the upper and lower skin after unloading in the original baseline implicit model. The residual hoop stresses (shown for the baseline model and further simulations) are on the face of the skin only (1-2 plane). During the process, the rivet expands against the hole and the contact pressure exceeds the yield point of the material ($\sigma_{11} < \sigma_y$). The material deforms so that $\sigma_{33} < 0$. This compressive hoop stress is analogues to cold working of holes with an expanding mandrel, done to prevent fatigue cracks that might initiate at the holes. The elastic deformation energy is not allowed full release after the process due to the large plastic deformation of the rivet. This leads to both compressive and tensile residual stresses in the skin. The compressive zone is balanced by the tensile zone away from the hole edge. This tensile hoop stress is critical for fatigue cracks that may initiate at the faying surface.

Max. Hoop Stress (MPa)	Upper	Lower
Tensile	68	137
Compressive	-199	-351

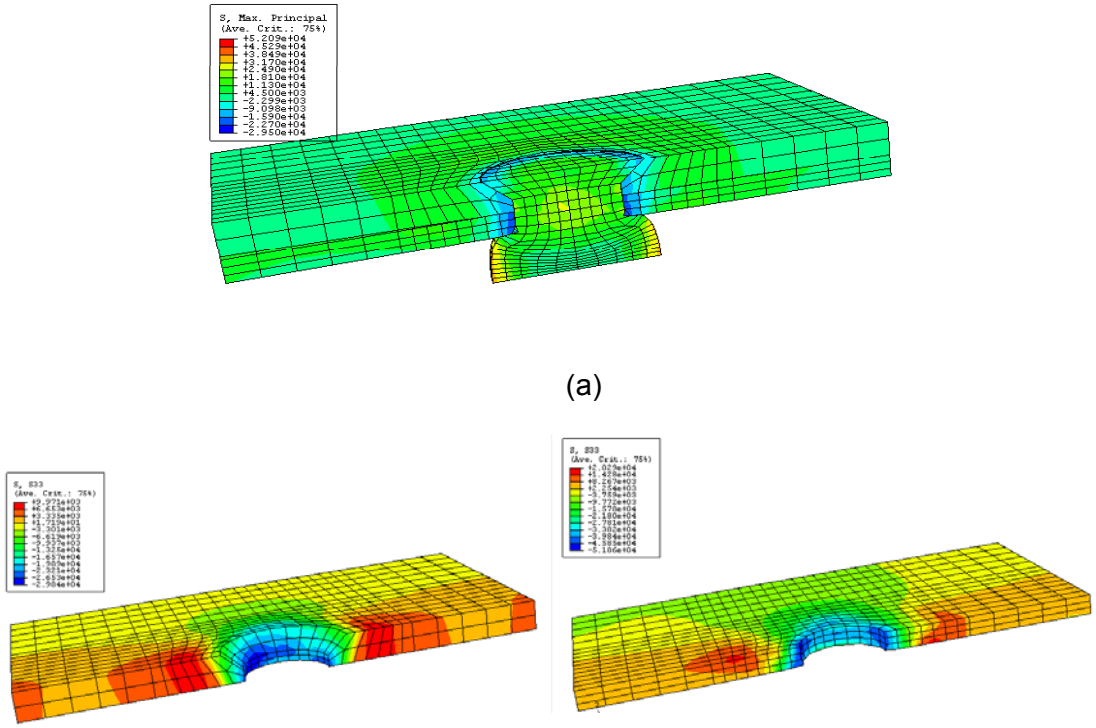

(a)

(b)

Figure 4.3 (a) Deformed shape and (b) residual hoop stress contours in the skin after unload in implicit analysis

The resulting interference is an indicator of the quality of the riveted joint. A high interference means a tighter connection between the rivet and the skin. A larger compressive stress was observed for both the hoop and radial stresses in the lower skin than in the upper skin. As a result the lower skin and the rivet will have a tighter connection as compared to the upper skin. The residual stresses show a through-

thickness variation as well as an unsymmetrical distribution (Figures 4.4 and 4.5). The resulting interference then also varies.

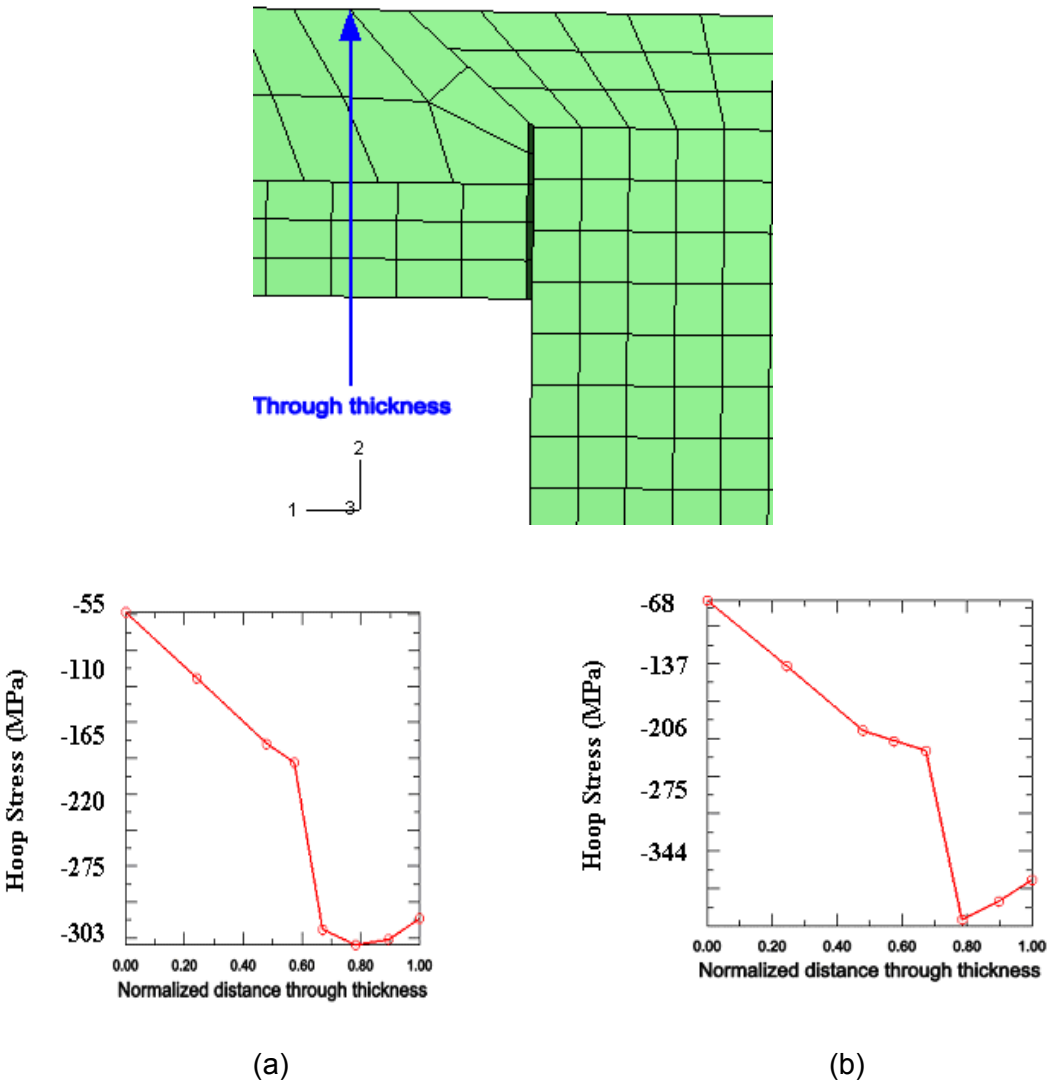

(a) (b)

Figure 4.4 An example of the through thickness and unsymmetrical variation of the hoop stress: (a) Constrained side (b) Unconstrained side

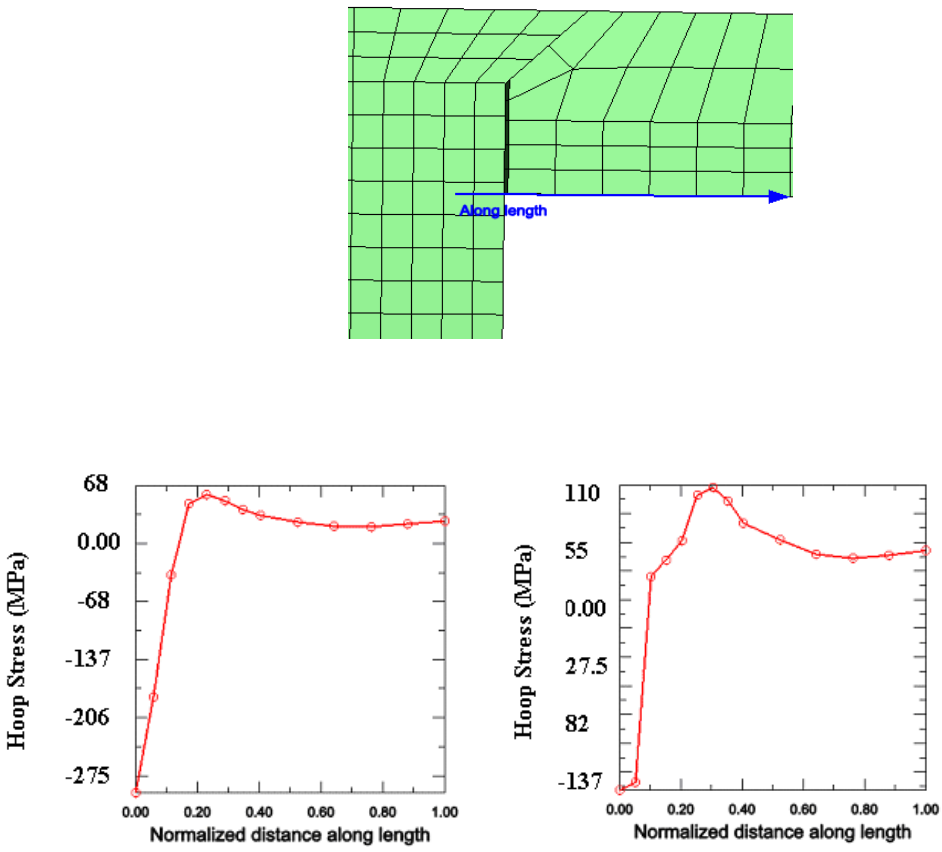

(a) (b)

Figure 4.5 An example of the unsymmetrical variation of the hoop stress along the length of the skin: (a) Constrained side (b) Unconstrained side

A separate analysis was also conducted to demonstrate the unsymmetrical nature of the local residual stress state that must be taken into account while analyzing process variations. In this analysis, the rivet deformation was simulated without any initial clearance between the rivet and the skin. Figure 4.6 shows the residual hoop stress contours in the model after unloading. The resulting symmetric deformation of the rivet without the initial hole clearance can be clearly observed from the contours.

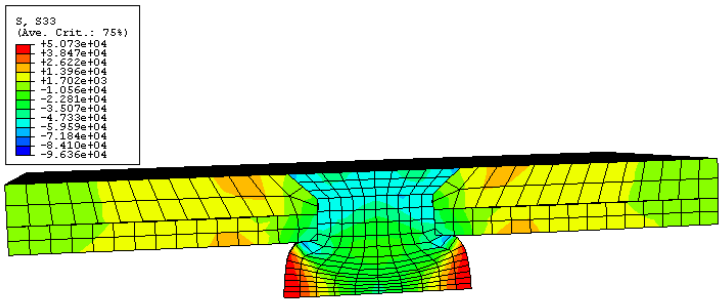

Figure 4.6 Symmetric stress state resulting from zero clearance between rivet and hole

In ABAQUS/ Explicit the rivet driven head displacement was applied using the smooth step loading amplitude function. Preliminary analysis showed that a time period of 0.001 sec was appropriate to obtain a quasi-static solution and achieve computational efficiency. Additional analyses were also conducted over a time period of 0.01 sec and 0.1 sec to ensure that there was no significant difference in the residual stress values. In all analyses it was ensured that the kinetic energy was negligible in comparison to the internal energy in the model. A small amount of material damping was also introduced in the explicit analysis to obtain a smoother kinetic energy response. For all of the explicit problems the rivet loading was analyzed in the solver and the unloading step was completed in Implicit using the ***IMPORT** option provided by ABAQUS. Figure 4.7 compares the equivalent plastic strain in the implicit and explicit analysis. Figure 4.8 shows the kinetic energy plot for the explicit analysis. The results show a good agreement indicating the ability of the dynamic solver to model the quasi-static problem. Figure 4.9 shows the residual stress state in the skin predicted by the explicit analysis. The tensile and compressive zone locations predicted by Explicit were observed to be similar to the ones predicted by Implicit. In comparison of the reported nodal values between the two solvers the Explicit values were noted to be approximately 20% larger than those computed by Implicit.

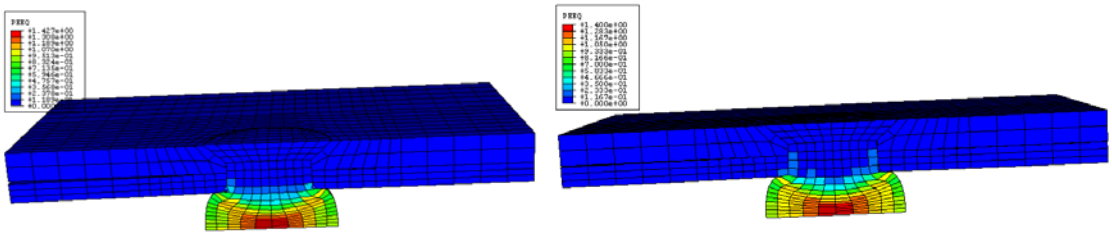

Figure 4.7 Comparison of the equivalent plastic strain contours from the Implicit (left) and Explicit (right) analysis

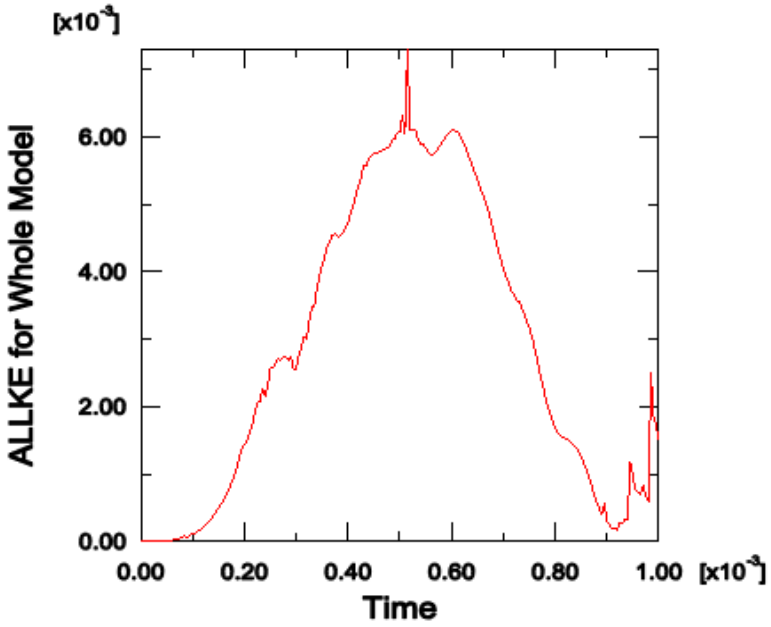

Figure 4.8 Kinetic energy plot for the whole model. A small amount of material damping results in a relatively smooth response.

Max. Hoop Stress (MPa)	Upper	Lower
Tensile	89	144
Compressive	-420	-599

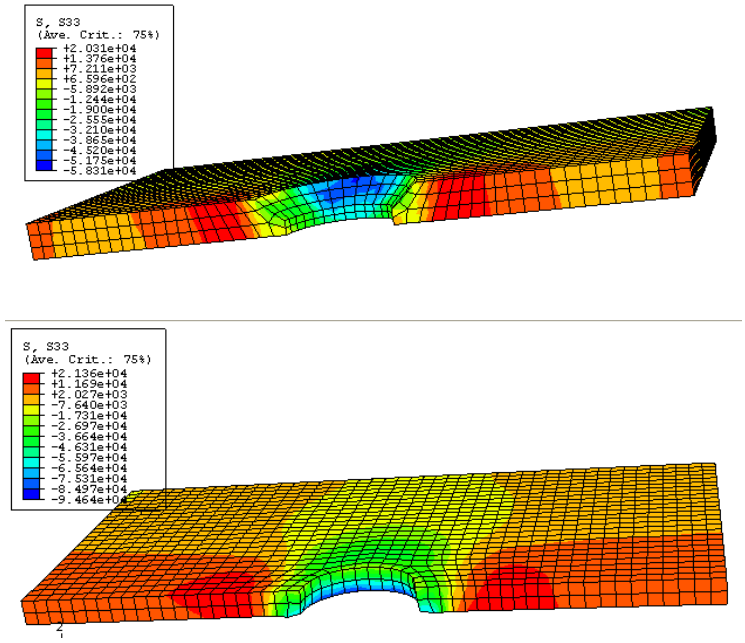

Figure 4.9 Residual hoop stress contours in upper and lower skin as predicted by explicit analysis

4.2 Rivet Deformation

The deformed model configuration for a range of rivet head displacement is shown in Figure 4.10. As the applied displacement increased, the rivet head increased in size. The crimping in the free ends of the skin was also observed to increase significantly in the range of applied displacement. The maximum rivet shank deformation (D_{max}/D) and the final rivet head height (H) are shown in Figure 4.11 as a function of the applied displacement. An applied rivet displacement above 3.3 mm corresponds to an over-driven rivet, while an applied rivet displacement below that corresponds to an

under-driven rivet. D_{max}/D and H were fitted with a linear regression cure and a power law regression equation expressed below,

Linear regression:

[5.2] $D_{max}/D = 0.1019d + 1.3452$ $R^2 = 0.9971$

[5.3] $H = -0.0002d + 0.0026$ $R^2 = 0.9951$

Power-law:

[5.4] $D_{max}/D = 1.4154d^{0.1632}$ $R^2 = 0.9302$

[5.5] $H = 0.0026d^{-0.323}$ $R^2 = 0.9269$

R^2 is the data-fit parameter and d is the rivet head displacement in the range of 3.3 mm to 4 mm. A similar equation for a squeeze-force controlled process has been presented by Li and Shi [21]. The above equations and the rivet deformation trends observed in Figure 4.11 are meant as a means to achieve the desired riveting quality. It should be noted that the equations presented above are for the particular configuration analyzed in this research. Similar equations can be developed for different geometries. Large D_{max}/D (larger rivet expansion) values are observed to increase the compressive zone near the hole edge, while enhancing the probability of fatigue cracks at the faying surface.

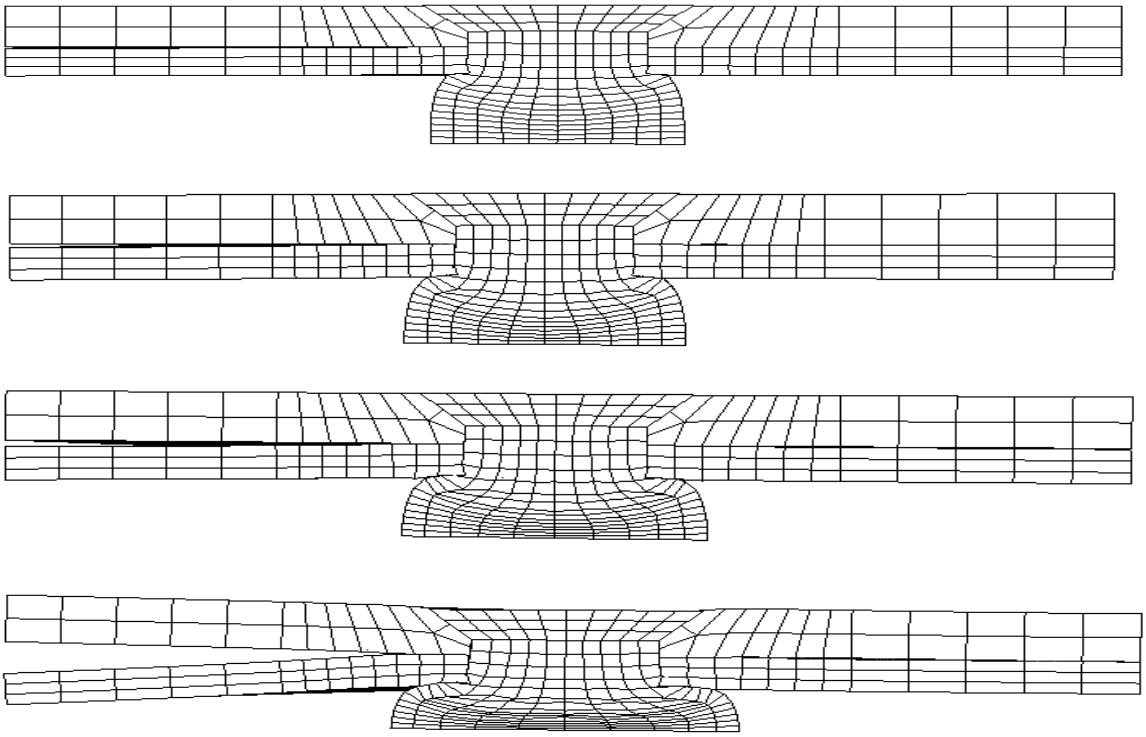

Figure 4.10 Deformed configuration for an applied displacement of 0.0027 m (0.11 in), 0.0033 m (0.13 in) (standard), 0.0035 m (0.14 in), 0.004 m (0.16 in) (top to bottom) respectively

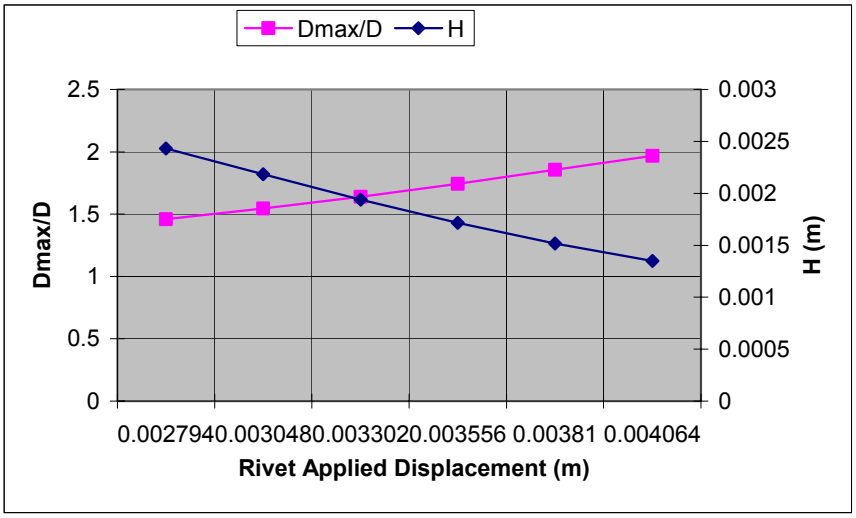

Figure 4.11 Rivet head deformation compared with applied displacement, where D_{max} is the maximum deformed diameter, H is the deformed tail height and D is the original rivet diameter

4.3 Effect of variations on baseline model

Parametric studies were conducted to observe effect of varying friction, increased hole clearance, a misaligned assembly of upper and lower skin, faying surface hole defects and presence of debris on the residual stress state in comparison with the original model [11]. Again, the tensile hoop stress (σ_{33}) is only on the faces of the upper and lower skin in the 1-2 plane. This is the critical stress of interest. The geometry parameters of the variations are specified in Table 4.2. A view of the finite element models is shown in Figure 4.12.

Table 4.2 Parametric variations

Parameter	Description
Friction effect	Varying coefficient of friction (0.2 to 1.1)
Clearance effect	Varying hole clearance (0.19 mm to 2 mm)
Misalignment effect	Holes same size but misaligned (0.04572 mm)
Geometry effect I	Lower plate hole size larger (0.20955 mm)
Geometry effect II	Upper plate hole size larger (0.20955 mm)
Defects effect I	Lower plate material removed in middle (scar-like)
Defects effect II	Lower plate material removed at interface
Defects effect III	Lower plate increased material removed at interface
Debris effect	Plates separated by debris
Increased Displacement	Displacement of rivet increased from 3.3 mm (standard) to 4 mm

Increased Rivet Displacement (Over-Driven Rivet)

An increase in the applied rivet displacement leads to a larger rivet-hole expansion consequently leading to an increase in both the compressive radial and hoop stresses around the hole periphery. A tighter interference can be achieved with an increase in the applied displacement.

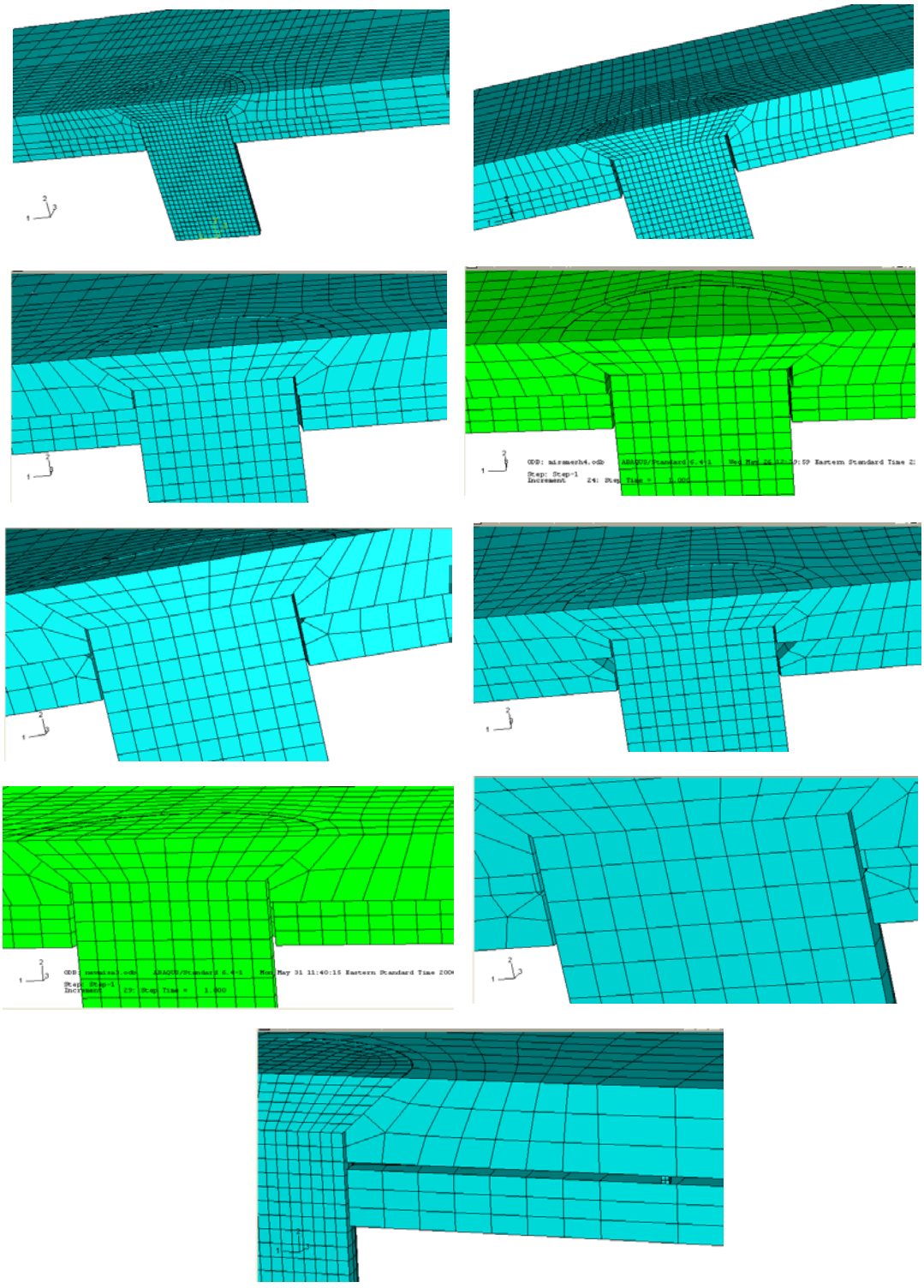

Figure 4.12 A view of the models showing reduced hole size, increase hole size, lower skin misalignment, increased upper skin hole size, hole defects such as scars and gouges, increased lower skin hole size and presence of debris

Also, the fatigue performance can be improved by retarding crack growth near the hole edges. The tensile hoop stress is pushed away from the hole edge but an increase in magnitude is observed in both the outer (52%) and the inner (25%) skin. This increases the potential for initiation and fatigue crack propagation at the faying surface.

Increased coefficient of friction

Increased friction leads to large frictional energy dissipation. A larger amount of the load is transferred at the faying surface. As a result, the upper skin shows an increase in the compressive hoop stress balanced by an increase in the tensile stress (22%). The tensile stress zone is also observed to move near the hole edge. The lower skin shows a decrease in the compressive hoop stress around the hole edge. The tensile hoop stress shows a decrease in magnitude (33%) but is also observed to increase in area.

Hole Misalignment

Hole misalignment increases the unsymmetrical deformation of the rivet. As the rivet expands, contact is established first with the lower skin unconstrained side. After full contact is made with the hole, the expansion proceeds normally. The misalignment effect leads to a larger rivet expansion against the upper skin increasing the compressive hoop stress and consequently the tensile (22%) stress. The lower skin shows a decreased compressive stress but the decrease is not significant so that the tensile hoop stress variation is affected by about 1%.

Decreased Lower Skin Hole Size

With a decrease in the lower skin hole size the rivet expansion is larger in the lower skin leading to an increase in the compressive residual hoop stress near the hole

edge and a tensile hoop stress increase (5%) at the faying surface. Due to the different hole sizes the rivet does not contact the upper skin uniformly leading to a localized compressive hoop stress increase consequently causing a tensile hoop stress increase (33%) at the mating surfaces.

Decreased Upper Skin Hole Size

With a decrease in the upper skin hole size, the rivet expansion is larger in the upper skin leading to an increase in the compressive and tensile hoop (11%) residual stresses. The rivet shows a “bulging” type deformation shape as it achieves contact with the lower skin. As a result, the rivet does not contact the lower skin completely and the compressive hoop stress is greater near the lower portion of the hole edge. The tensile hoop stress increases slightly (1%) but no change in location is observed. An example of the rivet deformation for such geometric variations is shown in Figure 4.13.

Presence of Debris

The presence of debris at the faying surface decreases the rivet expansion against the lower skin hole edge. Part of the rivet deformation results in the faying surface contact closing the debris gap. Reduction in rivet expansion shows a reduced compressive hoop stress near the lower skin hole edge and a reduced tensile hoop stress away from the hole edge (20%). The upper skin shows an average reduction in the compressive hoop stress. However, a local tensile hoop stress increase of 44% is observed near the inner surface of the hole on the constrained side.

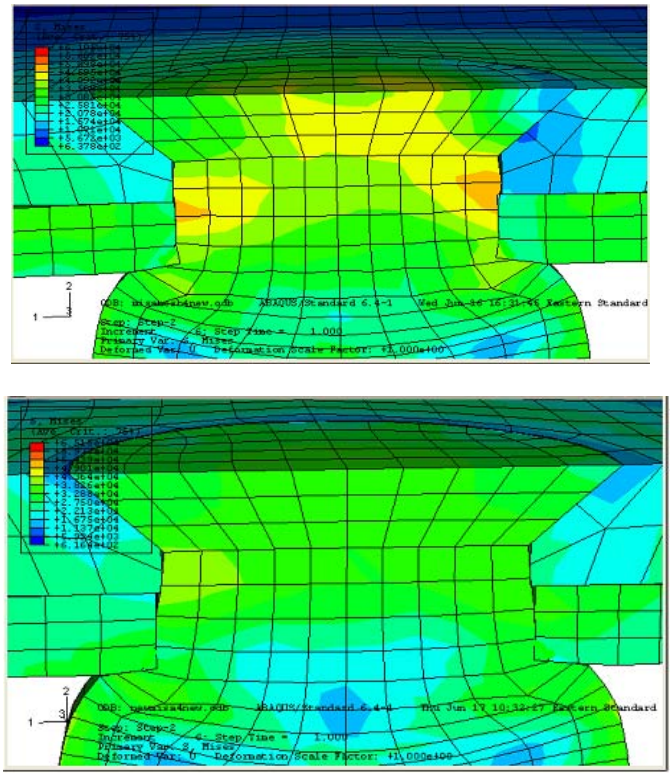

Figure 4.13 An example of the rivet bulging resulting from effects such as skin misalignment and varying hole sizes.

Decreased Hole Clearance

A decrease in the hole clearance leads to a greater rivet expansion. This causes a compressive hoop stress increase in both the upper and lower skin. The compressive zone also increases in size. The upper skin shows an overall increase in the tensile hoop stress of 22%. The lower skin shows a local increase in the tensile hoop stress but an overall decrease (20%). This effect requires a more detailed analysis.

Decreased Rivet Displacement (Under-Driven Rivet)

A decrease in the applied rivet displacement leads to a reduced rivet-hole expansion and consequently a “neat-fit” rivet connection. The under-driven rivet analysis showed the biggest threat to potential for fatigue damage. The under-driven rivet leads

to not only an increase in the tensile hoop stress but leads to concentration of the hoop tension at the hole for both the upper and lower skin. This residual hoop tension, especially with the effect of the sharp countersunk hole will prove to be a critical site for fatigue damage.

A summary of comparison of the residual stress variations for the parametric studies is shown in Table 4.3. For the simulations summarized in the table a strong quantitative variance in the residual hoop stress was observed for some parameters. Qualitatively the tensile hoop stress hoop stress remains concentrated away from the hole for both the upper and lower skin.

4.4 Effect of hole quality variations with under-driven rivets

The previous analyses were also conducted to assess the potential threat of under-driven rivets. It was observed from the analyses that under-driven rivets do not significantly change the hoop stresses quantitatively but it remains concentrated at holes for both the upper and lower skin. An example is shown in Figure 4.14.

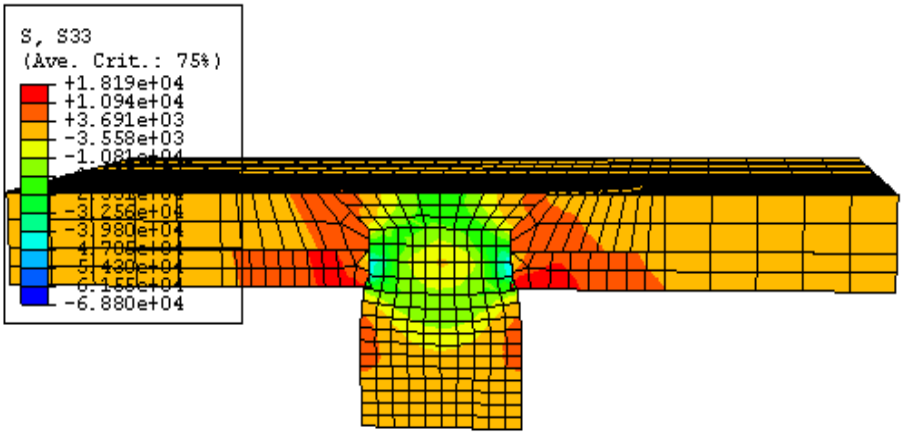

Figure 4.14 Under-driven rivets and effects such as skin misalignment.

Figure 4.15 shows a plot of the maximum tensile residual hoop stress as a function of rivet interference for the countersunk and the straight shank skin. The plot shown is only for variation in rivet interference. Other parameters such as debris and sealant were not considered in the analysis. It can be seen from the plot that as the rivet interference increases (going from under-driven to over-driven) there is a shift in location of the maximum tensile hoop stress with an increase in magnitude.

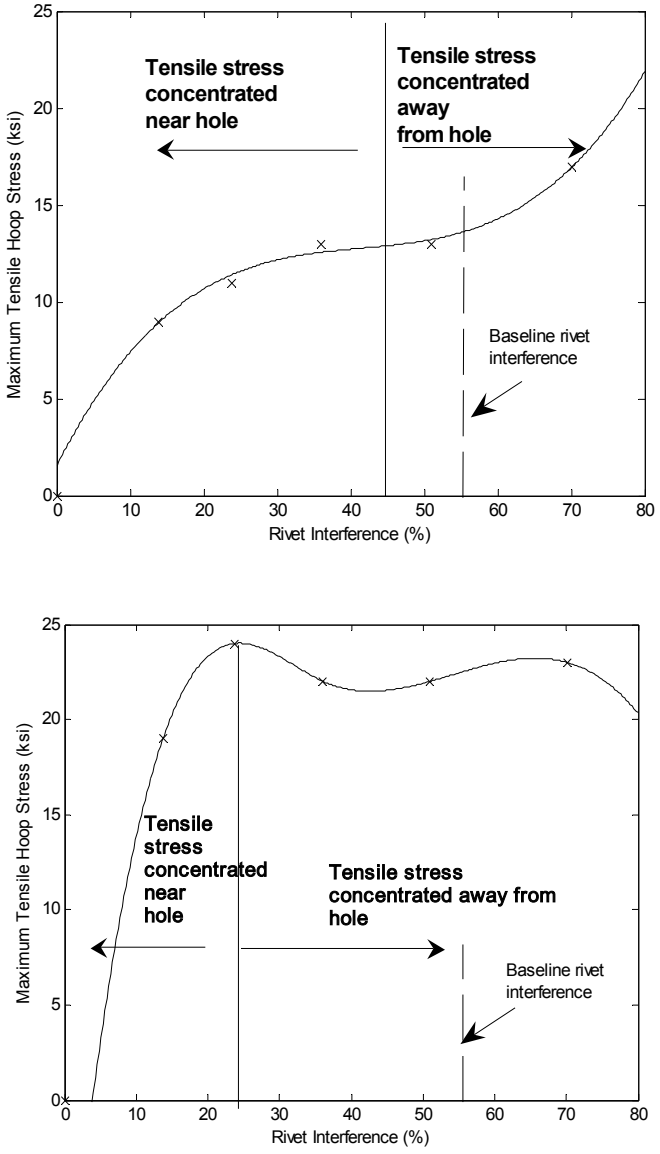

Figure 4.15 Maximum tensile hoop stress as a function of rivet interference. Countersunk skin (top) and Straight-shank skin (bottom)

Table 4.3 Comparison of radial and hoop stresses for the different parameters

	Hoop stress (MPa)				Radial stress (MPa)			
	Upper skin		Lower skin		Upper skin		Lower skin	
Baseline model	68	−199	137	−351	117	−206	158	−379
Over-driven rivet	131	−448	193	−468	179	−441	186	−448
Increased friction	75	−248	103	−372	110	−199	144	−386
Hole misalignment	75	−234	139	−344	110	−199	172	−344
Reduced lower skin hole	82	−282	144	−393	124	−234	172	−399
Reduced upper skin hole	68	−213	140	−386	110	−227	165	−372
Presence of debris	89	−234	110	−351	110	−199	144	−365
Reduced hole clearance	68	−248	110	−372	117	−248	151	−372

4.5 Effect of variations on baseline model with sealant

As stated previously, the sealant analysis presented a large distortion problem. The element distortions that occur during the analysis combined with the non-linear material model presented a significant difficulty for the implicit solver leading to explicit considerations. The sealant was modeled as a low stiffness linear elastic adhesive material (E= 0.85 GPa, ν = 0.31) [64] in Implicit. In Explicit the sealant was modeled as a non-linear hyperelastic material. The stress-strain data for the material [63] and an example of evaluation of test data for different strain energy functions is shown in Figure 4.16.

Elastomeric sealants are essentially incompressible materials. However, Explicit requires a small amount of compressibility in the analysis. The amount of sealant compressibility becomes important when the material is confined between adjacent stiffer components. Larger compressibility ratios will introduce high-frequency noise in the solution, lead to excessively small time increments and produce infeasible results. Trial analyses were conducted for Poisson's ratio ranging from 0.475 to 0.4999. A Poisson's ratio of 0.495 introduces the required compressibility in the solution without excessive run times.

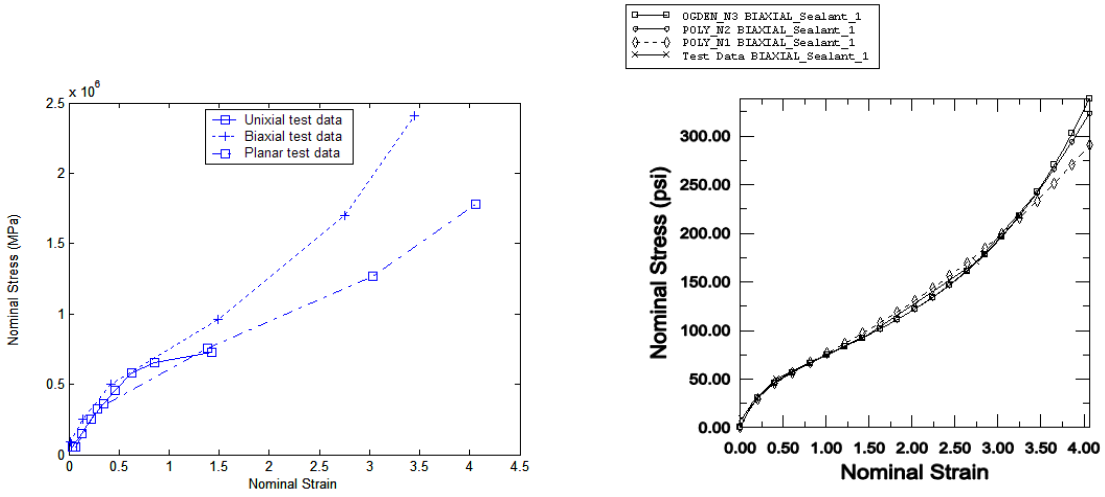

Figure 4.16 Stress-strain data for hyperelastic material model

The test data was evaluated for the different strain energy functions. Evaluating the strain energy function was important because the material model might become unstable at certain strain magnitudes leading to convergence issues. A first order polynomial strain energy potential was found to be stable for all strains and hence was implemented in the analysis. Figure 4.17 shows a view of the model with sealant. The sealant was modeled as a thin layer with a thickness of 0.127 mm. The sealant was constrained on one side while it was allowed to flow on the other side to capture the true effect. The sealant was modeled with C3D8R elements with enhanced hourglassing options and distortion control to model the sealant deformation. Near the hole where significant deformations were expected the sealant was modeled with a refined mesh through the thickness to minimize numerical errors. The model was implemented to observe the effects of interference and the presence of drill shavings on the residual stress state. For each case two simulations were conducted: one with the baseline interference, where the rivet was driven as per the specified standards and one with low interference, where the rivet was under-driven as observed in the teardown inspection.

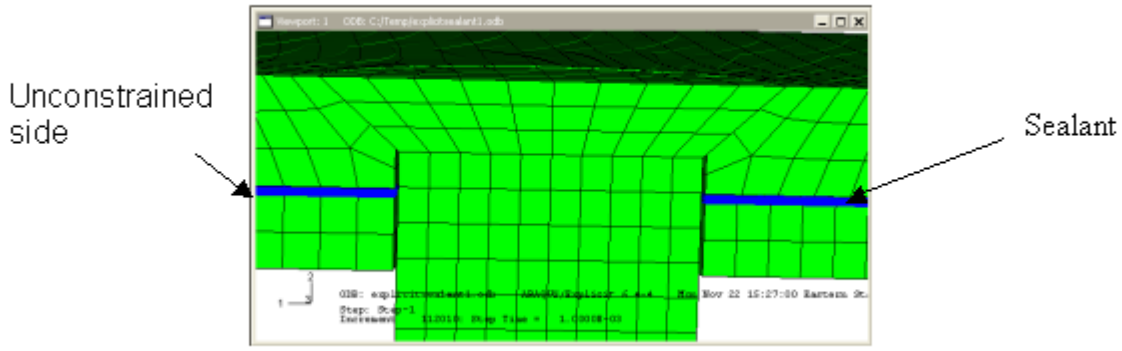

Figure 4.17 A view of the model with the sealant

Baseline interference and sealant

Figure 4.18 shows the final deformed plot for both the Implicit and Explicit analysis. The explicit results show the true sealant deformation near the hole as seen from the microscopy of rivet installation. Figures 4.19 and 4.20 shows the residual hoop stress in the upper and lower skin for both the analyses. For both the implicit and explicit cases a quantitative increase in the tensile hoop stress for the upper skin (28%, 58%) and for the lower skin (19%, 23%) was observed. Qualitatively the lower skin showed similar results while the upper skin showed a concentrated tensile stress near the countersunk edge.

Baseline interference and sealant coverage variation

The sealant coverage was reduced in an area next to the hole to observe the effect on the residual stress state (Figure 4.21). For the baseline interference no contact between the upper and lower skin was observed where the sealant coverage is reduced due to sealant flow taking place during riveting. The upper skin showed a shift in the tensile hoop stress near the countersunk edge. An increase in the tensile hoop stress

was also observed for both the upper (76%) and lower skin (13%). For the Implicit analysis a converged solution could not be obtained.

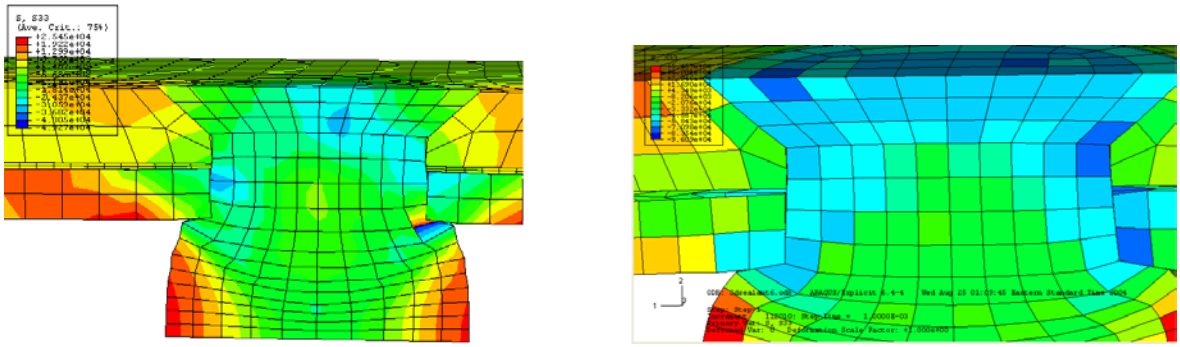

Figure 4.18 Final deformed shape with sealant: Implicit (left) and Explicit (right)

Max. Hoop Stress (MPa)	Upper	Lower
Tensile	96	172
Compressive	-165	-344

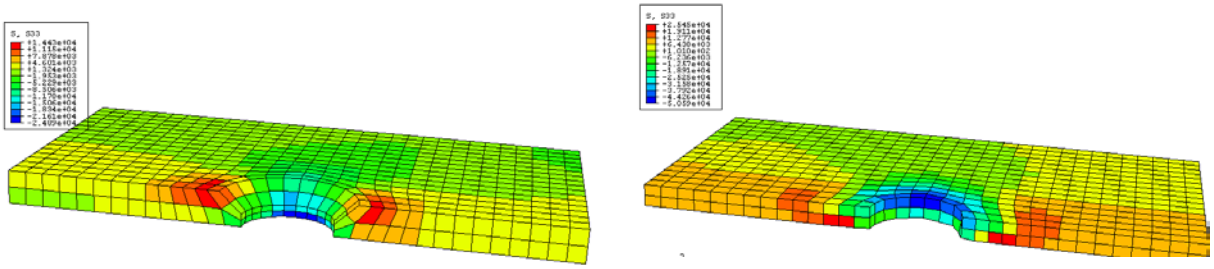

Figure 4.19 Residual hoop stress contour in implicit for the upper and lower skin

Max. Hoop Stress (MPa)	Upper	Lower
Tensile	213	179
Compressive	-393	-572

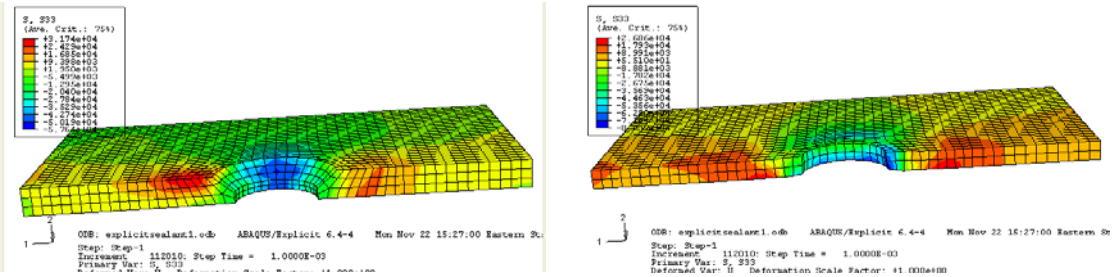

Figure 4.20 Residual hoop stress contour in explicit for the upper and lower skin

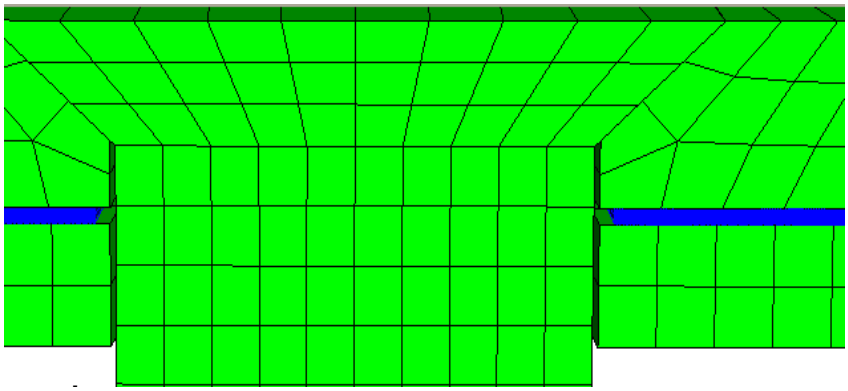

Figure 4.21 Model with sealant coverage reduced near hole

Baseline interference, sealant and drill shavings

Microscopy of the riveted lap joints revealed skin drill shavings embedded in the sealant. An analysis was conducted to observe the effects of baseline interference with embedded drill shavings present in the sealant. Figure 4.22 shows the finite element model along with a representative rivet section. The drill shaving prevents the sealant flow near the hole and strongly affects the rivet deformation. For both the implicit and

explicit cases a quantitative increase in the tensile hoop stress for the upper skin (9%, 116%) and for the lower skin (5%, 47%) was observed.

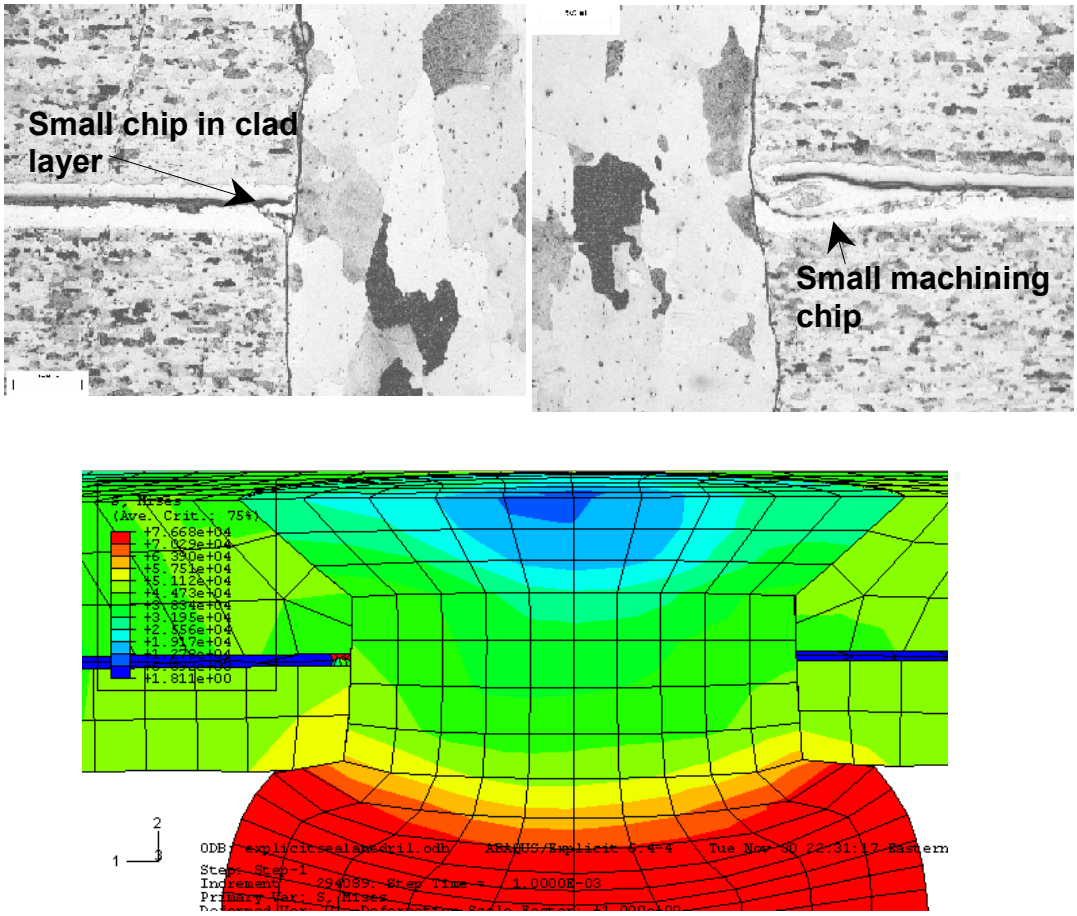

Figure 4.22 Rivet section showing drill shaving and deformed plot of representative finite element model in Explicit

Low interference and sealant

Figure 4.23 shows the final deformed plot for both the Implicit and Explicit analysis. In this case the rivet was under-driven to obtain the effect of reduced interference. Both analyses show a dominant tensile hoop stress near the hole edge for the upper and lower skin. The explicit analysis showed a stronger tensile zone at the faying surface unconstrained side. In both analyses a quantitative increase was

observed for the tensile hoop stress in the upper (Implicit-37.5%, Explicit-81%) and lower skin (Implicit-57%, Explicit-29%) in comparison with the analysis for low interference without sealant (not shown).

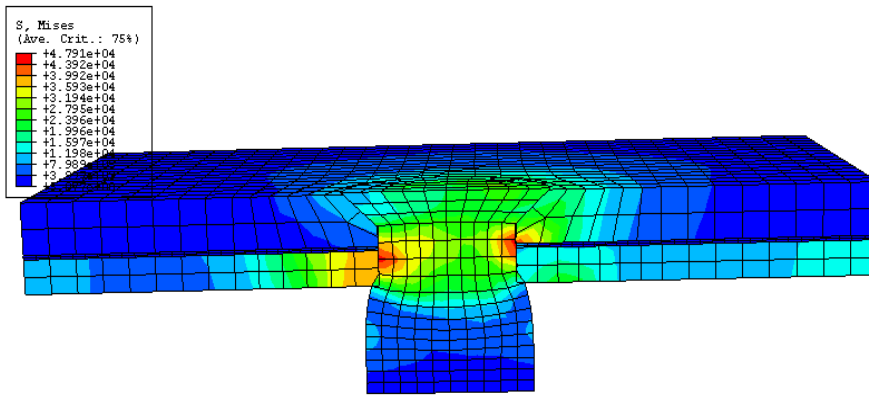

Figure 4.23 Final deformed shape with sealant and low interference in Implicit

Low interference, sealant and drill shavings

An analysis was conducted to observe the effects of low interference with embedded drill shavings present in the sealant. The tensile residual hoop stress remained concentrated near the holes at the rivet/skin interface with a quantitative increase of the residual tension in the upper skin (Implicit-62%, Explicit-109%) and in the lower skin (Implicit-45%, Explicit-47%).

Low interference and sealant coverage variation

In this case, the effect of low interference was analyzed with reducing the sealant coverage near the holes to observe the effect on the residual stress state. Even for low interferences the skin did not come into contact where the sealant coverage was reduced because of sealant flow in that area during the riveting process. Along with a quantitative increase in the tensile hoop stress for both the upper (109%) and lower (47%) the tensile zone was also observed to shift inside the hole. For the analysis in

implicit even for the linear elastic adhesive model a converged solution could not be obtained.

Rivet tilt and sealant

To simulate the rivet tilt (variation in rivet head deformation on opposite side of hole) observed from rivet microscopy the applied rivet head displacement was varied in magnitude across the straight shank rivet head (point of application). Figure 4.24 shows an example of the rivet section and representative finite element model. This method gives a first approximation of analyzing the residual stress state with an interference variation on both sides of the rivet hole. The residual hoop tension is observed to increase largely on one side of the hole for both the upper and lower skin.

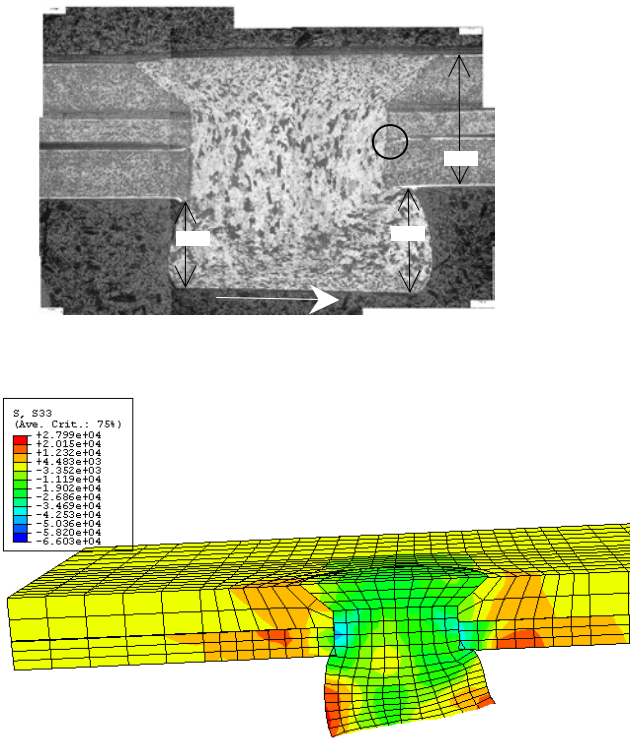

Figure 4.24 Rivet section showing rivet tilt and deformed plot of representative finite element model in Implicit

Table 4.4 Summary of residual hoop stress variations with sealant

Model	Residual Hoop Stress (MPa)							
	Implicit				Explicit			
	Upper skin		Lower skin		Upper skin		Lower skin	
Baseline	75	-206	144	-324	89	-420	144	-599
Baseline Interference with sealant	96	-206	172	-344	213	-393	179	-565
Baseline interference, sealant and drill shavings	82	-165	151	-344	193	-517	213	-482
Baseline interference and sealant coverage variation	N/A	N/A	N/A	N/A	158	-468	172	-579
Low interference	55	-124	96	-268	75	-206	117	-420
Low interference with sealant	75	-154	151	-303	137	-310	151	-386
Low interference, sealant and drill shaving	89	-144	137	-303	158	-324	172	-399
Low interference and sealant coverage variation	N/A	N/A	N/A	N/A	158	-468	172	-579
Rivet tilt and sealant	144	-220	158	-282	179	-310	193	-420

4.5 Effect of Load Transfer on Countersunk Joints

Joining of the two skins provides a path for load transfer. The load transfer ratio is defined as the ratio of the load transferred to the upper skin to the load applied to the lower skin (Figure 4.25). In order to analyze the effect of load transfer on the stress state in the model four different load transfer ratios were analyzed (0%, 25%, 50%, 100%). The applied stress (P1) was 96 MPa based on the remote tension experienced by the joint from fuselage pressurization. The cases were analyzed for low interference and high interference (Figures 4.26 and 4.27).

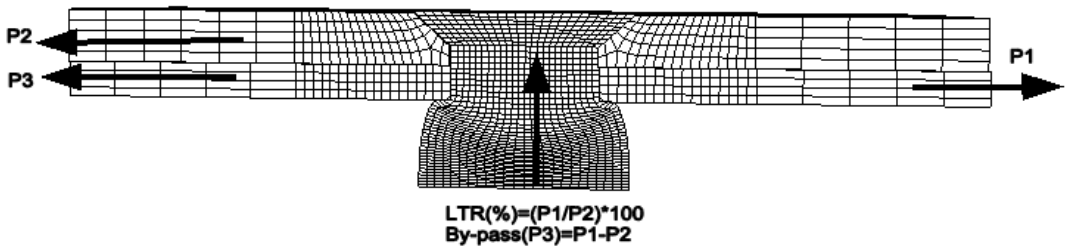

Figure 4.25 Definition of load transfer ratio in riveted lap joints

Park [65] has done a similar study but does not take into account the residual stress distribution resulting from rivet expansion. He observed that the maximum principal stress state moves away from the countersunk region of the upper skin to the straight shank region of the upper skin as the LTR exceeds 20%. Based on his results he concluded that surface cracks would initiate at the intersection or the straight bore for low load transfer while edge corner cracks would develop in the higher load transfer case. It is interesting to note that for low interference the maximum principal stress state remains concentrated near the bottom of the countersunk hole. As the LTR increases the stress concentration moves to the entire hole surface. For high interference and low load transfer the countersunk hole shows a strong compressive zone with the tensile stress concentrated at the faying surface. As the load transfer increases the stress state moves and remains concentrated at the countersunk hole.

4.6 Application of models to fretting fatigue

In an airframe, load transfer takes place at a local scale, which is contact at the rivet/skin interface. The global loading causes normal and shear loading of the rivet causing normal pressure and shear traction at the interface. The contact region consists

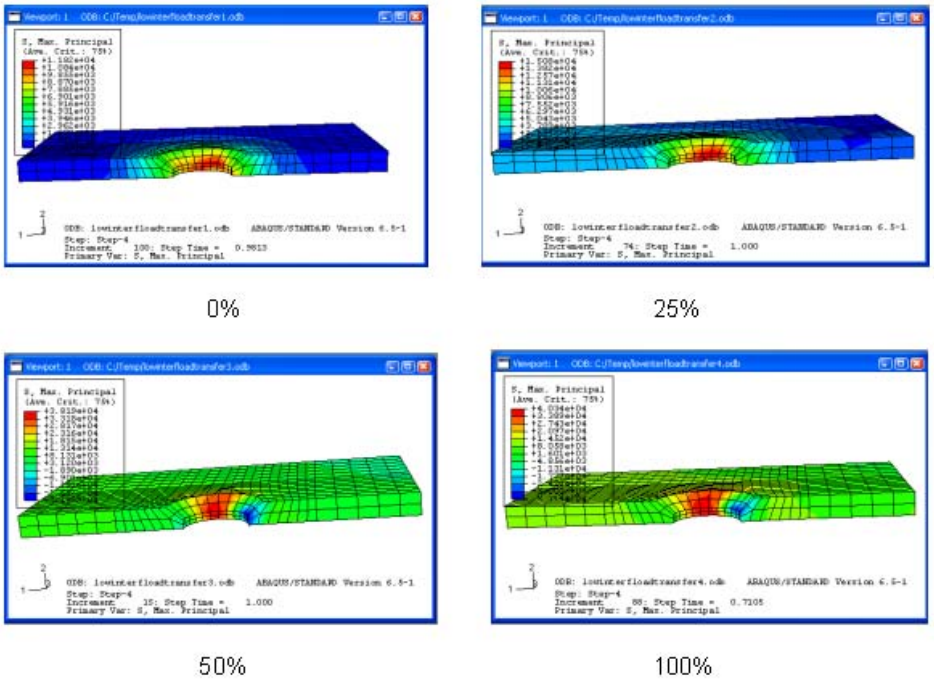

Figure 4.26 Effect of load transfer ratio on maximum principal stress state in the upper skin for under-driven rivets.

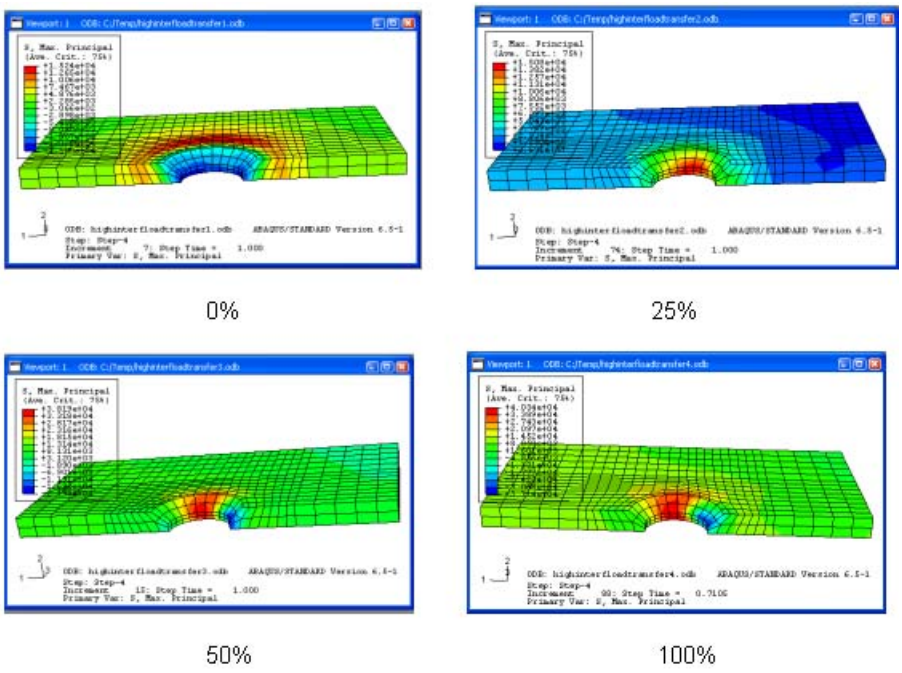

Figure 4.27 Effect of load transfer ratio on maximum principal stress state in the upper skin for under-driven rivets.

of a stick/slip zone. Small relative displacement in the slip zone results in increasing stress intensity at the edge of contact favoring the nucleation of cracks. The micro-slip between the skin and the rivet causes wear, and the associated cyclic stress nucleates small cracks. The high tangential stress can then propagate one or more of these cracks in to the bulk of the skin. This is the basic mechanism of fretting fatigue. Thus, the emergence of cracks from fastener holes can be attributed to fretting fatigue among other possible mechanisms of nucleation. The fretting fatigue behavior of contacting components depends on the contact geometry, contact pressure, and slip amplitude at the interface, material factors and environmental factors. The material pair and surface environment determine the friction coefficient and the tangential stresses generated at the interface. Presence of corrosion also plays an important role in crack initiation.

Fretting wear has been expressed in terms of volume of material abraded, V ($2NWf\delta$), or the average depth of the fretting damage also know as wear scar, y ($2NWp\delta$) [65]. Here, N is the number of fretting cycles, f is the normal contact force, p is the contact pressure, W is the specific wear rate and δ is the local slip amplitude. Fretting wear is favored by large values of W, p and δ. The amount of fretting wear is not proportional to the risk of critical crack formation. At large slip amplitudes cracks may be abraded away resulting in material loss. Efforts to understand fretting fatigue are divided into mechanistic and fretting map approach. The mechanistic approach links interfacial shear stresses, slip amplitudes and underlying bulk stresses to crack initiation. The fretting map approach [66] characterizes, the nature of material degradation at the interface under various slip amplitude, normal load, number of cycles etc. This approach proves to be more empirical as it involves repeated testing for different material pairs under different fretting conditions.

For the mechanistic approaches, Ruiz et al. [67] have proposed two design parameters to predict fretting fatigue crack initiations. The first one is $F_1=\tau\delta$, defined as the product of interfacial tangential shear stresses and slip amplitude. This parameter is a measure of the work expended per unit contact area. This parameter will fall to zero in the stick zone or outside the area of contact. The second parameter, $F_2=\sigma_{\theta\theta}.F_1$, is defined as the product of F_1 and the tensile stress just beneath the contacting surface. The peak of this parameter has been observed to coincide with crack initiation sites in dovetail joints. Conceptually, this parameter is similar to the multi-axial fatigue theory, which involves the product of maximum normal stress and strain amplitude as a basis for crack initiation.

In this work, the mechanistic fretting fatigue parameters were integrated with the finite element simulations to demonstrate the application of the models in predicting fretting fatigue. Analyses were conducted for low rivet interference and large rivet interference. The analyses were conducted in three steps with the same mesh as the baseline model: a rivet loading step, rivet unloading step and application of remote cyclic tensile load. The applied stress (P1) was 96 MPa, consistent with the remote tension on the joint imposed by the 55kPa fuselage pressurization. A 37% load transfer ratio was assumed since the joint modeled was from a three-rivet row configuration [62]. The remote loads were cycled for two cycles after which the model settled into a shakedown state. To enforce accurate stick/slip behavior in the model the Lagrange multiplier was invoked for the contact interactions between the different surfaces. However, it proved to be “notorious” to convergence. Due to increase in the computational cost and preclusion of the contact convergence (oscillating behavior) caused by the algorithm the contact constraint was switched to the default penalty method. Finally, the two slip parameters CSLIP1 and CSLIP2 computed by ABAQUS were combined to obtain an overall

estimate of the slip magnitude. For a countersunk configuration there are four locations where fretting might be of concern: (a) between the rivet shank and hole surface (b) between the two skins (c) between the rivet head and the skins and (d) between the countersunk rivet head and countersunk hole surface. These locations are identified in Figure 4.28.

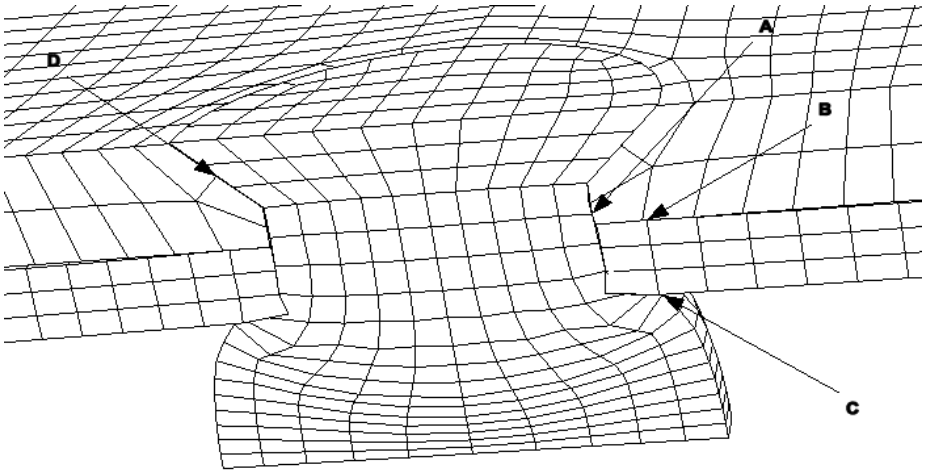

Figure 4.28 Possible locations susceptible to fretting in riveted lap joints

Fretting field A arises from the in-plane slip between the hole surface and rivet shank. Fretting field B is because of the in-plane slips between the panel surface and opposite panel hole edge and is present at symmetric 90 and –90-degree locations (Figure 4.29). Field C arises from the contact between the rivet head and skin. Fretting field D arises from the rubbing of the sharp chisel countersunk edge against the countersunk hole surface. Fretting field B is responsible for the in-plane load transfer to the rivet. Fretting damage in this region is severe but the compressive bulk stress might prevent this plasticized volume from crack initiation.

Figure 4.30 shows the angular variations of contact pressure at the rivet/hole interface (z=t) for different rivet interferences. This contact pressure and the parameters

discussed next are plotted at the faying surface (z=t) around the hole to characterize primarily the any skin-skin fretting. Increase in the applied rivet displacement increases the clamping provided by the formed rivet head leading to greater contact pressures. The damage parameter F_1 is plotted for all three cases.

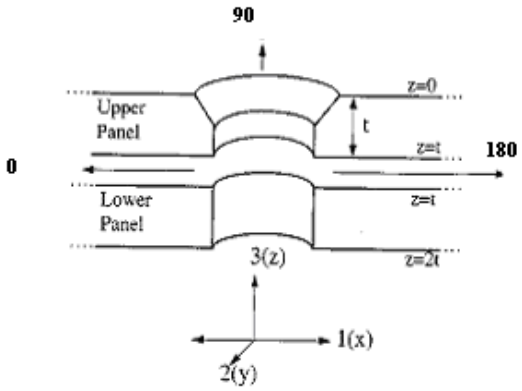

Figure 4.29 Angular locations and depth in the finite element model

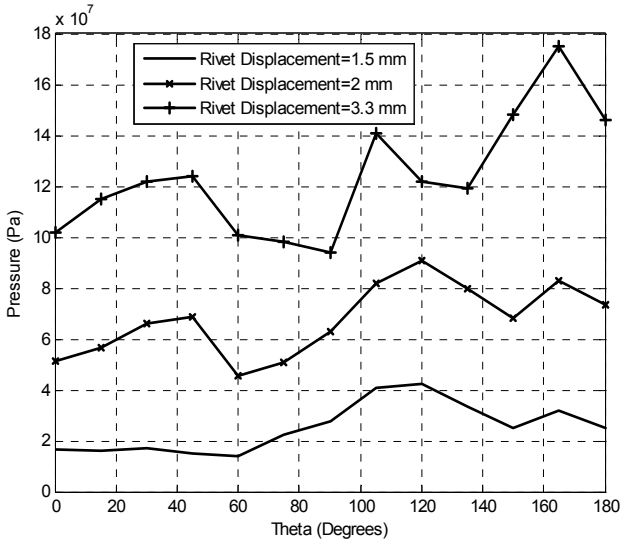

Figure 4.30 Angular variations of contact pressure at faying surface for different rivet interferences

This parameter gives no warning of crack initiation but indicates the contact area that might be subjected to severe fretting. For low rivet interferences (rivet displacement-

1.5 mm) a peak is observed at θ=120^o and another at θ=150^o (Figure 4.31). At larger rivet interferences (rivet displacement-2 mm,3.3 mm) the first peak shifts to θ=90^o . Figures 4.32 and 4.33 show a view of the faying surface for selected hole sections cut from the right hand side panel panel. In most of the figures, it can be observed that the general location of observed fretting is close to the peaks of the F_1 parameter. Figure 4.34 shows a plot of the tangential stress at the faying surface and a plot of the F_2 parameter around the hole. The low interference cases indicate a peak at θ=90^o . This is the possible location of crack initiation. At high interferences the bulk stress is compressive around the hole. This reduces the probability of crack initiation due to fretting at the rivet/skin interface but away from the hole at θ=90^o a presence of the bulk tensile zone will be the primary cause of crack initiation. The shift in the location of the damage parameters demonstrates the application of design tools for maximizing life of the structure.

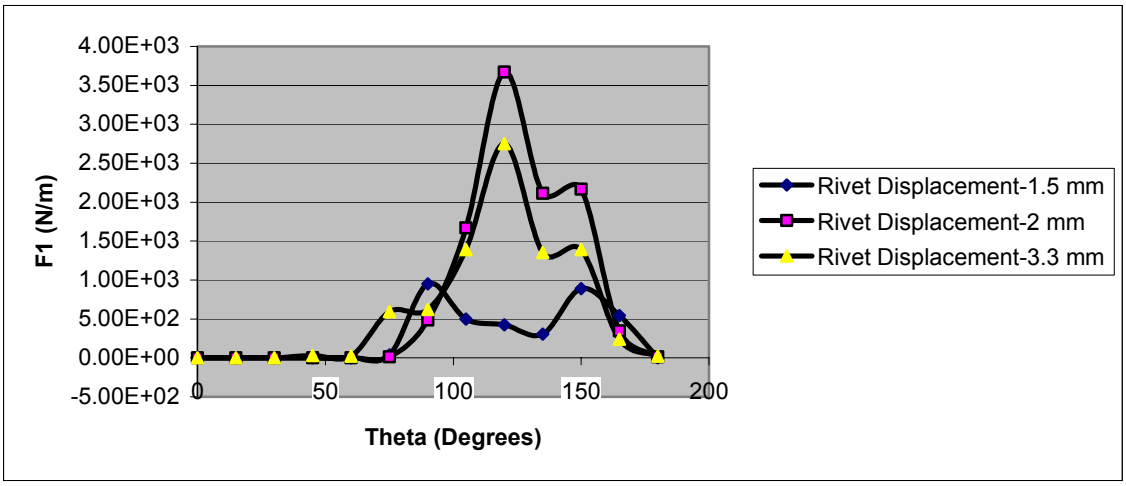

Figure 4.31 Angular variations of damage parameter F_1 at faying surface (z=t) for different rivet interferences

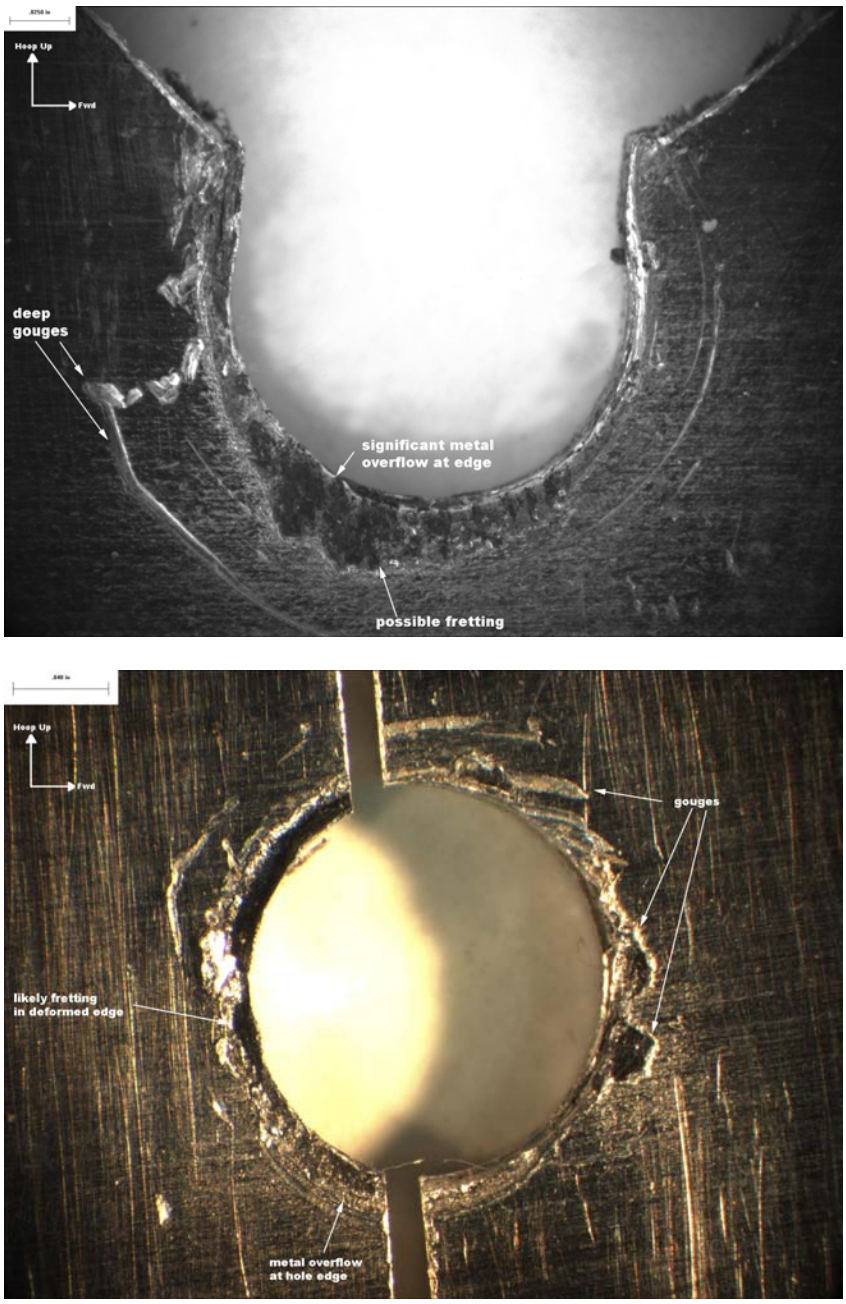

Figure 4.32 Examples of fretting damage observed for some rivet holes from the teardown inspection (faying surface, right hand side panel joint)

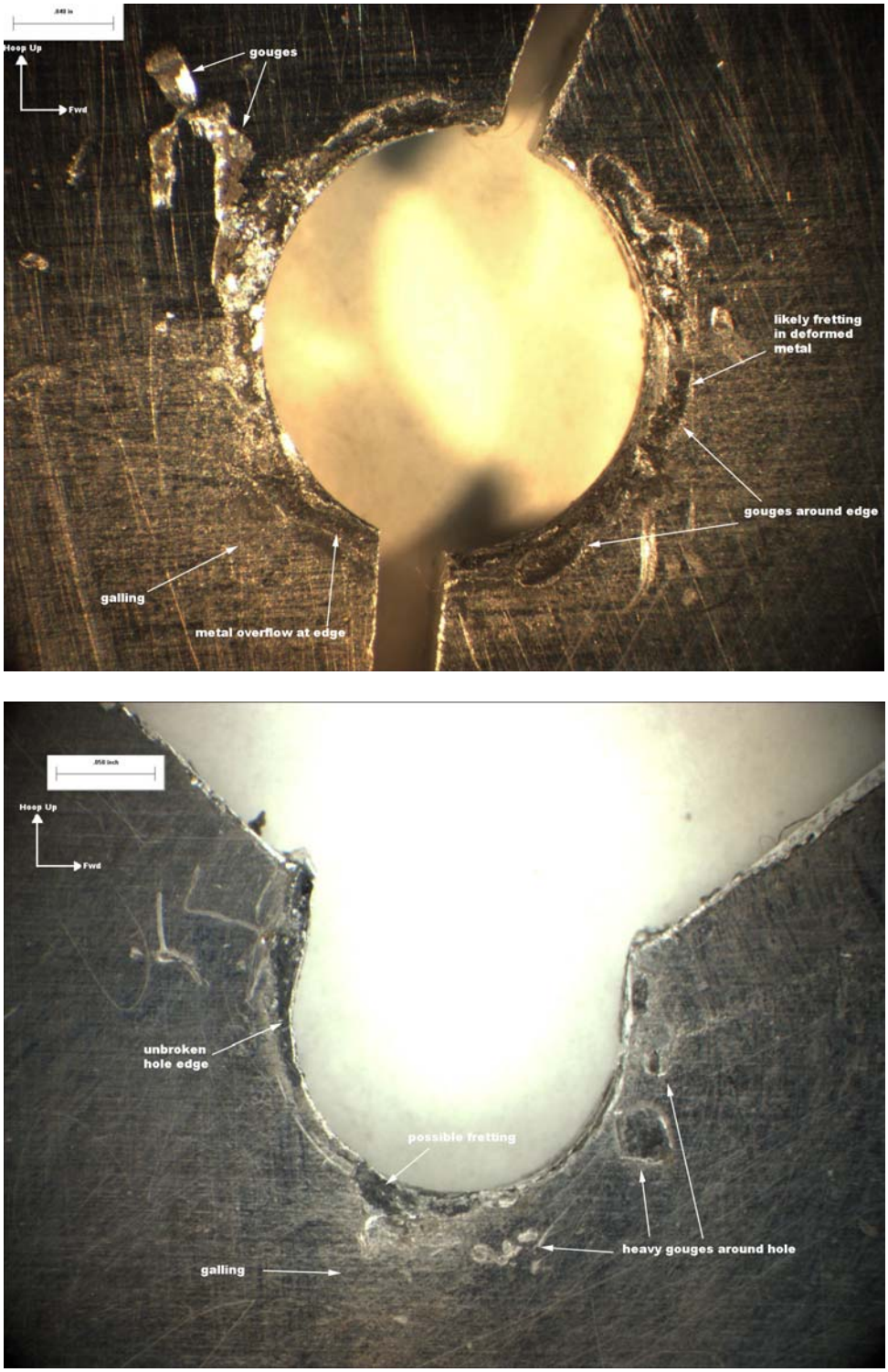

Figure 4.33 Examples of fretting damage observed for some rivet holes from the teardown inspection (faying surface,right hand side panel joint)

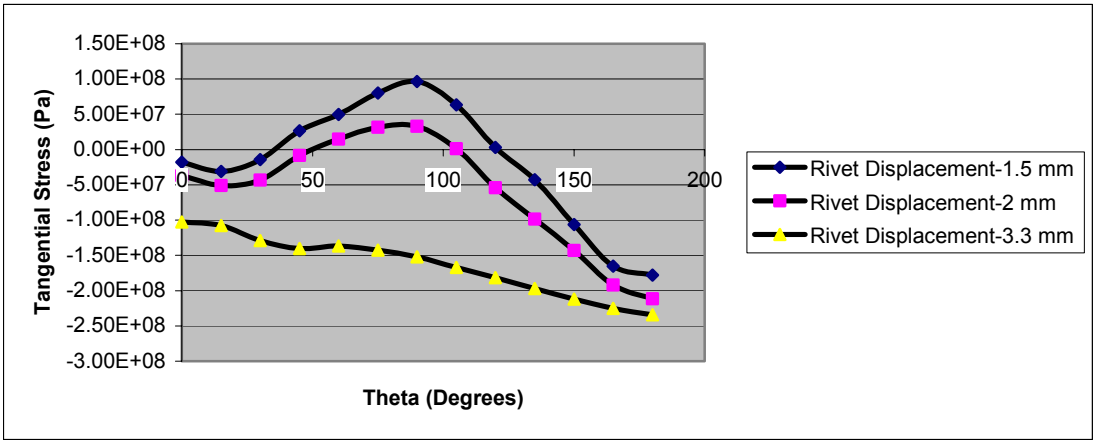

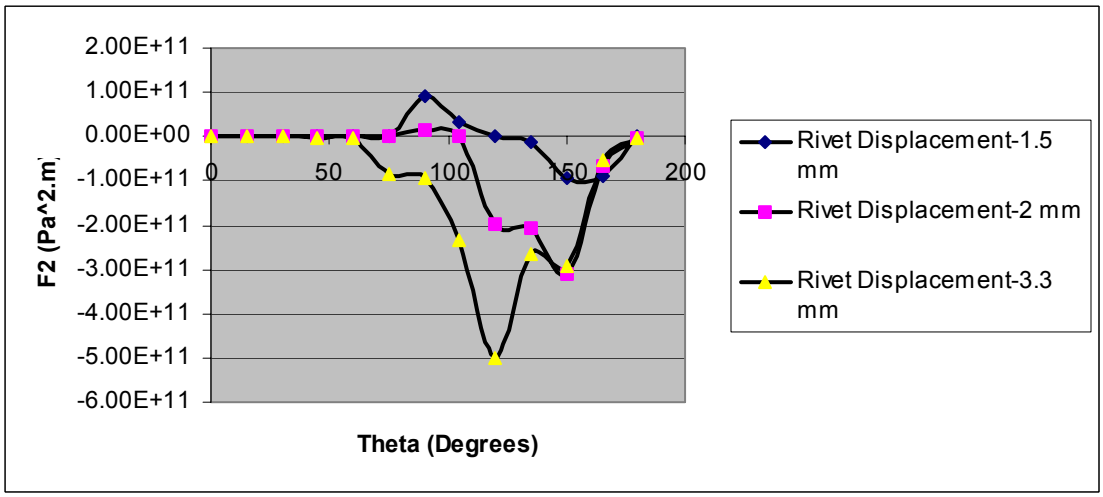

Figure 4.34 Angular variations of tangential stress and damage parameter F_2 at the faying surface (z=t) for different rivet interferences

4.8 Summary

The intent of this chapter was to investigate the effect of manufacturing process variations on the residual stress state generated in aircraft riveted lap joints. The investigation was carried out implementing quasi-static finite element approach similar to the one presented in Chapter 3. This chapter began with development of a baseline 3D riveted joint model designed to duplicate the end row of three-rivet row B727 fuselage

joint. Before final establishment of the model a several mesh designs had to be numerically evaluated. In carrying out those evaluations a mesh ratio of 0.7 was found to be successful in simulating the problem. The baseline model analysis showed a string compressive residual stress state around the rivet holes balanced by a tensile zone away from the hole. This stress distribution in the joint was found to be highly unsymmetric in nature. This unsymmetrical nature of the stress state was also demonstrated by a separate analysis conducted on the same model without assuming any initial rivet hole clearance.

This was followed by a similar baseline analysis conducted in ABAQUS/Explciit. Though the analysis was simulated quasi-statically, comparison of residual stress results predicted by the two solvers showed a 20% difference of between the values. This disparity was attributed to the inherent difference in the nature of the two solvers.

Additional finite element analyses were conducted to investigate the difference in residual stress state, if any, resulting from variations such as hole clearance, hole defects, sealant and debris. Comparison of the results for these models with baseline showed that the process variations affected the residual hoop tension quantitatively to some extent. Qualitatively under-driven rivets were observed to create a stress concentration at the hole. In summary of the observation of process variations on the residual stress state, under-driven rivets proved to be the biggest threat by creating a tensile stress concentration at the hole; this stress concentration was observed to be 40% greater in value than that for the baseline model. The finite element models were also implemented to demonstrate the importance of taking into account initial rivet interference when predicting the final stress state. This was achieved by observing the variation in stress state at the countersunk hole for different percentages of load transfer.

The finite element models were then utilized in conjunction with traditional fatigue damage parameters to predict the location of potential fretting damage in the joint. For

this purpose, the fatigue damage parameters were plotted at the rivet/skin surface for under-driven and baseline installed rivets. The peaks of the damage parameters agreed with the general location of fretting damage observed around the rivet holes.

Finally, a summary of different analysis techniques attempted in simulating the process was presented. Differences in simulating the process between two different analysis packages in terms of convergence were also noted.

Chapter 5: Global Fuselage Lap Joint Analysis

The previous chapter discussed the results from the development and implementation of a 3D one-rivet finite element model to investigate the effects of manufacturing process variations on the residual stress state in the skin. While those models demonstrated the sensitivity of residual stresses to process variations, they did not take into account the uneven load transfer and secondary bending resulting in the lap joint. As such, the present investigation focused on development of a global three-rivet fuselage lap joint, which takes into account the residual stresses resulting from rivet installation and in-service fuselage loads. The model behavior was designed to approximate the loading experience by the fuselage splices removed in the teardown inspection. Available results from the B727 teardown damage characterization provided validation to the analysis. Finally, the global models were implemented in conjunction with crack growth analysis to predict the approximate number of cycles to grow a crack of 0.2 inches at the critical holes.

5.1 Background

Observation of the influence of process variables on fatigue damage in fuselage splices depends on accurate determination of the local stress distribution. The local stress state in a fuselage lap joint depends on rivet/skin, skin/skin contact, residual stress resulting from installation, fuselage pressurization, friction and secondary bending effects. The load transfer in the splice is a difficult matter. This load transfer is done by rivet shear and also through friction between the sheets. This gives rise to a complex 3D stress distribution at the hole. Eastaugh et al [56] illustrated this in a photoelastic image.

They concluded that the stress was a cause of several loading conditions such as: clamping stress applied by rivet, biaxial tension in sheet, internal pressure applied by rivet expansion, out-of-plane bending due to joint eccentricity, pin loading at hole due to load transfer through rivet shear and surface shear within the clamping zone of rivet due to load transfer through friction.

5.2 Analysis

A schematic of the lap joint is shown in Figure 5.1. The joint joins two skins that are typically 5000-10,000 mm long. A fuselage frame is fastened to the skin every 5000 mm dividing the lap joint into 5000 mm bays. The 3-row lap joint is the structure typically susceptible to MSD. As shown, in Figure 5.1, the skins at the lap joint, have two critical areas; the outer skin at the top row of fastener holes, and the inner skin at the bottom fastener row. At both rows the fastener hole is loaded by far-field and hole-bearing stresses and is susceptible to accelerated crack initiation and growth.

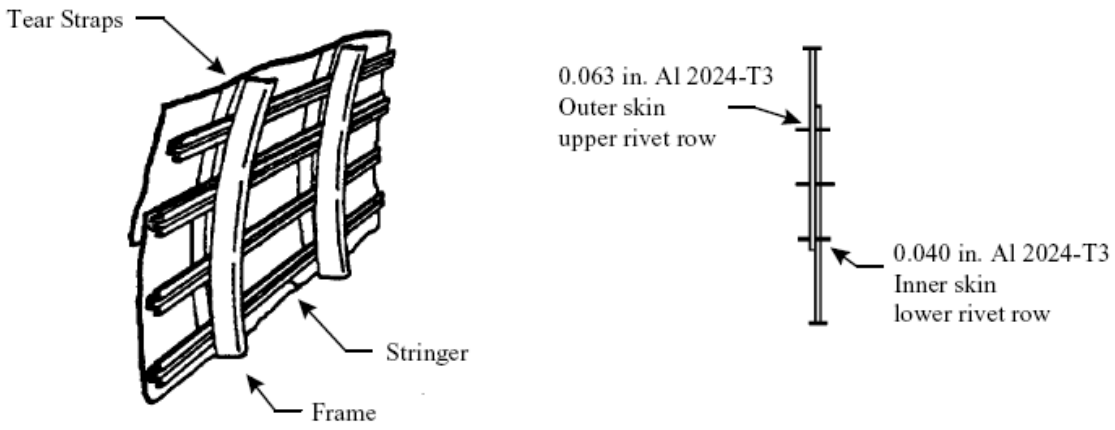

Figure 5.1 Schematic of lap joint typically susceptible to widespread fatigue damage

Figure 5.2 shows a typical three-rivet fuselage splice. Fuselage pressurization is the main fatigue load on the lap joint (55 kPa once per flight). As stated before, the flight load subjects the lap joint to hoop tension, longitudinal tension, out-of-plane bending and secondary bending. Out-of-plane bending causes pillowing of the skin between the stiffeners and distortion. This is also known as secondary bending caused by the action of hoop tension on the eccentricity inherent in single lap joints. Fatigue cracks start in or near the rivet holes. Determination of the stress distribution at the hole is thus of prime importance. The stress distribution is a combination of biaxial tension in the skin, clamping load applied by rivet, residual stresses due to rivet installation, out-of-plane bending and load transfer due to friction.

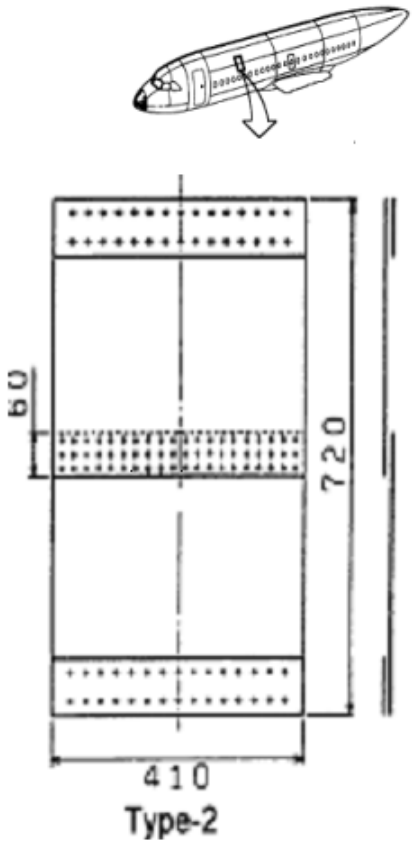

Figure 5.2 Typical three-rivet fuselage splice [62]

Figure 5.3 shows the geometry of the fuselage splice in the current study and the developed finite element model. The model, which had 27,660 nodes and 21,641 elements (93,645 DOF), was generated using ABAQUS/CAE 6.4-1 with C38DR reduced integration 8-node linear solid brick elements with a few triangular elements interspersed in the mesh. Spring elements with a stiffness of 175 kN/m connected to the middle rivet were used to represent the stringer. Symmetric boundary conditions were utilized and surface interactions were defined as contact pairs using the master-slave algorithm available in ABAQUS/Standard with the finite sliding option. The contact interaction was modeled with the Coulomb friction model. Formulation of the elemental stiffnesses based on current configurations from deformed nodal positions was provided using the NLGEOM option. Non-linear material data was implemented from Table 3.1.

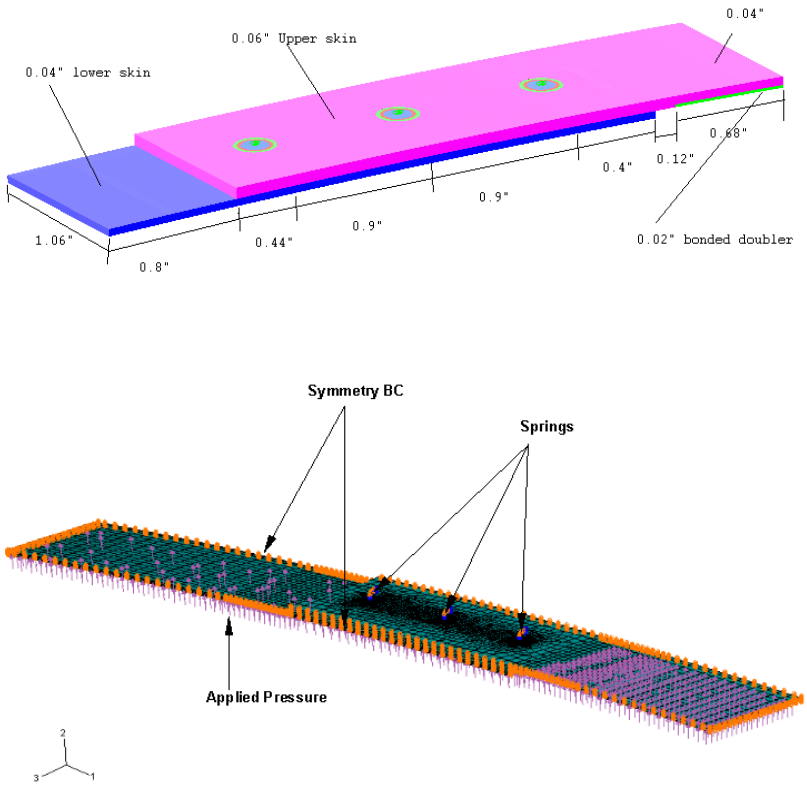

Figure 5.3 Geometry of the fuselage lap-joint model and finite element model analyzed in this study

The analysis was done in two steps. In the first step, three rings of elements at the rivet holes in the global model were oriented in their respective local cylindrical coordinate system. Eight element sets were created through the thickness for each rivet hole. The residual stresses at the end of unloading from the riveting model were computed at the centroid of each element for the three rings of elements around the rivet holes. The residual stresses were mapped from the riveting model to the element sets around the rivet holes for the global lap joint model as initial conditions. An equilibrium step was performed to resolve the contact conditions and check for consistency with the riveting model. This ensured that the global model had the residual stresses and plastic strains consistent with the riveting model and also allowed ABAQUS to check for equilibrium and iterate if necessary to achieve equilibrium. The results of the first step confirmed that the approach was correct and the contact conditions were resolved accurately. Once this step was completed successfully the fuselage pressure loading (55kPa) was applied to duplicate the loading experienced in service. The loads were cycled for three cycles. After two cycles the model settled into a periodic solution known as the shakedown state. A coefficient of friction of 0.2 was assumed in the baseline analysis. The final stress state from rivet installation is the only input to the global model. Hence, it does not recognize the past loading history and assumes a lesser work hardening than that may be occurring in service.

A mesh refinement study was conducted similar to the one conducted for the riveting process model. The mesh was refined around the three rivet holes and through the thickness to generate a model with 65,000 elements. The maximum principal stress at the critical rivet holes at the end of all the loading cycles showed 1% difference in comparison to the original model indicating numerical convergence. The stresses reported at the nodes around the rivet holes were compared to the stresses at the

integration points of the elements to ensure there was no significant difference between the two values.

Figure 5.4 shows the deformed plot (exaggerated) at the end of the application of residual stress and the cyclic pressure loading. The stress state in the inner and outer skin is shown in Figure 5.5. The maximum principal stress is located at the lower row hole in the inner skin (row A in Figure 1.4) and upper row hole in the outer skin (row C in Figure 1.4). The observation of the maximum principal stress at the lower row hole inner skin is consistent to the observed fatigue damage at the same location from the teardown inspection. Figure 5.6 shows the comparison. The stress varies around the hole as well as through the thickness for each hole illustrating the complexity of distribution. This is shown in figure 5.7.

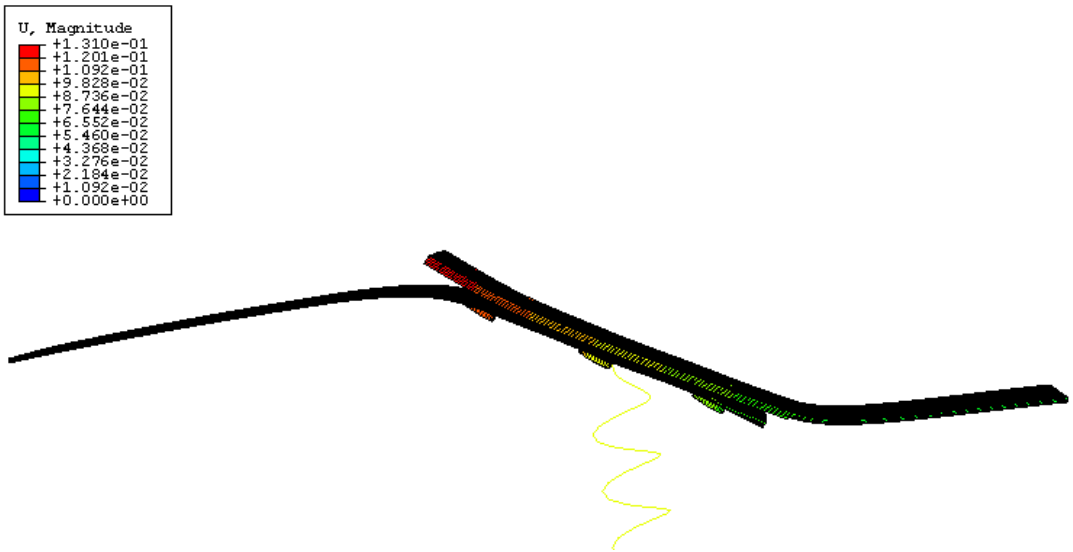

Figure 5.4 Deformed plot (exaggerated 20 times) of fuselage splice after residual stress application and cyclic pressurization

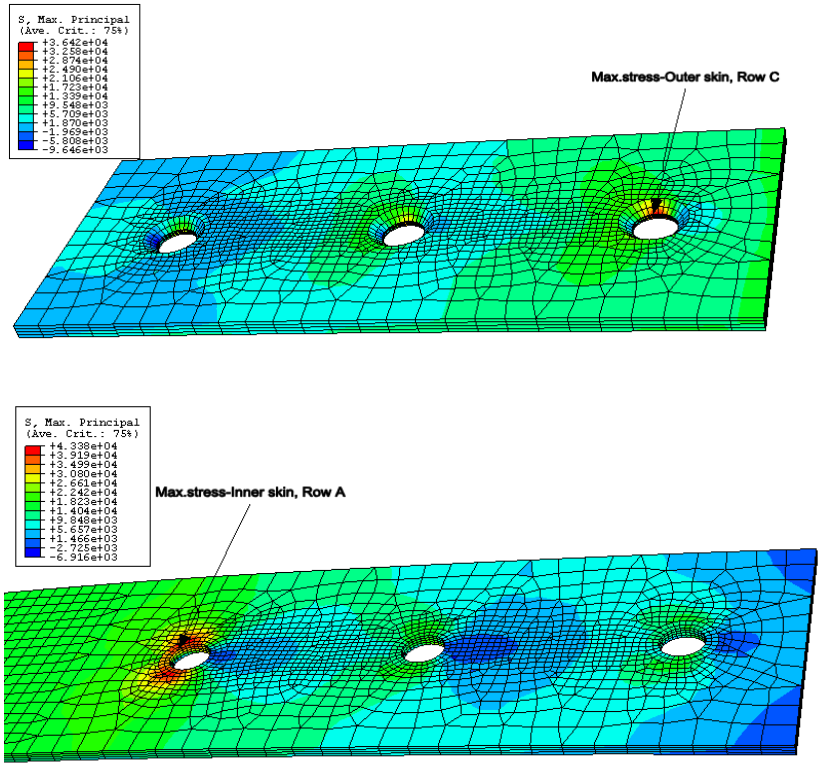

Figure 5.5 Maximum principal stress state in inner and outer skin

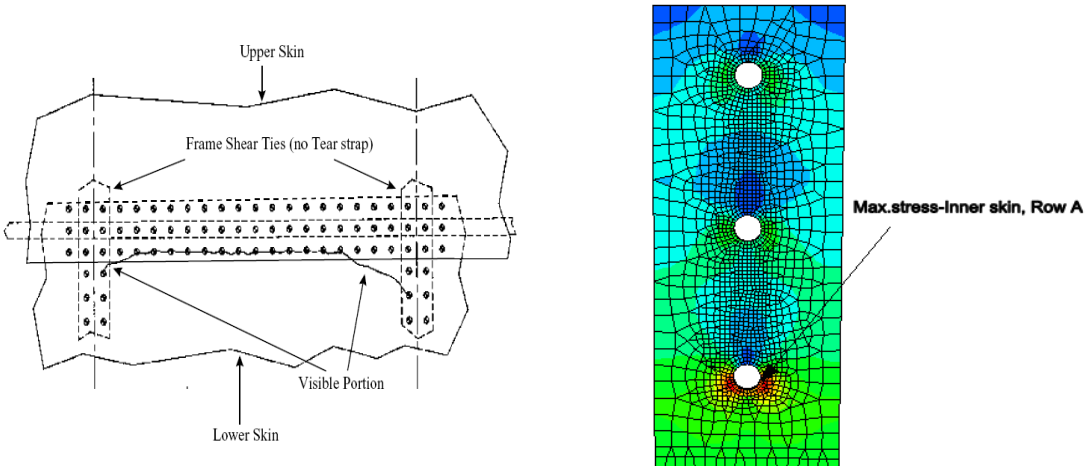

Figure 5.6 Comparison of cracking observed in teardown inspection and stress state predicted by the finite element analysis in the lap joint

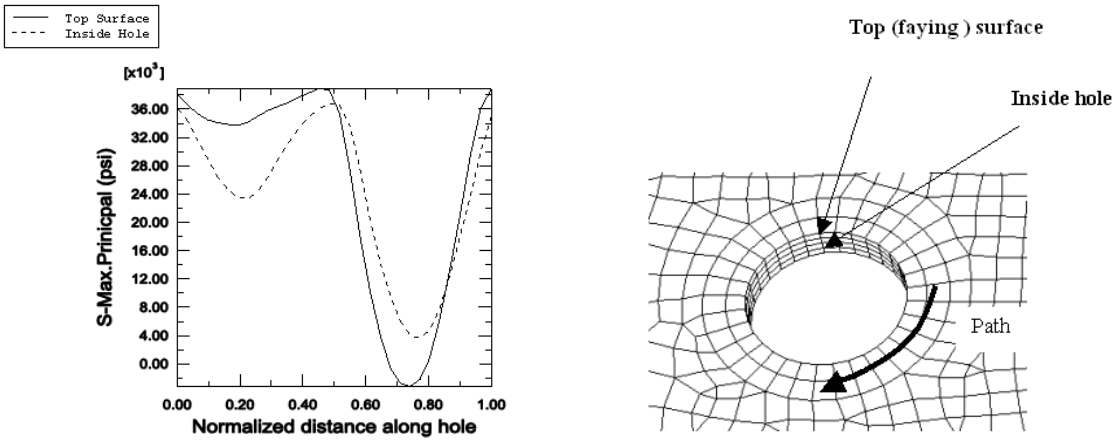

Figure 5.7 Complexity of stress distribution at the inner skin lower row rivet hole (row B)

A major finding from the teardown inspection was that the right hand side panel and the left hand side panel had been installed with a difference in the rivet spacing. The right hand side panel joint had an “average” rivet spacing (22.479 mm) as shown in Figure 5.1. The left hand side panel joint had a slightly larger rivet spacing (27.94 mm) between the lower and the middle rows. It was speculated that the difference in the spacing dimensions might reduce the bending stress at the lower rows leading to the better fatigue lives observed for the left hand side panel joint. To analyze this effect a fuselage splice model of the left hand side panel joint was constructed in ABAQUS/CAE. The model had 65,000 hexahedral elements and applied loading exactly similar to the right hand side panel analysis. Figure 5.8 shows a view of the model. The analysis, however, showed no difference in the stress state at the critical rivet row in the inner skin (Figure 5.9) indicating that the slightly increased rivet spacing did not significantly affect the stress state for either of the skins.

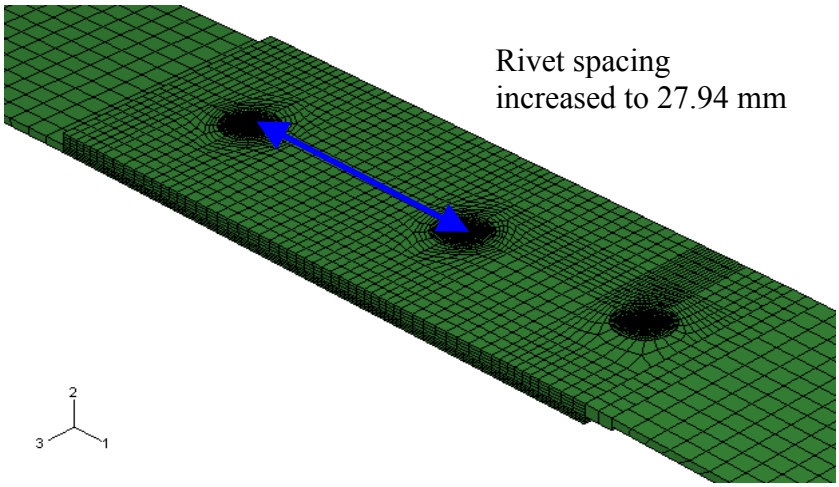

Figure 5.8 Fuselage splice model for the the left hand side panel joint with modified rivet spacing

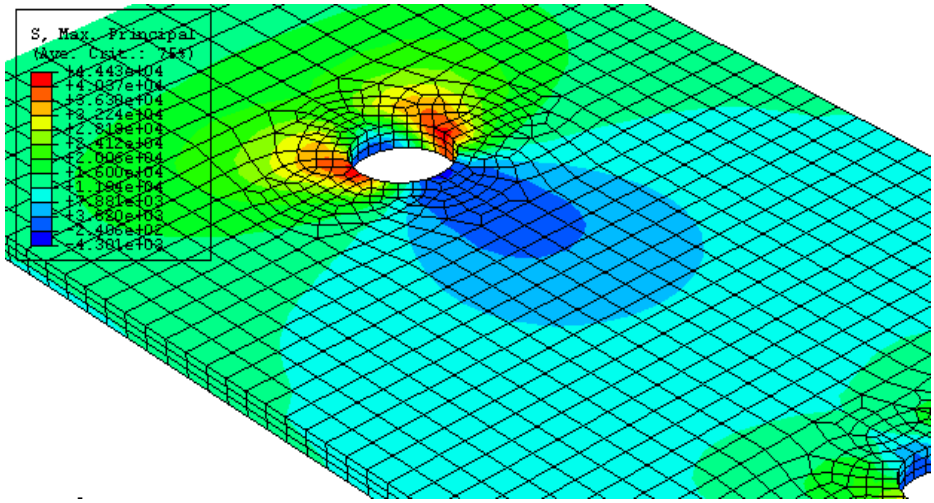

Figure 5.9 Stress state at the critical hole for the inner skin (the left hand side panel joint)

5.3 Fatigue crack growth analysis

Visual and high-frequency eddy current are some of the techniques used to inspect the lap-joint for cracks. These techniques cannot reliably detect cracks until they are a certain length. Initiation is typically considered as the appearance of a crack of 0.02 in. The strain-life model, Smith-Watson-Topper (SWT), can be applied to predict the crack nucleation at rivet holes in the lap joints. Smith et al. [68] first proposed the SWT model in 1970, which incorporated both cyclic strain range and maximum stress. The SWT model was selected because it had the capability to predict multi-axial fatigue life (fatigue life due to complex stress states where the three principal stresses are non-proportional or whose directions change during the loading cycle), it only used uni-axial fatigue properties and it had the capability to predict fretting fatigue life.

Work related to the development of the final SWT equation can be also found in the papers of Manson [46] and Coffin [47]. The applications of the SWT model to fretting can be found in the papers of Szolwinski, Harish and Farris [32,33,69-71]. According to the SWT criterion Eq. 6.1, a minimum nucleation life 2*Nf* corresponds to a maximum value of Γ as the exponents are less than zero.

The SWT model is expressed as

$$\Gamma = \sigma_{\max}\left(\frac{\Delta\varepsilon}{2}\right) = \frac{(\sigma_f')^2}{E}(N_N)^{2b} + \sigma_f'\varepsilon_f'(N_N)^{b+c} \quad [6.1]$$

Γ – SWT parameter,

$\frac{\Delta\varepsilon}{2}$ – maximum principal strain amplitude,

$\sigma_{\max}$ – maximum stress on the maximum principal strain plane.

E – elastic modulus,

N_N– number of cycles to crack nucleation under a certain stress and strain level.

σ_f' – fatigue strength coefficient (843 MPa)

ε_f' – fatigue ductility coefficient (0.174)

b – fatigue strength exponent (-0.096)

c – fatigue ductility exponent.(-0.644)

where the values for the parameters are based on uni-axial strain fatigue tests. Using the stress and strain results from the FE analysis and the material parameters the cycles N_N to nucleate a crack of 0.5 mm was related to the SWT model. Figure 5.10 shows a plot of the SWT parameter plotted with the number of cycles to crack nucleation N_N.

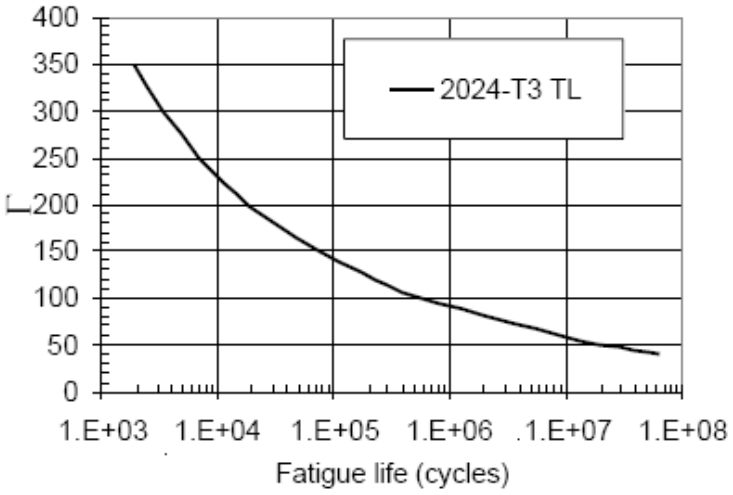

Figure 5.10 SWT parameter plotted with the number of cycles to crack nucleation N_N

The crack growth analysis determined the subsequent crack growth after the crack was nucleated to a certain length**.** The AFGROW software package was employed to perform this crack growth analysis. The crack growth analysis was carried out using the classic model of a corner crack at a straight hole in AFGROW and a combination of by-pass tension, bearing, and bending loading (Figure 5.11). For typical lap joints with 2, 3 and 4 rivet rows, finite-element analyses produce rivet loading (top rivet row) in

terms of the local stress as 0.5, 0.37 and 0.29, respectively. For example, for the 3-rivet row, 37% of the load is carried by the rivet loading and 63% of the load is the by-pass loading [62]. The applied remote stress (S) was 96 MPa with a 37% rivet stress and 67% by-pass stress (S_b). The results from the analysis in which the number of cycles (N_G) to grow a crack from 0.5 mm to 1.27 mm was determined. Using this approach the total number of cycles to nucleate and grow a crack to a length of 1.27 mm was determined to be 76,361 for the baseline model.

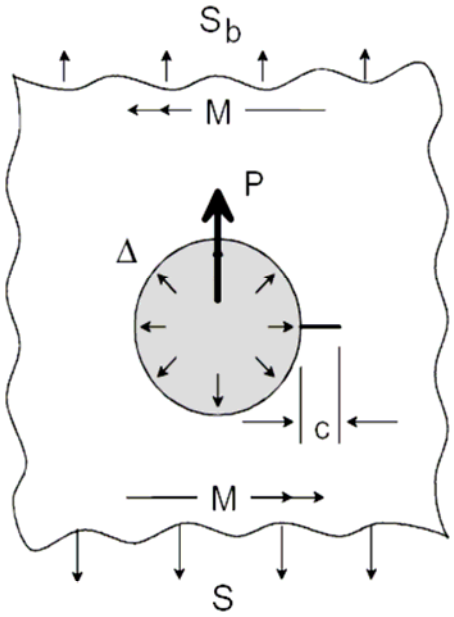

Figure 5.11 Schematic of model used for crack growth analysis [62]

5.4 Analysis of critical process variations

With confidence established in the developed model to predict the stress state at the hole, the analysis was implemented to observe the effect of process variations on the stress state at the hole and cycles to crack growth. Again, it is reiterated that these process variations investigated are based on actual observed service conditions. Hence,

a full factorial design of experiments was not established for the parametric variations. A summary of the results from this study is given in Table 5.1.

Effect of Under-driven rivets

The teardown inspection revealed that 60% of the rivets in the lap joint were under-driven. The average measured driven rivet head diameters in this case were documented to be 5.334 mm. To observe the effect of under-driven rivets on the fuselage the riveting process was analyzed iteratively by applying different displacements to the rivet to obtain approximately the same driven head diameter and importing the residual stress state to the fuselage splice model. Under-driven rivets reduced the rivet expansion leading to a tensile residual stress state at the rivet/skin interface. This caused a stress increase of approximately 15% at the critical rivet row A. The outer skin showed a stress increase at the critical row C as well as at the middle and bottom row of approximately 18%. This effect will reduce the life to crack nucleation in both outer and inner skin as well as create a multiple site damage scenario for the outer skin where cracks could originate from all three-rivet holes.

Effect of Over-driven rivets

The average measured driven rivet head diameters in this case were documented to be 6.096 mm. To observe the effect of over-driven rivets on the fuselage the riveting process was analyzed iteratively by applying different displacements to the rivet to obtain approximately the same driven head diameter and importing the residual stress state to the fuselage splice model. Over-driven rivets increase the rivet expansion leading to a strong compressive zone at the rivet/skin interface but increasing the tensile stress away from the hole. The maximum principal stress at row B rivet/skin interface reduced by approximately 30%. The maximum tensile stress was observed slightly

away from the hole approximately 10% higher than the baseline. The outer skin also showed a reduction in stress (10%) with a slight stress concentration only at row C. This will increase the nucleation life for cracks arising from hole quality issues particularly for the outer skin. The major threat in this case will be the tensile zone at row A that might be a potential site for fatigue damage.

Variation in rivet interference

To observe the effect of varied rivet interference along the rivet rows, the residual stresses from both the under-driven and over-driven analyses were utilized. The residual stress generated by the over-driven rivet was applied to row A while the residual stress generated by the under-driven rivet was applied to the middle and bottom row. For the lower skin, the maximum stress, which occurs away from the hole at row A, remains the same. A stress concentration can be observed at the bottom and middle holes. For the upper skin row A and the middle row shows a strong stress concentration at the rivet hole with an 18% increase in stress while the top row the compressive zone is dominant. Such variations of rivet interference might increase the propensity of fatigue damage combining any arising at over-driven holes with strong stress concentrations at under-driven or non-uniformly installed rivets.

Effect of sealant

The sealant analysis presents a large distortion problem. The sealant was modeled as a low stiffness linear elastic adhesive material (E= 0.85 GPa, ν = 0.31) [64] as a thin layer with a thickness of 0.127 mm. The sealant was constrained on one side and allowed to flow on the other side. The sealant was modeled with C3D8R elements using enhanced hourglassing options to model the sealant deformation. The presence of sealant showed a quantitative increase in the residual stresses. Qualitatively the tensile

zone remained concentrated away from the hole. For the inner skin the maximum principal stress showed a slight increase (5%) at row A. For the outer skin row C showed a 13% increase in the stress. A strong stress concentration was also observed at the middle row countersunk hole with a stress increase of almost 34 %. This increase can be attributed to residual stress increase as well as higher load transfer to the outer skin.

Effect of sealant and under-driven rivets

To observe the effect of under-driven rivets with sealant on the fuselage the sealant model was analyzed by applying 2.54 mm displacement to the rivet corresponding to the under-driven rivets and importing the residual stress state to the fuselage splice model. The presence of sealant showed an increase in the residual stresses with the tensile stress concentrated at the rivet/skin interface in comparison to the under-driven rivet without sealant. Compared to the analysis with under-driven rivets both the outer and inner skin showed similar stress concentrations with a slight increase in the maximum principal stress (5%).

Effect of sealant, drill shavings and under-driven rivets

Microscopy of the riveted lap joints revealed skin drill shavings embedded in the sealant. An analysis was conducted to observe the effects of low interference with embedded drill shavings present in the sealant. The drill shaving was modeled next to the hole with the sealant using the same material model of the skin. The drill shaving prevents the sealant flow near the hole, strongly affects the rivet deformation causing an increase in the residual stresses. Compared to the analysis with under-driven rivets both the outer and inner skin showed similar stress concentrations with a slight increase in the maximum principal stress (5%).

Effect of friction

To observe the effect of friction on the baseline model the residual stresses from the riveting process were imported to the fuselage splice model followed by cyclic pressurization, with a coefficient of friction of 1.1 between the outer and inner skin. Increase in friction between the skins led to lower load taken by the rivet, some of the load being taken by the interfacial friction. The maximum stress at row A reduced only slightly (2%).

Table 5.1 Summary of results from the parametric studies

Parameter	Max. Principal stress at critical row A in lower skin (MPa)	Number of cycles to grow a crack of length 1.27 mm (N_T)
Baseline Analysis	296	76,361
Under-driven rivets	337	41,548
Over-driven rivets	303	66,361
Variation in interference	303	66,361
Sealant analysis	310	60,761
Sealant and under-driven rivets	330	44,761
Sealant, drill shavings and under-driven rivets	337	41,548
Friction effect	289	90,761

5.5 Summary

The intent of this chapter was to implement the residual stress models analyzed previously to analyze the effects of load transfer in the fuselage splice. The chapter began with a brief background of the loads experienced by a typical lap joint, which lead to a complex stress state at the rivet holes. Based on the splice geometry of the B727 a 3-rivet row model was constructed to simulate the loading experience by the joint in service. Results from the analysis of this model showed an excellent correlation between

the location of the cracking observed in the teardown inspection and critical stress site indicate by the FE model. An important implementation of this model was to investigate the effect of different rivet spacing on the stress state at the critical hole. A comparison of the two previous analyses showed that slight differences in the rivet spacing did not significantly affect the stress state at the critical hole. This indicated that rivet spacing was not a cause of the differences in fatigue lives observed for the right hand side panel and the left hand side panel joints.

Finally, the global splice model was then implemented to observe the effects of under-driven rivets, sealant and friction on the stress state at the critical hole. Results from the analyses were used in subsequent crack growth analyses to obtain an approximation to grow a crack of 1.27 mm. Comparison of the results indicated that under-driven rivets in combination with sealant and drill shavings are the biggest threat to the propensity of fatigue damage at the critical rivet holes.

Chapter 6: Experimental Fatigue Testing

In reviewing the task of understanding fatigue in aircraft riveted lap joints consider the work already presented. First, a formulation of the mechanics of the riveting process allowed for the characterization of the conditions associated with fatigue. Of particular interest were the sharp gradients of tensile stress tangential to the surface at the edge of contact. Exact assessment of the contact conditions, though, hinged on accurate 3D finite element modeling of the riveting process and subsequent in-service load transfer. This characterization of the residual stress fields in the lap joint highlighted the potential dichotomous effects of the riveting process on fatigue of the joint.

The pursuit of interpreting manufacturing process variations into improved joint performance motivated experimental fatigue testing of riveted lap-joint specimens with the specific goal of forging a link between rivet installation and hole quality effects on fatigue performance of the joint. This chapter begins by providing background of the experimental study. Following this, the experimental results are compared with the finite element simulations through techniques such as Thermographic Stress Analysis (Appendix A). Some microscopic observations are presented regarding the nucleation of fatigue damage in the tested specimens. Finally, a comparison of the fatigue performance of the specimens is presented based on rivet installation and hole quality issues.

6.1 Fatigue test matrix

The matrix tested three parameters that showed high sensitivity in the FEA runs, were evident in the destructive evaluation, and were practical to control in specimen preparation:

- Rivet Installation: either 1) under-driven, 2) baseline, per specifications, or 3) over-driven.
- Hole Preparation/Debris Removal: either 1) drilled and deburred prior to assembly, or 2) sealed first, then drilled.
- Hole Quality: either 1) piloted then drilled or 2) single-step drilling

A fractional factorial matrix allowed for fewer experiments by not testing some interactions. It was critical that the interactions with rivet installation be fully tested, including all three levels of rivet installation. The least critical interaction was between hole preparation and hole quality. These tests were removed in the proposed test matrix. The advantage of the fractional factorial test matrix was that it allowed three tests per configuration with only twenty-seven total experiments. This advantage likely outweighed the disadvantage of neglecting hole preparation versus hole quality interactions. Other test matrix parameters that were considered included:

Rivets installed with surface sealant wet, dry or absent: could have been fabricated but was omitted only to reduce the size of the test matrix. Whether sealant was wet or dry during 727 lap-joint assembly was not discerned from teardown. Also, assembly with no sealant was not found.

Gap between sheets present/absent: such a gap would have been difficult to control during specimen preparation without causing artificial stress concentrations not represented in actual manufacture.

Debris between sheets present/absent: addressed somewhat by the hole preparation. Debris inclusion beyond that was difficult to control during specimen preparation, or to make representative. Table 6.1 gives details of the full factorial test matrix.

Table 6.1 Complete test matrix

No.	Test Type	No of specimens	ID	Brief Manufacturing Description
1	Rivet Under-driven, Sealant 26	3	U26S	Fabricate specimen, Drill Holes, Deburr
	single-step drilling		**Min. driven head thickness- 2.3 mm**	faying surface,seal surface, allow to dry,
				install rivet-underdriven
2	Rivet Under-driven, Sealant 95,	3	U95P	Fabricate specimen, seal surface,
	Piloted and drilled		**Min. driven head thickness- 2.3 mm**	drill pilot holes without curing sealant, no
				deburr, drill holes, no deburr, install rivet-underdriven
3	Rivet Under-driven, Sealant95,	3	U95S	Fabricate specimen, seal surface,
	single-step drilling		**Min. driven head thickness- 2.3 mm**	drill holes without curing sealant, no
				deburr, install rivet-underdriven
4	Baseline, Sealant26	3	B26S	Fabricate specimen, Drill Holes, Deburr
	single-step drilling		**Min. driven head thickness-1.7 to 2.3 mm**	faying surface, seal surface, allow to dry,
			Min. driven head diameter-5.5 mm	install rivet- baseline
5	Baseline, Sealant95,	3	B95P	Fabricate specimen, seal surface,
	piloted and drilled		**Min. driven head thickness-1.7 to 2.3 mm**	drill pilot holes without curing sealant, no
			Min. driven head diameter-5.5 mm	deburr, drill holes, no deburr, install rivet-baseline
6	Baseline, Sealant95,	3	B95S	Fabricate specimen, seal surface,
	single-step drilling		**Min. driven head thickness-1.7 to 2.3 mm**	drill holes without curing sealant, no
			Min. driven head diameter-5.5 mm	deburr, install rivet-baseline
7	Rivet Over-driven, Sealant26,	3	O26S	Fabricate specimen, Drill Holes, Deburr
	single-step drilling		**Min. driven head thickness-1.2 to 1.7 mm**	faying surface,seal surface, allow to dry,
			Min. driven head diameter-5.5 mm	install rivet-overdriven
8	Rivet Over-driven, Sealant95,	3	O95P	Fabricate specimen, seal surface,
	piloted and drilled		**Min. driven head thickness-1.2 to 1.7 mm**	drill pilot holes without curing sealant, no
			Min. driven head diameter-5.5 mm	deburr, drill holes, no deburr, install rivet-overdriven
9	Rivet Over-driven, Sealant95,	3	O95S	Fabricate specimen, seal surface,
	single-step drilling		**Min. driven head thickness-1.2 to 1.7 mm**	drill holes without curing sealant, no
			Min. driven head diameter-5.5 mm	deburr, install rivet-overdriven
	Total no. of specimens	**27**		

6.2 Specimen and test details

The lap joint specimens used in the series of tests were composed of two Al skins with dimensions specified in Figure 6.1. The specimens were based on NASM 1312-4 (Figure 6.2). Sheets were Al 2024-T3 with 3.968 mm countersunk rivets, as in the B727 joint. The top (countersunk) sheet was 1.524 mm, as required to prevent a knife-edge condition at the countersink. This configuration modeled the 1 mm outer skin bonded to a 0.5 mm doubler as in the B727 joint. The lower sheet was 1 mm, as in the 727 lap joint. Faying surface was sealed and assembled wet. A set of grip tabs were attached to the end of the joint to enable the specimens to be mounted securely in the load train of a 97.8 KN servo-hydraulic MTS test frame. Figure 6.3 shows a schematic of the assembled specimen. Installation of the rivets was accomplished with a quasi-static

displacement controlled machine. All specimens were assembled and riveted at the DAL facility in Atlanta, GA. Figure 6.4 shows a picture of the final specimens. The levels of

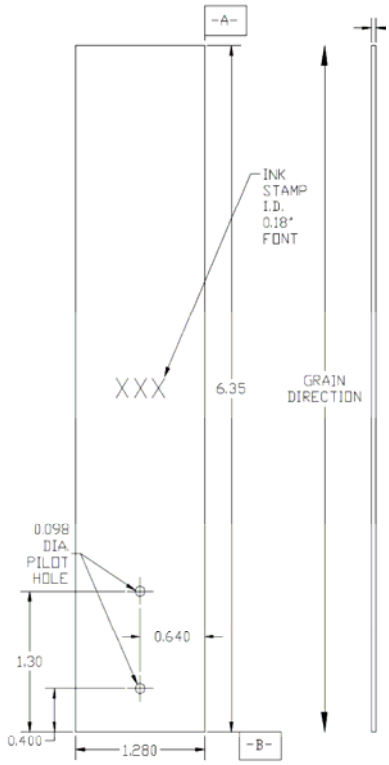

Figure 6.1 Specification of the joint

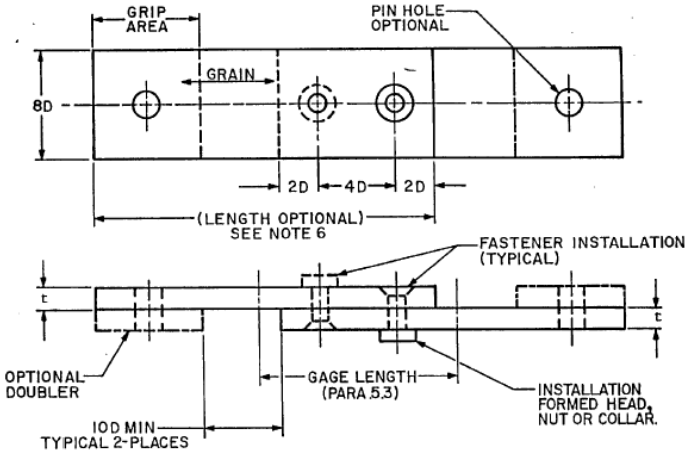

Figure 6.2 Schematic of the specimen based on NASM

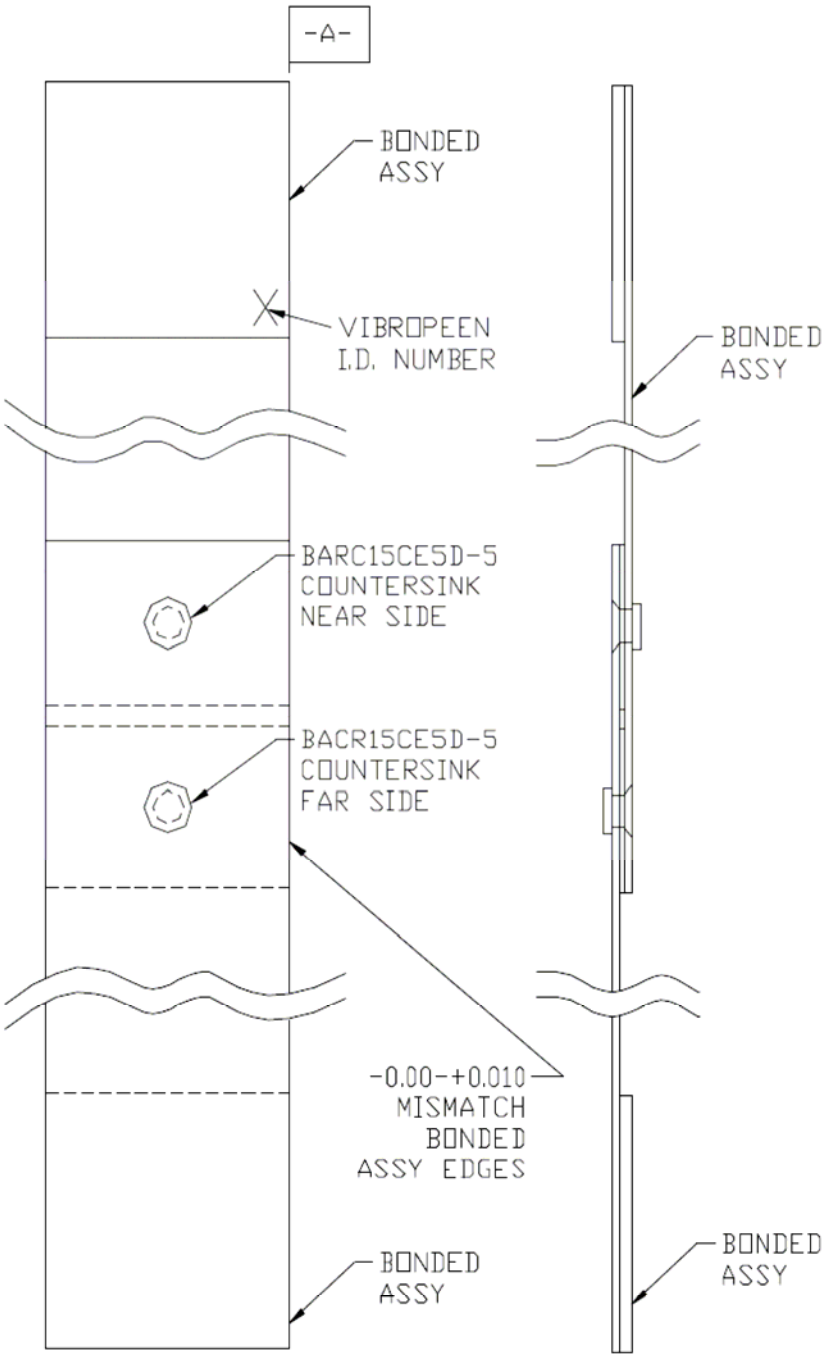

Figure 6.3 Schematic of the assembled joint

installation were based on the finite element simulations and observations from the teardown inspection. The aim of the varied installation was to provide a wide range of

interference and driven-head clamping constraint, with hopes of generating varying modes of fatigue failure in the joint.

Figure 6.5 compares an under-driven and baseline specimen. Evident is the difference in the formed rivet head diameter.

Figure 6.4 Final assembled and riveted specimens

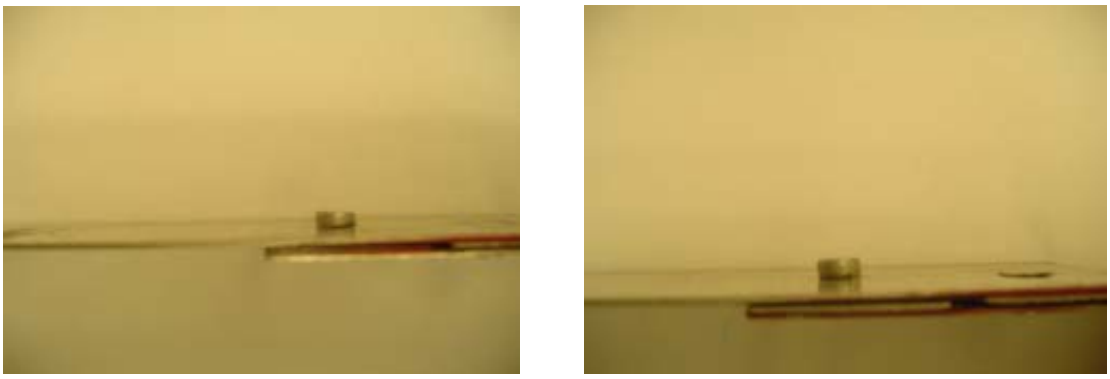

Figure 6.5 Comparison of baseline (left) and under-driven (right) specimens. Evident is the difference in tail diameters.

6.3 Test set-up

Twenty-one specimens were tested employing a 97.8 kN servo-hydraulic MTS test frame. The tests were conducted in a laboratory atmosphere (Figure 6.6) with

constant amplitude stress level of 124 MPa with an R ratio of 0.1 and frequency of 10 Hz. The stress level was based on testing of four dummy specimens at 96, 103, 117 and 124 MPa. The 124 MPa stress level was observed to be appropriate in terms of obtaining failure within a reasonable number of cycles. For each test the rivet head diameters and tail heights were recorded to ensure they were within specifications. The remaining six specimens were tested implementing a thermal imaging technique. The set-up and results obtained from the thermographic testing are discussed in Appendix A.

Figure 6.6 Fatigue test set-up

6.4 Fatigue testing results

Upon failure, each specimen was inspected carefully in an attempt to characterize the damage at and around the rivets. The process relied on optical microscopy and photographic cataloguing of the faying surface damage and interior of

the rivet holes. Failure in each specimen occurred, without exception, at the rivet driven head side either on the top or bottom rivet consistent with 50% load transfer (Figure 6.7). Correlation was noted between fatigue lifetimes and the controlled experimental parameters. A comparison of these fatigue lifetimes for the three different parameters is shown in the bar graphs below. The bar graphs (Figures 6.8, 6.9, 6.10) and the summary of the fatigue lifetimes reveals some trends: (1) Fatigue life increased with increasing rivet interference (2) No significant difference in fatigue life was observed at medium to high rivet interferences (3) No significant difference was observed in the fatigue life of the joints in comparison of the two sealants. For both the sealants a reduction in the adhesive quality was observed at the end of the test (Figure 6.11). Since the application of sealants is more as a corrosion inhibitor, in the absence of corrosion the less observed difference in the fatigue lives is not surprising. (4) In comparison of fatigue lives based on hole quality, again under-driven rivets show the maximum difference in life. Rivet deformation, which might lead to negation of hole quality issues (such as stress concentrations due to drilling procedures) might be less in this case.

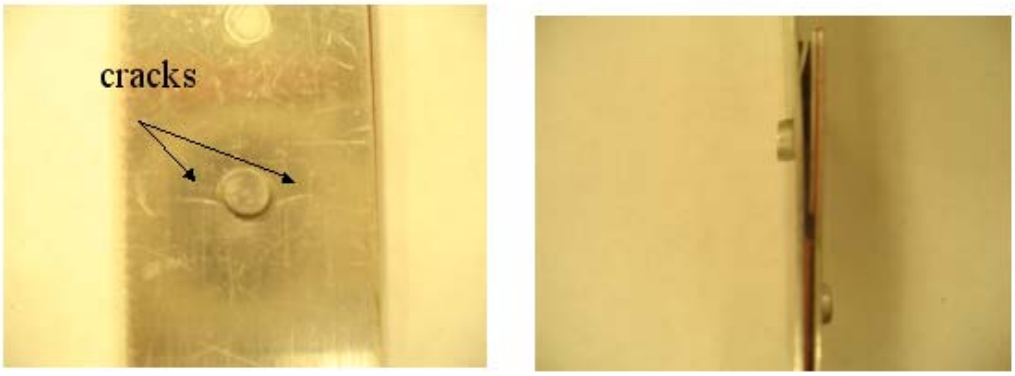

Figure 6.7 Observed failure location for specimens (left) and sealant separation (right)

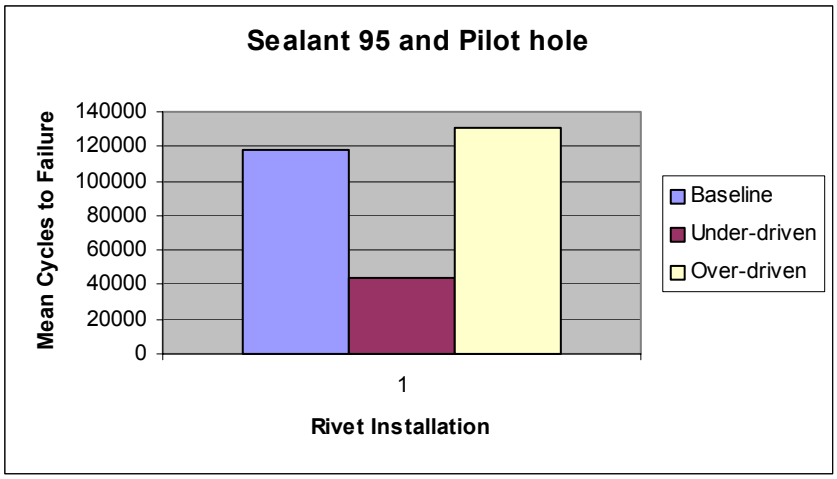

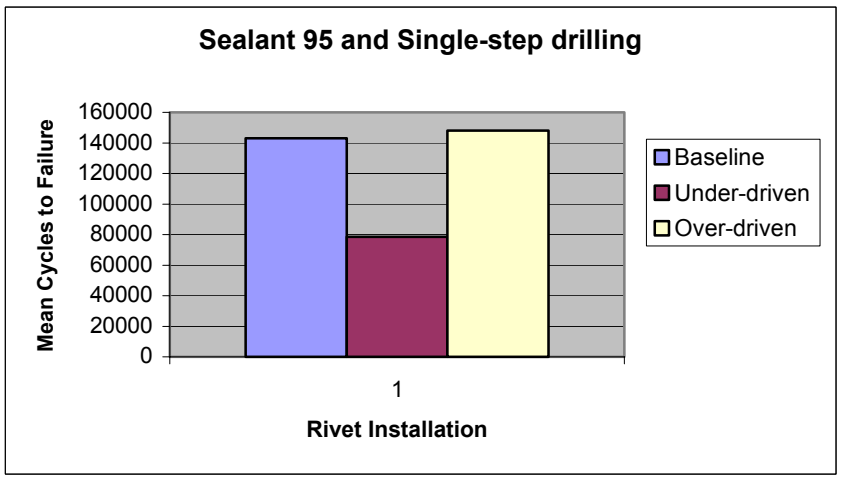

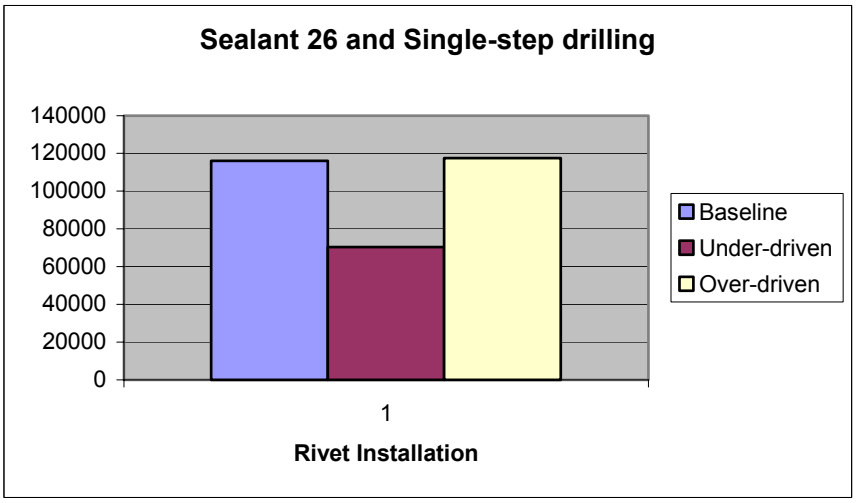

Figure 6.8 Comparison of fatigue lifetimes for rivet installation

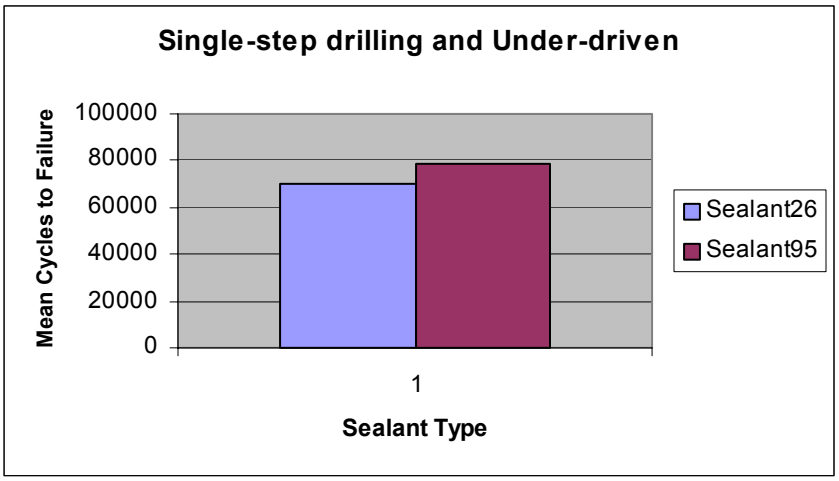

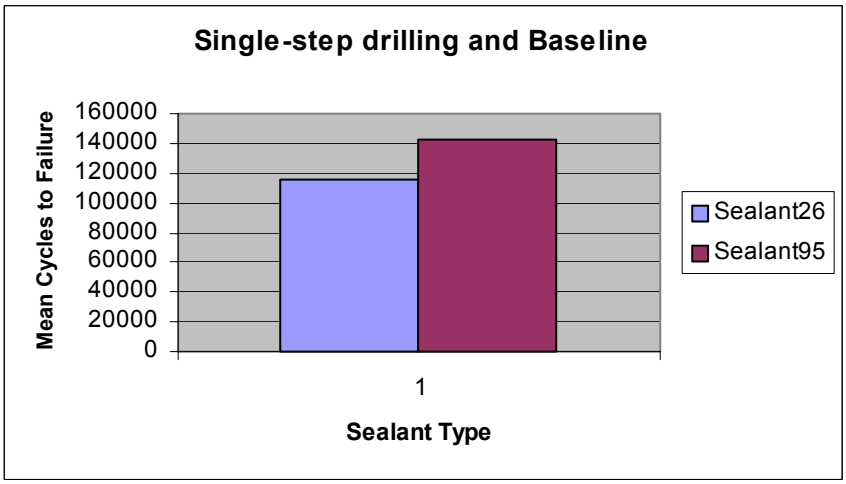

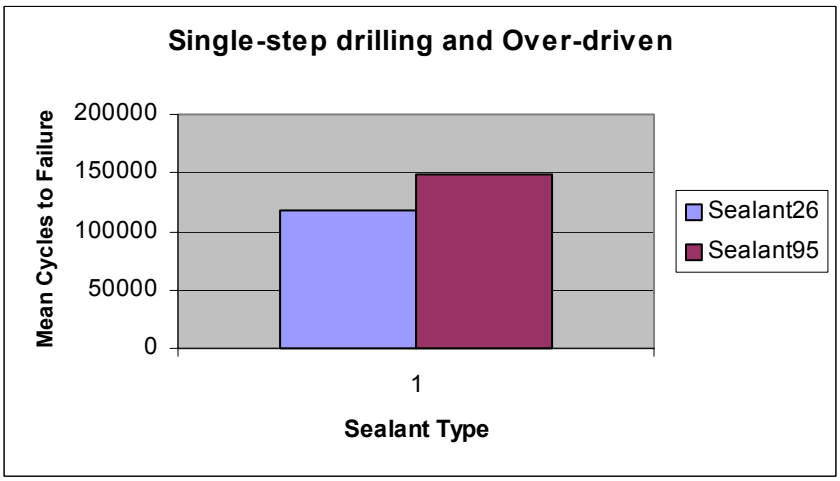

Figure 6.9 Comparison of fatigue lifetimes for sealant type.

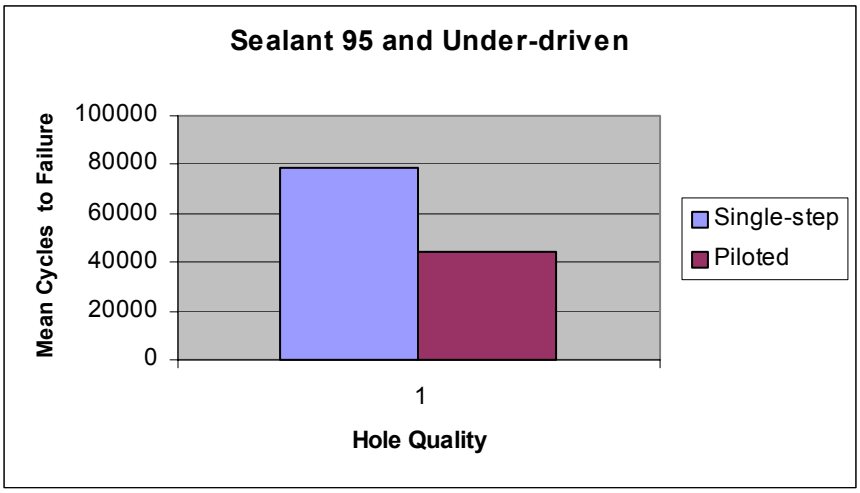

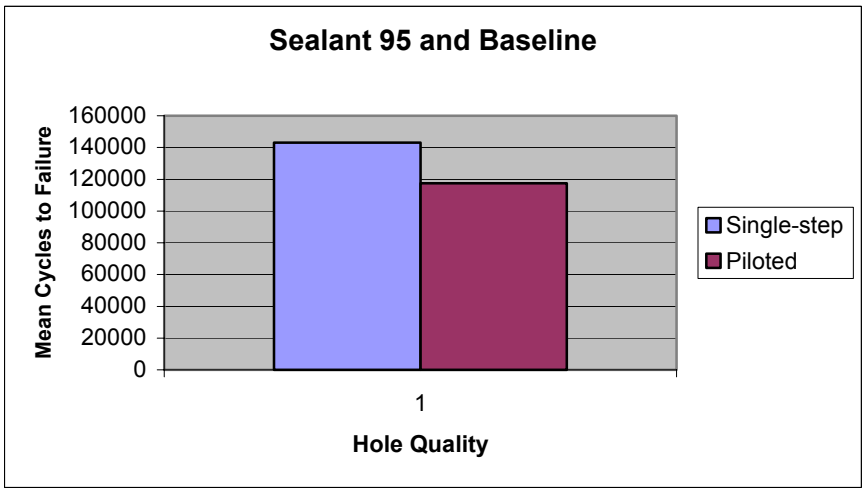

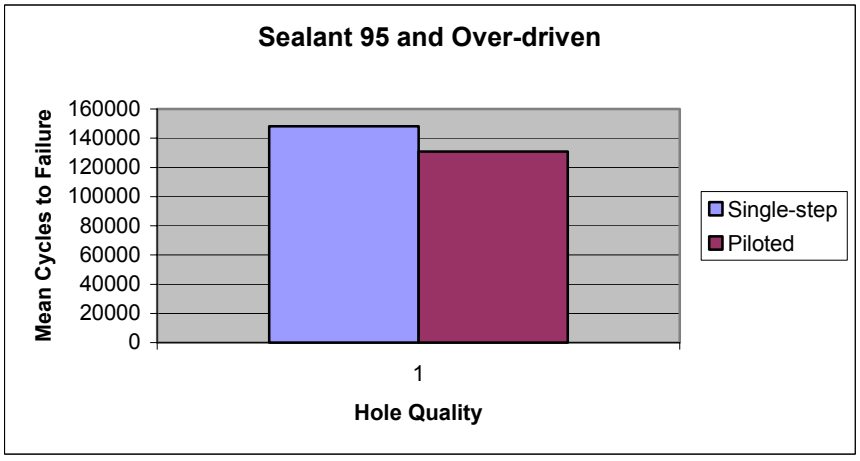

Figure 6.10 Comparison of fatigue lifetimes for hole quality

Table 6.2 Summary of mean cycles to failure

Specimen Type	ID	**Cycles to Failure (Mean Test Life)
Baseline,Sealant26,Single step	B26S	116039
Under-driven,Sealant26,Single step	U26S	70300
Over-driven,Sealant26,Single step	O26S	117566
Baseline,Sealant95,Single step	B95S	142983
Under-driven,Sealant95,Single step	U95S	78622
Over-driven,Sealant95,Single step	O95S	148094
Baseline,Sealant95,Pilot	B95P	117500
Under-driven,Sealant95,Pilot	U95P	44371
Over-driven,Sealant95,Pilot	O95P	130815

(5) After testing, the hole surfaces of both the single-step and piloted specimens were examined. There seemed to be no obvious differences between them in terms of surface quality. That is, the circumferential grooves observed in the holes were not limited to just single-step or piloted specimens. Majority of both type of specimens showed circumferential grooves. Detailed viewgraphs are presented in Appendix D. A measurement of surface roughness of the holes was beyond the scope of this work and hence is not presented in this thesis. (6) The Thermographic Stress Analysis was unable to detect the cycles to initiation of cracks in all the tested specimens. Cracks were identifiable only after 70,000-80,000 cycles. The detailed results of the TSA testing are discussed in Appendix A.

Concurrently a characteristic state of damage was observed at and around the rivet holes based on the rivet interference. Figures 6.11 and 6.12 displays photographs of the state of damage for around and near the rivet holes. The first specimen was baseline (S26S) and failed after 125,000 cycles. The second specimen was under-driven (U26S) and failed after 80,000 cycles, which is a 1.5 times shorter fatigue life. A part of this difference can be attributed to the compressive residual stress generated from increased rivet expansion in the baseline specimen. The faying surface of the baseline specimen showed signs of fretting debris at the rivet hole. Evidence of fretting debris was noted by black oxide deposited on the faying surface around the rivet hole. Similar

debris was observed in the under-driven specimen but the presence of debris was smaller than the baseline. This is consistent to the observed state of damage for joints tested by Szolwinski [13]. Increased clamping provided by larger driven heads leads to a large load transfer via friction at the faying surface. No direct correlation was observed for the state of fatigue damage for the specimens, that is, fretting alone was not a cause of crack initation. Effects of hole quality might have been dominant in crack initiation. Majority of the rivet holes were observed to have circumferential grooves. These grooves were similar to the ones observed in the teardown inspection for the right hand side panel joint holes and are estimated to originate from the drilling process. Effects of such drilling variations on open hole specimens are discussed elsewhere [71]. These hole quality issues especially for the under-driven rivets might have been a cause for crack initiation.

On the fracture surface of many fatigue cracks, ridges and several crack initiation nuclei were observed. It seemed as if one crack was composed of several cracks that were initiated and had grown on different levels independently of each other. The role of fretting is not clear. It may be the result of cracking or the cause, increasing the local stress and hence the crack driving force during early crack growth. The detailed damage characterization of the tested specimens showed faying surface crack origin for the baseline and over-driven rivets. Majority of the under-driven specimens showed hole surface crack origins. Recalling the results of the FE simulations conducted previously this is an excellent validation of the developed models. For baseline and over-driven models the tensile hoop stress is at the faying surface away from the hole, consistent with the cracking pattern observed in the experiments. For under-driven models the tensile hoop stress is concentrated at the hole surface, which is also consistent to the nucleation of cracks in the under-driven specimens.

Observations from the damage characterization of the specimens emphasize the link between riveting process parameters and fatigue of the lap joint. It is noted that this test program although not exhaustive, such as efforts by Piascik and Willard [52], attempted to establish a conclusive link between rivet installation, hole quality issues and the effect of these parameters on the propensity for fatigue damage at the faying surface of the riveted lap-joint.

6.5 Summary

This chapter began with a brief review of the work presented earlier and with an outline of the goals for experimental fatigue testing. This was followed by details of the tested specimens and a summary of the parameters under consideration. It was noted that parameters such as debris were difficult to produce consistently in the lap joint specimens and hence were not considered in the test matrix.

Details of the fatigue lifetimes for the tested specimens were also presented. A 2.5 to 3 times reduction in fatigue lifetime was noted for under-driven specimens in comparison to baseline and over-driven specimens. The effect of fretting on crack initiation though not clear it was observed that hole quality issues such as might have also been a cause of initiation. The experimental fatigue tests showed that under-driven lap joints have a significantly less fatigue life than over-driven or baseline riveted joints. The effects of hole quality were also observed to be dominant for under-driven rivets. The damage characterization showed faying surface crack origins for baseline and over-driven rivets while hole surface origins for under-driven rivets, which is consistent to the location of the tensile stresses, predicted by the finite element simulations.

Finally, observations from the damage characterization of the specimens reemphasized the link between riveting process parameters and fatigue of the lap joint.

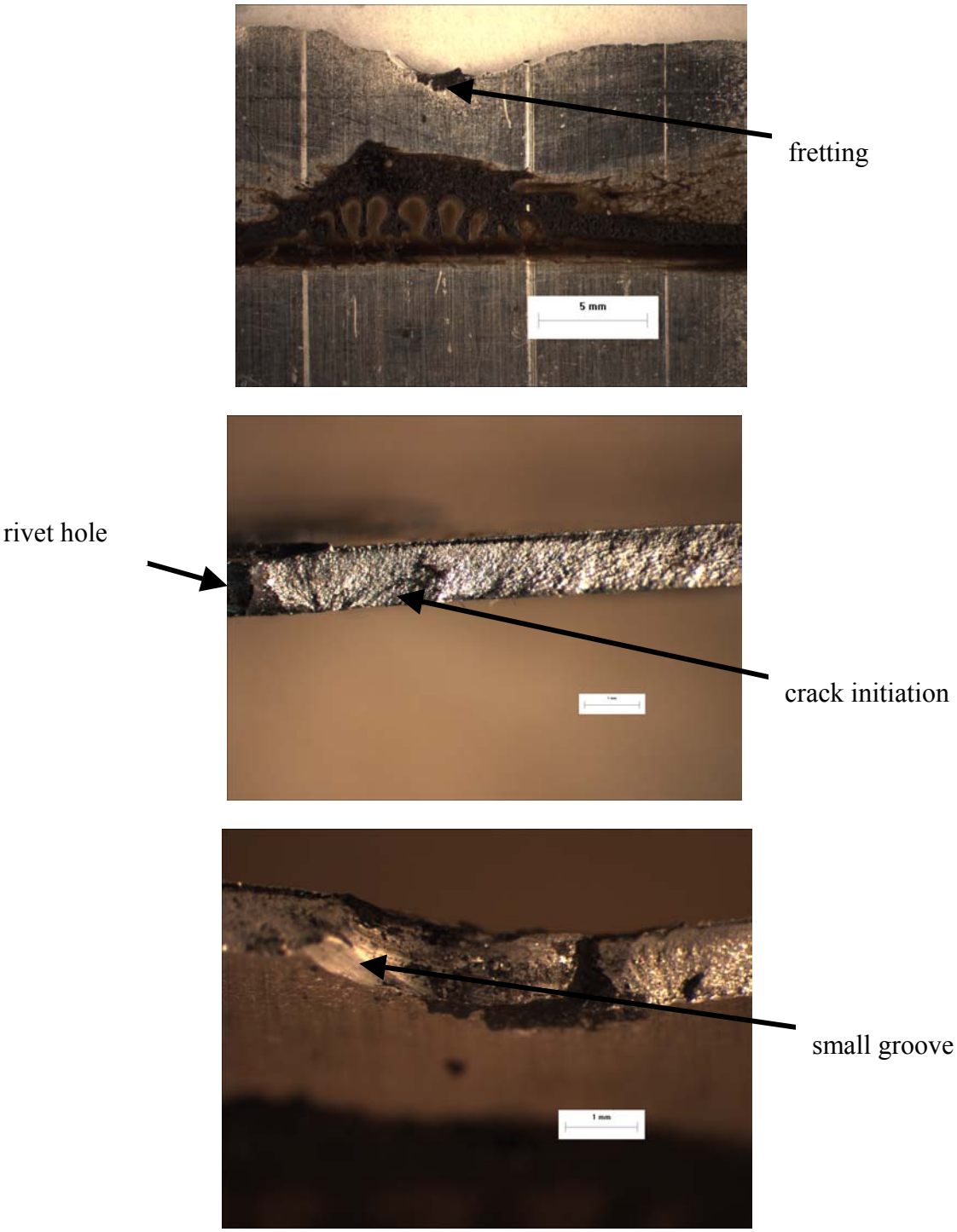

Figure 6.11 Optical micrographs for specimen S26S: view of the faying surface (top), view of the crack growth away from the hole (bottom), view of the rivet hole with a small groove (bottom)

multiple origins

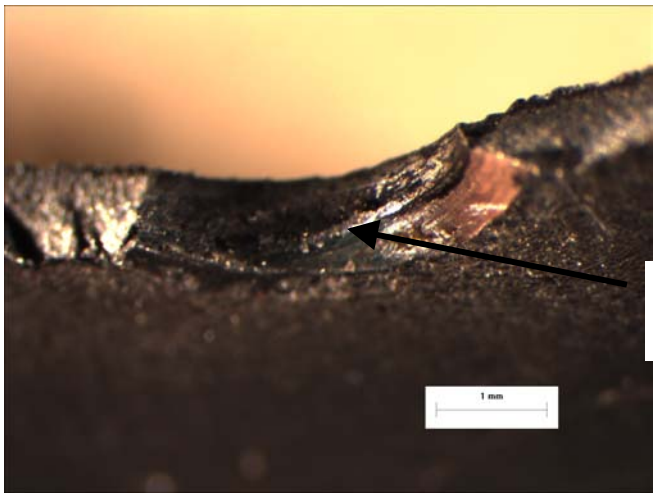

circumferential groove

Figure 6.12 Optical micrographs for specimen U26S: view of the faying surface (top), view of the crack growth (bottom), view of the rivet hole with a small groove (bottom)

Chapter 7: Summary and Conclusions

7.1 Summary

This overall investigation was conducted in four distinct phases, all of which were successful in achieving their stated goals. In the first phase, the goals were to verify and validate the intended quasi-static finite element modeling approach by demonstrating it could predict accurately the residual stress state that occurred in a previous investigation. The portion of this study carefully measured the deformation, residual strains and force-displacement data for a force-controlled rivet configuration. Additionally, the model results were also compared for both Implicit and Explicit solvers.

The second phase of this investigation utilized the FE modeling approach from the first phase to address the more practical problem of predicting the residual stress state in the riveted joint subjected to process variations. A 3D baseline model was developed for this purpose. The specifications of the model were same as that of the B727 joint. The goal of this investigation was to predict the differences in residual stress state for critical process variations. In conducting this investigation five main process variables were analyzed to observe their qualitative and quantitative effect on the residual stress state, namely: rivet interference, presence of sealant, presence of debris, hole quality effects and geometry effects.

The third phase of this investigation focused on development of a global three-rivet fuselage lap joint, which takes into account, the residual stresses resulting from rivet installation and in-service fuselage loads. The model behavior was designed to approximate the loading experience by the fuselage splices removed in the teardown inspection. Available results from the B727 teardown damage characterization provided validation to the analysis.

The pursuit of interpreting manufacturing process variations into improved joint performance motivated the final phase of experimental fatigue testing of riveted lap-joint specimens. The investigation was conducted with the specific goal of forging a link between rivet installation and hole quality effects on fatigue performance of the joint.

7.2 Conclusions

1. A number of finite element simulations were conducted for the riveting process using different techniques and their results presented in previous chapters. It can be concluded that with the correct implementation of FE tools (discussed in detail previously) the riveting process can be successfully simulated to obtain an accurate representation of the residual stresses resulting from the riveting process.
2. The rivet expansion in the baseline analysis led to both compressive and tensile residual stresses in the skin. This tensile hoop stress observed away from the hole is critical for fatigue cracks that may initiate at the faying surface.
3. An increase in the applied rivet displacement led to a larger rivet-hole expansion consequently causing an increase in both the compressive radial and hoop stresses around the hole periphery. This indicated that the fatigue performance could be improved by retarding crack growth near the hole edges. The tensile hoop stress was pushed away from the hole edge but an increase in magnitude is observed in both the outer (52%) and the inner (25%) skin. This meant an increase in the potential for initiation and fatigue crack propagation at the faying surface.

4. Effects such as skin misalignment, hole defects and hole geometry increased the unsymmetrical deformation of the rivet. A significant quantitative increase in the tensile hoop stress was observed because of this rivet “bulging”.
5. A decrease in the applied rivet displacement led to a reduced rivet-hole expansion and consequently a “neat-fit” rivet connection. The under-driven rivet analysis proved to be the biggest threat to potential for fatigue damage. The under-driven rivet caused not only an increase in the tensile hoop stress but also a stress concentration of the hoop tension at the hole for both the upper and lower skin. This residual hoop tension, especially with the effect of the sharp countersunk hole will prove to be a critical site for fatigue damage.
6. The analyses with sealant showed an increase in residual hoop tension for both the upper (20-80%) and lower skin (20-60%).

(i) For the cases where the rivet was driven as specified (baseline) the upper skin showed a shift in the tensile zone near the countersunk edge which might be a probable location for fatigue cracking. For the lower skin the tensile zone remained concentrated at the faying surface (away from the hole). For low interference or under-driven rivets with the sealant an increase in tensile hoop stress was observed with the tensile zone concentrated near the rivet/skin interface for both the upper and lower skin.

(ii) Rivet tilt also showed a similar tensile zone concentrated largely on one side of the hole due to the unsymmetric rivet deformation. For such type of installed rivets the stress distribution seems to suggest that both the upper and lower skin would be susceptible to fatigue damage at the rivet/skin interface. Also for such cases the presence of sealant might not show any beneficial effects.

(iii) Presence of drill shavings in the sealant showed a large increase in the tensile hoop stress for both the upper (40-60%) and lower (50-110%) skin. The tensile hoop stress was also observed to remain concentrated at the rivet/skin interface for low interferences. Rivets installed with low interference (under-driven) with drill shavings might be a major cause of fatigue crack initiation at the rivet/skin interface.

(iv) The presence of sealant showed an increase in the residual tensile stress state as compared to the analysis without sealant. For rivets, which are, installed per specifications (baseline) the effect of sealant on any fatigue damage might not be significant. For cases where rivets are under-driven or tilted the effects of sealant combined with any drill shavings might increase the propensity for fatigue crack nucleation at the rivet/skin interface.

7. Damage parameters were implemented in conjunction with the FE models to predict the location of fretting damage in the joint. For low rivet interferences a peak was observed at $\theta=120^{o}$ and another at $\theta=150^{o}$. At larger rivet interferences the first peak shifted to $\theta=90^{o}$. In most of the cases, it was observed that the general location of fretting noted in the teardown damage characterization was close to the peaks of the F_1 parameter. The low interference cases indicated a peak at $\theta=90^{o}$ for the damage parameter F_2 which indicates the potential for crack initiation. This is the possible location of crack initiation. At high interferences the bulk stress was observed to be compressive around the hole. This will reduce the probability of crack initiation due to fretting at the rivet/skin interface but away from the hole at $\theta=90^{o}$ a presence of the bulk tensile zone will be the primary cause of crack initiation.

8. The maximum principal stress at the end of the load application was located at the lower row hole in the inner skin (row A in Figure 1.3) and upper row hole in the outer skin (row C in Figure 1.3). The observation of the maximum principal stress at the lower row hole inner skin was consistent to the observed fatigue damage at the same location from the teardown inspection.
9. A major finding from the teardown inspection was that the right hand side panel and the left hand side panel lap joints had been installed with a difference in the rivet spacing. The right hand side panel joint had an “average” rivet spacing (22.479 mm) as shown in Figure 5.1. The left hand side panel joint had a slightly larger rivet spacing (27.94 mm) between the lower and the middle rows. It was speculated that the difference in these spacings, might reduce the bending stress at the lower rows leading to the better fatigue lives observed for the left hand side panel joint. To analyze this effect a fuselage splice model of the left hand side panel joint was constructed in ABAQUS/CAE. The analysis, however, showed no difference in the stress state at the critical rivet row in the inner skin indicating that the slightly increased rivet spacing did not significantly affect the stress state for either of the skins.
10. Finally, the global splice model was then implemented to observe the effects of under-driven rivets, sealant and friction on the stress state at the critical hole. Results from the analyses were used in subsequent crack growth analyses to obtain an approximation to grow a crack of 1.27 mm. Comparison of the results indicated that under-driven rivets in combination with sealant and drill shavings are the biggest threat to the propensity of fatigue damage at the critical rivet holes.
11. The summary of the observed fatigue lifetimes for the tested specimens revealed (1) Fatigue life increased with increasing rivet interference (2) No significant

difference in fatigue life was observed at medium to high rivet interferences (3) No significant difference was observed in the fatigue life of the joints in comparison of the two sealants. Since the application of sealants is more as a corrosion inhibitor, in the absence of corrosion the less observed difference in the fatigue lives was not surprising. (4) In comparison of fatigue lives based on hole quality, again under-driven rivets show the maximum difference in life. Rivet deformation, which might lead to negation of hole quality issues (such as stress concentrations due to drilling procedures) might be less in this case.

12. Evidence of fretting debris was noted by black oxide deposited on the faying surface around the rivet hole. No direct correlation was observed for the state of fatigue damage for the specimens, that is, fretting alone was not a cause of crack initation. Effects of hole quality might have been dominant in crack initiation.
13. The damage characterization showed faying surface crack origins for baseline and over-driven rivets while hole surface origins for under-driven rivets, which is consistent to the location of the maximum tensile hoop stress, predicted by the finite element simulations.

7.3 Recommendations for rivet installation

Figure 4.15 shows a plot of the maximum tensile residual hoop stress as a function of rivet interference for the countersunk and straight shank skin respectively. The figure shows the percentage of rivet interference at which the tensile hoop stress changes location from being concentrated near the hole to away from the hole. In light of the influence rivet installation has on the residual stress state in the skin it is strongly recommended that rivets installed with interference less than 35-40% (under-driven) interference (55% being the baseline) should not be used in service. Such rivets would

tend to promote fatigue damage much earlier than rivets installed with a much higher interference. It is also recommended that the above plots be used a rough guideline in installing rivets to ensure at least a small compressive zone around the holes especially for the sharp countersunk skin. Finally, a rivet interference ranging from 50-70% is recommended in service. At much higher interferences the rivet clamping might lead to a much higher load transfer increasing the probability of fretting crack initiation in the tensile hoop stress zone away from the holes at the faying surface.

7.4 Future Work

The combined results of the computational and experimental investigations provided a great deal of insight into how the residual stress state affects the proclivity for fatigue damage in riveted lap joints. In order to further improve in preserving the structural integrity of aging aircraft, a sequence of recommendations based on the results from this work follows, with the implicit assumption that some or all could and eventually should integrate numerical and experimental tools:

1. Residual stress is complicated by hole quality effects. A model is needed relating stress intensity (SIF) to the gouge mark geometry. The model would need to take into account size and shape of the gouge. Implementing the already developed FE models into SIF determination would be an excellent initial start.
2. The exact cause of gouging observed both in the teardown and the tested specimens is still a mystery. Determining exactly which factors in the hole drilling technique cause this gouging would be a worthy study.

3. This study focused on fatigue testing of a limited number of specimens. An exhaustive program based primarily on fatigue testing of specimens with under-driven/baseline rivets and hole quality issues (such as gouging) should be setup. This will ensure to eliminate any scatter associated with the testing as well as provide a database of effect of hole quality issues on fatigue behavior of riveted lap joints.

APPENDIX A: THERMOGRAPHIC STRESS ANALYSIS

To characterize the near-surface response driving fatigue damage, a thermal imaging system capable of capturing sequences of temperature profiles was implemented in conjunction with a fatigue testing set-up. The thermographic testing was conducted in collaboration with the research group of Dr. Rami Haj-Ali in the School of Civil Engineering. The experimental procedure used was modeled closely from the work of El-Hajjar [72]. The thermal measurements were acquired with a Delta Therm DT 1500 thermoelasticity measurement system, which uses a liquid nitrogen cooled infrared camera. The TSA system operates by recording the temperature change of the specimen under fatigue loading as seen in Figure A.1. A focal plane array in the IR camera is employed to detect the incident radiant energy emitted from the specimen's surface during testing and convert it to an electrical signal [72]. The software in the system coordinates a reference signal from the test frame load cell to ensure that only true temperature changes are monitored. Hundreds of cycles are collected and averaged to improve the signal to noise ratio. In order to properly track stress states in the material, strain gages or other means should be used to correlate the received IR information to a known stress value.

The goal of this investigation was to establish TSA capabilities for such riveted lap joints to detect crack initiation and compare the in-plane strains predicted by the FE models to those predicted by the TSA. The test frame employed for these tests was a MTS 810 servo hydraulic test system 22.5 kN with 76 mm SURFALLOY grips. The specimens had to be tabbed prior to testing in order to conform to the larger grips. Also, a thin coat of Krylon Ultra Flat black paint was applied to the surface of the HTCL coupon to cut down on environmental noise and improve surface emissivity. The specimen was then centered in the grips to eliminate off axis loading and the testing was initiated. The infrared (IR) signal from the coat is measured while the specimen is loaded and a combined material factor (k_{ε}), comprised of mechanical and thermal properties, is

calibrated such that the measured IR signal can be related to the sum of the in--plane direct strains (Eq. A.1). The theoretical derivation of this new method assumes adiabatic conditions and applies a thermomechanical theory. Complete details of the derviation can be found elsewehere [72].

[A.1] $$\Delta\varepsilon_{\alpha\alpha} = k_{\varepsilon} S \qquad \alpha = 1,2$$

Six specimens were tested at a frequency of 5 Hz. Since the fatigue testing machine employed for the TSA technique was set-up for thicker specimens the amplitude had to be adjusted to obtain the same stress levels (124 MPa) as those applied to the twenty-one specimens tested in the Material Properties Research Lab.

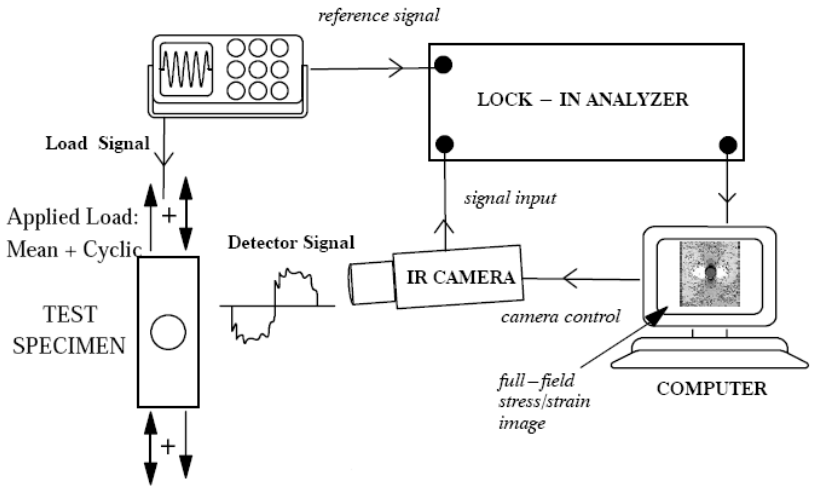

Figure A.1 Schematic TSA system [72]

Figure A.2 shows a thermographic image taken at the start of the test (10 cycles). Figure A.3 show images after 90,000 and 120,000 cycles respectively. The tips of the cracks are clearly visible in the pictures. For all the tested specimens the cracks

were visible only after 70,000-80,000 cycles. No clear indication of cycles to initiation was obtained. The set-up of the specimen dictated a LTR of approximately 50%. This meant that the cracks could initiate on either side limiting the use of TSA. In one case, the specimen was coated on both sides and thermal images were captured by flipping the specimen after a certain number of cycles.

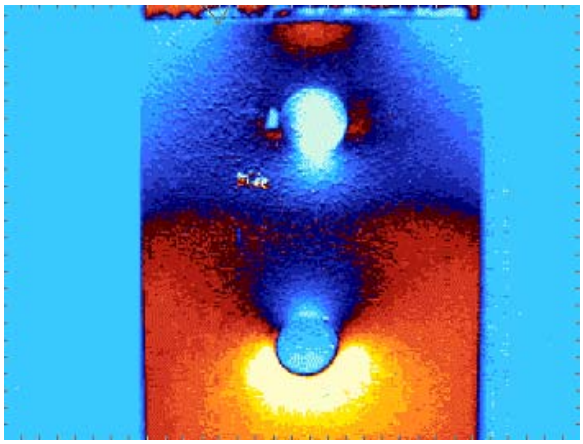

Figure A.2 Thermal image of specimen (B26S) after 10 cycles

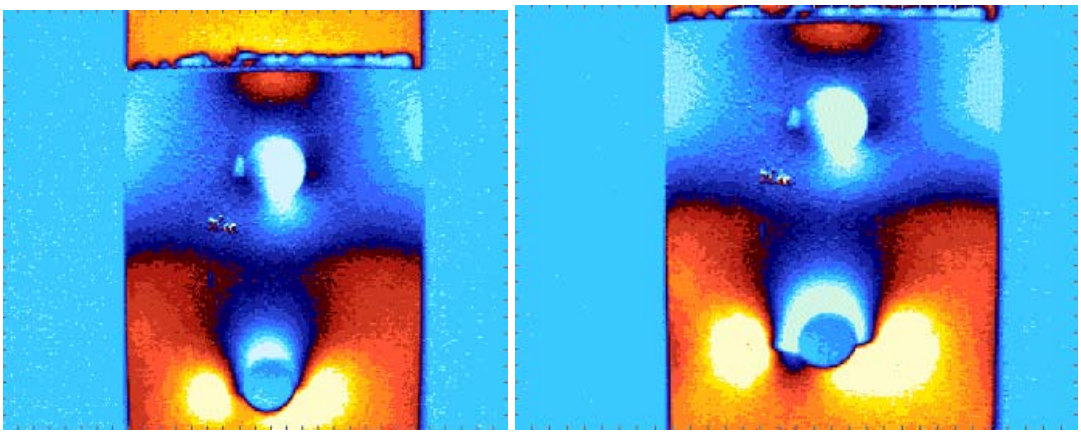

Figure A.3 Thermal image of specimen (B26S) after 90,000 cycles (left) and 120,000 cycles (right). Tips of the cracks are clearly visible.

A detailed view of the meshed, symmetric 3D finite element model and the applied boundary conditions designed to simulate the specimen is shown in Figure A.4. The model, which had 6457 nodes and 3947 elements, was generated using ABAQUS/CAE 6.4-1 with C38DR reduced integration 8-node linear solid brick elements. The process was simulated in three steps: a loading step in which the rivet was deformed to achieve the appropriate driven head size, an unloading step in which the rivet was allowed to springback followed by the 124 MPa tensile loads, assuming 50% load transfer. Figure A.5 shows the direction of measurement of surface strains taken to validate with the TSA results.

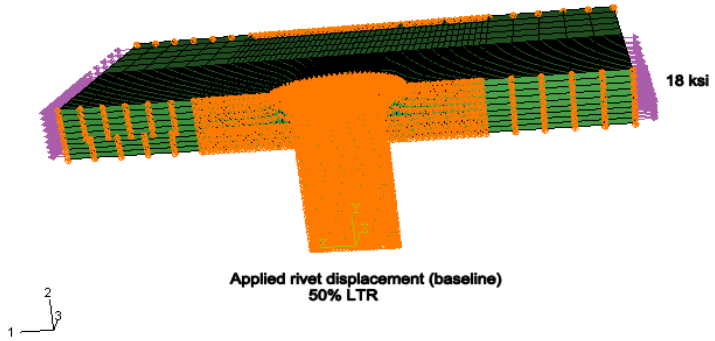

Figure A.4 FE model of specimen

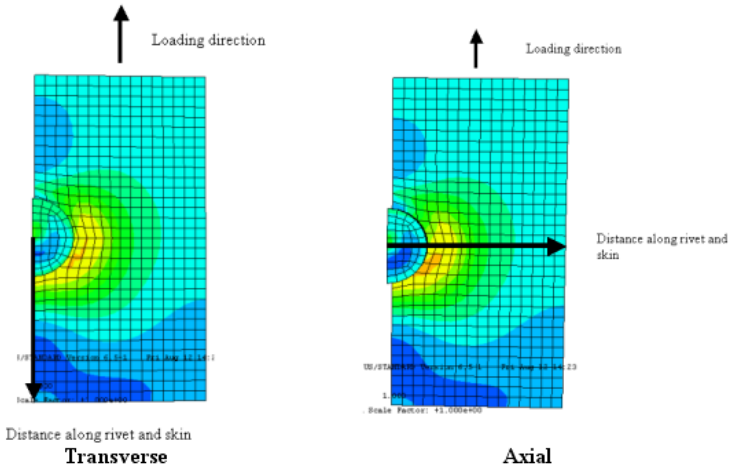

Figure A.5 Direction of measurement of strain values extracted from the FE model to compare to the TSA predictions

Figure A.6 shows a comparison of the strains from the FE to the TSA for both the transverse and axial directions. The transverse measurement shows a good comparison. A discrepancy can be observed for the axial measurement at the bottom of the rivet head. It is uncertain whether the inaccuracies in the FE modeling or the TSA or both are responsible for the observed discrepancy.

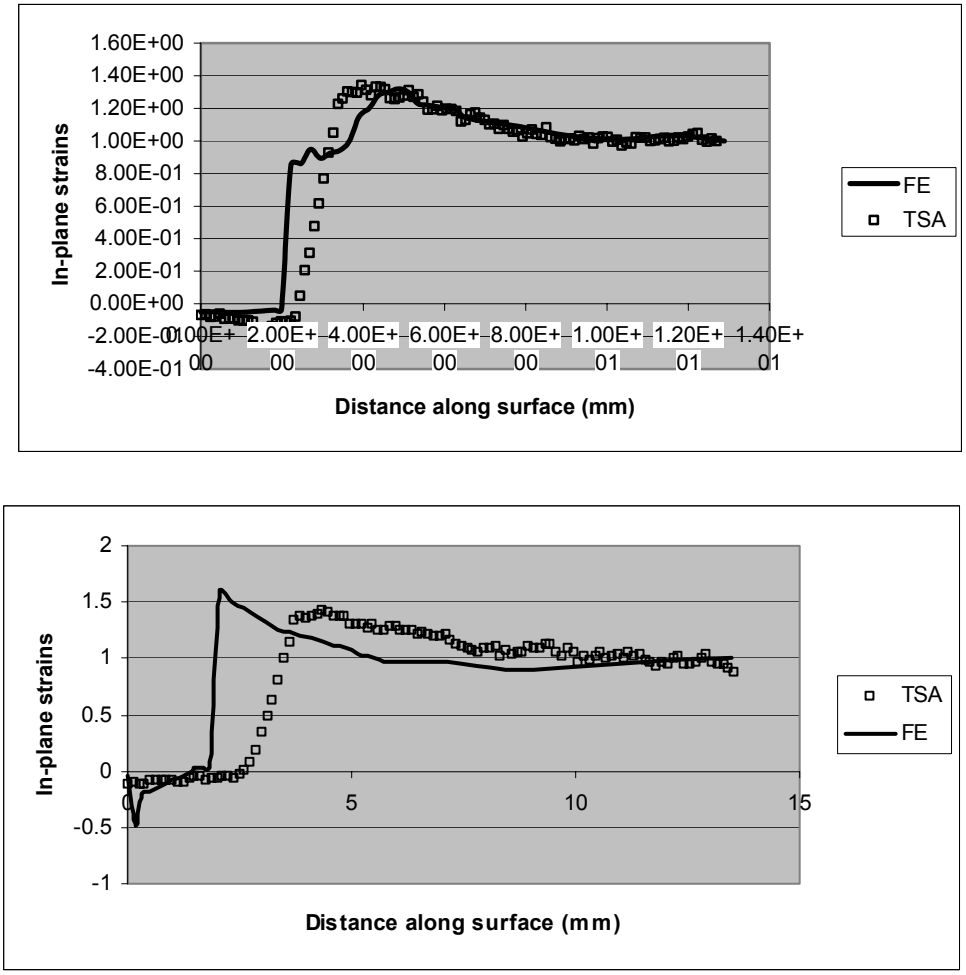

Figure A.6 Comparison of the surface strains predicted by the FE model to those measured by the TSA. Transverse direction (top) and Axial (bottom).

APPENDIX B: SOME MODELING CONSIDERATIONS

Different analyses techniques were attempted for the riveting models and their solutions were compared. An analysis conducted with full integration assumed for the linear elements showed no difference in the stress solution but consumed twice the run time required for the analysis with reduced integration. An analysis conducted with fixed time incrementation failed to converge even for time increments as less as 6.25e-03. Though obvious, automatic time incrementation should always be applied for such non-linear problems. A 3D force controlled riveting model was simulated at the National Research Council, Canada using MSC.MARC near the end of this work [22]. This model was an extension of the axisymmetric analysis [21] conducted by the same researchers (Figure B.1). The model had 5560 linear reduced integration elements and 7431 nodes (Figure B.2). Three steps were defined in the analysis: a range of squeeze forces from 35.59 kN to 53.39 kN was applied with a rigid pusher to the rivet head, the force was then reduced to zero (unload) follower by 98.5 MPa of joint tensile loading applied at the right end.

It is very interesting to note that the same analysis conducted in ABAQUS with 32,186 reduced integration linear elements and 43,468 nodes failed to converge in the third (tensile loading) step (Figure B.3). The analysis aborted at the same time increment for the range of applied squeeze forces. It was ensured that the contact areas near the rivet hole had a much finer mesh. Stabilization techniques were also attempted but did not show any success. Equivalent displacement control loading was implemented to replace the force control loading but the analysis still did not converge. The skin-skin bending during the tensile loading stage led to excessive penetration of the skin surfaces near the rivet holes causing ABAQUS to cut-back and abort.

The analysis can be attempted with a much more refined mesh for the upper skin especially for the sharp countersunk edge along with Automatic Tolerances to obtain

convergence. This analysis however would require more powerful computing facilities and hence was not attempted in this work.

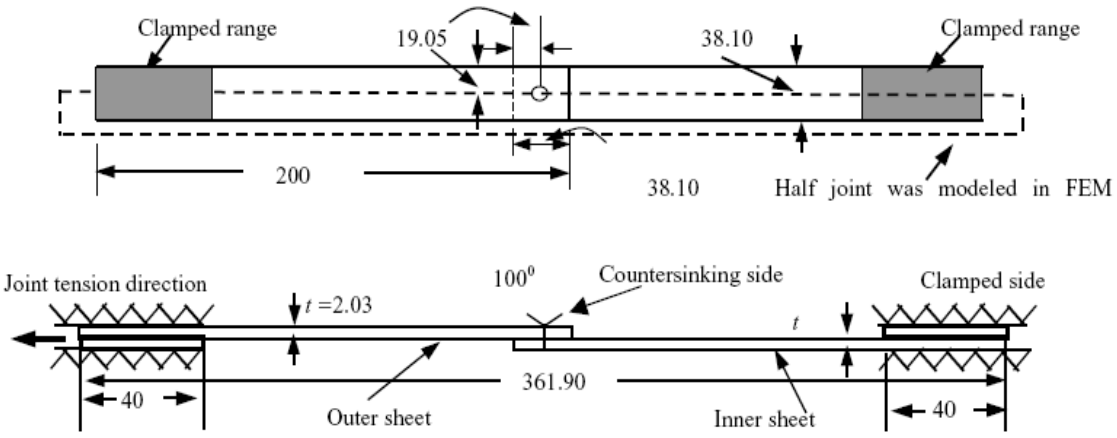

Figure B.1 Geometric configuration of riveted joint analyzed by Li et al. [22]

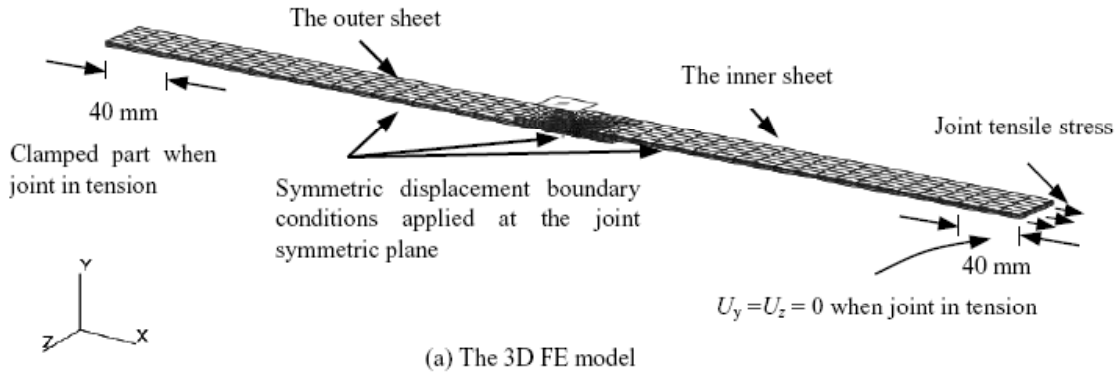

Figure B.2 FE model and BC's of the 3D riveted joint model analyzed by Li et al. [22]

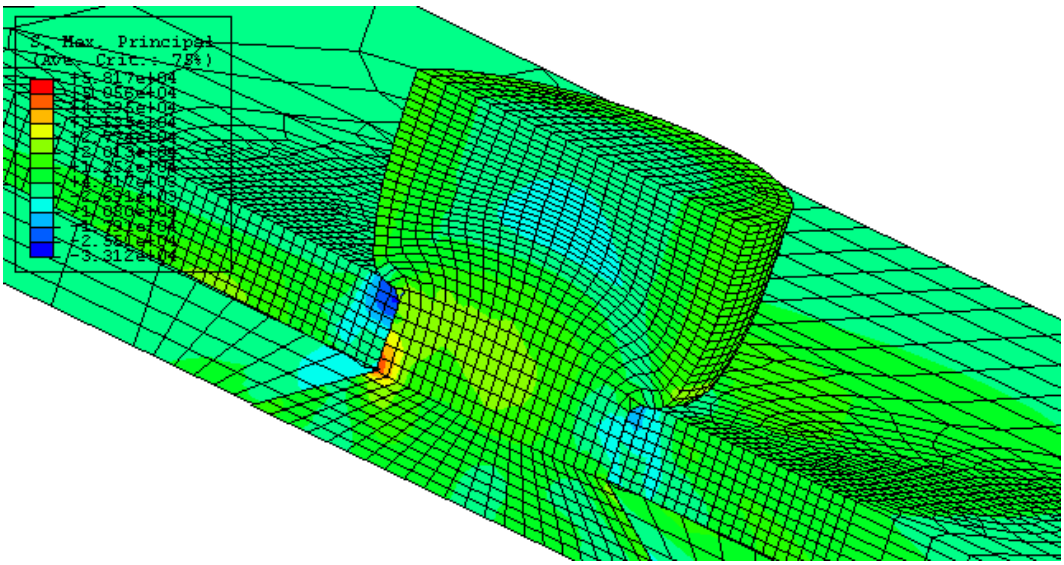

Figure B.3 Same model analyzed in ABAQUS. The picture shows the stress state for a solution that aborted at a time increment of 0.27 in the tensile loading stage

APPENDIX C: ABAQUS CAPABILITIES

The ABAQUS® [63] finite element code was chosen to perform all the simulations conducted throughout these investigations. ABAQUS is a general-purpose code that has been successfully implemented to solve a wide variety of problems in the areas of structural analysis and other disciplines of mechanical engineering. Additionally, ABAQUS allows certain interactions among multiple engineering disciplines such as thermal-electrical and thermal-structural coupled-field problems. This chapter provides highlights of workings of the code [63] including its element library, contact capabilities, material constitutive behaviors and non-linear solution capabilities. Particular emphasis is placed on the specific qualities of the code with regard to correctly accounting for the structural phenomena that comprise the simulations conducted in this work.

Element Library

There is a wide range of elements that are available in ABAQUS. This extensive element library provides the user with a powerful set of tools for solving many different problems. Each element in ABAQUS is characterized by: Family, Degrees of freedom, Number of nodes, Formulation and Integration.

Family refers to the element in a particular type of analysis such as continuum (solid), beam, shell, thermal, spring etc. Degrees of freedom are the fundamental variables calculated in the analysis. These might be translations in the 1,2,3 directions for a structural analysis or temperature for a heat transfer analysis. The number of nodes of an element determines the order of interpolation. The variables in the analysis are computed at the nodes of the element. At any other point in the element the variables are interpolated. Elements that have nodes only at the corners such as an 8-noded brick use linear interpolation in each direction. Such elements are called linear or first-order elements. Elements that have midside nodes in addition to the nodes at the corners such as a 20-noded brick element use quadratic interpolation in each direction. Such

elements are called quadratic or second-order elements. An element's formulation refers to the mathematical theory used to define the element's behavior. All of the stress/displacement elements in ABAQUS are based on the *Lagrangian* or *material* description of behavior: the material associated with an element remains associated with the element throughout the analysis, and material cannot flow across element boundaries. In the alternative, *Eulerian* or *spatial* description, elements are fixed in space as the material flows through them. ABAQUS uses numerical techniques to integrate various quantities over the volume of each element. Using Gaussian quadrature for most elements, ABAQUS evaluates the material response at each integration point in each element. When using continuum elements, the user must choose between full or reduced integration, a choice that can have a significant effect on the accuracy of the element for a given problem. An example of a continuum element in ABAQUS is shown below.

C3D20: Continuum Family, Three DOF, 20 Nodes, Full Integration

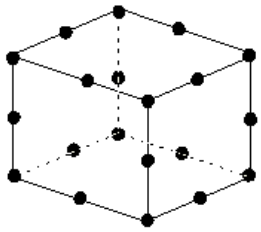

Figure C.1 C3D20 continuum element in ABAQUS [63]

Continuum Elements

Continuum or solid elements can be used to model a wide variety of components. Continuum elements model small blocks of material in any component. This stress/displacement family of elements is one of the most comprehensive element library available in ABAQUS. For three-dimensional elements the user has a choice of

hexahedrons, tetrahedrons, and wedges; for two-dimensional elements the choice is between triangles and quadrilaterals. There are linear and quadratic versions for each of these basic element shapes. The user has a choice between full and reduced-integration elements for hexahedrons and quadrilaterals.

Element Integration

The expression “full integration” refers to the number of Gauss points required to integrate the polynomial terms in an element's stiffness matrix exactly when the element has a regular shape. The meaning of a regularly shaped hexahedral or quadrilateral element is: the edges of the element are straight, the edges meet at right angles and any edge nodes are at mid-point of the edge. Fully integrated linear elements use two integration points in each direction while quadratic elements use three integration points in each direction. Reduced integration can only be used with quadrilateral and hexahedral elements. Reduced integration linear elements have one integration point located at the centroid of the element.

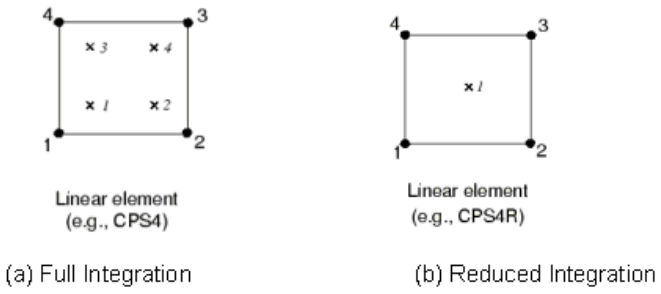

Figure C.2 Integration points in 2-D linear elements [63]

Element Types and Selection

The following gives an overview of the continuum elements available in ABAQUS for structural analysis. Based on this overview particular solid elements are chosen and discussed in light of the specific needs of this investigation.

Table C.1 ABAQUS Solid Element Types

Element	Description	Active DOF
CPE3	3-node linear plane strain	1,2
CPE6	6-node quadratic plane strain	1,2
CPS3	3-node linear plane stress	1,2
CPS6	6-node quadratic plane stress	1,2
C3D4	4-node linear tetrahedron	1,2,3
C3D6	6-node linear triangular prism	1,2,3
C3D8	8-node linear brick	1,2,3
C3D10	10-node quadratic tetrahedron	1,2,3
C3D15	15-node quadratic triangular prism	1,2,3
C3D20	20-node quadratic brick	1,2,3
CAX3	3-node linear axisymmetric	1,2
CAX4	4-node bilinear axisymmetric	1,2
CAX6	6-node quadratic axisymmetric	1,2

Choosing between first and second order elements

The continuum elements in ABAQUS can be used for linear analysis and for complex nonlinear analyses involving contact, plasticity, and large deformations. In first-order plane strain, generalized plane strain, axisymmetric quadrilateral, hexahedral solid elements, and cylindrical elements, the strain operator provides constant volumetric strain throughout the element. This constant strain prevents mesh “locking” when the material response is approximately incompressible. The fully integrated elements (such as C3D8) exhibit shear locking (excessive stiffness in bending) and hence should be avoided for bending dominated problems. The reduced integration elements exhibit hourglassing (no stiffness in bending). A refined mesh of the reduced integration elements should be used for bending dominated problems to obtain accurate results.

Second order elements in ABAQUS provide several features: higher accuracy than first-order elements for problems that do not involve complex contact conditions, impact, or severe element distortions, effective representation of stress concentrations, effective modeling of curved surfaces with fewer elements. The fully integrated elements (such as C3D20) do not exhibit shear locking, as their edges are able to curve, hence

avoiding the formation of spurious shear stresses. The reduced integrated elements also show hourglassing but using a sufficiently refined mesh produces accurate results.

First-order triangular and tetrahedral elements are overly stiff and exhibit slow convergence with mesh refinement. A fine mesh may be needed to obtain results of sufficient accuracy. ABAQUS provides a “modified” version of these triangular and tetrahedral elements (such as C3D10M). They are recommended for contact problems because the contact forces are consistent with the direction of contact. These elements also perform better in analyses involving impact, in analyses involving nearly incompressible material response, and in analyses requiring large element distortions.

Choosing between full and reduced integration elements

Reduced integration uses a lower-order integration to form the element stiffness. Solution run-time can be drastically decreased with reduced-integration elements, especially for 3D problems. Consider an example of an analysis with C3D20 element which has 27 integration points versus the one with C3D20R element which has only 8; Element assembly is approximately 3.5 times costly for the former. The user can choose between full and reduced-integration only for quadrilateral and hexahedral elements. First-order reduced integration elements such as C3D8R can display hourglassing. This means that the elements can distort in such a way that the computed strains at the single integration point are zero. This leads to uncontrolled mesh distortion. These elements do have the capability of hourglass control, but this is effective only with fine meshes.

Second-order reduced-integration elements (excluding C3D27R and C3D27RH) do not have the same difficulty and can be used in all cases when the solution is expected to be smooth. First-order elements should be used when large strains or very high strain gradients are expected.

In ABAQUS the fully integrated elements do not exhibit hourglassing. They however might display shear or volumetric locking. Shear locking is possible in first order fully integrated elements subjected to bending. The internal formulation of these elements causes spurious shear strains, making the elements too stiff in bending. For problems involving incompressibility in the solution, second-order, fully integrated elements may exhibit volumetric locking when the plastic strains are on the order of the elastic strains. The first-order, fully integrated quadrilaterals and hexahedra use reduced integration on the volumetric terms and do not lock with almost incompressible materials. Reduced-integration, second-order elements exhibit volumetric locking for almost incompressible materials only after significant straining occurs. Volumetric locking can be accompanied by hourglassing in such cases. A refined mesh in the regions of high plastic strains may resolve the issue.

Choosing between quadrilateral, triangular and tetrahedral elements

Many automatic-meshing algorithms use triangular and tetrahedral elements because of their versatility. These elements increase user convenience to mesh complex shapes. However, a solution obtained from these elements is very costly compared to that obtained by using hexahedrons. Some other advantages that quadrilaterals and hexahedrons offer in comparisons to triangles and tets are: better convergence rate and less sensitivity to mesh orientation. However, triangles and tetrahedra are less sensitive to initial element shape, whereas first-order quadrilaterals and hexahedra perform better if their shape is approximately rectangular. The elements become much less accurate when they are initially distorted. Fully integrated first-order triangles and tets also exhibit volumetric locking. The recommended usage of these elements is only as a filler material.

The modified elements display much better performance in complex analyses. They are however more expensive computationally than lower-order quadrilaterals and hexahedron. They may sometimes also require a more refined mesh for the same level of accuracy. In ABAQUS/Explicit they are provided as an attractive alternative to the lower-order triangles and tetrahedron to take advantage of automatic triangular and tetrahedral mesh generators. One more disadvantage of the modified triangular and tetrahedral elements is incompatiblity with the regular second-order solid elements in ABAQUS/Standard and hence these elements should not be connected with these elements in a mesh.

Hybrid elements

Hybrid elements are available only in ABAQUS/Standard. Their primary purpose is to model incompressible and almost incompressible material behavior. When the material response is incompressible, the solution to a problem cannot be obtained in terms of the displacement history only, since a purely hydrostatic pressure can be added without changing the displacements. Linear elastic materials, which have a bulk modulus much greater than the shear modulus, exhibit nearly incompressible material behavior. Extremely large changes in pressure are obtained with small variations in displacements. A pure displacement-solution in this case is very sensitive numerically to problems such as computer round-off errors. Hence, the pressures stress is treated as an independently interpolated basic solution variable coupled to the displacement solution through constitutive and compatibility conditions. This internal formulation forms the groundwork for hybrid elements. Since these elements have more internal variables they are more computationally expensive.

Choosing elements for problems with plasticity

Incompressibilty imposed by plasticity in metals limits the type of elements that can be used for elasto-plastic simulations. This limitation arises from the kinematic constraint imposed on element behavior namely constrainment of constant volume at the element integration point. In some cases, this actually makes the element overconstrained. Elements that cannot resolve this contraint suffer from volumetric locking, that is, overly stiff response. Fully integrated, second-order, solid elements are very susceptible to volumetric locking in elastic-plastic simulations. The ABAQUS fully integrated, first-order, solid elements do not suffer from volumetric locking because ABAQUS actually uses a constant volume strain in these elements. Reduced-integration, solid elements have fewer integration points at which the incompressibility constraints must be satisfied. Therefore, they are not overconstrained and can be used for most elastic-plastic simulations. In simulations, with plastic strains exceeding 20-40% second-order, reduced integration elements should be used cautiously and with fine meshes.

Rigid bodies

In ABAQUS a rigid body is a collection of nodes and elements whose motion is governed by the motion of a single node, known as the *rigid body reference node*. The shape of the rigid body is defined as an analytical surface or discrete rigid body. The analytical surface is obtained by revolving or extruding a 2D geometric profile. A discrete rigid body is obtained by meshing the component with nodes and elements. The shape of the rigid body remains constant during an analysis. The body can undergo large rigid

body motions. Computation of mass and inertia for a discrete rigid body can be based upon contribution from its elements. It can also be assigned specifically.

BC's governing the motion of a rigid body are applied to the rigid body reference node. Contact and nodal connections are used for interaction of rigid bodies and deformable elements. Rigid bodies are typically used to model very stiff components. These components may be fixed or undergoing large rigid body motions. In forming analyses, rigid bodies are an excellent choice for modeling components such as punches, dies, rollers etc. The computational efficiency provided by rigid bodies is the primary reason for choosing them above deformable elements. Element-level computations are avoided and relatively small effort is required to update the motion of the nodes and assemble concentrated/distributed loads.

Material Models

The material library in ABAQUS allows most engineering materials to be modeled, including metals, plastics, rubbers, foams, composites, granular soils, rocks, and plain and reinforced concrete. This section only discusses three of the most commonly used material models: linear elasticity, metal plasticity, and rubber elasticity.

Classical Metal Plasticity

The yield and inelastic flow of a metal at relatively low temperatures, where creep effects are not important and loading is relatively monotonic, can typically be described with the classical metal plasticity. Standard Mises or Hill yield surfaces with associated plastic flow are implemented in ABAQUS for this purpose. Perfect plasticity and isotropic hardening definitions are both available in the classical metal plasticity models. The Mises and Hill yield surfaces assume that yielding of the metal is independent of the

equivalent pressure stress. The Mises yield surface is used to define isotropic yielding. It is defined by giving the value of the uniaxial yield stress as a function of uniaxial equivalent plastic strain, temperature, and/or field variables on the data lines or by defining the yield stress in user subroutines.

The Hill yield surface allows anisotropic yielding to be modeled. A reference yield stress must be given, and the user must define a set of yield ratios. ABAQUS provides two types of work hardening: perfect plasticity and isotropic hardening. In perfect plasticity the yield stress does not change with plastic strain while in isotropic hardening means the yield surface changes size uniformly in all directions such that the yield stress increases (or decreases) in all stress directions as plastic straining occurs.

If isotropic hardening is defined, the yield stress can be defined in tabular form or described through user subroutines. If the tabular form is used, the yield stress must be given as a tabular function of plastic strain and, if required, of temperature and/or other predefined field variables. The yield stress at a given state is simply interpolated from this table of data, and it remains constant for plastic strains exceeding the last value given as tabular data. Associated plastic flow is used. Therefore, as the material yields, the inelastic deformation rate is in the direction of the normal to the yield surface (the plastic deformation is volume invariant). ABAQUS optionally allows for plastic dissipation to result in the heating of a material. The option is typically used in the simulation of bulk metal forming or high-speed manufacturing processes involving large amounts of inelastic strain where the heating of the material caused by its deformation is an important effect. The option is applicable only to adiabatic thermal-stress analysis or fully coupled temperature-displacement analysis. Only a Mises yield surface can be used in an adiabatic analysis.

When defining plasticity data in ABAQUS, the user must provide *true stress* and *true strain*. ABAQUS requires these values to interpret the data in the input file correctly.

ABAQUS approximates the smooth stress-strain behavior of the material with a series of straight lines joining the given data points. Any number of points can be used to approximate the actual material behavior; therefore, it is possible to use a very close approximation of the actual material behavior. The material data defines the true yield stress of the material as a function of true plastic strain. The first piece of data given defines the initial yield stress of the material and, therefore, should have a plastic strain value of zero.

Hyperelasticity

The hyperelastic material model is isotropic and nonlinear. The material model is valid for materials that exhibit instantaneous elastic response up to large strains. Rubbers and elastomers are typical examples of materials that are modeled with hyperelastic formulation. This model requires the usage of non-linear geometry since it is intended for finite strain applications. The shear flexibility of most elastomers is large compared to it's compressibility. In applications where the material is not highly confined, it is quite satisfactory to assume that the material is fully incompressible. In cases where the material is highly confined the compressibility must be modeled correctly to obtain accurate results.

The hyperelastic material model can be used with continuum elements. For continuum elements hyperelasticity can be used with the pure displacement formulation elements or with the "hybrid" (mixed formulation) elements. Because elastomeric materials are usually almost incompressible, fully integrated pure displacement method elements are not recommended for use with this material, except for plane stress cases. If fully or selectively reduced-integration displacement method elements are used with the almost incompressible form of this material model, a penalty method is used to impose the incompressibility constraint in anything except plane stress analysis. The

penalty method can sometimes lead to numerical difficulties; therefore, the fully or selectively reduced-integrated "hybrid" formulation elements are recommended for use with hyperelastic materials.

ABAQUS describes hyperelastic materials in terms of a "strain energy potential," $U(\varepsilon)$, which defines the strain energy stored in the material per unit of reference volume (volume in the initial configuration) as a function of the strain at that point in the material. There are several forms of strain energy potentials available in ABAQUS to model approximately incompressible isotropic elastomers: the Arruda-Boyce form, the Mooney-Rivlin form, the neo-Hookean form, the Ogden form, the polynomial form, the reduced polynomial form, the Yeoh form, and the Van der Waals form.The polynomial form of the strain energy potential is the one that is most commonly used. Its form is

[C.1] $$U = \sum_{i+j=1}^{N} C_{ij} (\overline{I_1} - 3)^i (\overline{I_2} - 3)^j + \sum_{i=1}^{N} \frac{1}{D_i} (J_{el} - 1)^{2i}$$

where U is the strain energy potential; J_{el} is the elastic volume ratio; $\bar{I}_1$ and $\bar{I}_2$ are measures of the distortion in the material; and N, C_{ij} and D_i are material parameters, which may be functions of temperature. The C_{ij} parameters describe the shear behavior of the material, and the D_i parameters introduce compressibility. All zero values for D_i means that the material is fully incompressible. If the number of terms, N, is one, the initial shear modulus, μ_0, and bulk modulus, K_o, are given by

[C.2] $$\mu_0 = 2(C_{01} + C_{10}) \quad \text{and} \quad K_0 = \frac{2}{D_1}$$

If the material is also incompressible, the equation for the strain energy density is

[C.3] $$U = C_{10}(\overline{I_1} - 3) + C_{01}(\overline{I_2} - 3)$$

This expression is commonly referred to as the *Mooney-Rivlin* material model. If C_{01} is also zero, the material is called *neo-Hookean*.

The user must provide ABAQUS with the relevant material parameters to utilize a hyperelastic material. For the polynomial form these are N, C_{ij} and D_i. ABAQUS can also accept test data directly and calculate the material parameters using a least squares fit. The experimental tests for which ABAQUS can fit data are: Uniaxial tension and compression, Equi biaxial tension and compression, Planar tension and compression (pure shear), Volumetric tension and compression. Unlike plasticity data, the test data for hyperelastic materials must be given to ABAQUS as nominal stress and nominal strain values. Volumetric compression data only need to be given if the material's compressibility is important.

The quality of the results from a simulation using hyperelastic materials strongly depends on the material test data provided to ABAQUS. It is common for the material model determined from the test data to be unstable at certain strain magnitudes. A stability check is performed by ABAQUS to determine the strain magnitudes where unstable behavior. The user should check this information carefully since the simulation may not converge if any part of the model experiences strains beyond the stability limits. The stability checks are done for specific deformations, so it is possible for the material to be unstable at the strain levels indicated if the deformation is more complex. Likewise, it is possible for the material to become unstable at lower strain levels if the deformation is more complex.

Non-linear analysis

A nonlinear structural problem is one in which the structure's stiffness changes as it deforms. In a nonlinear analysis the stiffness matrix of the structure has to be assembled and inverted many times during the course of the analysis, making it much more expensive to solve than a linear analysis. Since the response of a nonlinear system is not a linear function of the magnitude of the applied load superposition cannot be applied to obtain the solution. Each load case must be defined and solved as a separate analysis.

There are three sources of non-linearity in structural mechanics simulations:

1. Material non-linearity: Most metals have a fairly linear stress/strain relationship at low strain values, but at higher strains the material yields, at which point the response becomes nonlinear and irreversible

2. Boundary non-linearity: This occurs if the boundary conditions change during the analysis. Boundary non-linearities are extremely discontinuous: when contact occurs during a simulation, there is a large and instantaneous change in the response of the structure.

3. Geometric non-linearitiy: Geometric non-linearity occurs whenever the magnitude of the displacements affects the response of the structure. This may be caused by: Large deflections or rotations, snap through, Initial stresses or load stiffening. If the deflection is small, the analysis can be considered as being approximately linear. However, if the deflections are large, the shape of the structure and, hence, its stiffness changes. In addition, if the load does not remain perpendicular to the structure, the action of the load on the structure changes significantly. Both of these effects contribute to the nonlinear response of the structure. Incorporating the effects of geometric non-

linearity in an analysis requires only minor changes to the input file. The user just needs to add the NLGEOM parameter to the *STEP option.

Solution of nonlinear analysis

The nonlinear load-displacement curve for a structure is shown in Figure C.3

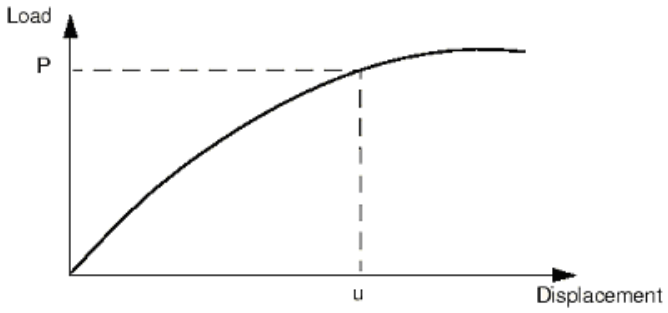

Figure C.3 Non-linear load-displacement curve [63]

ABAQUS implements the Newton-Raphson method to obtain solutions for nonlinear problems. In a nonlinear analysis the solution cannot be calculated by solving a single system of equations, as would be done in a linear problem. Instead, the solution is found by applying the specified loads gradually and incrementally working toward the final solution. Therefore, ABAQUS breaks the simulation into a number of *load increments* and finds the approximate equilibrium configuration at the end of each load increment. It often takes ABAQUS several iterations to determine an acceptable solution to a given load increment. The sum of all of the incremental responses is the approximate solution for the nonlinear analysis.

Consider the external forces, *P*, and the internal (nodal) forces, *I*, acting on a body (Figure C.4). The internal loads acting on a node are caused by the stresses in the elements that contain that node. For the body to be in equilibrium, the net force acting at

every node must be zero. Therefore, the basic statement of equilibrium is that the internal forces and the external forces must balance each other: P-I=0.

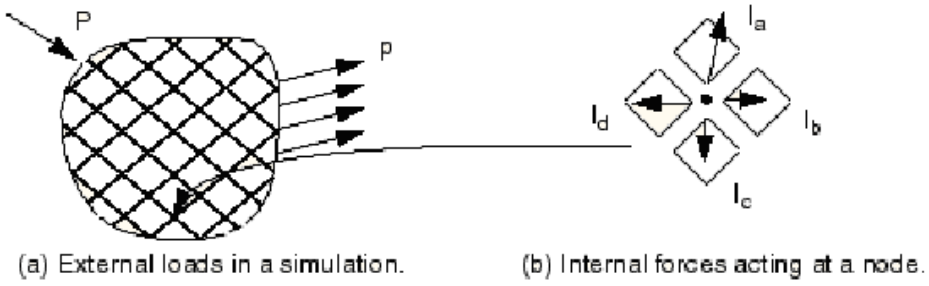

Figure C.4 Internal and external loads on a body [63]

It is important for the user to understand the difference between an analysis *step*, a load *increment*, and *iteration*. The load history for a simulation consists of one or more steps. The user defines the steps, which generally consist of an analysis procedure and loading. Different BC's and analysis procedure options can be specified in each step. An increment is part of a step. In nonlinear analyses the total load applied in a step is broken into smaller increments so that the nonlinear solution path can be followed. The user suggests the size of the first increment, and ABAQUS automatically chooses the size of the subsequent increments. At the end of each increment the structure is in (approximate) equilibrium. An iteration is an attempt at finding an equilibrium solution in an increment. If the model is not in equilibrium at the end of the iteration, ABAQUS tries another iteration. With every iteration, the solution ABAQUS obtains should be closer to equilibrium; sometimes ABAQUS may need many iterations to obtain an equilibrium solution. When an equilibrium solution has been obtained, the increment is complete. The nonlinear response of a structure to a small load increment, ΔP_0, is shown in Figure

C.5. ABAQUS uses the structure's initial stiffness, ΔK_0 which is based on its configuration at, u_0 and ΔP to calculate a *displacement correction*, c_a, for the structure. Using, c_a the structure's configuration is updated to u_a.

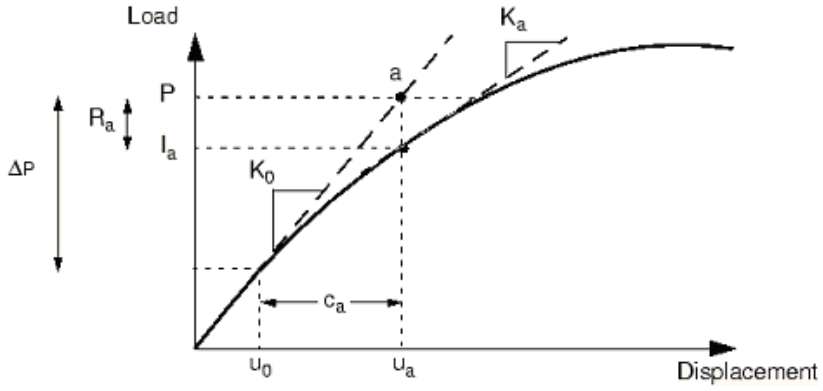

Figure C.5 First iteration in an increment [63]

ABAQUS forms a new stiffness, K_a, for the structure, based on its updated configuration, u_a. ABAQUS also calculates the structure's internal forces, I_a, in this updated configuration. The difference between the total applied load, P, and I_a can now be calculated as: $R_a = P - I_a$, where R_a is the *force residual* for the iteration. AT every DOF in the model if R_a results to be zero point *a* in Figure C.5 would lie on the load-deflection curve, and the structure would be in equilibrium. In a nonlinear problem it is almost impossible to have R_a equal zero. Hence, ABAQUS compares the computed value to an initial tolerance. If R_a is less than this force residual tolerance, ABAQUS accepts the structure's updated configuration as the equilibrium solution. This tolerance value is set to 0.5% of an average force in the structure, averaged over time. The spatially and time averaged force are automatically computed during the analysis. If R_a is less than the current tolerance value, R_a and P_a are in equilibrium, and R_a is a valid equilibrium

configuration for the structure under the applied load. This however is not the only check performed by ABAQUS. The code also checks that the displacement correction, c_a, is small relative to the total incremental displacement, $\Delta u = u_a - u_0$. Both convergence checks must be satisfied before a solution is said to have *converged* for that load increment. The exception to this rule is the case of a *linear* increment, which is defined as any increment in which the largest force residual is less than 10^{-8} times the time-averaged force. Another (or several) iterations may be performed by ABAQUS if the solution from the iteration is not converged. This second iteration uses the stiffness, K_a, calculated at the end of the previous iteration together with R_a to determine another displacement correction, c_b that brings the system closer to equilibrium.

For each iteration in a nonlinear analysis the model stiffness matrix needs to be assembled and a system of equations needs to be solved. Each iteration is equivalent to conducting a complete linear analysis. For ease and efficient solution of non-linear problems ABAQUS automatically adjusts the size of the load increments. Only an initial increment is suggested by the user. ABAQUS applied all of the loads defined in the first increment if no initial increment size is suggested by the user. For problems with dominant non-linearity ABAQUS will have to reduce the increment size repeatedly, resulting in wasted CPU time. Hence, the user should provide a reasonable initial increment size.

The number of iterations needed to find a converged solution for a load increment will vary depending on the degree of non-linearity in the system. If the solution has not converged within 16 iterations or if the solution appears to diverge, ABAQUS abandons the increment and starts again with the increment size set to 25% of its previous value. ABAQUS then attempts to find a solution with this smaller increment. This increment size is reduced repeatedly, in case ABAQUS fails to obtain convergence.

A maximum of five cutbacks of increment size in an increment before the analysis aborts.

The user may also add the **INC** parameter to specify the maximum number of increments allowed during the step. The analysis is terminated by ABAQUS if it needs more increments than this limit to complete the step. The default number of increments for a step is 100 but if significant non-linearity is present in the simulation, the analysis may require many more increments.

In a nonlinear analysis a step takes place over a finite period of “time”. This “time” has no physical meaning in a purely static solution (without inertial effects or rate-dependent behavior). The data line on the procedure option used in the step specifies the initial time increment and the total time for the step. For example,

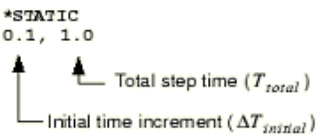

defines a static analysis that occurs over 1.0 units of time and has an initial increment of 0.1. These data also specify the proportion of load applied in the first increment. The initial load increment is given by:

$$\frac{\Delta T_{initial}}{T_{total}} \times \text{Load magnitude.}$$

The choice of initial time increment can be critical in certain nonlinear simulations, but for most analyses an initial increment size that is 5% to 10% of the total step time is usually sufficient. The total step time is set to 1.0 in static simulations. With this time 50% of the total load is applied when the step time is 0.5. An analysis is terminated if a large number of cutbacks (due to convergence problems) reduce the

increment size below the minimum allowable time increment, $\Delta T_{\min}$, which is 10^{-5} times the total step time. The user may want to specify different minimum and/or maximum allowable increment sizes on the basis of the problem under consideration.

Linear Equation Solvers

Linear equation solution in ABAQUS is done using a direct, Gauss elimination method using a sparse solver. This part of the analysis is often the most time consuming. A large part if disk space is consumed by the storage of the equations. If the system of equations has a sparse structure a multi-front technique is used that reduces the computational time. The sparse solver can be executed in parallel to reduce the solution time for large problems.

Boundary Non-linearity

Many engineering problems involve contact between two or more components. In these problems a force normal to the contacting surfaces acts on the two bodies when they touch each other. If there is friction between the surfaces, shear forces may be created that resist the tangential motion (sliding) of the bodies. Contact simulations are typically conducted to identify the areas on the surfaces that are in contact and to calculate the contact pressures generated.

Contact conditions are a special class of discontinuous constraint, because forces are applied only when the two surfaces are in contact. When the two surfaces separate, no constraint is applied. The FE code has to be able to detect when two

surfaces are in contact. Then it must apply the required constraints. It must also detect separation of surfaces and enforce subsequent removal of constraints.

The distance separating two surfaces is called the clearance. With zero clearance between the surfaces the contact constraint is applied. There is no limit in the contact formulation on the magnitude of contact pressure that can be transmitted between the surfaces. Separation of surfaces when the contact pressure between them becomes zero or negative. The contact constraint is then removed. This surface interaction behavior, is referred to as “hard” contact.

The change in contact pressure that occurs when a contact condition changes from “open” (a positive clearance) to “closed” (clearance equal to zero) sometimes makes it difficult to complete contact simulations. In contact simulations, ABAQUS should detect contact at a particular point and also calculate sliding between the two contacting surfaces. Since this is a complex computation ABAQUS separates simulations based on the magnitude of sliding, namely small sliding analysis or finite sliding analysis. Small sliding is difficult to define but is typically used to refer to problems where a point contacting a surface does not slide more than a small fraction of a typical element dimension. This is a relatively less expensive computation.

ABAQUS establishes the relationship between the slave nodes and the master surface at the beginning of the simulation, in case of small sliding analysis. ABAQUS determines which segment on the master surface will interact with each node on the slave surface. It maintains these relationships throughout the analysis, never changing which master surface segments interact with which slave nodes. If geometric non-linearity is included in the model by using the **NLGEOM** parameter on the ***STEP** option, the small-sliding algorithm accounts for any rotation and deformation of the master surface and updates the load path through which the contact forces are transmitted. In contrast to small sliding, the finite-sliding contact formulation requires that ABAQUS

constantly determine which part of the master surface is in contact with each slave node. This results in a complex computation, the level of complexity increasing for contact between deformable bodies.

The analysis may need to take into account frictional resistance if the two interacting surfaces are rough. *Coulomb friction* is a common friction model used to describe the interaction of contacting surfaces. The model characterizes the frictional behavior between the surfaces using a coefficient of friction, μ. The product μp, where p is the contact pressure between the two surfaces, gives the limiting frictional shear stress for the contacting surfaces. The contacting surfaces will not slip (slide relative to each other) until the shear stress across their interface equals the limiting frictional shear stress, μp. For most surfaces μ is normally less than unity. The solid line in Figure C.6 summarizes the behavior of the Coulomb friction model: there is zero relative motion (slip) of the surfaces when they are sticking (the shear stresses are below μp).

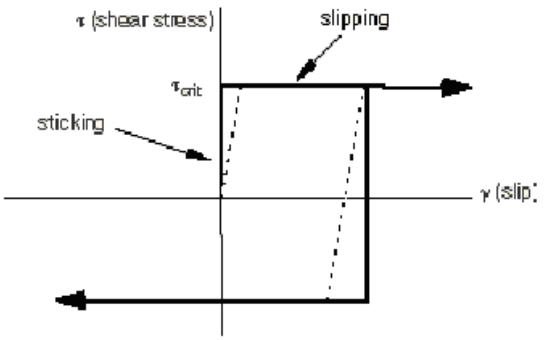

Figure C.6 Frictional behavior [63]

Convergence problems are often caused by discontinuous stick-slip behavior. Since simulation of ideal friction behavior is very difficult a penalty friction formulation with an allowable “elastic slip,” shown by the dotted line in Figure C.6 is used by ABAQUS. The “elastic slip” is defined the small amount of relative motion between the

surfaces that occurs when the surfaces should be sticking. The penalty stiffness (the slope of the dotted line) is chosen automatically by ABAQUS. This results in an allowable “elastic slip” that is a very small fraction of the characteristic element length. For most applications, this penalty formulation is sufficient to model any frictional behavior. When ideal stick-slip frictional behavior must be included (such as fretting problems) the “Lagrange” friction formulation can be used. The “Lagrange” friction formulation uses more computer resources because of additional variables imposed by ABAQUS for each surface node with frictional contact. The Lagrange formulation also exhibits a slower rate of convergence.

The inclusion of friction in a model adds unsymmetric terms to the system of equations being solved. For values of μ less than about 0.2, the magnitude and influence of these terms are quite small and the symmetric solver is sufficient for the analysis. For higher coefficients of friction, the unsymmetric solver is invoked automatically by ABAQUS. This improves the convergence rate. The user has the flexibility of selecting the unsymmetric solver by including the **UNSYMM=YES** parameter on the ***STEP** option. It should be noted however that the unsymmetric solver requires twice as much computer memory and scratch disk space in comparison to it’s symmetric counterpart.

ABAQUS uses a pure master-slave contact algorithm: nodes on one surface (the slave) cannot penetrate the segments that make up the other surface (the master). No restrictions on the master surface are placed by the algorithm. The master surface can penetrate the slave surface between slave nodes, as shown in Figure C.7.

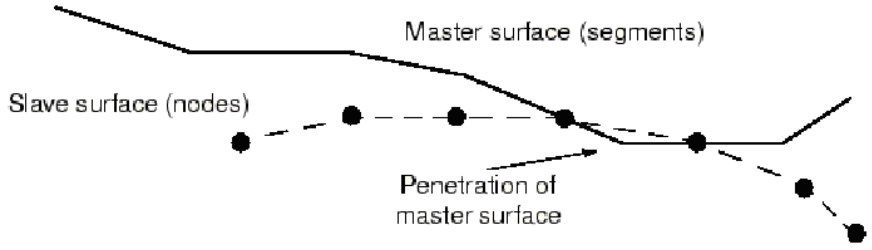

Figure C.7 The master surface can penetrate the slave surface [63]

The order of the two surfaces given on the ***CONTACT PAIR** option is very important. This order determines which surface is the master surface and which is the slave surface. The first surface is taken to be the slave surface, and the second is the master surface. The user must carefully select the slave and master surfaces in order to achieve the best possible contact simulation. Typical rules that are followed are: the slave surface should be the more finely meshed surface; and if the mesh densities are similar, the slave surface should be the surface with the softer underlying material.

First-order elements should be typically selected for the slave surface. Second-order elements can cause problems in contact simulation This is due to the way in which consistent nodal loads are calculated for these elements for a constant pressure. The consistent nodal loads for a constant pressure, *P*, on a second-order, two-dimensional elements with area A are shown in Figure C.8.

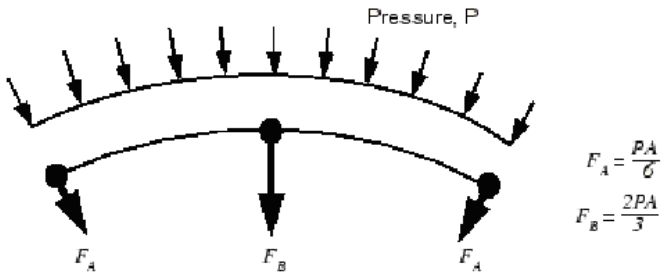

Figure C.8 Equivalent nodal loads for a constant pressure on a two-dimensional, second-order element [63]

Important decisions are based by the contact algorithms depending on the forces acting on the slave nodes. The algorithms find it difficult to distinguish if the force distribution represents a constant contact pressure or an actual variation across the element. Equivalent nodal forces for a three-dimensional, second-order brick element prove to be more confusing. This is because they do not have the same sign for a constant pressure. This makes correct working of the algorithm very difficult, especially for non-uniform contact simulations. In order to avoid such problems, ABAQUS automatically adds a mid-face node to any face of a second-order, three-dimensional brick or wedge element that defines a slave surface. For a second-order element face with a mid-face node the equivalent nodal forces have the same sign for a constant pressure. They still differ considerably in magnitude.

The equivalent nodal forces for applied pressures on first-order elements always have a consistent sign and magnitude. The contact algorithm therefore, faces no ambiguity about the contact state that a given distribution of nodal forces represents. If the geometry is complicated and requires the use of an automatic mesh generator, the modified second-order tetrahedral elements (C3D10M) in ABAQUS should be used. These elements are designed to be used in complex contact simulations. Regular second-order tetrahedral elements (C3D10) have zero contact force at their corner nodes. This leads to poor predictions of the contact pressures. The modified second-order tetrahedral elements can calculate the contact pressures accurately.

ABAQUS/Standard implements the Newton-Raphson technique discussed earlier for the contact algorithm. The state of all contact pairs is examined the start of each increment to establish whether slave nodes are open or closed. In Figure C.9, *P* denotes the contact pressure at a slave node and *h* denotes the penetration of a slave node into the master surface. If a node is closed, ABAQUS determines whether it is sliding or sticking. A constraint is applied by ABAQUS for each closed node and any constraint is

removed from any node where the contact state changes from closed to open. An iteration is then carried out and the model configuration updated based on the calculated corrections.

Before checking for equilibrium of forces or moments, checks are performed for changes in the contact conditions at the slave nodes. Any node where the clearance after the iteration becomes negative or zero has changed status from open to closed. Any node where the contact pressure becomes negative has changed status from closed to open. If any contact changes are detected in the current iteration, ABAQUS labels it a *severe discontinuity iteration* and no equilibrium checks are carried out.

The contact constraints are modified to reflect the change in contact status after the first iteration. A second iteration is then attempted by ABAQUS. This procedure is repeated until there are no changes in contact status. This iteration becomes the first equilibrium iteration, and ABAQUS performs the normal equilibrium convergence checks. Another iteration is performed if the convergence checks fail. The internal count of equilibrium iterations to zero for every severe discontinuity iteration. This iteration count is used to determine if an increment should be abandoned due to a slow convergence rate. The entire process is repeated until convergence is achieved.

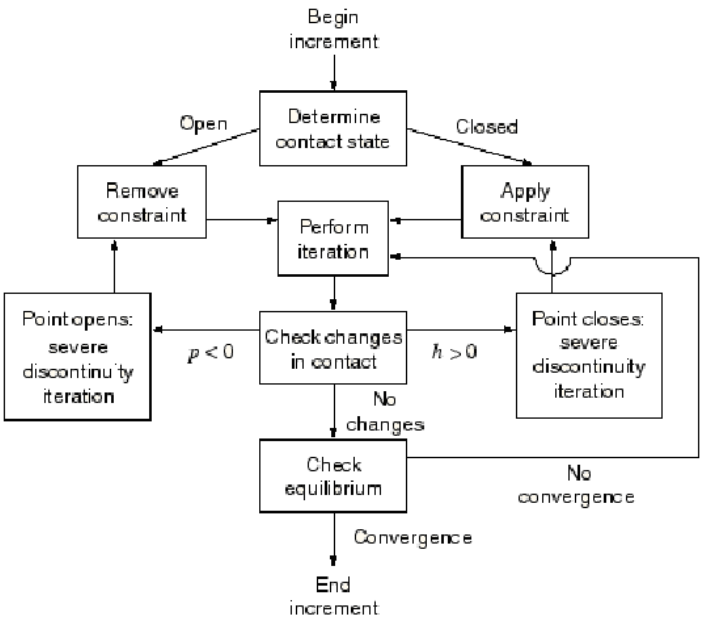

Figure C.9 Contact logic [63]

The user can separate the two types of iterations to see how well ABAQUS is coping with the contact calculations and how well it is achieving equilibrium. If the number of severe discontinuity iterations is high but there are few equilibrium iterations, ABAQUS is having difficulty determining the proper contact conditions. Any increment needing more than twelve severe discontinuity iterations is abandoned and a cutback occurs. If there are no severe discontinuity iterations, the contact state is not changing from increment to increment.

Explicit Solvers

A wide variety of non-linear solid mechanics problems can be solved with the explicit dynamics procedure in ABAQUS. This method is sometimes complimentary to an implicit analysis (ABAQUS/Standard). From a user standpoint, the distinguishing characteristics of the explicit and implicit methods are:

Explicit methods require a small time increment size. This size that depends on the highest natural frequencies of the model. This size is independent of the type and duration of loading. Simulations generally take on the order of 10,000 to 1,000,000 increments, but the computational cost per increment is relatively small.

In Implicit methods increment size is generally determined from accuracy and convergence considerations. Implicit simulations typically take orders of magnitude fewer increments than explicit simulations. In Implicit, since a global set of equations must be solved in each increment, the cost per increment is far greater than that of an explicit method.

The explicit method is designed for solving high-speed dynamic events that require many small increments to obtain a high-resolution solution. If the duration of the event is short, the solution can be obtained efficiently. Formulation of contact conditions is extremely easy in the explicit method and can be enforced on a node-by-node basis without iteration. The nodal accelerations can be adjusted to balance the external and internal forces during contact. The explicit method displays the lack of a global tangent stiffness matrix, which is required with implicit methods. Iterations and tolerances are not required since the state of the model is advanced explicitly.

With the explicit method the state of the model is advanced through an increment of time, Δt. This is based on the state of the model at the start of the increment at time *t*. The amount of time that the state can be advanced and still remain an accurate representation of the problem is typically quite short. The increment will exceed a stability limit if it is larger than this maximum amount of time. Exceeding the stability limit might lead to numerical instability and consequently an unbounded solution. The stability limit has a great effect on reliability and accuracy. Hence, a consistent and conservative estimate is necessary. For computational efficiency ABAQUS/Explicit chooses the time increments to be as close as possible to the stability limit without exceeding it.

ABAQUS/Explicit adjusts the time increment size throughout the analysis so that the stability limit, based on the current stage of the model, is never exceeded. The stability limit is a mathematical concept resulting from the numerical model. It is directly proportional to element size and inversely proportional to the wave speed of the material. The wave speed of the material in turn is directly proportional to the stiffness and inversely proportional to density. Thus, the mass density influences the stability limit. Scaling the mass density can increase analysis efficiency. Models might typically have regions containing few localized small or poorly shaped elements that control the stability limit. By scaling the mass of only these elements the stability limit can be increased without affecting the overall dynamic behavior of the model. There are two approaches used in mass scaling: the user can define a scaling factor directly or define a desired element-by-element stable time increment for the elements whose mass is to be scaled. However, the user should be cautious when employing mass scaling since significantly changing the mass of the model may change the physics of the problem.

The material model affects the stability limit through its effect on the dilatational wave speed. In a linear material the wave speed is constant. The only changes in the stability limit during the analysis are a result of changes in the smallest element dimension during the simulation. In a nonlinear material, such as a metal with plasticity, the wave speed changes as the material yields and the stiffness of the material changes. The effective wave speed in the model is monitored by ABAQUS/Explicit throughout the analysis, and the current material state in each element is used for stability estimates. After yielding, the stability limit increased due to a decrease in the stiffness.

Since the stability limit is roughly proportional to the shortest element dimension, it is advantageous to keep the element size as large as possible. However, accurate analyses typically require a fine mesh. To obtain the highest possible stability limit while

using the required level of mesh refinement a uniform mesh should be used. Even a single small or poorly shaped element can reduce the stability limit drastically.

Comparison of Implicit and Explicit Solvers

ABAQUS/Explicit and ABAQUS/Standard are capable of solving a wide variety of problems. The characteristics of implicit and explicit procedures dictate which method is appropriate for a given problem. For those problems that can be solved with either method, the question of which analysis tool to use has a direct bearing on the efficiency with which the problem is solved.

Each iteration in an implicit analysis requires solving a large system of linear equations. This leads to large computational and memory requirements. As the problem size increases, the equation solver requirements grow very rapidly. The maximum size of an implicit analysis that can be solved on a given machine often is dictated by the amount of disk space and memory available on the machine.

ABAQUS/Standard must iterate to determine the solution to a nonlinear problem In contrast, ABAQUS/Explicit determines the solution without iterating by *explicitly* advancing the kinematic state from the previous increment. A static analysis may typically require a large number of time increments using the explicit method. However, the analysis can be more efficient in Explicit if the same analysis in ABAQUS/Standard would require many expensive iterations. ABAQUS/Explicit requires much less disk space and memory than ABAQUS/Standard for the same simulation.

Using the explicit method, the computational cost is proportional to the number of elements and roughly inversely proportional to the smallest element dimension. Mesh refinement, therefore, increases the computational cost by increasing the number of elements and reducing the smallest element dimension.

There are certain static or nearly static problems that can be simulated well with either solver. Typically, these problems would be solved with ABAQUS/Standard. But since they may have difficulty converging because of contact or material complexities, Explicit might be a feasible option.

Quasi-static analysis considerations

Obtaining solution of quasi-static problems with Explicit requires some special considerations. A static solution is, by definition, a long-time solution. It is often computationally impractical to analyze the simulation in its natural time scale since it would require a large number of small increments. To obtain an economical solution, the event must be accelerated in some way. As the event is accelerated, the state of static equilibrium evolves into a state of dynamic equilibrium in which inertial forces become more dominant. The process must be modeled in the shortest time period in which inertial forces are negligible.

Performing an analysis in the natural time for a quasi-static process will probably produce accurate static results. The user can increase the loading rate so that the same physical event occurs in less time as long as the solution remains nearly the same as the true static solution and dynamic effects remain insignificant.

Applied loading in a quasi-static analysis should be as smooth as possible to obtain an accurate solution. Stress waves can be caused by sudden, jerky movements leading to “noise”. Negligible acceleration variations between increments, ensures smooth loading. If the acceleration is smooth, it follows that the changes in velocity and displacement are also smooth. ABAQUS has a simple, built-in type of amplitude called **SMOOTH STEP** that automatically creates smooth loading amplitude. The user defines time-amplitude data pairs using ***AMPLITUDE, DEFINITION=SMOOTH STEP**. ABAQUS/Explicit then automatically connects each of the provided data pairs with

curves. The first and second derivatives of the curves are smooth and slopes are zero at each of the provided data points. The user can thus apply a displacement loading with **SMOOTH STEP** using only the initial and final data points. The intervening motion will be smooth. A quasi-static analysis can then be performed without generating waves due to discontinuity in the rate of applied loading.

In a static analysis the lowest mode of the structure usually dominates the response. Using the period of the lowest mode the user can estimate the time required to obtain the proper static response. Typically, the user should increase the loading time to 10 times the period of the lowest mode to be certain that the solution is truly quasi-static.

Artificially increasing the speed of forming events is necessary to obtain an economical solution. The suggested approach to determining an acceptable velocity involves running a series of analyses at various speeds. The user should perform the analyses in the order of fastest to slowest since the solution time is inversely proportional to the velocity. Then the user should examine the results of each analysis, specifically the deformed shapes, stresses, and strains vary with speed. At some point the solutions should converge to steady-state. This is an indication that as inertial effects become less significant, differences in simulation results also become less significant.

Springback is often an important part of a forming analysis because the springback analysis determines the shape of the final, unloaded part. Forming simulations can be simulated well with Explicit. However, springback poses some difficulties. The main problem with performing springback simulations within ABAQUS/Explicit is the amount of time required to obtain a steady-state solution. Typically, the loads must be removed very carefully, and damping must be introduced to make the solution time reasonable.

Springback typically involves no contact and usually includes only mild nonlinearities. Hence, ABAQUS/Standard can be used to solve springback problems much faster than ABAQUS/Explicit can. The approach is to solve forming analysis in Explicit and to import the completed forming model from ABAQUS/Explicit into ABAQUS/Standard.

Mass Scaling

Mass scaling enables an analysis to be performed economically without artificially increasing the loading rate. For simulations involving a rate-dependent material or rate-dependent damping, such as dashpots the solution can be obtained economically only with mass scaling. Increasing the loading rate is not an option in such cases. This is because material strain rates increase by the same factor as the loading rate. As the properties of the model change with the strain rate, artificially increasing the loading rate artificially changes the process.

Ensuring quasi-static analysis results

The most standard means of evaluating whether or not a simulation is producing an appropriate quasi-static response involves studying the various model energies. The following is the energy balance equation in ABAQUS/Explicit:

$$E_I + E_V + E_{KE} + E_{FD} - E_W = E_{total} = \text{constant} \quad [3.4]$$

where E_I is the internal energy (both elastic and plastic strain energy), E_V is the energy absorbed by viscous dissipation, E_{KE} is the kinetic energy, E_{FD} is the energy

absorbed by frictional dissipation, E_W is the work of external forces, and E_{TOTAL} is the total energy in the system.

In a quasi-static analysis, the work applied by the external forces is nearly equal to the internal energy of the system. The viscously dissipated energy is generally small unless viscoelastic materials, discrete dashpots, or material damping are used. Inertial forces are negligible in a quasi-static analysis because the velocity of the material in the model is very small. These conditions imply that the kinetic energy in the analysis should be very small. The kinetic energy of the deforming material should not exceed a small fraction (typically 5% to 10%) of its internal energy throughout most of the process.

A global energy balance is reported by ABAQUS at the end of the analysis. This includes the kinetic energy of any rigid bodies with mass. The deformable bodies are of interest when evaluating the results. Hence, the kinetic energy of the rigid bodies should be subtracted from E_{TOTAL} when evaluating the energy balance.

Contact Formulation

Contact constraints are imposed by the penalty method in Explicit for general contact. This method searches for node-into-face and edge-into-edge penetrations in the current configuration. An automatic value of the penalty stiffness is chosen automatically by ABAQUS/Explicit. This is to ensure that the effect on the time increment is minimal yet the penetration is not significant. The user can override this penalty stiffness by specifying a penalty scale factor or a “softened” contact relationship. A kinematic contact formulation is imposed for the contact pair algorithm. This achieves precise compliance with the contact conditions using a predictor/corrector method. The increment at first proceeds under the assumption that contact does not occur. At the end of the increment if ABAQUS detects an overclosure, the acceleration is modified to obtain a corrected configuration. In this configuration, the contact constraints are then enforced. The normal

penalty contact method can also be enforced for contact pairs. This can model some types of contact that the kinematic method cannot. When the penalty contact formulation is used, equal and opposite contact forces with magnitudes equal to the penalty stiffness times the penetration distance are applied to the master and slave nodes at the penetration points.

In the pure master-slave approach one of the surfaces is the master surface and the other is the slave surface. As the two bodies come into contact, the penetrations are detected and the contact constraints are applied according to the constraint enforcement method (kinematic or penalty). Regardless, of the method pure master-slave weighting resists only penetrations of slave nodes into master facets. Penetrations of master nodes into the slave surface can go undetected, as shown in Figure C.10. This can be avoided by sufficient mesh refinement of the slave surface.

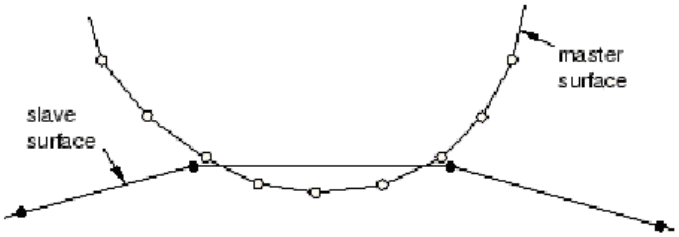

Figure C.10 Penetration of master nodes into slave surface with pure master-slave contact [63]

Balanced master-slave contact (Figure C.11) apporach applies the pure master-slave approach twice. It reverses the surfaces on the second pass. One set of contact constraints is obtained with surface 1 as the slave, and another set of constraints is obtained with surface 2 as the slave. A weighted average of the two computations gives the acceleration corrections or forces.

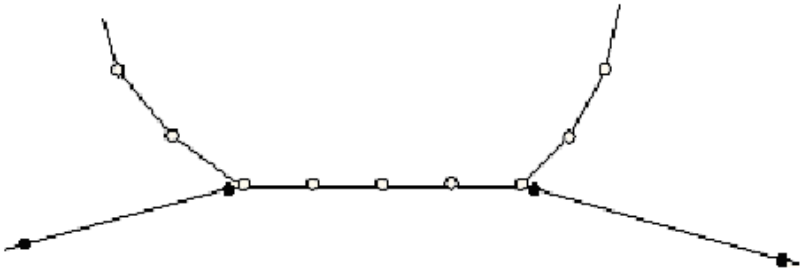

Figure C.11 Balanced master-slave contact constraint with kinematic compliance [63]

This balanced approach minimizes the penetration of the contacting bodies resulting in greater solution accuracy. The user can specify weight of the average for balanced master-slave contact with the contact pair algorithm using the **WEIGHT** parameter on the ***CONTACT PAIR** option. The default weight is 0.5. This results in the same weight being used for each of the acceleration corrections. Setting WEIGHT to 1.0 specifies a pure master-slave relationship with the first surface as the master surface. Conversely, a weight of zero means that the second surface is the master surface.

The balanced master-slave approach does not require high mesh refinement on the slave surface. Mesh refinement is generally most important with pure master-slave contact between deformable and rigid bodies. Figure C.12 shows an example of the penetration that can occur if the slave surface is meshed poorly in comparison to the dimensions of the features on the master surface.

Figure C.12 Example of inadequate slave surface discretization [63]

Any initial overclosures will be removed by ABAQUS/Explicit by adjusting the undeformed coordinates of nodes on contact surfaces. The balanced master-slave approach adjusts both surfaces while the pure master-slave approach adjusts only the slave surface. No initial strain or stress is caused by displacements associated with these adjustments. In case of conflicting constraints, initial overclosures may not completely resolved by repositioning nodes. Severe mesh distortions can result near the beginning of an analysis when the contact pair algorithm is used.

In subsequent steps any nodal adjustments to remove initial overclosures cause strains that can cause severe mesh distortions because the entire nodal adjustments occur in a single, very brief increment leading to large values of accelaration. Such a large acceleration applied to a single node typically will cause ABAQUS to give warnings about deformation speed exceeding the wave speed of the material and warnings about severe mesh distortions. It is very important that in Step 2 and beyond any new contact surfaces that the user defines are not overclosed.

A common case of initial overlcosure of two surfaces is shown in Figure C.13. All of the nodes on the contact surfaces lie exactly on the same arc of a circle. The mesh of the inner surface is finer than that of the outer surface. Also, the element edges are linear. Both these reasons cause some nodes on the finer, inner surface to initially penetrate the outer surface.

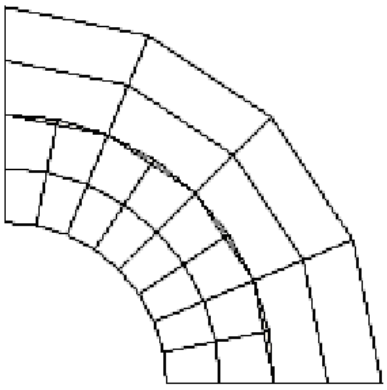

Figure C.13 Original overclosure of two contact surfaces [63]

Figure C.14 shows the initial, strain-free displacements applied to the slave-surface nodes by ABAQUS/Explicit for pure master-slave approach. This geometry is stress free. The default balanced master-slave approach causes a different initial set of displacements resulting in a mesh that is not entirely stress free.

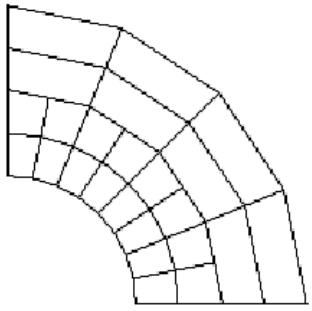

Figure C.14 Corrected contact surfaces [63]

Special analysis techniques

The following sections describe in brief two common and important analysis techniques available in ABAQUS.

Transferring results between implicit and explicit

ABAQUS provides the capability to import a deformed mesh and its associated material state from ABAQUS/Standard into ABAQUS/Explicit and vice versa. New model information can be specified during the import analysis. For analysis with several analysis stages this capability proves to be extremely useful for problems. Contact definitions specified in the original analysis and the contact state are not imported. Contact can be defined again in the import analysis by specifying the surfaces and contact pairs. The user cannot use the exact contact definitions that were used in the original analysis. This is due to the differences in the contact capabilities between ABAQUS/Standard and ABAQUS/Explicit. When the first step in the ABAQUS/Standard import analysis is a ***STATIC** procedure the imported stresses are defined at the start of the analysis as the initial stresses in the material. Then an additional set of artificial stresses is defined at each material point. These stresses are equal in magnitude to the imported stresses but are of opposite sign. The sum of the material point stresses and these artificial stresses creates zero internal forces at the beginning of the step. The internal artificial stresses are ramped off linearly in time during the first step. Thus, at the end of the step the artificial stresses have been removed completely and the remaining stresses in the material will be the residual stress state associated with static equilibrium. Once static equilibrium has been obtained, subsequent steps can be defined using any analysis procedure.

Specifying initial conditions

Initial conditions are specified for particular nodes or elements, as appropriate. The user can provide the required data on the data lines of the ***INITIAL CONDITIONS** option, in an external input file, by a user subroutine or by the results file of a previous ABAQUS analysis. When initial stresses are given the initial stress state may not be an

exact equilibrium state for the finite element model. Therefore, the user should include an initial step to allow ABAQUS to check for equilibrium and iterate, if necessary, to achieve equilibrium. It might happen that the equilibrating step does not converge. This indicates that the initial stress state is far from equilibrium with the applied loads and that significantly large deformations could be generated. In such cases, the user should recheck the specified initial stresses and loads.

Overcoming convergence problems

The following section describes in brief some techniques that can be applied to large-deformation contact simulations exhibiting convergence problems:

1. Analysis completed but gross penetration of surfaces:

When a coarsely discretized surface is used as a slave surface, the master surface nodes can grossly penetrate the slave surface. To define contact accurately, use a refined mesh to create the slave surface.

2. Contact oscillating in severe discontinuity iterations:

Use ***CONTACT DAMPING** to activate viscous damping between contact surfaces. ABAQUS/Standard activates viscous damping in the contact direction at all slave nodes. This viscous damping acts across the clearances of all slave nodes of the contact pair, using a damping coefficient calculated automatically in such a way that a smooth motion should be obtained. In rough terms, initial contact should be obtained in the first part of the step, and in the second part of the step damping is reduced continuously to zero while contact continues to be established. As a result, at the end of the step all viscous forces introduced by this option are removed.

3.Analysis aborts because of initial overclosures

Whenever a node involved in contact is penetrating its master surface, ABAQUS tries to resolve the overclosure in a single increment. If the overclosure occurs during the simulation and is so severe that a converged solution cannot be obtained, ABAQUS will cut back on the increment size in an attempt to reduce the magnitude of the overclosure. However, if the overclosure is present at the start of the analysis, cutting back the increment size will not solve the problem. In this case use the ***CONTACT INTERFERENCE** option to allow ABAQUS to resolve the excessive overclosure gradually during the first step of the analysis.

4. Avoiding premature cutbacks in difficult analyses

Sometimes it is useful to increase both I_0 (Equilibrium iterations at which check is made whether residuals are increasing) and I_R (Equilibrium iteration at which logarithmic convergence check begins). These two data items can be raised to more appropriate values for severely discontinuous problems by increasing them individually on the ***CONTROLS** option.

5. Improving solution efficiency in a problem that involves a high coefficient of friction

The solution efficiency can sometimes be improved in an analysis that involves a high coefficient of friction by using both ***CONTROLS**, **ANALYSIS=DISCONTINUOUS** and ***STEP**, **UNSYMM=YES**.

6. Severe discontinuity iterations

A “severe discontinuity” in a model's behavior is caused by a change in contact conditions (a gap or interface opening or closing), by friction changing from slipping to sticking. In static analysis a severe discontinuity forces iteration with the contact conditions changed. A limit, I_S, is placed on the number of iterations caused by severe discontinuities in an increment. If more than I_S iterations are required for severe discontinuities, the increment is begun again with a time increment size of D_S times the

abandoned increment size (for automatic time incrementation). If fixed time incrementation was chosen, the analysis terminates with an error message. The values of I_S and D_S are defined on the first and second data lines, respectively, of the ***CONTROLS, PARAMETERS=TIME INCREMENTATION** option.

7. Accuracy of solution versus convergence

The default control parameters defined in ABAQUS are designed to provide reasonably optimal solution of complex problems involving combinations of nonlinearities as well as efficient solution of simpler nonlinear cases. However, the most important consideration in the choice of the control parameters is that any solution accepted as "converged" is a close approximation to the exact solution of the nonlinear equations. The ***CONTROLS, PARAMETERS=FIELD** option allows many control parameters to be reset. If this option is used to define less strict convergence criteria, there is a risk that results may be accepted as converged when they are not sufficiently close to the exact solution of the system. Use caution when resetting solution control parameters. Lack of convergence is often due to modeling issues, which should be resolved before changing the accuracy controls.

8. Excessive element distortion

Use **DISTORTION CONTROL=YES** to activate a constraint that acts to prevent negative element volumes or other excessive distortion for crushable materials. The **DISTORTION CONTROL** parameter is not relevant for linear kinematics and cannot prevent elements from being distorted due to physically unrealistic deformation. This parameter is available only in the Explicit solver.

9. Negative eigenvalues

Negative eigenvalue messages indicate a lack of stability of the model with the tangent stiffness matrix not being positive definite. Typically, these messages mean that a buckling or bifurcation load has been exceeded. In many cases, negative eigenvalues

might be because one part of the assembly is not restrained and rigid body motions exist in the model. The presence of negative eigenvalues does not necessarily mean that the analysis will not converge though it may lead to convergence difficulties.

10. ABAQUS version 6.4-1 versus version 6.4-4

Solving large distortion analyses with hyperelastic materials might be a problem in version 6.4-1. The riveting analysis with sealant (discussed in detail earlier) modeled with a hyperleastic material aborted in version 6.4-1. The exact analysis run in version 6.4-4 was successful.

11. Difficulties in contact convergence

If the model has sharp corners on the contact surfaces: Smooth the surface. Nodes on the slave surface can be caught in folds in the master surface, causing convergence difficulties when the surrounding elements deform to take this into account. The elements making up the slave surface should be small enough to be able to resolve the geometry. A rough guideline is to use 10 elements around a 90° corner. If the physical problem has a sharp concave fold, use two separate surface definitions. Sharp convex folds cannot be modeled with a reasonable finite element mesh. Smooth the fold with a radius larger than the element size on the slave surfaces. A rough guideline is to use 10 elements around a 90-degree corner.

12. ABAQUS version 6.4-4 versus version 6.5

Solving large distortion analyses with hyperelastic materials might be a problem in version 6.5. The riveting analysis with sealant (discussed in detail earlier) modeled with a hyperleastic material aborted in version 6.5. The exact analysis run in version 6.4-4 was successful. A possible explanation is the simultaneous use of balanced master-slave contact with no separation assumed between the contact surfaces for the hyperelastic material might be causing the model to go unstable in 6.5. Successful

completion of the job in 6.4-4 without surface penetration and not considering explicit "noise" might be attributed to bugv63_4767 in version 6.5.

13. Importing models in ABAQUS version 6.4

ABAQUS 6.4 does not allow for importing analysis results between Implicit and Explicit if the model is defined as an assembly of part instances. The user needs to implement the command given below to generate an input file independent of part and assembly options to carry out the import.

Command: m = mdb.models['Model-1'].setValues(noPartsInputFile=ON)

Summary

Capabilities of the ABAQUS finite element code were discussed in context of the present investigations. The discussion began with a review of the element library with particular attention paid to continuum elements. Some criterion for selection of elements between choices of first and second order interpolation, full and reduced integration, tetrahedral and hexahedral elements were discussed. It was pointed out that first-order reduced integration elements are a good choice for problems with contact and plasticity because of their ability to use constant volumetric strain thus avoiding volumetric locking.

It was also noted that replacement of deformable bodies with rigid bodies to simulate tooling in forming problems reduces computational resources significantly.

Following the discussion of element selection material constitutive behaviors were discussed with specific attention paid to rate-independent plasticity problems. In ABAQUS standard Mises or Hill yield surfaces are used to model class metal plasticity with the Miser yield surface used to define isotropic hardening. It was worthy to observe that the user must provide *true stress* and *true strain* data while defining plasticity in ABAQUS.

Following material models, sources of non-linearity in generic problems were pointed out. The working of the commonly implemented Newton-Raphson algorithm for solving non-linear problems was discussed. Special attention was given to modeling contact non-linearities in the code. It was noted that surface-to-surface contact elements have become the defacto standard for complex contact problems due to their superior performance in addressing such simulations. These elements can be included in the model using the master-slave approach available in ABAQUS.

After addressing contact modeling issues attention was given to discussing explicit solvers available in ABAQUS typically used for analyzing impact and difficult metal forming problems. The advantages and disadvantages of both implicit and explicit methods in solving problems were discussed. Finally, some techniques for simulating problems quasi-statically in explicit were also discussed. It was pointed out that comparing the energy response at the end of the analysis is an excellent measure of ensuring a truly quasi-static analysis. It was also noted that there would always be some difference between the stresses reported by implicit and those computed by explicit due to the inherent nature of the two solvers.

The final discussion in this chapter focused on some special analysis techniques available in ABAQUS in context of the investigations carried out herein. These included the ability of ABAQUS to transfer results between implicit and explicit, an advantage in forming problems. Finally, some techniques that could be valuable in overcoming convergence problems in contact simulations were pointed out and discussed.

APPENDIX D: ARCHIVE OF LAP JOINT FAILURES

The following presents a summary of the damage observed in sixteen other tested lap joints. At the minimum, the summary provides a photograph of the faying surface and the fracture surface of the failed holes.

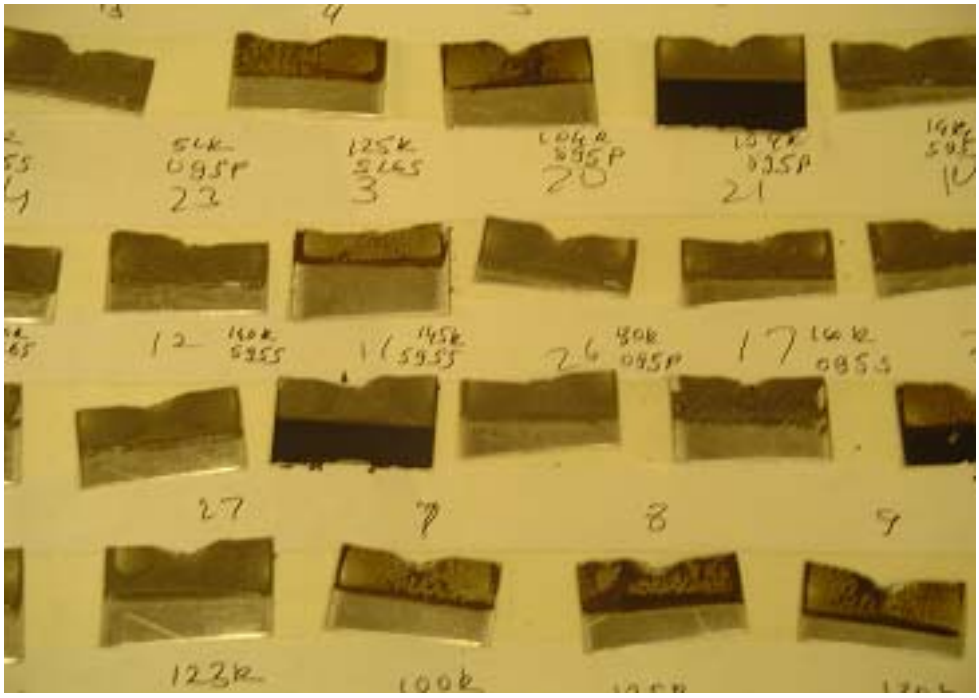

Figure D.1 A view of the coupons cut for damage characterization

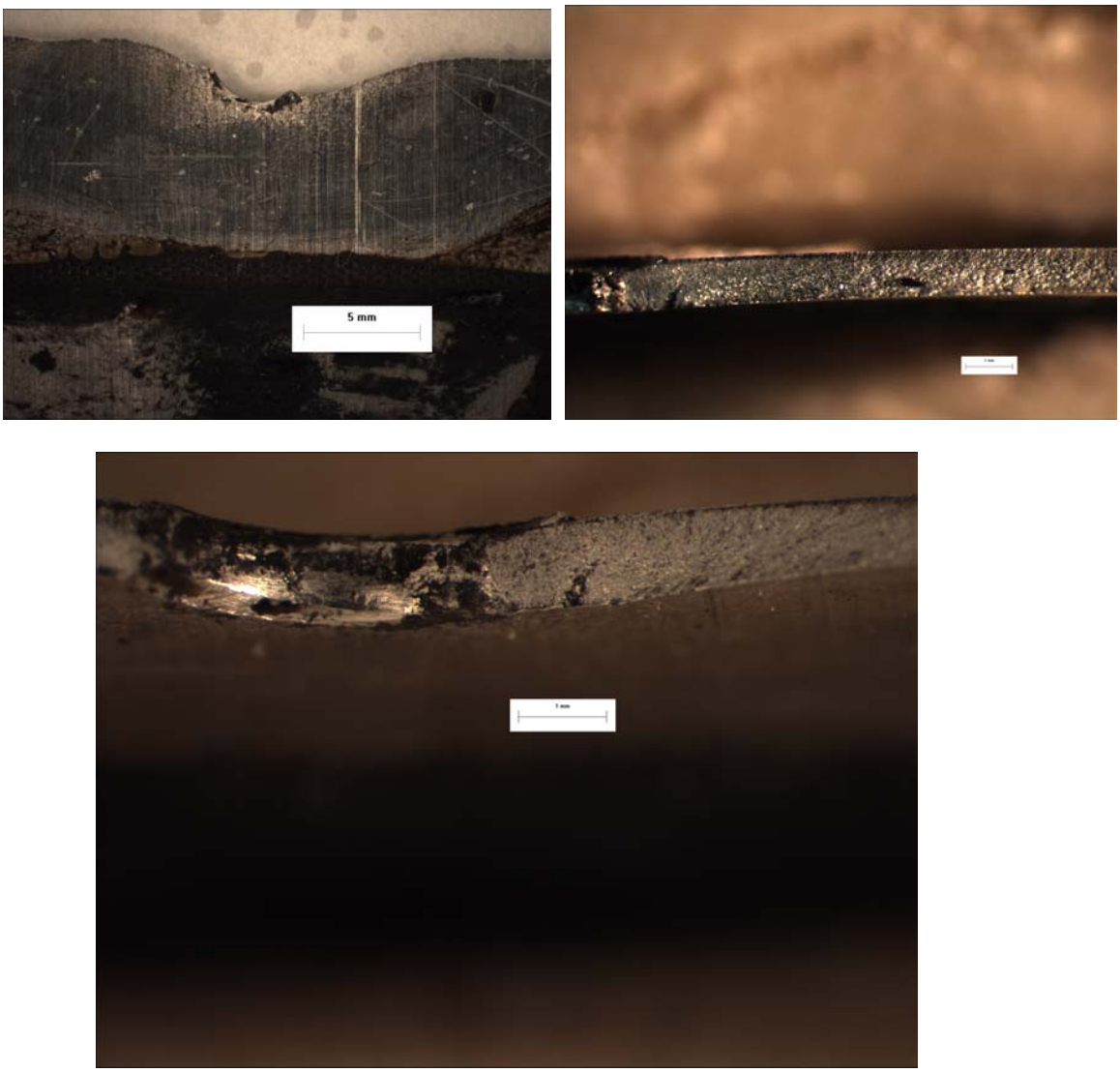

Figure D.2 Damage characterization of specimen 02

Lap Joint 02: B26S

Cycles to failure: 125,000

Macroscopic Observations:

- Some fretting at hole edge on faying surface.
- Faying surface crack origin.
- Circumferential groove observed in hole.

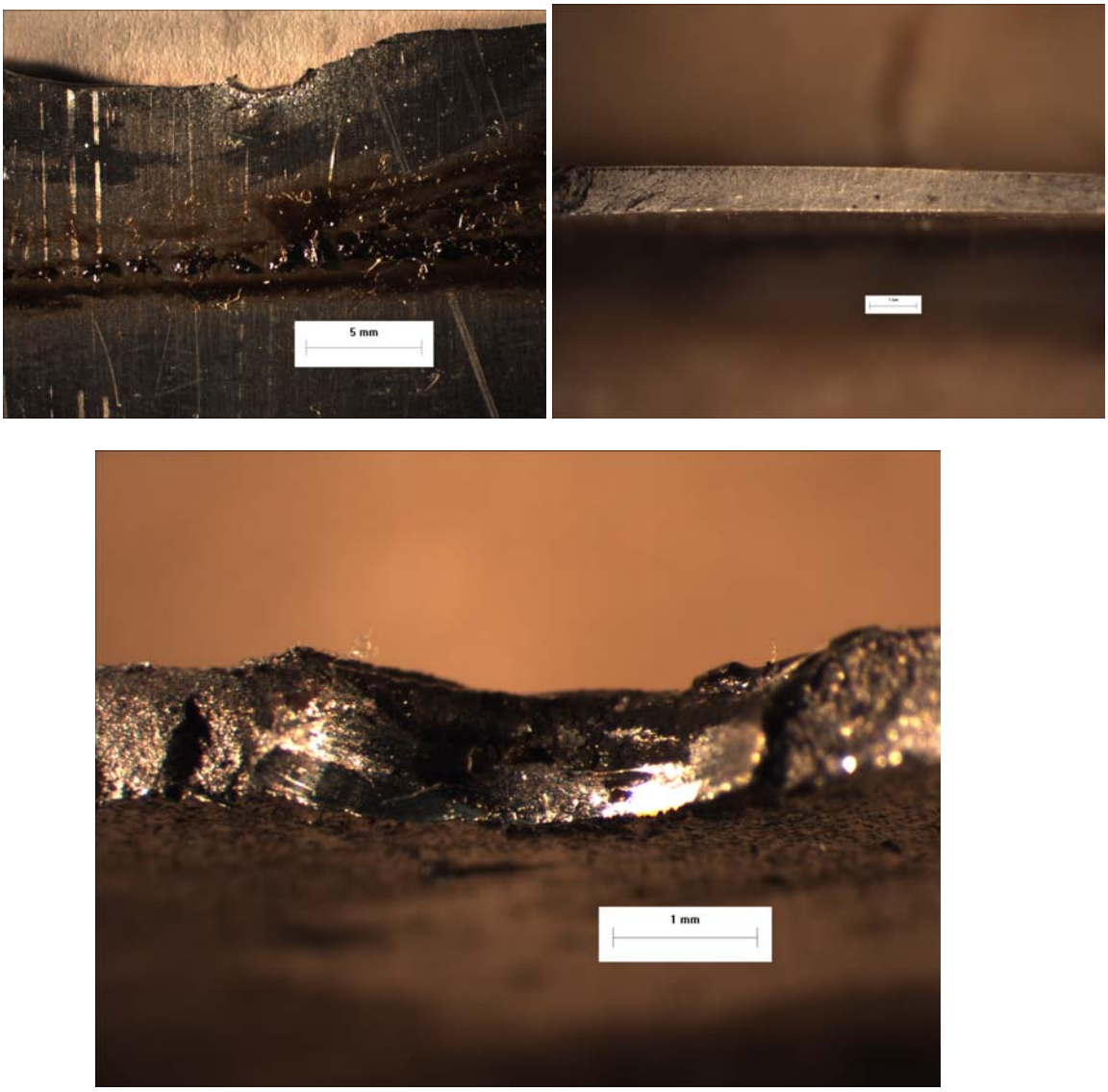

Figure D.3 Damage characterization of specimen 04

Lap Joint 04: U26S

Cycles to failure: 80,000

Macroscopic Observations:

- No significant fretting at hole edge on faying surface.
- Faying surface crack origin, possible hole surface origin.
- Circumferential groove observed in hole.

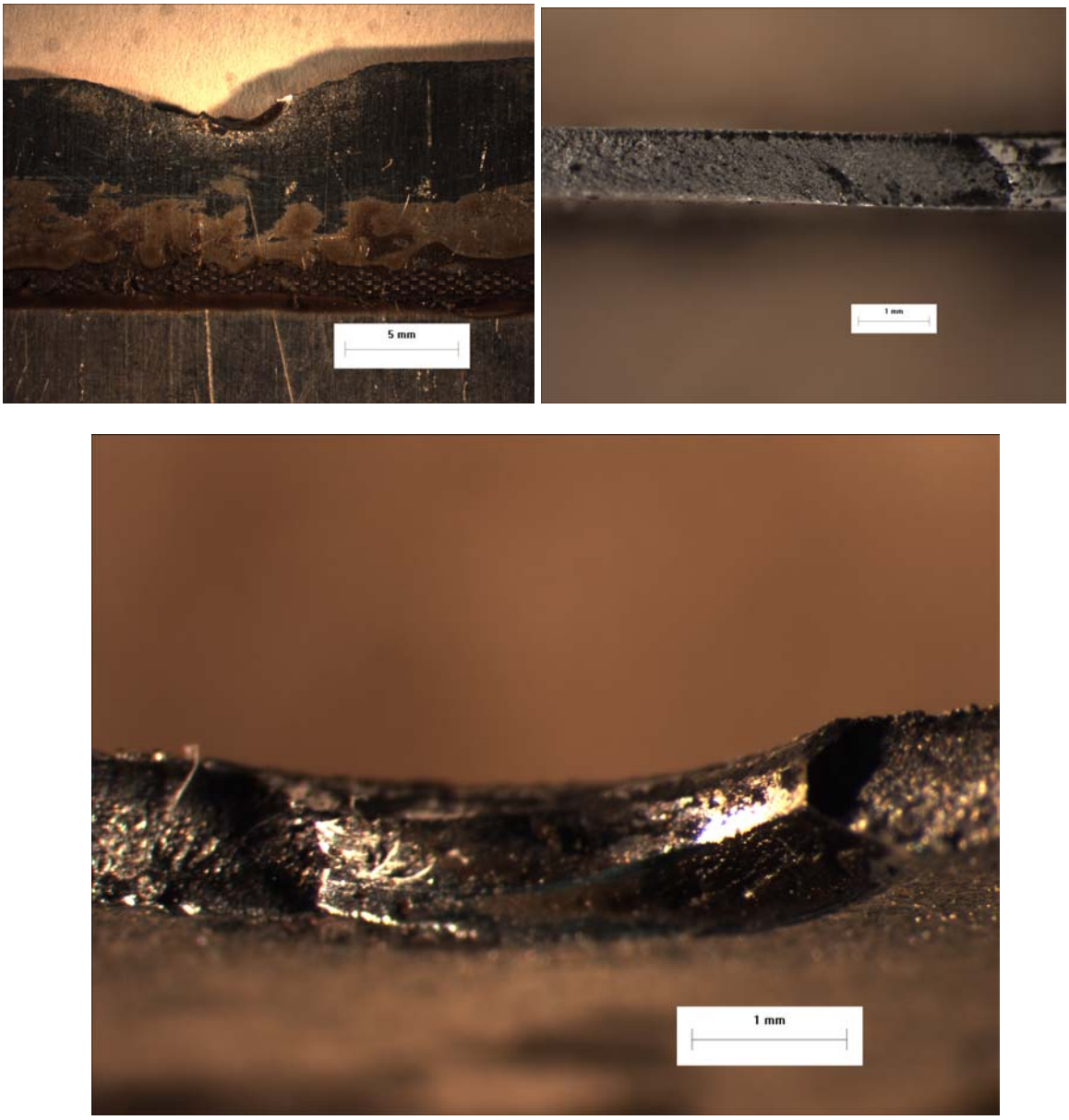

Figure D.4 Damage characterization of specimen 07

Lap Joint 07: O26S

Cycles to failure: 100,000

Macroscopic Observations:

- Some fretting at hole edge on faying surface.
- Faying surface crack origin.
- Circumferential groove observed in hole.

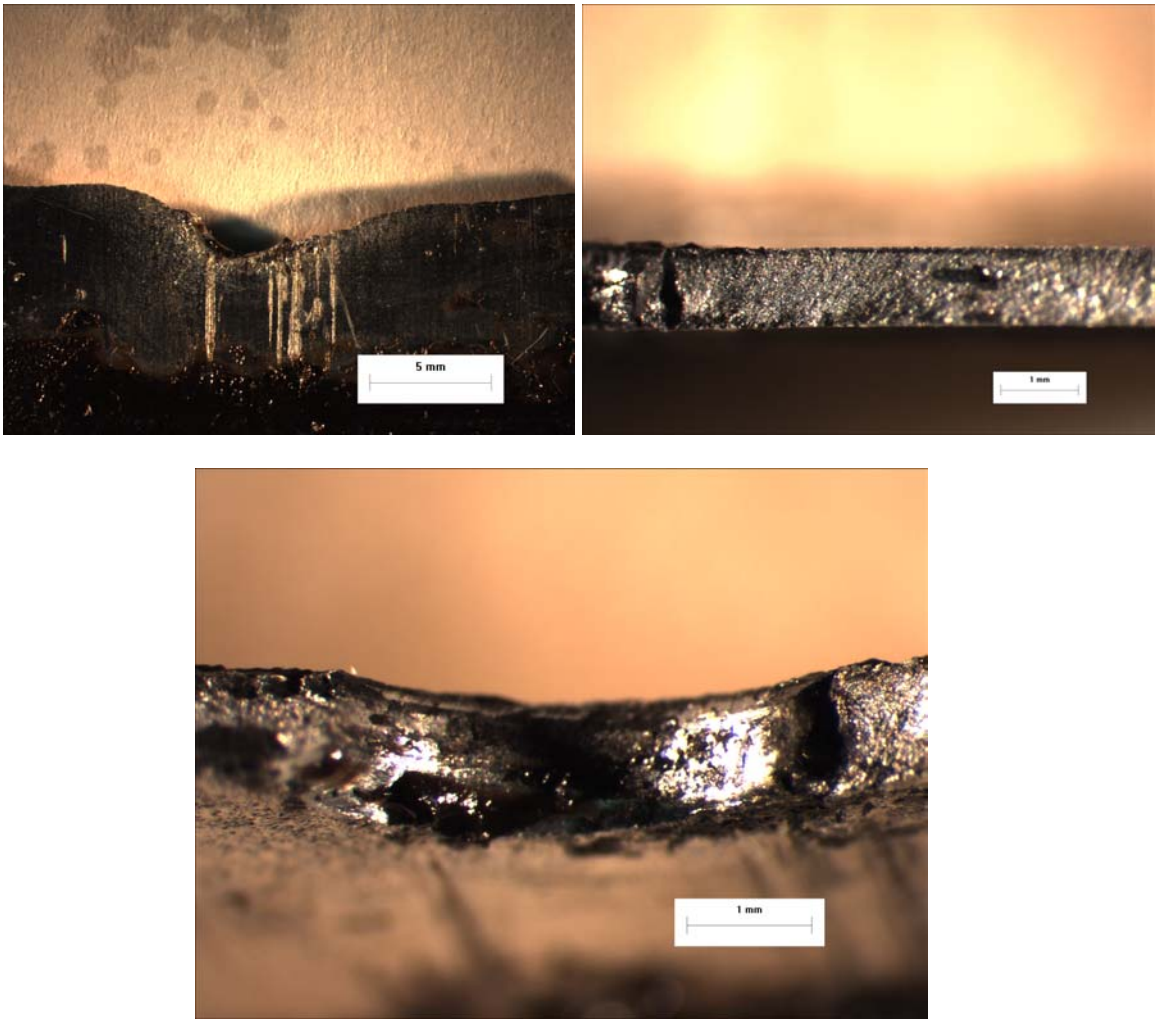

Figure D.5 Damage characterization of specimen 08

Lap Joint 08: O26S

Cycles to failure: 125,000

Macroscopic Observations:

- Some fretting at hole edge on faying surface. Scratches on coupon due to possible damage.
- Faying surface crack origin.
- Circumferential groove observed in hole.

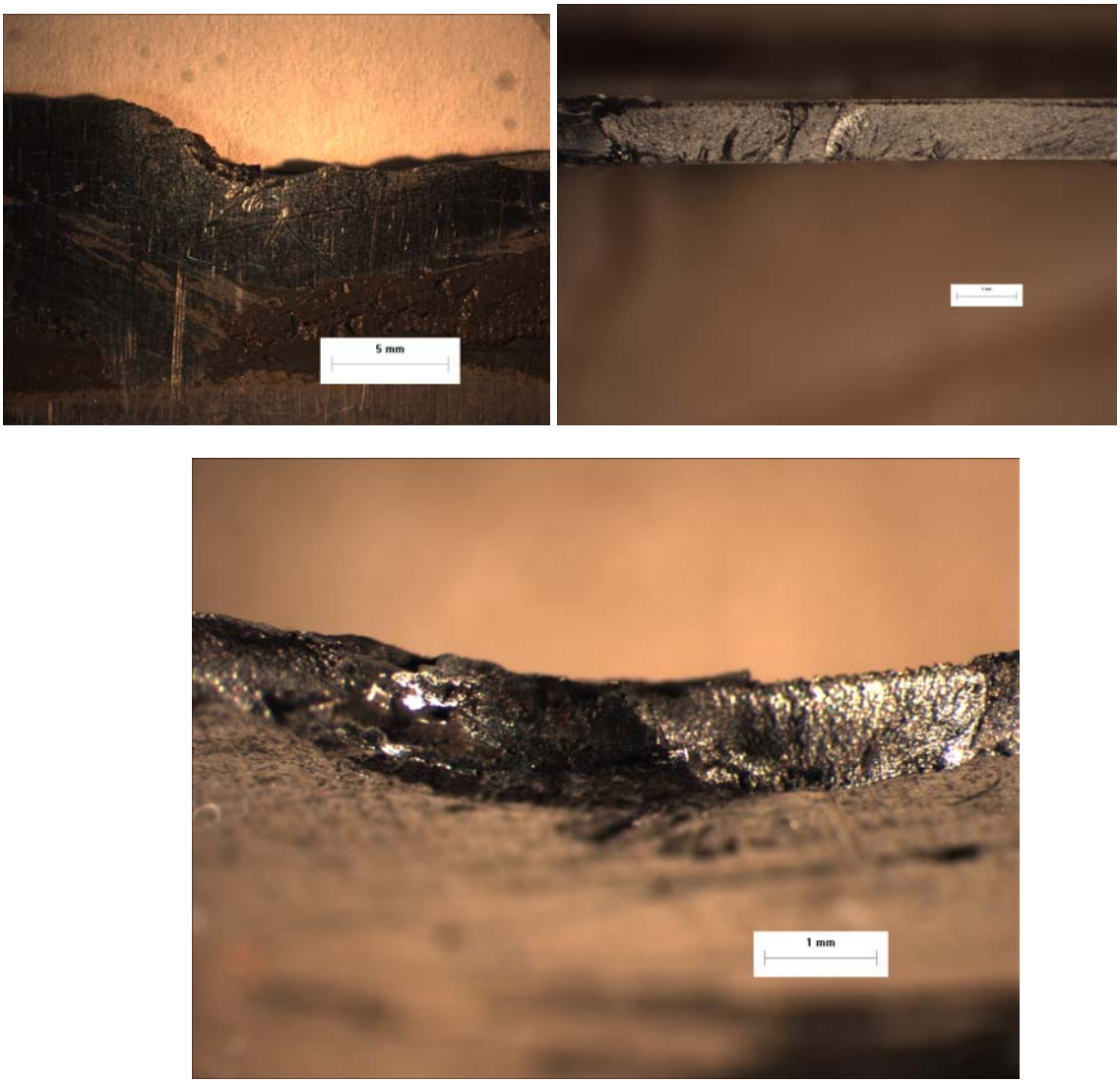

Figure D.6 Damage characterization of specimen 10

Lap Joint 10: B95S

Cycles to failure: 144,000

Macroscopic Observations:

- Some fretting at hole edge on faying surface. Scratches on faying surface due to possible coupon damage.
- Multiple faying surface crack origin, possible hole surface origin.
- No circumferential groove observed in hole.

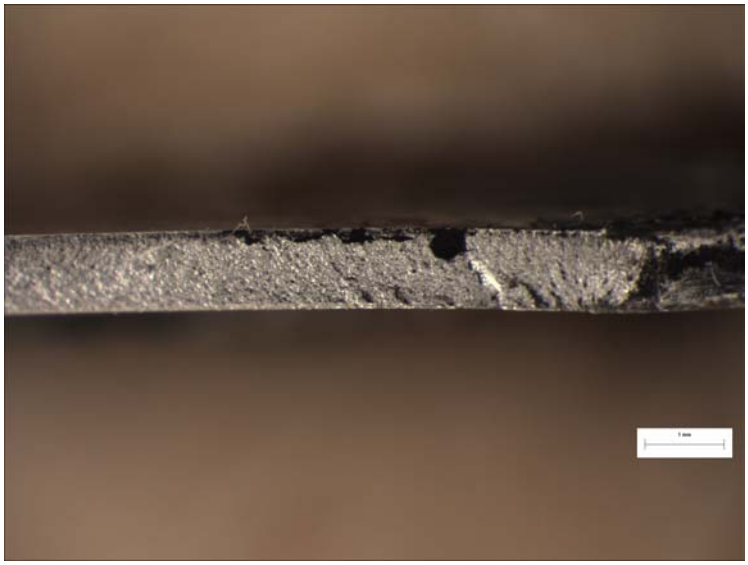

Figure D.7 Damage characterization of specimen 11

Lap Joint 11: B95S

Cycles to failure: 145,000

Macroscopic Observations:

- Some fretting at hole edge on faying surface.
- Faying surface crack origin.
- No circumferential groove observed in hole.

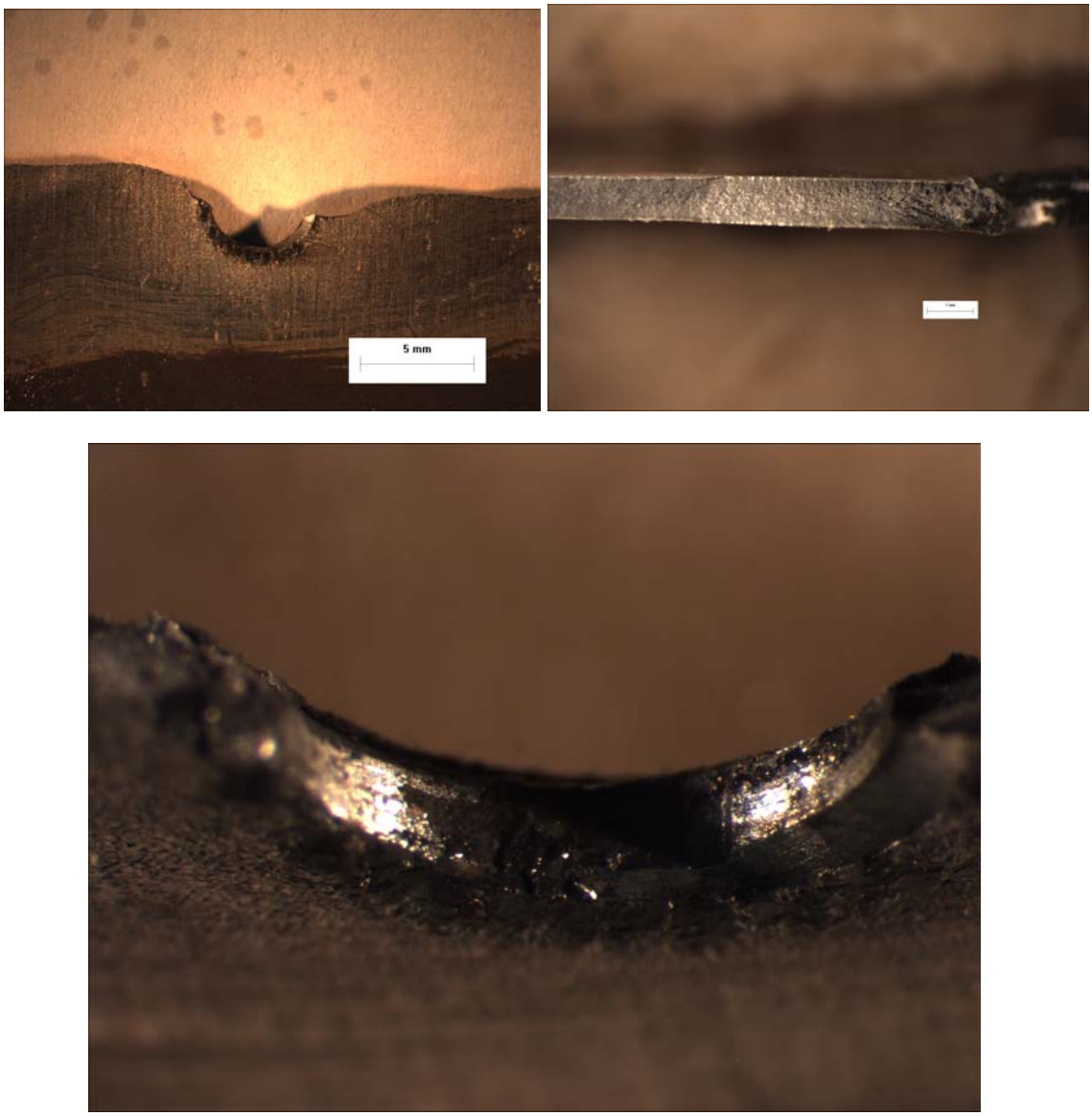

Figure D.8 Damage characterization of specimen 13

Lap Joint 13: U95S

Cycles to failure: 60,000

Macroscopic Observations:

- Some fretting at hole edge on faying surface.
- Faying surface origin and hole surface origin.
- No circumferential groove observed in hole.

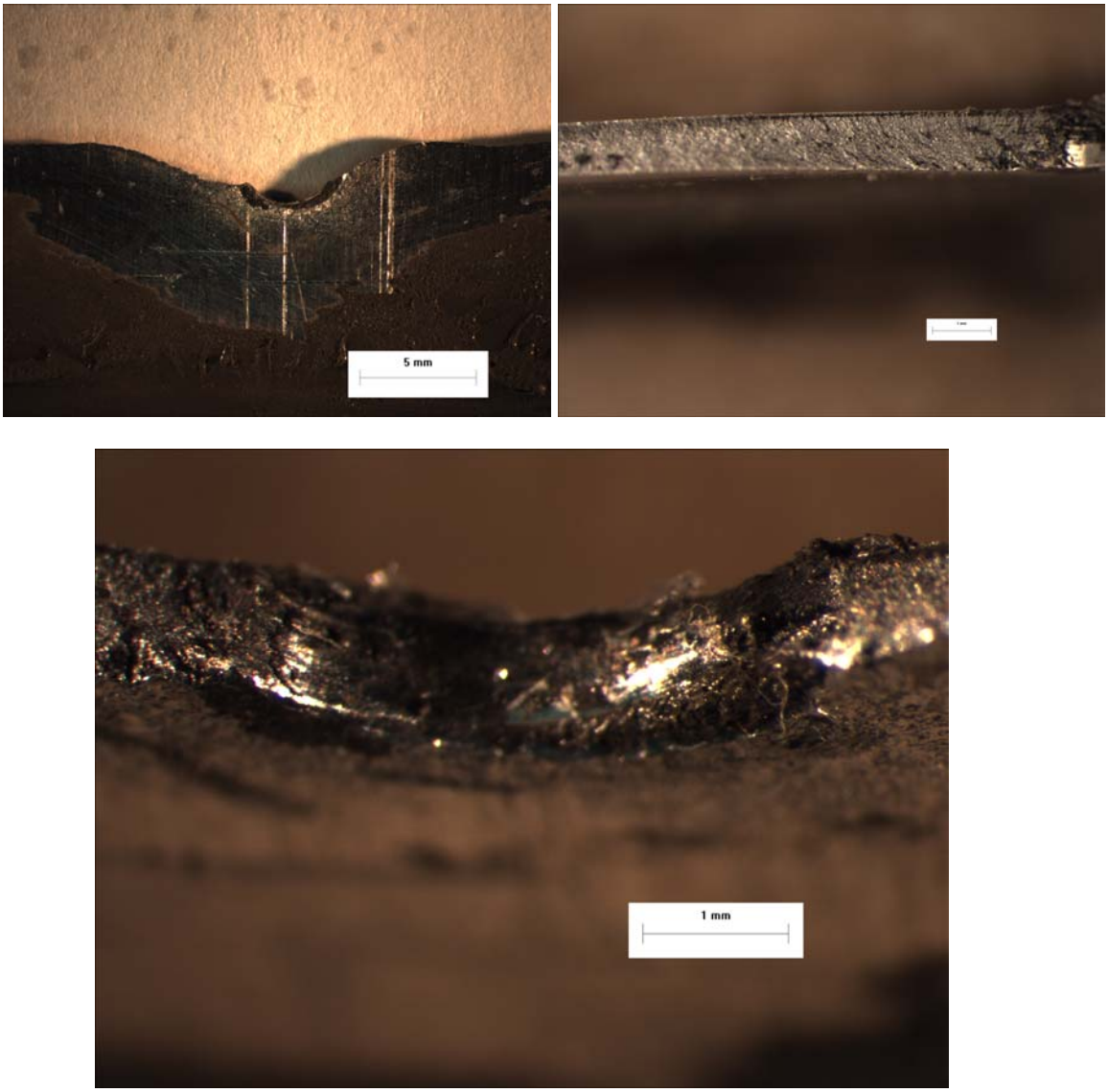

Figure D.9 Damage characterization of specimen 14

Lap Joint 14: U95S

Cycles to failure: 81,000

Macroscopic Observations:

- Some fretting at hole edge on faying surface.
- Faying surface origin and hole surface origin.
- No circumferential groove observed in hole.

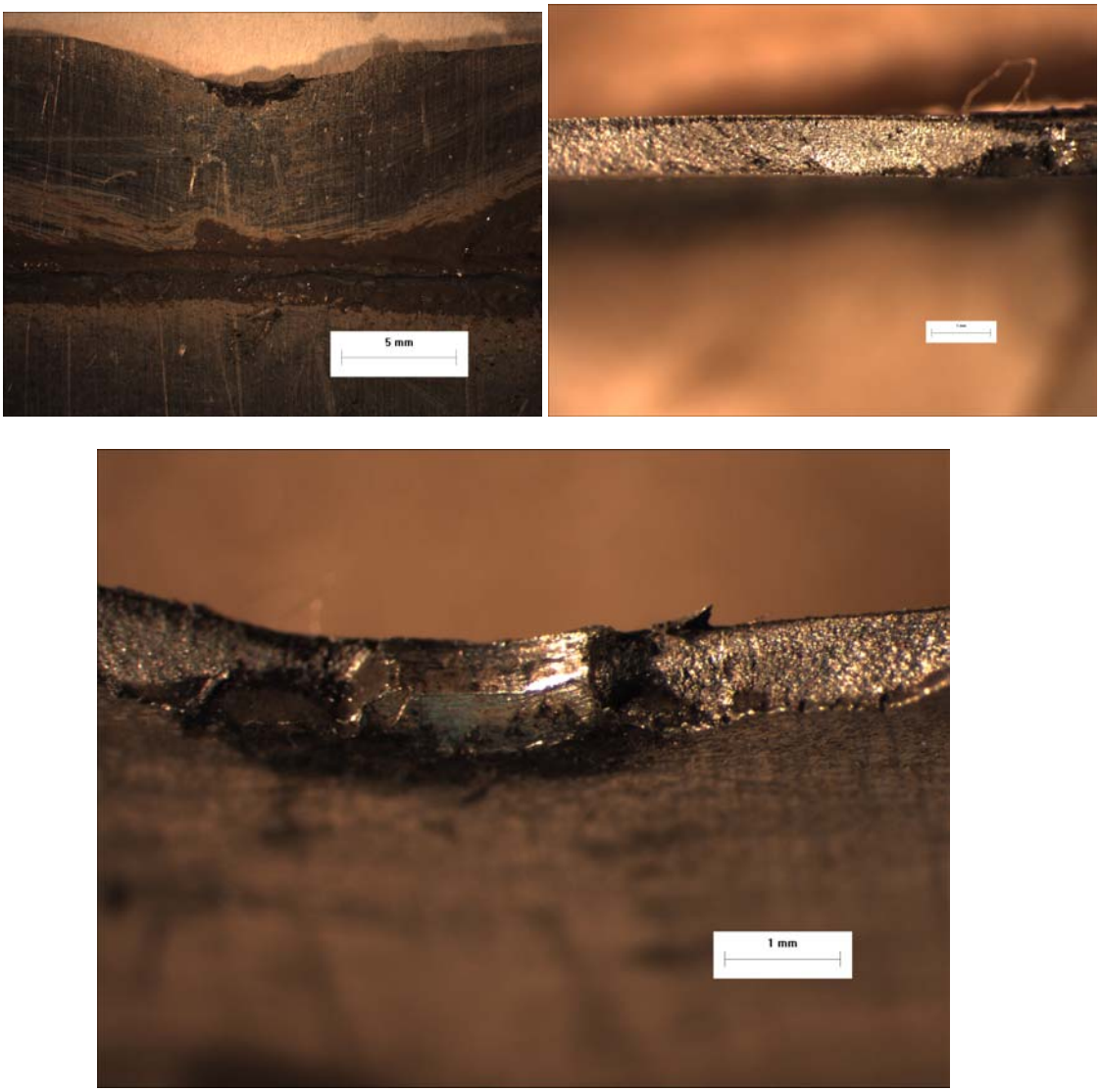

Figure D.10 Damage characterization of specimen 16

Lap Joint 16: O95S

Cycles to failure: 140,000

Macroscopic Observations:

- Some fretting at hole edge on faying surface.
- Faying surface origin.
- Circumferential groove observed in hole.

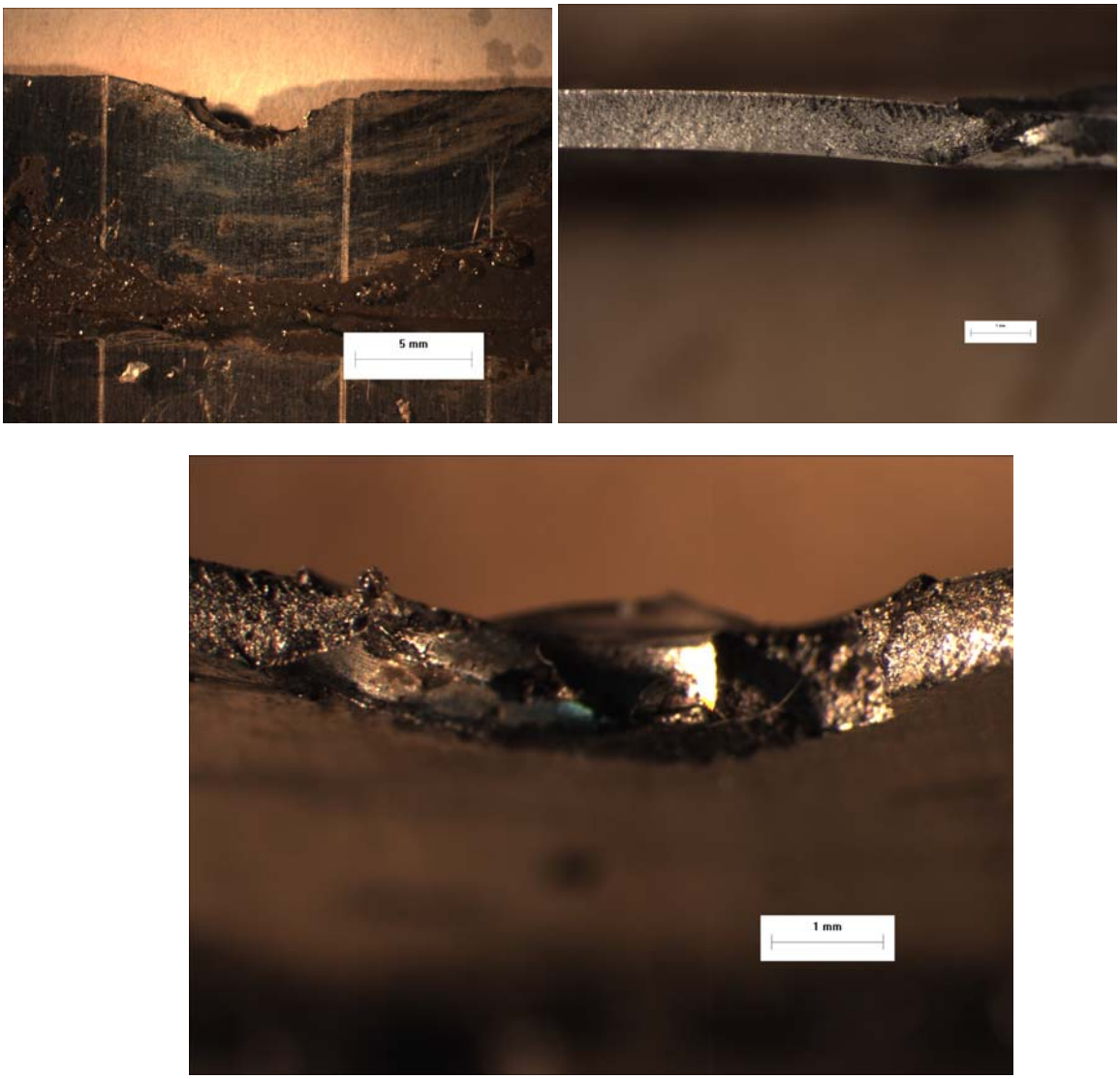

Figure D.11 Damage characterization of specimen 17

Lap Joint 17: O95S

Cycles to failure: 160,000

Macroscopic Observations:

- Some fretting at hole edge on faying surface.
- Exact crack origin difficult to determine. Possible faying surface slightly near hole.
- No circumferential groove observed in hole.

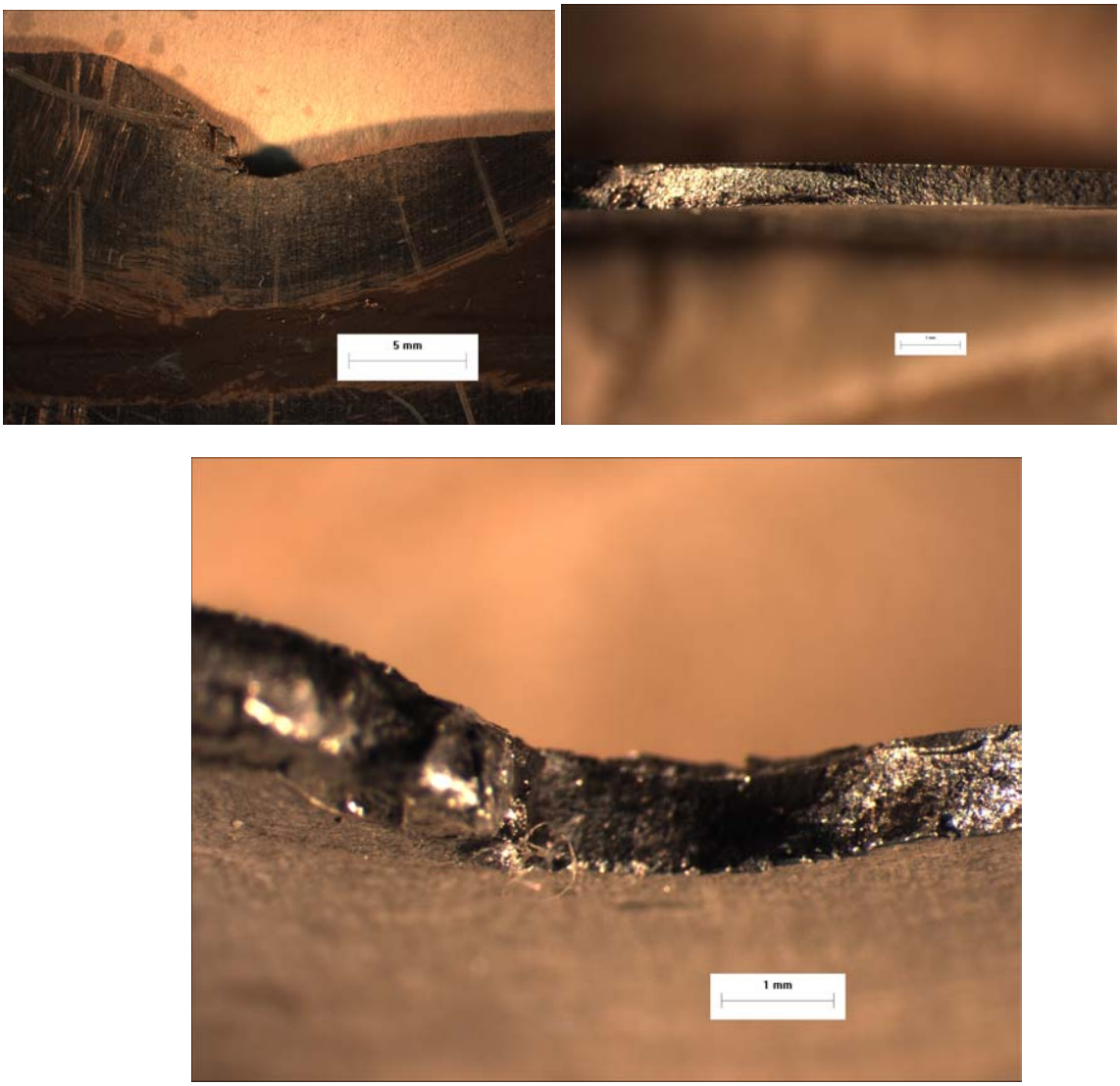

Figure D.12 Damage characterization of specimen 19

Lap Joint 19: S95P

Cycles to failure: 150,000

Macroscopic Observations:

- Some fretting at hole edge on faying surface.
- Faying surface origin and hole surface origin.
- No circumferential groove observed in hole.

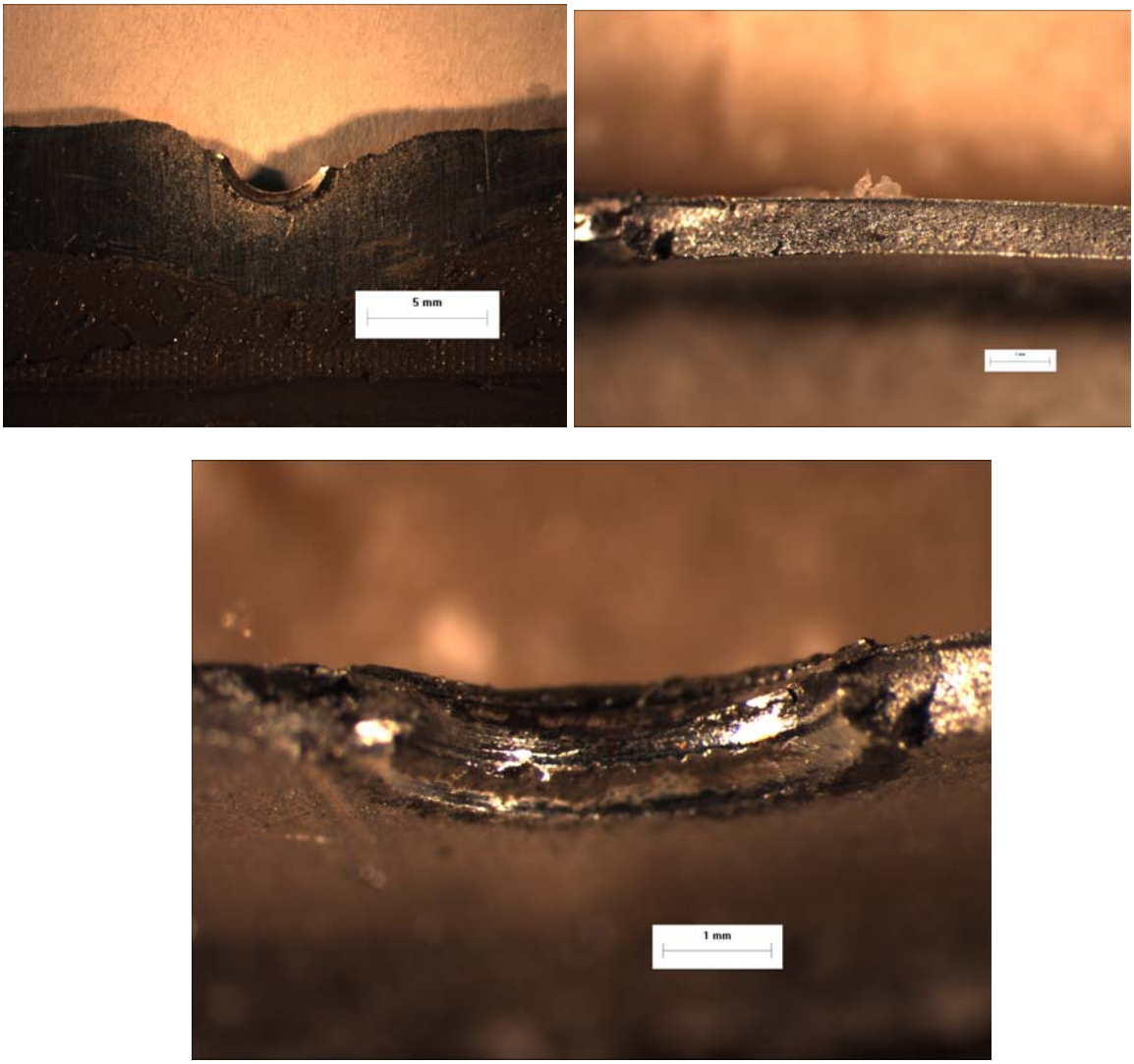

Figure D.13 Damage characterization of specimen 20

Lap Joint 20: S95P

Cycles to failure: 104,000

Macroscopic Observations:

- No significant fretting at hole edge on faying surface.
- Faying surface origin.
- Circumferential groove observed in hole.

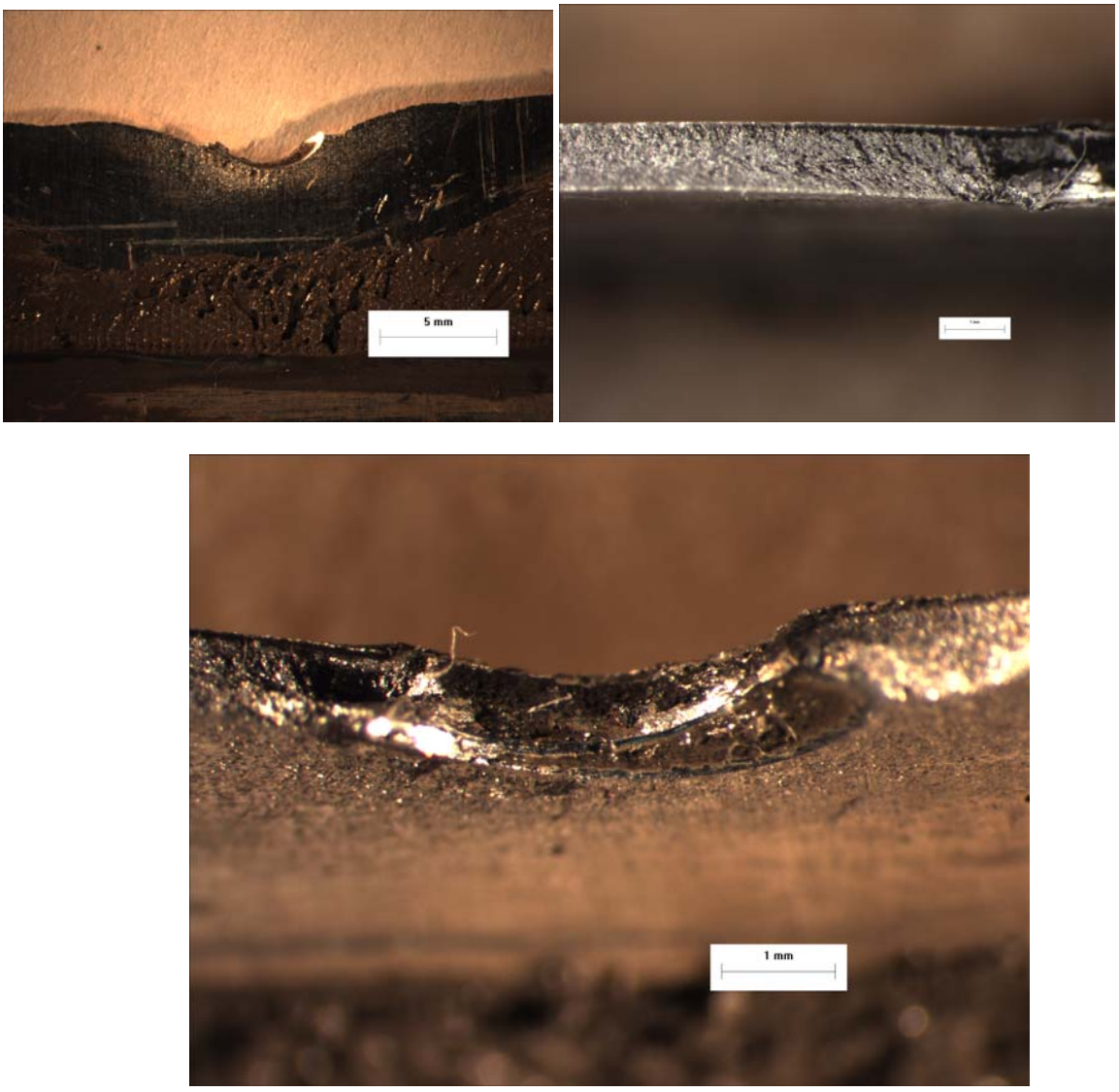

Figure D.14 Damage characterization of specimen 22

Lap Joint 22: U95P

Cycles to failure: 42,000

Macroscopic Observations:

- Some fretting at hole edge on faying surface.
- Hole surface origin.
- Circumferential groove observed in hole.

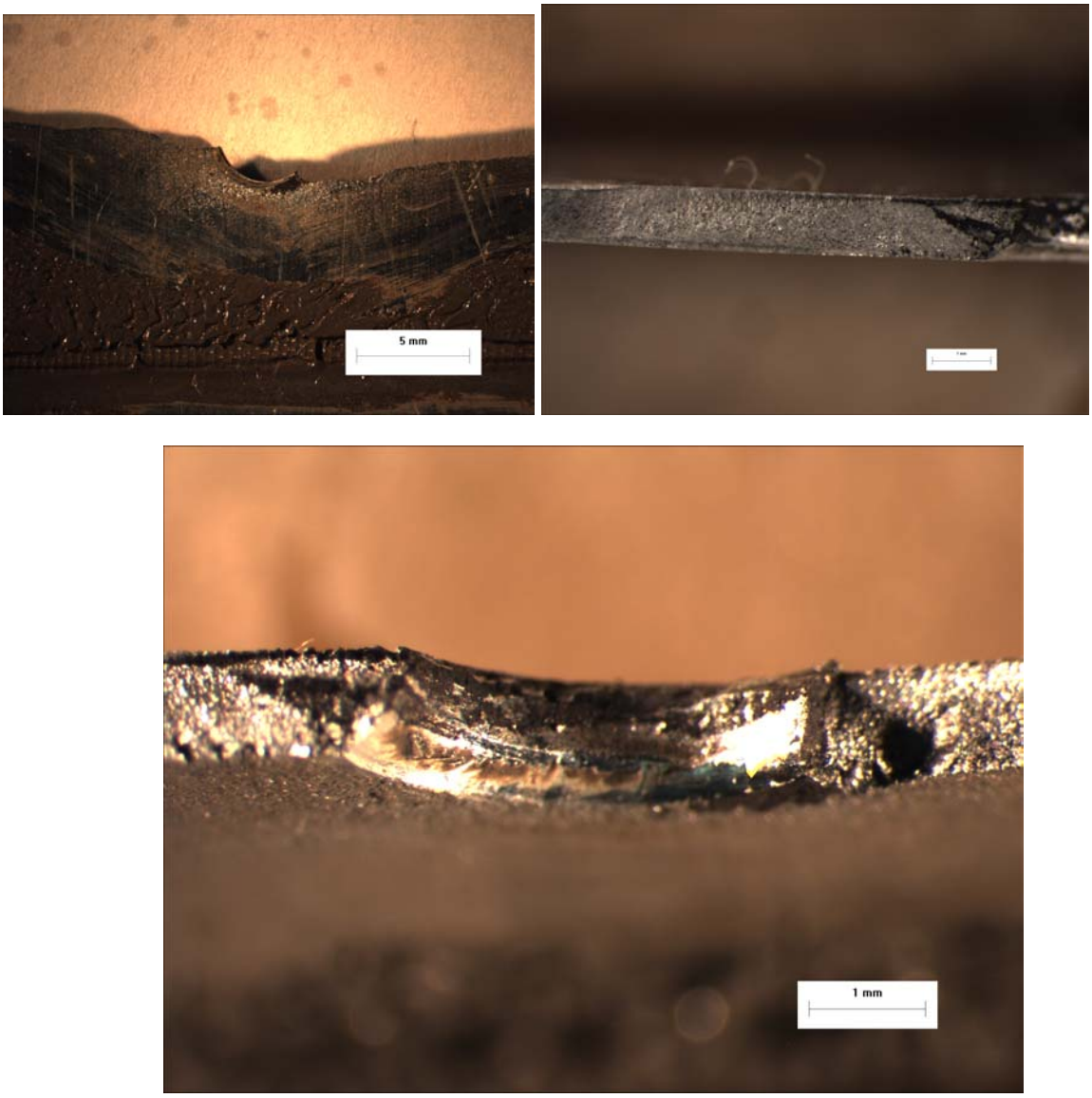

Figure D.15 Damage characterization of specimen 23

Lap Joint 23: U95P

Cycles to failure: 52,000

Macroscopic Observations:

- Some fretting at hole edge on faying surface.
- Hole surface origin.
- Circumferential groove observed in hole.

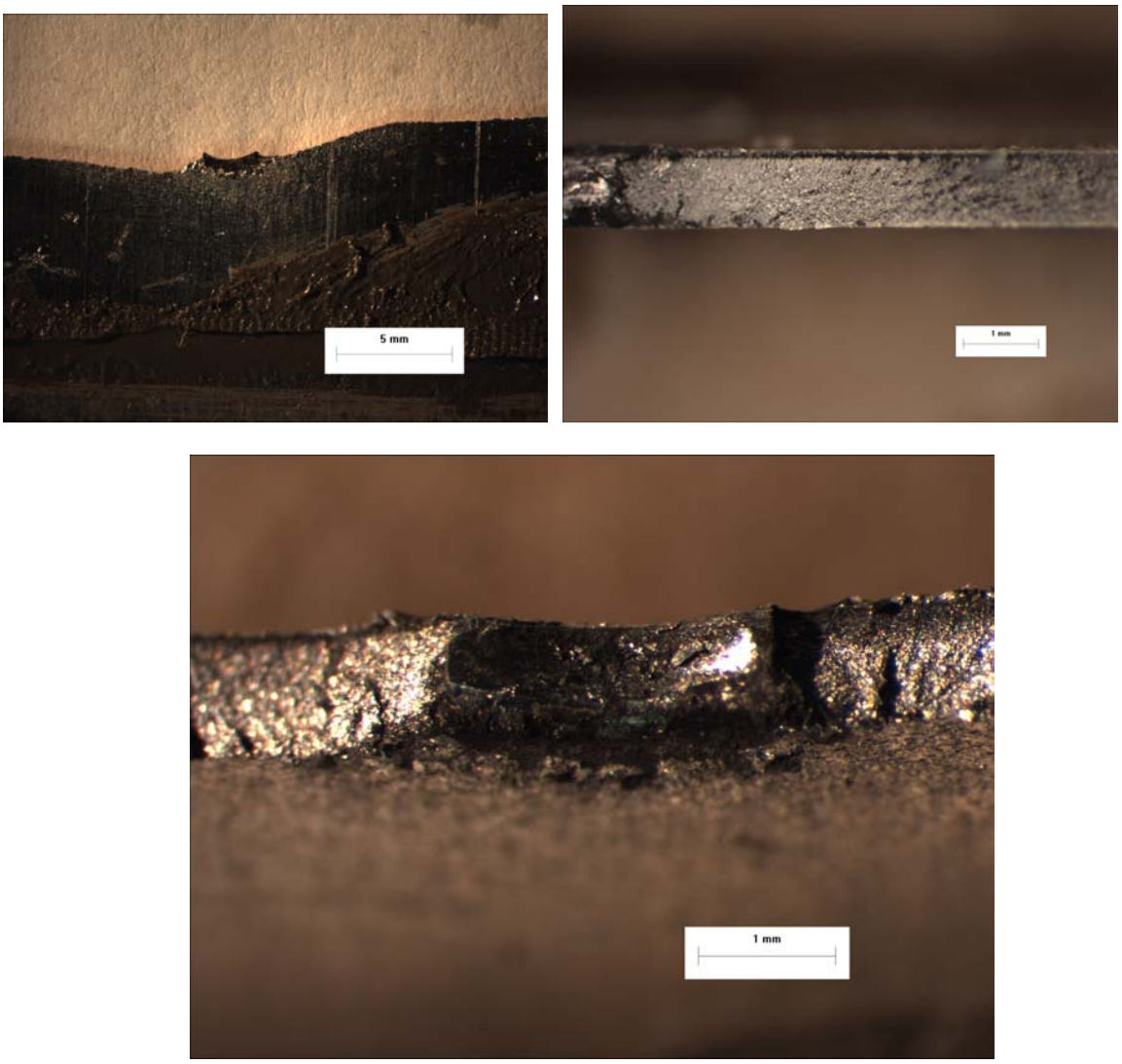

Figure D.16 Damage characterization of specimen 26

Lap Joint 26: O95P

Cycles to failure: 130,000

Macroscopic Observations:

- Some fretting at hole edge on faying surface.
- Faying surface origin.
- Circumferential groove observed in hole.

Figure D.17 Damage characterization of specimen 27

Lap Joint 27: O95P

Cycles to failure: 123,000

Macroscopic Observations:

- No significant fretting at hole edge on faying surface.
- Faying surface origin. Possible hole surface origin.
- Circumferential groove observed in hole

References

1. Airworthiness Assurance Working Group (AAWG) report Recommendations for Regulatory Action to prevent Widespread Fatigue Damage in the Commerical Airplane Fleet, revision A, June 29, 1999, J.McGuire and J. Foucault, Chairpersons.

2. Bakuckas, J.G., Carter, A., 2003, "Destructive Evaluation and Extended Fatigue Testing of Retired Aircraft Fuselage Structure: Project Update", Proceedings of the 7th Joint DoD/FAA/NASA Conference on Aging Aircraft, New Orleans, Louisiana, pp. 1-12.

3. Reithmaeir, L., *Standard Aircraft Handbook*, Tab AERO, Blue Ridge Summit, 5th ed., 1991.

4. Park, J.H., Atluri, S.N., 1993, " Fatigue Growth of Multi-Cracks Near a Row of Fastener-Holes in a Fuselage Lap-Joint", *Computational Mechanics*, 13, pp.189-203.

5. Muller, R.P., 1995, *An Experimental and Analytical Investigation on the Fatigue Behavior of Fuselage Riveted Lap Joints*, PhD Thesis, Delft University of Technology, Delft, The Netherlands.

6. Langrand, B., Deleotombe, E., Markiewicz, E., Drazetic, P., 2001, "Riveted Joint Modeling for Analysis of Airfrarme Crashowrthiness", *Finite Elements in Analysis and Design*, Vol.48, pp.21-44.

7. Fitzgerald, T.J., Cohen, J.B., 1994, "Residual stresses in and around rivets in clad aluminum alloy plates", *Materials Science and Engineering*, A188, pp. 51-58.

8. Nepershin, R.I., Knigin, V.V., 1992, "Interferences and Residual Stresses in Riveted Joints", *Journal of Machinery, Manufacture and Reliability*, No.5, pp.47-51.

9. Yarkovets, A.I., Sirotkin, O.S., Firsov, V.V., Kisilev, N.M., 1987, "Processes for ensuring long life of riveted and bolted joints in aircraft structures", *Mashinostroyeniye*, Moscow.

10. Demina, N.I., Volkov, A.K., 1989, "The Influence of the Interference of a Rivet on the Mechanical Properties of D16 Alloy Sheet in Biaxial Tension", Cambridge Science Abstracts, Aluminum Industry Abstracts, Accession No. 01901145-0483, Vol.21, No.3, March, pp.407-409, ISSN 0039-2316.

11. Ryzhova, T.B., 1994, "Estimation of the reliability of ultrasonic quality control of riveted joints with clearance", *Russian Journal of Nondestructive Testing*, v. 30, pp.418-421.

12. Slater, W.J., 1994, *Static Strength of Riveted Joints in Fiber Metal Laminates*, PhD Thesis, Delft University of Technology, Delft, The Netherlands

13. Szolwinski, M.P., Farris, T.N., 2000, “Linking Riveting Process Parameters to the Fatigue Performance of Riveted Aircraft Structures”, *Journal of Aircraft*, Vol.37, No.1, pp.130-137.

14. Fawaz, S.A., 1997, *Fatigue Crack Growth in Riveted Joints*, PhD Thesis, Delft University of Technology, Delft, The Netherlands

15. Deng, X., Hutchinson, J.W., 1998, “The Clamping Stress in a Cold Driven Rivet”, I*nternational Journal of Mechanical Sciences*, v.40, pp.683-694.

16. Ryan, L., Monaghan, J., 2000, “Failure Mechanism of Riveted Joint in Fibre Metal Laminates”, *Journal of Materials Processing Technology*, v.103, pp.36-43.

17. Swenson, D.V., Chieh-Chien, C., Derber, T., 1992, "Analytical and Experimental Investigation on Fatigue of Lap Joints, Advances in Fatigue Lifetime Predictive Techniques, ASTM STP 1122, pp.449-459.

18. Weissberg, V., Wander, K., Ithzakov, R., 1988, " A New Approach to Load Transfer in Bolted Joints", 16th Congress of the International Council for Aeronautical Sciences, Jerusalem, Israel, Vol. 1, pp.96-101

19. Sundarraj, M. Dattaguru, B., Ramamurthy, T.S., 1995, " Analysis of a Double Shear Lap Joint with a Interference Fit Pin, *Computers and Structures*, Vol. 55, no. 2, pp.357-363.

20. Ekvall, J.C., 1986, "Fatigue of Riveted Metallic Joints", ASTM Special Technical Publication, 927, pp.172-189.

21. Li, G., Shi, G., 2003, “Effect of the Riveting Process on the Residual Stress in Fuselage Lap Joints”, *Canadian Aeronautics and Space Journal*, Vol.50, No.2, pp.91-105..

22. Li, G., Shi, G., Bellinger, N.C., 2005, “Studies of Residual Stress in Single-Row Countersunk Riveted Lap Joints”, 46th AIAA Structures, Structural Dynamics and Materials Conference,18-21 April 2005, Austin, TX, AIAA 2005-2024.

23. Imanaka M., 1995, “Fatigue Strength of Adhesive/Rivet Combined Lap-joints”, *Journal of Adhesion*, Vol. 49, pp. 197-209.

24. Liu J., Sawa T., 1999, “Stress Analysis and Strength Evaluation of Single-Lap Adhesive Joints Combining Rivets Subjected to External Bending Moments”, *Reliability, Stress Analysis, and Failure Prevention Issues in Adhesive and Bolted Connections*, *ASME Proceedings*, Vol. 105.

25. Dechwayukul, C., Rubin, C., Hahn, G., 2003, "Analysis of the Effects of Thin Sealant Layers on Aircraft Structural Joints”, *AIAA Journal*, Vol.41, No. 11, pp. 2216-2228.

26. Fung, C-P and Smart, J., 1994, “An experimental and numerical analysis of riveted single lap joints”, *Proc. Instn. Mech. Engrs. –G- J. of Aerospace Engineering*. v.208, n.2, pp. 79-90.

27. Bellinger, N.C., Krishnakumar, S., and Komorowski, J.P., 1994, “Modeling of pillowing due to corrosion in fuselage lap joints”, *Canadian Aeronautics and Space Journal*, v. 40 (3), pp. 125-130.

28. Shi, G., Bellinger, N. and Xiong, Y., 2000, “Three-dimensional nonlinear finite element modeling and analysis of riveted lap joints with corrosion pillowing”, in *Advances in computational engineering & science*, v.II, ed. by Atluri, Satya N. and Brust, Frederick W., Tech Science Press, pp. 1542-1547.

29. Patronelli, L., Langrand, B., Deletombe, E., Markiewicz, E., Drazétic, P., 2000, “New experimental procedure for analysis of rivet material mechanical properties”, *ONERA, TP, No. 2000-32*.

30. Mindlin, R.D., 1949, “Compliance of Elastic Bodies in Contact”, *Journal of Applied Mechanics*, pp.259-268.

31. Hoeppner, D.A, III, Elliot, C.D., Moesser, M.W., 1996, The Role of Fretting Fatigue on Aircraft Rivet Hole Cracking. FAA Technical Report DOT/FAA/AR-96/10.

32. Szolwinski, M.P., Harish, G., Farris, T.N., 1995, “Experimental Observation of the Effect of Contact Parameters on Fretting Fatigue Crack Nucleation”, Proceedings of the 1995 USAF Structural Integrity Program Conference, San Antonio.

33. Szolwinski, M.P., Farris, T.N., 1998,“Observation, Analysis and Prediction of Fretting Fatigue in 2024-T352 Aluminum Alloy”, *Wear*, 221:24-36.

34. Finney, J.M, Evans, R.L., 1995, “Extending the Fatigue Life of Multi-Layer Metal Joints”, *Fatigue and Fracture of Engineering Materials and Structures*, pp.1231-1247.

35. Hurricks, P.L., 1970, “Mechanism of Fretting”, *Wear*, 15:389-409.

36. Waterhouse, R.B., Taylor, D.E., 1971, “The Initiation of Fatigue Cracks in a 0.7% Carbon Steel by Fretting”, *Wear*, 17:139-147.

37. Nishioka, K., Hirakawa, K., 1969, “Fundamental Investigations of Fretting Fatigue”, Part 3, *Bulletin of JSME*, 12(51): 397-407.

38. Endo, K., Goto, H., 1976, “Initiation and Propagation of Fretting Fatigue Cracks”, *Wear*, 38:311-324.

39. Hills, D.A., Nowell, D., O’Connor, J.J., 1988,“On the Mechanics of Fretting Fatigue”, *Wear*, 125:129-146.

40. Iyer, K. A., 1997, *Three-Dimensional Finite Element Analyses of the Local Mechanical Behavior of Riveted Lap-joints,* Ph.D. thesis, Materials Science and Engineering, Vanderbilt University, Nashville, TN.

41. Nowell, D. and Hills, D.A. (1990), “Crack initiation criteria in fretting fatigue”, *Wear*, v. 136, pp. 329-343.

42. Socie, D., 1987, “Multiaxial fatigue damage models”, *J. Eng. Mater. Technol*., v. 109, pp. 292-298.

43. Socie, D., 1993,“Critical plane approaches for multiaxial fatigue damage assessment”, in *Advances in Multiaxial Fatigue—ASTM STP 1191*, ASTM, PA, pp. 7-36.

44. Swalla, D., 1999, *Fretting Fatigue Damage Prediction Using Multiaxial Fatigue Criteria*, MS Thesis, Georgia Institute of Technology, Atlanta, GA.

45. Coffin, L. F. Jr., 1954, A study of the effects of cyclic thermal stresses on a ductile metal. *Trans. ASME*, v. 76, pp. 931-950.

46. Manson, S.S., 1953, “Behavior of materials under conditions of thermal stress”, *Heat Transfer Symposium*. University of Michigan Engineering Research Institute, pp. 9-75.

47. Walker, K., 1970, “The effect of stress ratio during crack propagation and fatigue for 2024-T3 and 7075-T6 aluminum”, in *Effects of environment and complex load history on fatigue life. ASTM STP 462*, American Society of Testing and Materials,Philadelphia, Pennsylvania. pp. 1-14.

48. Beuth, J.L. and Hutchinson, J.W., 1994, “Fracture analysis of multi-site cracking in fuselage lap joints”, *Computational Mechanics*, v. 13, pp. 315-331.

49. Vlieger, H. and Ottens, H.H., 1998, “Uniaxial and biaxial tests on riveted fuselage lap joint specimens”, *Report No. DOT/FAA/AR-98/33*, U.S. Department of Transportation, Federal Aviation Administration.

50. Fawaz, S.A., Schijve, J., de Koning, A.U., 1997, Fatigue crack growth in riveted joints, ICAF 97 – Fatigue in new and aging aircraft; Proceedings of the 19th ICAF Symposium, Edinburgh, UK, Junes 18-20, v. 1, pp. 553-574.

51. Newman, Jr. J.C., Raju, I.S., 1985, “Stress intensity factor equations for cracks in three-dimensional finite bodies subjected to tension and bending loads”, *NASATP-85793*.

52. Piascik, R.S, Willard, S.A, Miller M., 1994, "The characterization of widespread fatigue damage in fuselage", NASA 95N14920.

53. Wang, D.Y., 1982, "A study of small crack growth under transport spectrum loading", AGARD-CP-328, paper 14, 1983. Shorter version in ASTM STP 761, American Society for Testing and Materials, 1982:181–211.

54. Potter, J.M., Yee, B.G.W., 1983, "Use of small crack data to bring about and quantify improvements to aircraft structural integrity", AGARDCP-328, paper 4.

55. Lucas, F.M., Silva, Goncalves, J.P.M., Oliveira, F.M.F., P.M.S.T. de Castro, 2000, “Multiple Site Damage in Riveted Lap-Joints: Experimental Simulation and Finite Element Prediction, *International Journal of Fatigue*, Vol. 22, pp.319-338.

56. Eastaugh, G.F. Simpson, D.L., Straznicky, P.V., Wakeman, R.B., 1995, "A special uniaxial coupon test specimen for the simulation of multiple site fatigue crack growth and link-up in fuselage skin splices", NASA 96N24261.

57. Pitt, S., Jones, R., 1997, "Multiple-site and widespread fatigue damage in aging aircraft", *Eng. Failure Anal* ., Vol.4(4), pp.237–257.

58. Schijve, J., 1994, "Fatigue of aircraft materials and structures", *Int. J.Fatigue* Vol.16 (1), pp. 21–32.

59. Part 2 of the U.S. National Transportation Safety Board Report on the Fuselage Failure of an Aloha Airlines Boeing 737-200 in April 1988. In: Aviation Week and Space Technology, 4 September– 15 September 1989.

60. Maclin, J.R., 1991, "Performance of fuselage pressure structure. In: International Conference on Aging Aircraft and Structural Airworthiness", NASA CP 3160,pp.67–74.

61. Liao, M., Shi, G., Xiong, Y., 2001, "Analytical Methodology of Predicting of Predicting Fatigue Life Distribution of Fuselage Splices", *International Journal of Fatigue,* pp.177-185.

62. Harris, C.E., Piascik, R.S., Newman, J.C., 1999, "A Practical Engineering Approach to Predicting Fatigue Crack Growth in Riveted Lap Joints", NASA ICAF-CEH.

63. Hibbitt, Karlsson and Sorensen, Inc., 2003, ABAQUS/Standard 6.3/6.5 User’s Manual, Hibbitt, Karlsson and Sorensen, Inc., Pawtucket, RI.

64. Li, G., Sullivan, P.L., 2001, “Finite Element and Experimental Studies on Single-Lap-joints in Tension”, *Journal of Adhesion and Adhesives*, Vol.21, pp. 211-220.

65. Waterhouse, R.B., 1981, "Avoidance of Fretting Fatigue Failures", *Fretting Fatigue*, Applied Science Publishers Limited, pp.221-240

66. Vingsbo, O. Soderberg, S., 1981, "On Fretting Maps", *Wear*, 126, pp.131-147.

67. Ruiz, C., Boddington, P., Chen, K., 1984, ‘‘An Investigation of Fatigue and Fretting in Dovetail Joints,’’ *Exp. Mech*., 24, No. 3, pp. 208–217.

68. Smith, K.N., Watson, P., Topper, T.H., 1970, “A stress-strain function for the fatigue of metals”, *J. Mater.,* v. 5 (4), pp. 767-778.

69. Harish, G., Farris, T.N., 1997, “Modeling of skin/rivet contact: application to fretting fatigue”, A collection of technical papers, *AIAA/ASME/ASCE 38th Structural Dynamics, And Materials Conference,* v. 4, AIAA/Reston, VA, pp. 2761-2771.

70. Harish, G., Farris, T.N., 1998, “Effect of fretting contact stresses on crack nucleation in riveted lap joints”, AIAA paper 98-1746.

71. Harish, G., Farris, T.N., 1999, “An integrated approach for prediction of fretting crack nucleation in riveted joints”, *AIAA paper 99-1340*, April 1999.

71. Carter, R., 2003, *Assessment of hole drilling procedures on resulting fatigue lives*, M.S. Thesis, Georgia Institute of Technology, Atlanta, GA.

72. El-Hajjar, R.F., 2004, *Experimental Study and Analytical Modeling of Translayer Fracture In Pultruded FRP Composites*, PhD Thesis, Georgia Institute of Technology, Atlanta, GA.